Gravity and Magnetic Signatures of Different Types of Spreading in the Atlantic: Characterisation of Ocean-Continent Transition

Gabriella Alodia
School of Earth and Environment
University of Leeds

Submitted in accordance with the requirements for the degree of
Doctor of Philosophy

December 2021

The candidate confirms that the work submitted is her own, except where work which has formed part of jointly authored publications has been included. The contribution of the candidate and the other authors to this work has been explicitly indicated below. The candidate confirms that appropriate credit has been given within the thesis where reference has been made to the work of others The majority of the work included in this thesis has not been peer-reviewed and published.

The work in Chapter 2 of the thesis has appeared in a pre-print publication as follows: **Alodia, G.**, Green, C. M., McCaig, A. M. and Paton, D. A. (2020). Slope-Weighted Eccentricity: Automatic Terrain Classification of Atlantic Ocean Crust, *Earth and Space Science Open Archive*, `doi: 10.1002/essoar.10502634.1`. The work has been reviewed and is ready to be resubmitted. I led the study and wrote the manuscript, as well as developing the automatic terrain classification technique under the supervision of CMG and AMM. All authors discussed the results and commented on the manuscript at all stages.

Acknowledgements

This thesis will not exist without the full support of my supervisors, Chris Green and Andrew McCaig, as well as the research partner, Getech, plc. I would also like to thank Roger Clark and Ross Parnell-Turner who have given their time to read through and examine my work. And to Douglas Paton, who have been a part of the supervising team for most of the time I spent working on this PhD project.

I would not be able to carry out my study at the University of Leeds without the trust given by the Indonesian Endowment Fund for Education (LPDP), who have been sponsoring my studies ever since I carried out my masters. I would also like to thank my now colleagues at Institut Teknologi Bandung (ITB) for pushing me to get a PhD as soon as possible ever since I was still working as a short-term academic assistant. I am looking forward to work with you all in my upcoming academic career.

A very special thanks to Joe Cann, who has introduced me to the world of mid-oceanic ridge sciences. Thank you for giving me a chance to take part on the SR1806 Cocos-Nazca Cruise, which became my first ever experience of being a scientist on an international research cruise!

To Ezekiel Yenne, my fellow PhD in gravity and magnetic topic. I truly do not know how I would cope with this topic without you! Also to Roxana Stanca, for everything outside of our academic life! And to Peidong Shi, Georgian Manuc, and Daniel Tek for always working at the office at late hours. I will surely miss those moments, although the only thing we said to each other was ”See you tomorrow!”

To the SR1806 Science Party: Emily Klein, Debbie Smith, Charlie Dunham, Elya Latypova, Iker Blasco, Scott Curry, Ben Wernette, Sara Afshar, and Dominik Zawadszki. To Ross Parnell-Turner, who have been guiding the geophysical processing remotely, and to the whole SR Crew.

To the TN365 Science Party: especially to Henry Dick and Maurice Tivey. Also to my fellow watchstanders: Ma Qiang, John Greene, and Fiona Clark, and my cabin mate: Sarah Newnes. I would also like to thank InterRidge for sponsoring my involvement in this cruise.

To my dearest fellow Indonesian PhD Students in Leeds, for our productive writing camps and good humour: Triana R. Hadiprawoto, Saaduddin, Guntur P. Kusuma, M. Hizbul Wathon, Bintan Titisari and M. Taufikurrakhman. And a special thanks to Dandy A. Purawijaya for literally everything!

To my moral support: Angelina Prima, Gendis, and Panji. Rekha Sarbatta, Ayesha, Yahya, Idris, Adil, and Ahmed. Sanskruti Nakrani, Alix Dupas, and Clemence Enaud. Bonna Hativa and Myles. Eva Wishanti. And to my pre-examiners: Arnadi Murtiyoso, Anita T. Saraswati, and Alvina K. Kuncoro. The 'mock viva' was so much fun!

To everyone who have shared their PhD journey through my *@kenapaphd* podcast. You make me feel less alone and hopefully others too. To PPI UK, 18th ISIC, Leeds Bhangra Society, Get Out Get Active, and ICAF 2020. My playgrounds as a person who is too awkward to socialise without any common goals.

To the "Shut Up and Write!" sessions provided by the University of Leeds Library, as well as the people I met during the sessions. Having a dedicated writing session throughout the week has helped me a lot, especially during the pandemic when the time just flew by without us even noticing!

To my family: Mama Wita Anggraini, Papa Ohan Adiputra, and Dick Perthino Sebastian. Thank you for supporting my decisions and for raising me in a loving and colourful environment. I am partly glad that the pandemic has brought me to finish this thesis and have the viva voce at my own home.

To my aunt Windrati, my uncle Jeffry Gang, my cousins Jevonda E. Bamitha and Jevin E. Faradias, my grandma Astuti and my late grandpa Bambang Soeroso for a lifetime of support. To my other late grandpa, whom path as a sailor I partly inherent, Wijono Martodihardjo. And to my new family members: Ibu Indriarni Yuliati, Bapak Lintang Aru Widjojo, and Bondan Wisnuaji Putra. Thank you for the support and for understanding my unusual path of life.

This thesis is dedicated to Mas Bimoseno Pratama Putra. My loving, bold, and brainy husband. He knows everything: my ups and downs, my cries in the middle of the day when my paper got rejected or if anything went wrong, my joy every time I accomplished even the very minor goal, and all my fear. Thanks for sticking up with me this whole time. I only hope I would be able to do the same for you. My husband! I am addressing you as a husband! Love you :)

”Physics is really nothing more than a search for ultimate simplicity,
but so far all we have is a kind of elegant messiness.”

——Bill Bryson (2003)

Abstract

Magmatic accretion and tectonic extension have been recognised as the driving forces that forms the oceanic crust at mid-ocean ridges. At slow-spreading ridges, as the melt supply falls below a critical level, the plate separation is accommodated by long-lived detachment faulting rather than the typical magmatic accretion. The detachment fault accommodates exhumation of lower-crust and upper-mantle rocks to the ocean floor, forming domed structures known as Oceanic Core Complexes (OCCs). These domed structures are commonly found at one side of the spreading axis, indicating the occurrence of asymmetric spreading, as opposed to the symmetric fault-bounded abyssal hills commonly found over magmatic crust. Meanwhile, parts of the ultra-slow-spreading ridges are completely devoid of magmatism, where large detachment faults form continually at both axis flanks to facilitate the plate separation. At passive continental margins, these crustal morphologies are not recognisable by shipboard multibeam bathymetry data, as they have been buried by sediments deposited from the continental crust. Hence, this study aims to classify the types of oceanic crust based on the gravity and magnetic characteristics observed over the spreading axis by: (1) characterising the different types of spreading by quantifying parameters observed in shipboard multibeam bathymetry of an active slow-spreading ridge; (2) assessing and improving established gravity and magnetic data enhancement techniques to characterise and classify crustal types of a slow-spreading ridge, and; (3) applying the assessed enhancement techniques to the available gravity and magnetic data over a passive continental margin.

A novel automatic terrain classification technique, namely the slope-weighted eccentricity (SWE) is established based on the parameterisation of the shape, directionality, and curvature of the ocean floor where shipboard multibeam bathymetry data has been made available. The technique is developed at the 13-15° N Mid-Atlantic Ridge (MAR), where fault-bounded abyssal hills and domed OCCs are found along the spreading axis. The region is classified in SWE values, representing the general directionality of the terrain, where SWE ≤ 0.68

± 0.09 represents tectonic terrain, $0.68 \pm 0.09 < \mathrm{SWE} < 0.80 \pm 0.07$ represents extended terrain, and $\mathrm{SWE} \geq 0.80 \pm 0.07$ represents magmatic terrain.

Investigation by means of gravity and magnetic anomalies are also conducted to investigate spreading evolution and the crustal thickness variation in the 21-24° MAR region, where shipboard gravity and magnetic surveys are made available. Crustal thickness is computed from the isostatic mantle Bouguer anomaly (IMBA), a type of gravity anomaly developed in this study by removing the gravity effects observed within the water-crust and crust-mantle interfaces. The IMBA provides a measure of depth to Moho which are comparable to the depth to Moho interpreted from five refraction seismic surveys, with the mean discrepancy of less than 0.5 km at three of the survey lines, and less than 1 km at the rest of the survey lines. The evolution of the alternating spreading modes over 10 Ma is then identified by comparing the SWE number and computed crustal thickness over time through the interpreted magnetic chrons.

The crustal thickness computation as well as a number of existing gravity and magnetic data enhancement techniques are also applied to a larger set of data over the Labrador Basin, where a composite of field magnetic surveys is made available. Consistent with the recognised characteristics of ultra-slow-spreading ridge morphology, a significant area of thin crust is identified across the basin, where upper-mantle rocks are likely to be exhumed through large detachment faulting and went through a high degree of serpentinisation. One potential OCC with the size of around 20 km is found close to the extinct axis using the mantle Bouguer anomaly (MBA), pseudogravity of magnetic anomaly, and the automated coherency lineament analysis and selection (ACLAS) techniques.

This thesis has contributed to the establishment of a new grid-based interpretation technique that is tested and ready to be applied to shipboard multibeam bathymetry at various areas, as well as testing and applying several existing gravity and magnetic interpretation techniques to identify and characterise crustal structures.

Abbreviations

ACLAS	Automated coherency lineament analysis and selection
AF	African plate
FAA	Free-air anomaly
FZ	Fracture zone
GMRT	Global Multi-Resolution Topography synthesis
GMT	Generic Mapping Tool software
HD	Hyperextended domain
IEDA	International Earth Data Alliance
IMBA	Isostatic mantle Bouguer anomaly
KFZ	Kane fracture zone
LDEO	Lamont-Doherty Earth Observatory
LoG	Laplacian-of-Gaussian filter
MAR	Mid-Atlantic Ridge
MARK	Mid-Atlantic Ridge at Kane
MBA	Mantle Bouguer anomaly
NA	North American plate
NCEI	National Centers for Environmental Information
NOAA	National Oceanographic and Atmospheric Administration
NTD	Non-transform discontinuity
NVZ	Neo-volcanic zone
OBS	Ocean bottom seismometer
OCB	Ocean-continent boundary
OCC	Oceanic core complex
OD	Oceanic domain
PsGr	Pseudogravity
RCT	Residual crustal thickness
RMBA	Residual mantle Bouguer anomaly
RTP	Reduced-to-pole

SA	South American plate
SFZ	Southern fracture zone (at 21-24 N MAR)
SVDR	Second vertical derivative
SWE	Slope-weighted eccentricity
TD	Transitional domain
TDR	Tilt derivative
THDR	Total horizontal derivative
UTM	Universal Transverse Mercator
VDR	First vertical derivative

Contents

List of Figures

List of Tables

Chapter 1

Introduction

1.1 Rationale

In recent years it has been recognised that parts of slow-spreading ridges are characterised by typical magmatic spreading, while other parts are characterised by the formation of detachment faults. The growing number of discovery of areas dominated by detachment faults gave rise to questions related to the origin and evolution of these faults. This leads to studies on the underlying magmatic and tectonic activities in the oceanic crust through shipboard geophysical survey and ocean floor sampling.

The different types of spreading results in two distinct morphology, namely the magmatic and tectonic terrain. The magmatic terrain is characterised by linearly fault-bounded abyssal hills at both flanks of the ridge axis, while tectonic terrain is characterised by detachment faults that expose deep-seated rocks in the form of sporadic massifs. These massifs are now termed oceanic core complexes (OCC). These two features are key to understanding the thermal regime of the spreading axis.

As these oceanic crust features are buried at the passive margins, this study intends to explore the use of potential field data, i.e. gravity and magnetic anomalies, to characterise the features based on the signatures resulting from a number of potential data enhancement techniques. The characterisation will support risk assessment in the early stages of petroleum exploration, as the convex-upward geometry of the detachment fault is very different from the convex-downward or bookshelf faults normally found in thinned continental crust. If such faulting were accompanied by sedimentation, different sedimentary architectures would be expected. Understanding these processes is crucial in deep water sedimentary basins that span the ocean-continent transition, as there are substantial risks associated with not understanding the thermal regime and consequent hydrocarbon maturation from the source rock and likely structural and stratigraphic trap configuration. In addition, the study will enhance our understanding of the nature and the evolution of the oceanic crust, specifically at slow- to ultra-slow-spreading ridges.

1.2 Geological setting

1.2.1 The mid-ocean ridges: From continental rifting to full seafloor spreading

Over the years, it has been recognised that continental rifting was initiated either by a development of an upper mantle hotspot above a lower mantle plume or by a far-field tectonic stresses (Sengör & Burke, 1978). In both cases, when the continental crust stretched and separated in an approximately perpendicular direction to the initial rupture, a final continental break-up occurred, often followed by the formation of a region of highly extended terrain over the stretched upper crust. The rifting process ceases when the brittle stretching stops before reaching a critical value of strain necessary for the formation of an ocean basin, and subsequent subsidence takes place due to cooling (Sleep, 1971). A proto-oceanic trough then forms as the stretching allows a construction of a new ocean basin. The remaining parts of the rift then formed conjugate passive margins dominated by broad regional subsidence due to cooling following attenuation of the continental lithosphere.

The continental extension can be described in various models. Two of the most widely accepted models are the pure-shear model McKenzie (1978) and the simple-shear model Wernicke (1985). The pure-shear model results in a symmetric pattern of crustal and lithospheric thinning across pairs of conjugate margins, while in the simple-shear model, extension occurs along low-angle detachment faults and/or shallow-dipping crustal shear zones resulting in asymmetric pair of upper-plate and lower plate margins (Louden & Chian, 1999). The asymmetricity occurs as in the simple-shear model, the relative extension of crust and mantle lithosphere along any incipient detachment is nonuniform. These two models can be seen in Figure 1.1.

Over an actively upwelling plume, basaltic melts may be generated by adiabatic decompression melting when the mantle advectively rises beneath thinning lithosphere (Parsons & McKenzie, 1978). A large volume of magma intrusion is then produced at rifts initiated above or near the mantle plumes, as the elevated temperature facilitates melting at deeper levels (White & McKenzie, 1989). Where the consecutive rifting and spreading is accommodated by the high pressure and shear drag exerted by the asthenosphere on the lithosphere, the conjugate margins are termed passive margins. Hence, the deposited sediment strata during and following the break-up record the detailed history of the crustal movements over the area (Steckler & Watts, 1982). On the other hand, the sedimentary sequence also masks the syn-rift faults, intrusions, and sediments informing the break-up processes. Following the break-up, the opening of the ocean left the margin to become a divergent plate boundary termed mid-ocean ridge, where the creation of new oceanic crust is accommodated.

The mid-ocean ridge is classified according to its spreading rate, proportional to the upwelling rate of the mantle and the degree of melt produced. In this study, I will be focusing on slow-spreading and ultra-slow-spreading ridges. A slow-spreading ridge is defined when the full spreading rate falls between 1-5 cm/year, or 10-50 km/Ma (Macdonald, 1982). The ridge morphology is characterized by a 1.5-3.0 km deep median valley tens of kilometres wide with confined volcanism forming the axial volcanic ridge, which generally coincides with the central anomaly magnetic high or the Brunhes normal chron (Tivey & Johnson, 1987). Spreading centres are divided into segments, where the depth of the median valley is greatest at the segment ends, reflecting a lower magmatic input and a greater tendency of rifting. The ends of these segments are marked either by ridge-ridge transform faults or non-transform offsets, which will be explained more thoroughly in 1.2.3. If melt delivery over the segments falls below a critical level, the magmatic accretion is replaced by long-lived detachment faulting to accommodate the plate separation, which will be explained more thoroughly in 1.2.4.

Close to the Euler pole, spreading must occur in a highly oblique environment and forms another ridge morphology characterizing an ultra-slow-spreading ridge (Cannat *et al.*, 2006; Mendel *et al.*, 1997). Lower axial valley relief is observed, and melt delivery is focused away from the axis, building a thick crust largely by eruptions directly to the seafloor (Cannat *et al.*, 1999). However, some segments of the ultra-slow-spreading ridge appear to have little sign of seafloor volcanism, replaced by direct mantle exhumation to the seafloor through detachment faulting (Dick *et al.*, 2003; Sauter *et al.*, 2013).

1.2.2 Crustal structure and composition

As plates separate, the mantle upwelling is closely followed by decompression melting which produces layers of basaltic lavas erupted at the upper crust, and diabase and gabbros underneath resulting from a slower cooling and crystallisation. The diabase is formed as sheeted dykes as a response to tensional fracturing over deeper seated rocks underneath the upper crust, while gabbros are thought to form through fractional crystallisation of a slow-cooling melt at an intermediate depth near the base of the crust (Carbotte & Scheirer, 2004; O'Neill & Jenner, 2012; Smith & Cann, 1992). The upper mantle is composed of ultramafic rocks, marking the boundary of the petrologic Moho, which is typically found somewhat deeper than the seismological Moho. The generalised stratigraphy is similar to the ophiolite complex, which is the on-land exposures of inferred oceanic crust, and can be seen in Figure 1.2. This stratigraphy is matched with the typical P-wave velocity profile in the oceanic crust (Christeson *et al.*, 2019), which is explained in Table 1.1.

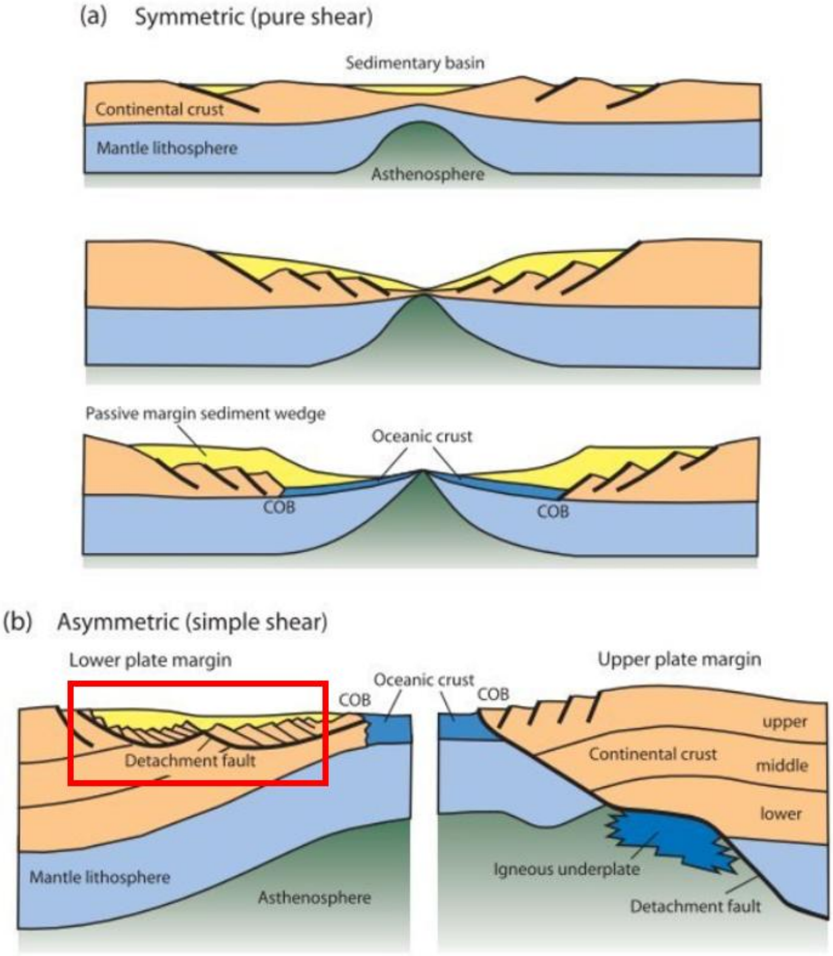

Figure 1.1: Conjugate margins illustrating pure-shear (McKenzie, 1978) and simple-shear (Wernicke, 1985) models, after Allen & Allen (2013), Lister *et al.* (1986), and Chian *et al.* (1995). (a) Symmetric margin (pure shear), and (b) asymmetric margin (simple shear) with continental detachment faults shown in the red rectangle. COB: continent-ocean boundary.

Following the melting, oceanic crust typically acquires a strong thermo-remanent magnetisation as the minerals cool below the magnetic blocking temperature or the Curie temperature (580°C), and sometimes chemical remanent magnetisation following alteration. The magnetisation over each layer has been studied over the years and it is found that most of the magnetisation is confined to the freshly erupted upper-crust basalt (Johnson & Tivey, 1995). The acquired field within this layer is parallel to the Earth's field at the time of the cooling, which enables the oceanic crust to be dated. However, when the oceanic crust formed during a quiet magnetic period of prolonged single polarity (e.g., during the Late Jurassic and the Late Cretaceous), the dating is not quite straightforward. There are still debates regarding the cause of both periods of prolonged single polarity, now widely known as the Jurassic and the Cretaceous quiet zones (Barrett & Keen, 1976). The low-amplitude magnetic anomalies over these zones causes difficulty both in crustal age dating and crustal structure identification (Larson & PITMAN III, 1972). Other than that, magnetisation can also occur to exhumed peridotites that undergo chemical remanent magnetisation through serpentinisation (Oufi *et al.*, 2002). The study found that the magnetic susceptibility increases rapidly for levels of serpentinisation over 75%, making it responsible for a significant component of the observed anomalies. The magnetisation of typical oceanic rocks can be seen in Table 1.2.

The gravitational response of the oceanic crust depends on the density of each layer. At passive margins with little to no presence of salt, volcanic, and carbonate rocks, the density of each layer of sediments follows an exponential density-depth curve (Cowie & Karner, 1990), with densities varying from $1.95 \times \mathrm{kg/m^3}$ to $2.60 \times 10^3\ \mathrm{kg/m^3}$. The underlying oceanic crust generally has higher density than the continental crust ($\sim$2.80 $\times 10^3\ \mathrm{kg/m^3}$), with the density of the mantle around $3.30 \times 10^3\ \mathrm{kg/m^3}$. These density values are used to correct the water-crust and crust-mantle interfaces over a mid-ocean ridge, or water-sediment, sediment-crust, and crust-mantle interfaces over a passive margin, using Fourier methods (Parker, 1973).

Another important component of the whole crustal structure is the isostatic compensation in the oceanic lithosphere. McKenzie & Bowin (1976) recognise three models of isostatic compensation: (1) no compensation, where the observed gravity anomalies are thought to be produced solely by the density contrast; (2) simple Airy isostasy, where both long- and short- wavelength topography is compensated by the variations in the crustal thickness, and; (3) compensation including an elastic plate, where only long-wavelength features are compensated as they bend the plate. In this study, I use the third model to compensate the isostatic response of the oceanic crust over an elastic plate. The illustration of these isostatic compensation models can be seen in Figure 1.3. Lastly, the base of the oceanic lithosphere is found at the depth in which its mechanical behaviour changes from rigid to plastic.

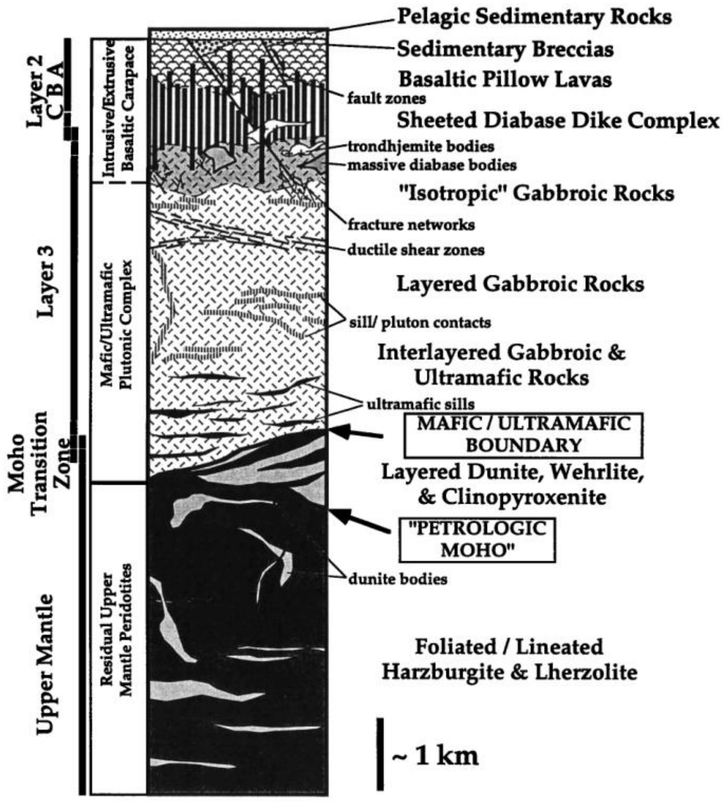

Figure 1.2: Prevailing view of the internal structure and composition of oceanic crust at magmatic ridge and correlations with seismic data, after Karson (1998). Acoustic velocities of rock samples from these units measured under laboratory conditions are commonly correlated with the generalized seismic velocity structure of the oceanic lithosphere.

Table 1.1: Global seismic velocity structure of the oceanic crust at slow-spreading ridges, after Christeson *et al.* (2019)

Layer	**Lithology**	**Thickness (km)**	**P-wave (km/s)**
Layer 2	Basaltic lava	1.98±0.67	3.23±0.58
Layer 3	Gabbro: top layer	4.19±1.20	6.12±0.28
	Gabbro: base layer		7.07±0.12
Layer 4	Upper mantle	-	7.67±0.28

Table 1.2: Magnetisations of typical oceanic rocks, after Searle (2013)

Rock type	**Magnetisation (A/m)**	**Susceptibility (SI)**	**Reference**
Young basalt	40-42	-	Johnson & Tivey (1995)
Basalts	2.1-2.7	-	Lowrie (1997) Harrison (1976)
Basalts	5.24-5.4	0.02-0.04	Pariso & Johnson (1991)
Dykes	1.6	0.02	Pariso & Johnson (1991)
Gabbro	2.5	-	Pariso & Johnson (1993)
Olivine gabbro	1-2	-	Pariso & Johnson (1993)
Moderately serpentinised peridotite	<5	<0.05	Oufi *et al.* (2002)
Strongly serpentinised peridotite	4-10	0.07	Oufi *et al.* (2002)

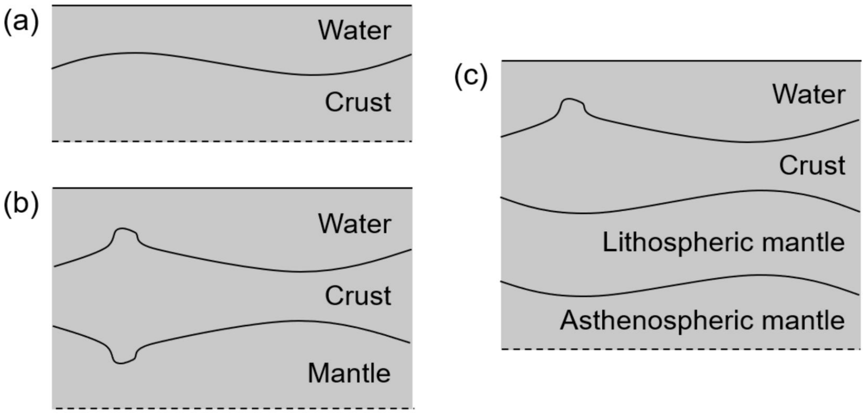

Figure 1.3: Models for isostatic compensation in the oceanic lithosphere, modified after McKenzie & Bowin (1976) and Searle (2013). (a) No compensation. (b) Simple Airy isostatic compensation. (c) Compensation including an elastic plate. Explanation of each model can be found in the text.

1.2.3 Ridge axis, transform faults, and non-transform offsets

As explained in 1.2.1, the ridge axis is usually orientated roughly normal to the spreading direction. Over slow-spreading to ultra-slow-spreading ridges, the ridge axis is formed as a broad median valley caused by tectonic thinning and necking of the lithosphere (e.g., Buck *et al.*, 2005; Chen & Morgan, 1990). They are offset along their lengths by a variety of structures which split the ridge into spreading segments. Depending on their length, the offsetting structures are defined as transform faults and non-transform offsets that host most of the seismicity over the mid-ocean ridge.

Generally, spreading segments mark the presence of a mantle upwelling over a variety of locations in the oceanic lithosphere. As each of the segments spreads nearly orthogonal to the axis, ridge-ridge transform faults are formed as new plate boundaries (Figure 1.4). As the transforms are slipping in a circle about a rotation pole, many of these transform faults reflect the original geometry of the continental break-up (Morgan, 1968). The transform faults are characterised by transform valleys, partly as an isostatic response to thinner crust at the transform (White, 1984) and partly due to the thermal contraction and plate extension normal to the transform direction (Pockalny *et al.*, 1996). At ridge-transform intersections, the transform valleys produce deep basins called nodal basins which have been interpreted as a result of the viscous head loss of the rising mantle asthenosphere and due to a regional isostatic balancing force (Sleep & Biehler, 1970). The continuously slipping transform faults leave traces of inactive scars called fracture zones, marking ancient spreading directions of the adjacent plates.

While transform faults offset ridge segments on scales down to ~100 km, closer-spaced ridge offsets are marked by structures of a few tens of kilometres called non-transform offsets or discontinuities (NTDs). Unlike the transform faults, these small offsets lack evidence of slipping forces. The closely-spaced ridge segments form an oblique offset that may migrate up and down the axis, leaving trails of shallow V-shaped valleys (e.g., Pockalny *et al.*, 1995).

1.2.4 Magmatic accretion and tectonic extension

Parts of slow- to ultra-slow-spreading ridges are characterised by typical magmatic spreading (e.g., Macdonald, 1982), detachment faulting (e.g., Cann *et al.*, 1997), and smooth volcanic seafloor (e.g. Cannat *et al.*, 2006). These features are formed based on the degree of magmatism occurs in the ridge axis. (Buck *et al.*, 2005) introduced the fraction of the plate separation rate, M, which illustrates the accommodation of plate separation through magmatic dyke opening. $M = 0$ defines the condition where dykes account for none of the plate separation, while $M = 1$ is where dykes accommodate all the plate separation. The study found that detachment faulting occurs at one side of

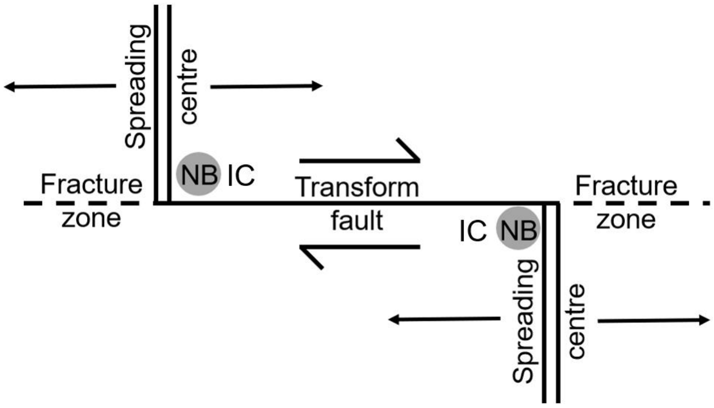

Figure 1.4: Ridge-ridge transform fault. Modified from Searle (2013). A left-lateral offset of the plate boundary is accompanied by right-lateral slip on the transform fault. Nodal basins (NB) forms at inside corners (IC) of the ridge-transform junctions.

the ridge when the magmatic accretion falls under 50%, or where $M = 0.5$, while the other flank experienced a normal magmatic accretion. (Tucholke *et al.*, 2008) refine the study by experimenting with models with a variation of M values and found that this asymmetry occurs only when $\sim 0.3 \leq M \leq 0.5$ (Figure 1.5). When the M value falls below the critical value, or as low as $M \leq 0.2$, the resulting seafloor at both flanks might consist almost entirely of faulted surfaces. This morphology is similar to the smooth seafloor observed at ultra-slow-spreading ridges, e.g. in the Southwest Indian Ridge (Cannat *et al.*, 2006).

The different spreading modes of spreading are identified by observing the bathymetry in the near-ridge environment. In the study of (Biari *et al.*, 2017), magmatic spreading is depicted by the formation of a volcanic-volcanic seafloor pair over the ridge, while a more tectonic one forms a corrugated-volcanic seafloor pair. The corrugation depicts the presence of detachment faults at one side of the ridge. These two types of seafloors are commonly found at slow-spreading ridges. In ultra-slow-spreading ridges, parts of the spreading ridge are characterised with excess volcanism and thick crust, while other parts appear to have been completely devoid of volcanism for millions of years (e.g., Sauter *et al.*, 2013). Therefore, at axes with little to no axial volcanism, a smooth-smooth seafloor pair formed, depicting the relatively symmetrical faulted surfaces as explained in (Tucholke *et al.*, 2008). The illustration of these three pairs of seafloors can be seen in Figure 1.6.

It is common to find at least two different types of seafloor morphology in a near-axis area bounded by two transform faults. For instance, the magmatic and tectonic pairs are found in an area bounded by the Fifteen-twenty and Marathon fracture zones (Smith *et al.*, 2008). The variation of the morphology of the seafloor along the spreading axis will be discussed in this subsection.

Magmatic accretion over slow-spreading ridge

Interpretive models of magma chambers were introduced in Sinton & Detrick (1992), whose initial assumption is that all mid-oceanic ridges are created as a result of fully magmatic processes, with variations in geometry relating to spreading velocity, the magma supply, and its cooling (Calvert, 1995). When the melt delivery is greater than the critical level, fissuring and normal faulting occurs over the magmatically accreted ridge axis as a response to the tension over the newly formed lithosphere. These fissures and faults grow both in length and offsets, linking to form larger faults, and are found within the axial volcanic ridge during the time of the accretion. Some of the fissures grow into fractures, allowing emplacement of new melt.

The magmatic accretion is characterised by linearly fault-bounded abyssal hills (e.g., Macdonald, 1982), which consist of the axial magma chamber and the inward dipping normal faults. The accretion, followed closely by normal faulting, commonly occurs in the brittle environment where the magma supply is followed closely by the fast cooling of the lithosphere. These faults have moderate offsets and are roughly symmetrical across-axis. In effect, the crustal layers are still intact, with no lower-crust rock exhumation to the seafloor.

Tectonic extension over slow-spreading ridge

Numerical modelling suggests that a change of style of spreading occurs when the melt supply falls as low as ∼50% of that required to accommodate plate separation (e.g., Buck *et al.*, 2005). As the magmatic component falls below a critical level, the plate separation is accommodated by long-lived detachment faulting rather than magmatic accretion (e.g., Tucholke & Lin, 1994). This detachment faulting breaks down the simple layered model of the crustal structure, specifically at the ends of the ridge segments, where the mantle melt delivery is a lot less compared to those at the middle of the segments. The limitation of the lava flow at these segment ends, coupled by creation of transform faults from two opposing spreading axes, allows an exhumation of lower-crust and upper-mantle materials to the ocean floor. This strong tectonic extension at one flank of the axis leads to a strongly asymmetrical pattern across the axis, as detachment faults can take up between 70% and 100% of the relative plate motion (e.g., Okino *et al.*, 2004).

The geometry of detachment faults is documented in the 'Chapman Model' as a community statement and consensus on the definition of OCCs (Escartín & Canales, 2011). The term 'detachment' itself originates from the clear discontinuity between upper-plate and lower-plate rocks discovered at this typical low-angle fault, originally observed at continental crust (Buck, 1988). The presence of oceanic detachment faults and OCCs is identifiable by massifs, generally with corrugated surfaces, indicating the exhumation of deeper rocks through a rolling-hinge mechanism (Buck, 1988; Hamilton, 1988; Wernicke, 1985). The first identified candidates of OCCs are published in Cann *et al.* (1997), where two local massifs located at the inside corners of the Atlantis FZ were studied. The exposure has led to studies of potential faulting that cause the lower-crust and upper-mantle materials to be exposed using various sets of geophysical data (e.g., Blackman *et al.*, 1998; Tucholke *et al.*, 1998), dredging and submersible vehicle dives (e.g., Blackman *et al.*, 2002; Dick *et al.*, 2008; MacLeod *et al.*, 2002), and deep drilling (e.g., Blackman *et al.*, 2004; Dick *et al.*, 2000).

The following studies, e.g., Smith *et al.* (2008), revealed that detachment faulting apparently governs a larger part of the whole spreading segments. Numerous sporadic massifs are identified at the 13-15° N of MAR, which locations are consistent with several ultramafic samples (e.g., Escartín & Cannat, 1999) and thin crust inferred from gravity data (Smith *et al.*, 2008). MacLeod *et al.* (2009) then carried out a study at the southern part of the 13-15° N MAR area to explain the life cycle of the OCCs (Figure 1.8). According to the study, an OCC is active when the magma supply is waning, triggering the thinning of the crustal layer that allows the formation of secondary hydrous minerals such as talc and serpentine. These minerals cause the weakening of the lithosphere, strain localisation at certain faults, followed by rotation of the footwall. The rotating mechanism of the footwall often resulted in corrugation parallel to the spreading direction (e.g., Buck, 1988; Cann *et al.*, 1997). The OCC becomes inactive when sufficient magma is emplaced at its nucleation point (the spreading axis), overwhelming the development of the fault. The flux melt from the Neo-Volcanic Zone (NVZ) delivered to the fault's footwall will ultimately terminate the OCC.

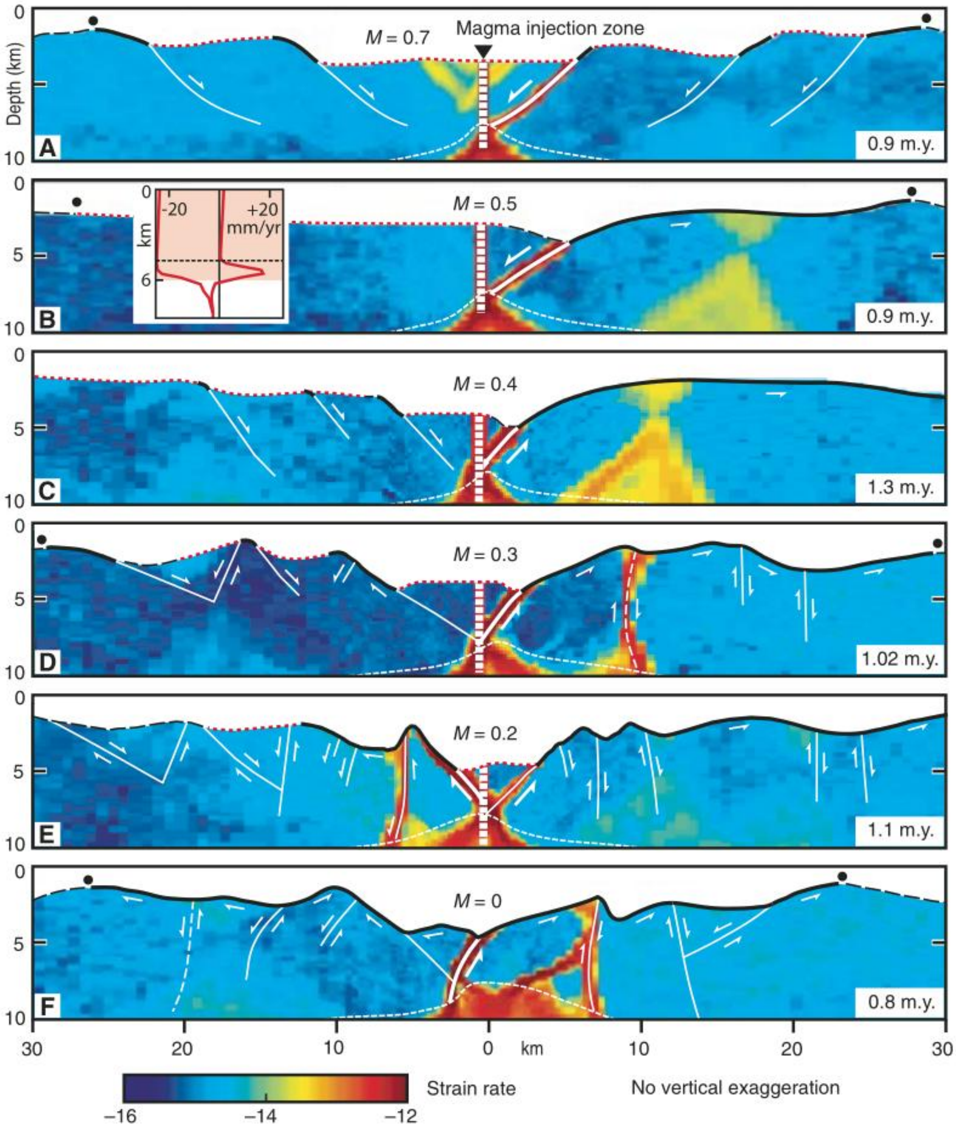

Figure 1.5: Snapshots of modelled fault behaviour for values of M (the fraction of total plate separation taken up by accretion of melt) between 0.7 and 0, after Tucholke *et al.* (2008). Dots: breakaways of initial faults. Dashed seafloor: original model of seafloor. Red dotted seafloor: seafloor formed dominantly by magmatic accretion. Solid bold seafloor: fault surface. Inset B shows the direction and magnitude (mm/yr) of flow of material in each plate immediately adjacent to 6-km-high magma injection zone (shaded). Dashed near-vertical lines: faults initiated $\geq$ 4 km off axis. Dashed horizontal line: depth where detachment intersects injection zone.

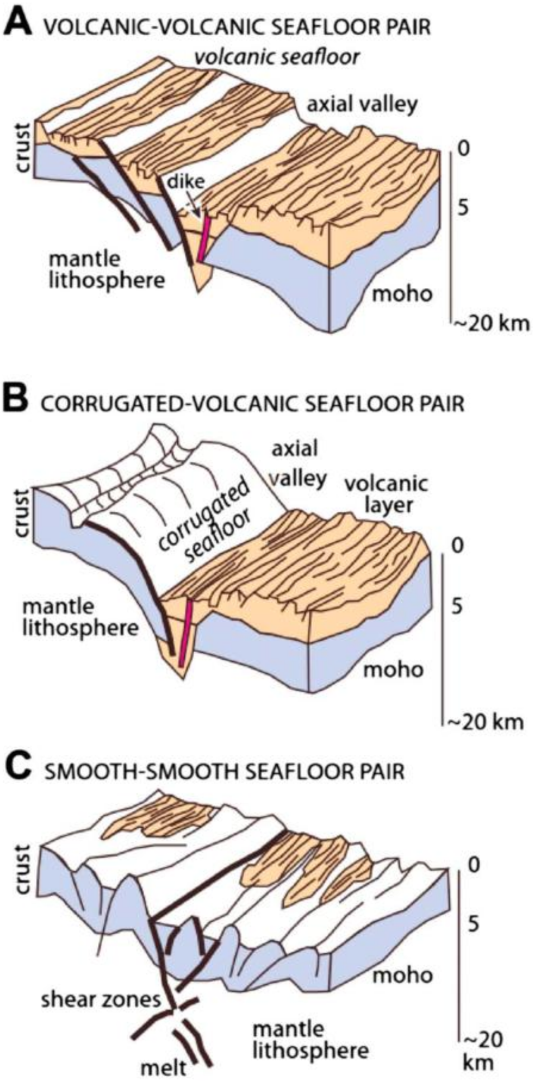

Figure 1.6: Lithosphere-scale sketches of the axial region at magma-poor spreading axis, shown in order of decreasing melt supply, after (Biari *et al.*, 2017). Modes A (volcanic-volcanic) and B (corrugated-volcanic) develop at slow- to ultra-slow-spreading segments. Mode C (smooth-smooth or smooth-volcanic), with little to no axial volcanism, appears specific to magma-poor ultra-slow-spreading ridges (after Cannat *et al.* (2006) and Dean *et al.* (2015)).

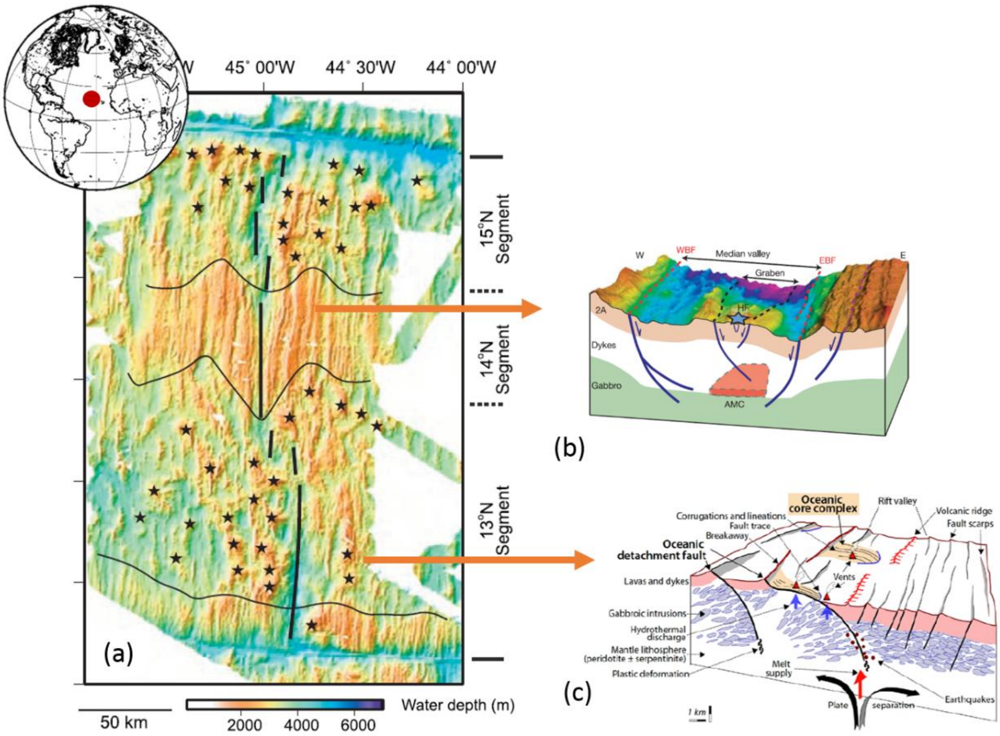

Figure 1.7: Illustration of the different types of spreading over a slow-spreading ridge. (a) An area between Fifteen-Twenty and Marathon Fracture Zones, after Smith *et al.* (2008), where both types of spreading are observed. Stars represent OCCs; (b) The geometry of the magmatic type of spreading, in which the Axial Magma Chamber (AMC), faults, and subsurface layers in the Lucky Strike Volcano are studied, after Singh *et al.* (2006); (c) Diagram of oceanic detachment fault from the Chapman Conference on Detachments in Oceanic Lithosphere, after Escartín & Canales (2011).

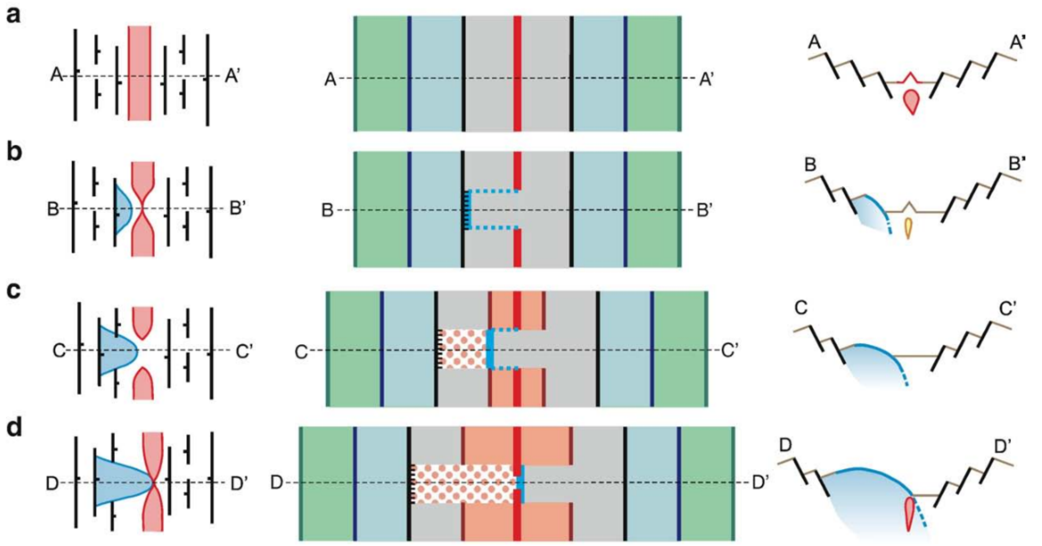

Figure 1.8: Illustration of the life cycle of OCC, after MacLeod *et al.* (2009). As the fault evolves from the zone of emergence towards the spreading axis (a), the main locus of plate separation which was centred in the zone of emergence is also migrated towards the axis (b) until they are both in line (c). NVZ is then triggered in the subsurface of the axis, increasing magma supply and delivering melt (d). The flux of melt from this NVZ is delivered to the fault's footwall, which in time will ultimately terminate the development of the OCC the detachment zone (dyking).

Magmatism and tectonism over ultra-slow-spreading ridges

At separation rate of < 10 km/Ma, the spreading ridges experience another form of magmatic accretion and tectonic extension over its segments (Dick *et al.*, 2003). The underlying mantle can be unusually cold (e.g., Mendel *et al.*, 1997) and the spreading can occur in a highly oblique orientation (e.g. at Southwest Indian Ridge) with only a small component of normal opening (e.g., Cannat *et al.*, 2006). Magmatism is confined to small areas where the plate separation is orthogonal to the local plate boundary (Figure 1.9). The magmatic input to the lithosphere is reduced by the occurrence of long segments of oblique axes, and further diminished over the highly oblique axes. Over these amagmatic segments, large detachment faults form continually to drive the plate separation but dipping in alternating directions and occur on a time scale of ~1 Ma (Figure 1.10). The detachment faulting results in exposures of highly serpentinised peridotites at both flanks of the ridge (Michael *et al.*, 2003). The symmetric, smooth-flanked ridges up to 2000 m high morphology is defined as smooth seafloor (Cannat *et al.*, 2006).

1.2.5 Passive continental margin types and the subsequent sedimentary deposition

During break-up, the upper-crust deforms by brittle extensional faulting, while the ductile lower-crust and upper-mantle deform by plastic stretching and thinning. At regions where the latter occurs, lateral offset and a wide variety of asymmetric structures involving detachment faulting may develop (Lister *et al.*, 1991). Following break-up, a new ocean basin is formed, as well as its conjugate passive continental margins. According to Keen (1987), passive continental margins involve strongly attenuated continental crust stretched over a region of 50-150 km, and exceptionally as much as 400-500 km, overlain by thin or thick sediment prisms. This type of margin is characterised by seaward-thickening prisms of marine sediments overlying a faulted basement with syn-rift sedimentary sequences.

Passive continental margins can be categorised as volcanic and non-volcanic margins based on its underlying volcanic activities. Specifically, White *et al.* (2003) classify parts of the Atlantic Ocean margins as ‘hot’ and ‘cold’ margins (Figure 1.11). In areas of ‘hot’ margins (e.g. at East Greenland margin), lithospheric thinning has taken place over an upwelling mantle plume. Kilometre-thick piles of seaward-dipping lava flows are found close to the seabed, indicating the underplating lava flows. Meanwhile, in areas of ‘cold’ margins (e.g. at Labrador and Iberian margins), little evidence of magmatism is found prior to the forming of the oceanic crust. Several tens of kilometres wide exposures of mantle rocks are found, suggesting the occurrence of oceanic detachment faulting. The cross-profile illustration of the passive margin structures can be seen in Figure 1.12.

Finally, the subsequent sediment deposits over the passive margins have been formed during three successive stages (Montadert *et al.*, 1979). The first stage occurs prior to the rifting, where continental basement may already be overlain by sediments. The second stage, defined as the syn-rift, occurs over the time of initial rifting and continental stretching. The syn-rift sediments may extend to the continental borderlands and are typically deposited in half-grabens as a result of stretching and thinning of the continental crust and lithosphere. The last stage, defined as the post-rift, occurs subsequent to continental break-up and onset of seafloor spreading. The strata are characterised by a post-rift break-up unconformity and are generally un-faulted, indicating a quieter tectonic environment. The deposited sediments also affected the local isostatic equilibrium by presenting a flexural effect due to the sediment loading. The illustration of the sedimentary facies deposited over these stages can be seen in Figure 1.13.

1.3 Aim and objectives

The aim of this study is to classify the types of basement at a passive continental margin based on characteristics observed close to the spreading axis. In doing so, I conduct observations on the bathymetry, gravity, and magnetic data over parts of the Mid-Atlantic Ridge (MAR), followed by observations over the extinct ridge and the continental margin of the Labrador Basin. To achieve it, the specific objectives are:

1. To develop an automatic terrain classification over known structures. The algorithm is built based on the parameterisation of the shape, directionality, and curvature of the seafloor around the Central Mid-Atlantic Ridge observed in shipboard multibeam bathymetry data. The seafloor will be classified based on its modes of spreading.

2. To apply blind trial of the developed algorithm and compare the results with gravity and magnetic data over slow-spreading ridges enhanced by more widely known techniques. Assessments of these techniques are also carried out to broaden our understanding of the nature and evolution of the oceanic crust over a slow-spreading ridge.

3. To apply the assessed techniques to characterise and classify the crustal types over a less studied continental margin based on modes of spreading.

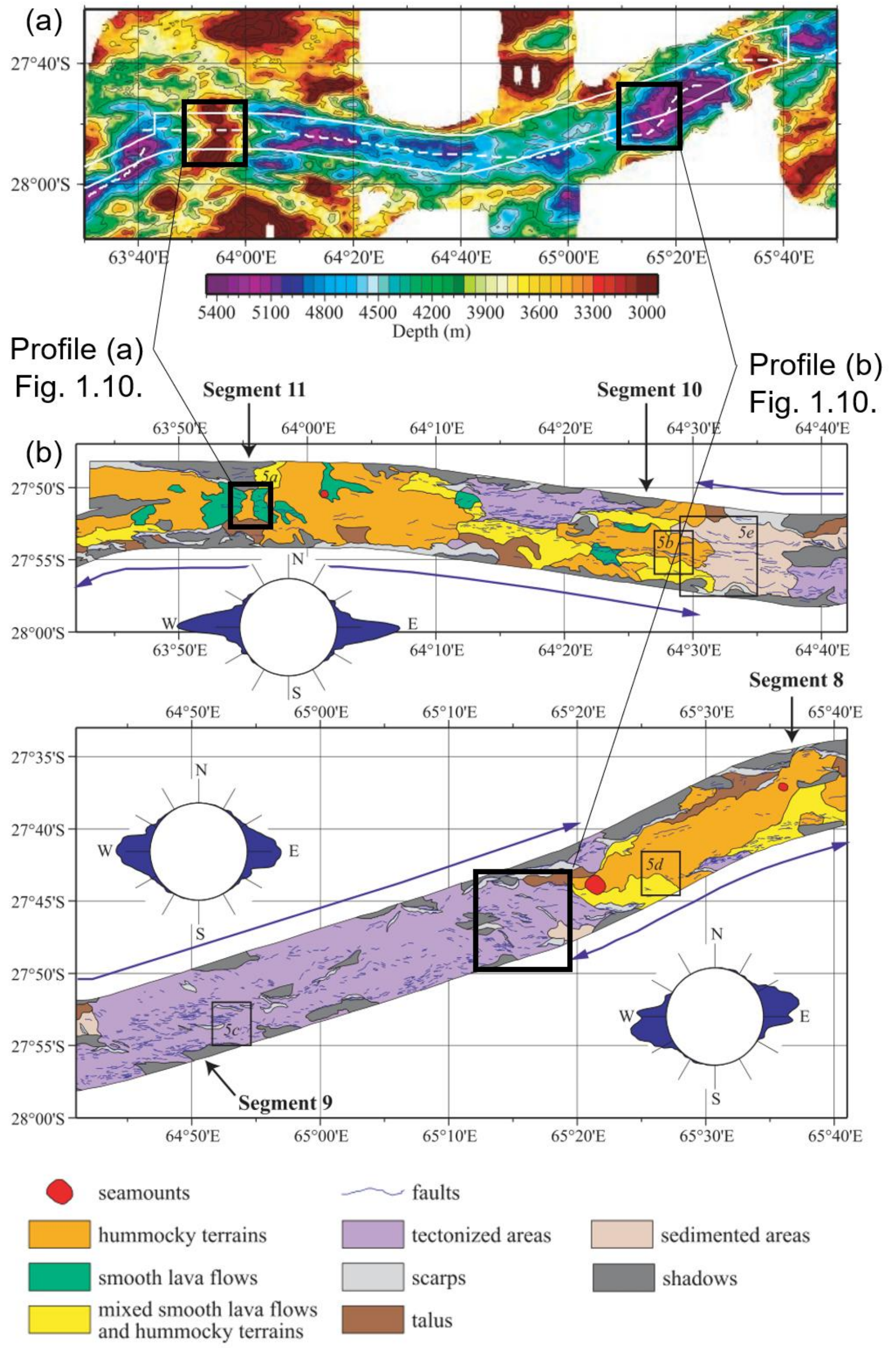

Figure 1.9: Illustration of the different types of spreading over an ultra-slow-spreading ridge. (a) Bathymetry of the Southwest Indian Ridge between 63° 30' E and 65° 50' E, after Sauter *et al.* (2004); (b) Map of the volcanic textures and tectonised areas identified on side scan sonar images, after Sauter *et al.* (2004).

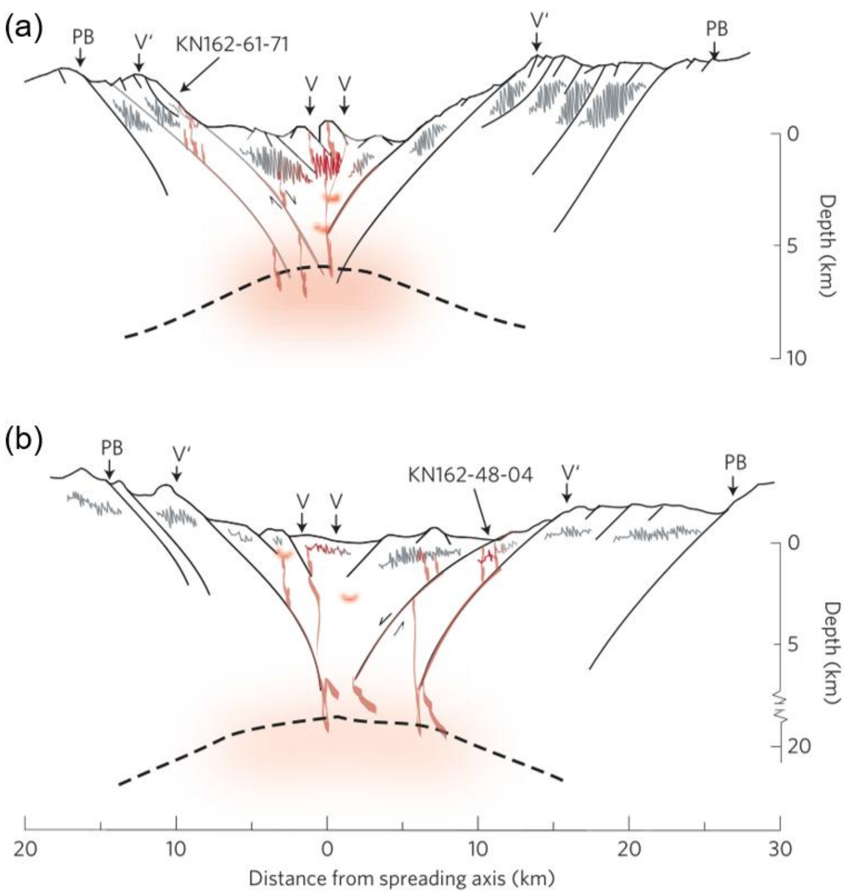

Figure 1.10: Illustrated profiles of selected magmatic (a) and tectonic (b) areas over the ultra-slow-spreading ridge axes, after Standish & Sims (2010). The profiles contain the neovolcanic zone (V), the plate boundary zone (PB, active faulting), and the crustal accretion zone (V'). The intensity and width of the melt injection zone (red) and the thickness of the sheeted dykes (grey) indicate the robustness of melt generation.

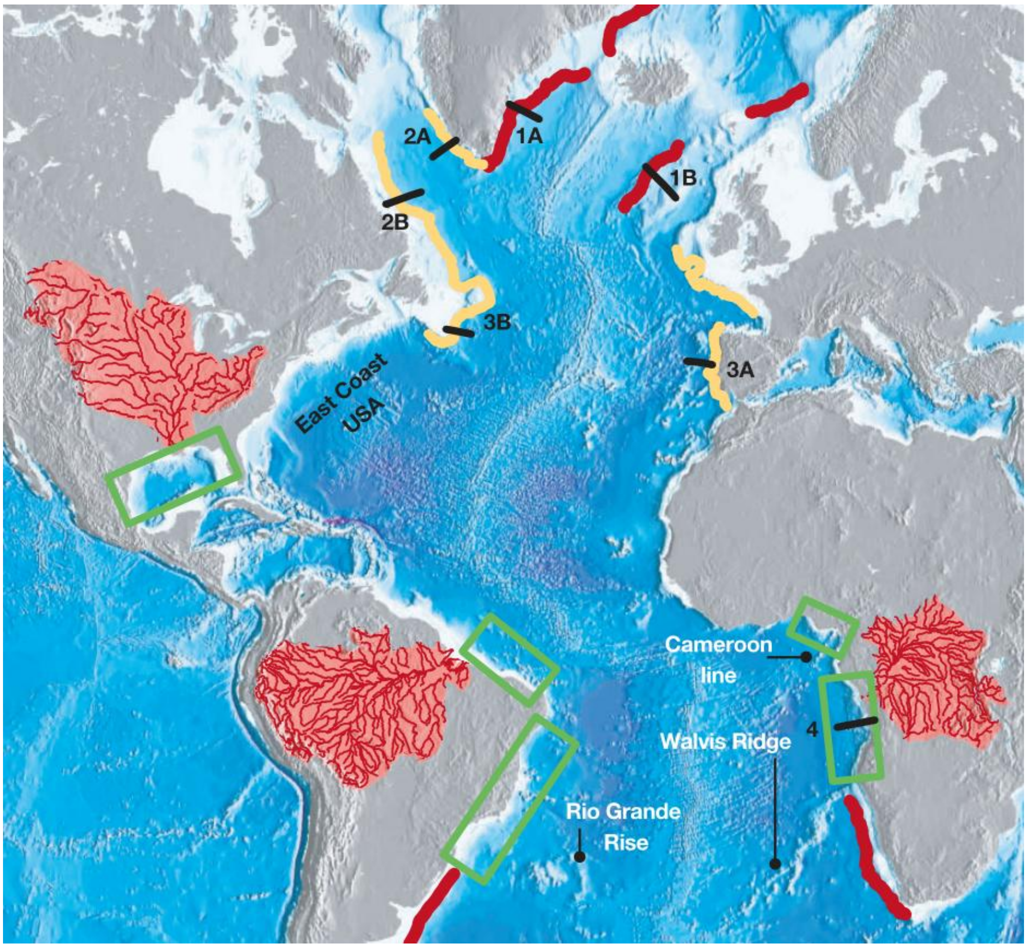

Figure 1.11: Margin categories in the Atlantic Ocean, after White *et al.* (2003). Red lines: 'Hot' margins, where large volumes of magma were generated by rifting over a mantle plume. Yellow lines: 'Cold' margins, where there is evidence for exhumation and serpentinisation of the lithospheric mantle. Green boxes: Zones of deep-water exploration. Pink and red regions: Drainage catchments. The study focuses on the 'cold' margins of Labrador Sea at 2A and 2B.

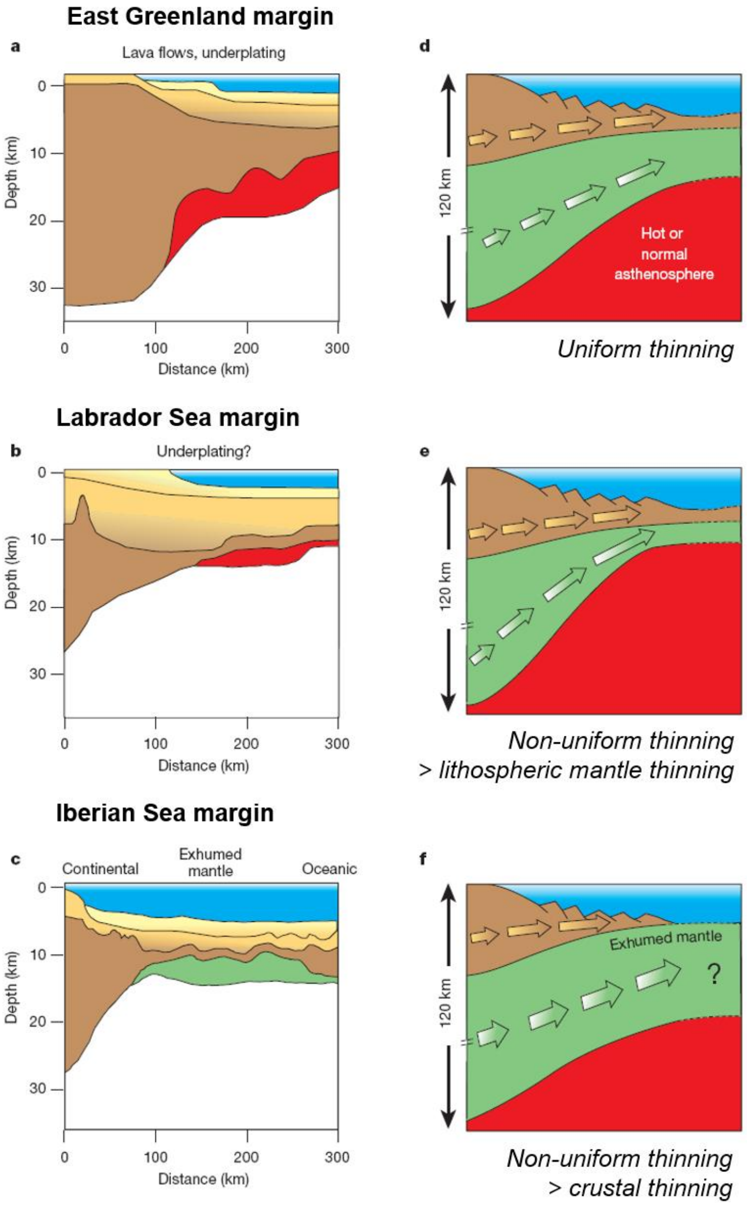

Figure 1.12: Structure and evolution of extensional margins, modified after White *et al.* (2003). (a), (b), and (c) are cross-sections that illustrate the crustal structure of one side of three conjugate margin pairs from the North Atlantic Ocean (1A-B, 2A-B, and 3A-B seismic lines at Figure 1.11, respectively). Blue: sea water. Yellow and light brown: sedimentary rocks. Dark brown: crust. Red: magmatic underplating. Green: serpentinised mantle rock. (d), (e), and (f) are illustrations of three possible configurations of crustal and lithospheric mantle thinning. Blue: sea water. Brown: crust. Green: lithospheric mantle. Red: asthenospheric mantle.

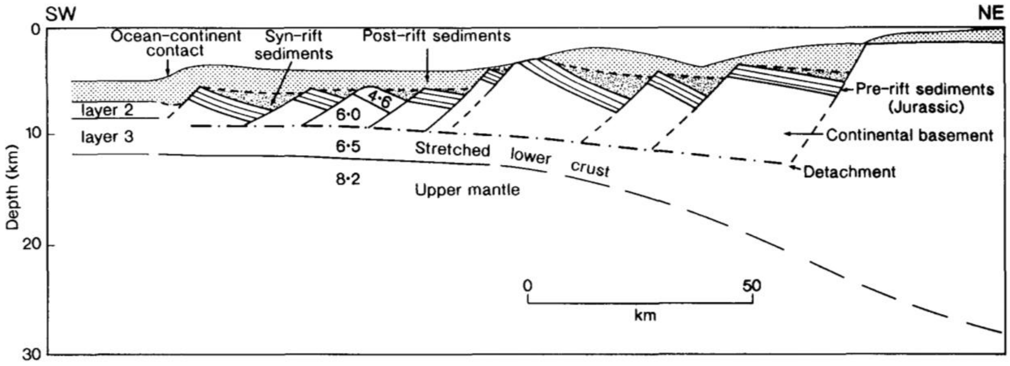

Figure 1.13: Example of the structure of a 'cold' margin at the Bay of Biscay showing thin post-rift sediments, after Bott (1992), based on De Charpal *et al.* (1978) and Le Pichon & Barbier (1987). Shown in figure: early Cretaceous syn-rift sediments, tilted fault blocks of continental basement overlain by Jurassic pre-rift sediments, detachment surface separating lower and upper crust, and continent-ocean contact beyond foot of slope and pattern of crustal thinning.

1.4 Data repositories

This research exploits a wide range of data, spanning from multi-resolution bathymetry data, ship-borne gravity and magnetic data, satellite-derived gravity and magnetic data, globally-synthesized/gridded gravity, magnetic, and sediment thickness data, interpreted 2D seismic reflection lines, interpreted 2D seismic refraction lines, and seismicity/earthquakes observed by hydrophones. The list of the data repositories and the cited publications used throughout the study can be seen in Table 1.3.

Table 1.3: List of data repositories and citations

Data	Type	Source	Link/citation
Bathymetry	Multi-resolution	GMRT[1]	gmrt.org/GMRTMapTool
	Satellite-derived	SIO[2]	topex.ucsd.edu/marine_grav
	Global synthesis	Getech	getech.com
Gravity anomaly	Ship-track	IEDA[3]	app.iedadata.org/databrowser
	Satellite-derived	SIO	topex.ucsd.edu/marine_grav
	Global synthesis	Getech	getech.com
Magnetic anomaly	Ship-track	IEDA	app.iedadata.org/databrowser
	Global synthesis	EMAG2v2[4]	Maus *et al.* (2009)
	Global synthesis	EMAG2v3[5]	Meyer *et al.* (2017)
	Global synthesis	Getech	getech.com
Sediment thickness	Global synthesis	Globsed[6]	Straume *et al.* (2019)
Seismic reflection	Interpreted profiles	Published study	Gouiza & Paton (2019)
Seismic refraction	Interpreted OBS profiles	Published studies	Dannowski *et al.* (2010)
			Dannowski *et al.* (2011)
			Dannowski *et al.* (2018)
			Kahle *et al.* (2016)
			Delescluse *et al.* (2015)
Seismicity	T-wave source locations	Published study	Smith *et al.* (2003)

[1] GMRT: Global Multi-Resolution Topography [2] SIO: Scripps Institution of Oceanography [3] IEDA: Interdisciplinary Earth Data Alliance [4] EMAG2v3: Earth Magnetic Anomaly Grid version 2 [5] EMAG2v3: Earth Magnetic Anomaly Grid version 3 [6] Globsed: Total Sediment Thickness of the World's Oceans and Marginal Seas

1.5 Thesis roadmap

The thesis will be arranged in five chapters.

In Chapter 1, I have provided the rationale, geological setting based on literature review, aim and objectives, data repositories, and the roadmap of the thesis. The general nomenclature and concepts used in this thesis is also discussed in this chapter.

In Chapter 2, I will focus on the use of multibeam bathymetry data to characterise the different types of terrain resulting from the different types of spreading. The characterisation will be carried out based on the shapes and directionality of the key features observed over the different types of terrain. The observed characters are then used to develop an automatic terrain type classification technique over a slow-spreading ridge. The technique is tested and applied over synthetic and real-world terrain patches, representing the tectonic and magmatic terrain, before being applied to a set of multibeam bathymetry data through a moving window. I selected the 13-15° N area of the MAR as the study area, where the distinct types of spreading have been observed.

In Chapter 3, I will combine the newly developed technique with other established gravity and magnetic data enhancements to characterise and classify the two types of terrain over an asymmetric ridge. The goal of this chapter is to observe how the fully exposed oceanic crust is depicted by the gravity and magnetic signatures. The chapter will be preceded by the fundamental concepts of each geophysical data enhancements to understand the basis of the applications. I also assess how each technique will aid the interpretation over a fully exposed oceanic crust as it will be applied over a sedimented continental margin in the following chapter. In addition, the resulting classification will lead us to better understand the nature and the evolution of the asymmetric spreading occurring over the 21-24° N area of the MAR.

In Chapter 4, I will apply the techniques that have been assessed in the previous chapter to classify the types of terrain over a sedimented continental margin area. Because the oceanic crust has been buried by the sediments coming from the continent, I carried out the characterisation using gravity and magnetic data as they express the physical characteristics of the buried oceanic crust in the ocean-continent transition. I selected the Labrador Basin as my study area based on the good coverage of field magnetic survey data. The resulting classification will be compared to published interpreted 2D seismic profiles to further assess the reliability of each technique.

In Chapter 5, I will present the general summary of the whole study and discuss the key findings that have been obtained. I will first discuss the characterisation of the different types of spreading over the ridge axis before discussing the crustal type classification over sedimented area and passive continental margins. I also provide recommendations for future work and end the chapter by summarising the key findings that are presented in this thesis.

References

Allen, P. A., & Allen, J. R. (2013). *Basin analysis: Principles and application to petroleum play assessment*. John Wiley & Sons. 4

Barrett, D., & Keen, C. (1976). Mesozoic magnetic lineations, the magnetic quiet zone, and sea floor spreading in the northwest Atlantic. *Journal of Geophysical Research*, *81*(26), 4875–4884. 5

Biari, Y., Klingelhoefer, F., Sahabi, M., Funck, T., Benabdellouahed, M., Schnabel, M., Reichert, C., Gutscher, M.-A., Bronner, A., & Austin, J. (2017). Opening of the central Atlantic Ocean: Implications for geometric rifting and asymmetric initial seafloor spreading after continental breakup. *Tectonics*, *36*(6), 1129–1150. 9, 13

Blackman, D. K., Cann, J. R., Janssen, B., & Smith, D. K. (1998). Origin of extensional core complexes: Evidence from the Mid-Atlantic Ridge at Atlantis fracture zone. *Journal of Geophysical Research: Solid Earth*, *103*(B9), 21315–21333. 11

Blackman, D. K., John, B. E., Ildefonse, B., Ohara, Y., MacLeod, C. J., & Miller, D. J. (2004). Integrated Ocean Drilling Program Expeditions 304 and 305 Scientific Prospectus Oceanic Core Complex Formation, Atlantis Massif Oceanic core complex formation, Atlantis Massif, Mid-Atlantic Ridge: Drilling into the footwall and hanging wall. 11

Blackman, D. K., Karson, J. A., Kelley, D. S., Cann, J. R., Früh-Green, G. L., Gee, J. S., Hurst, S. D., John, B. E., Morgan, J., Nooner, S. L., Ross, D. K., Schroeder, T. J., & Williams, E. A. (2002). Geology of the Atlantis Massif (Mid-Atlantic Ridge, 30 N): Implications for the evolution of an ultramafic oceanic core complex. *Marine Geophysical Researches*, *23*(5), 443–469. 11

Bott, M. (1992). Passive margins and their subsidence. *Journal of the Geological Society*, *149*(5), 805–812. 22

Buck, W. R. (1988). Flexural rotation of normal faults. *Tectonics*, *7*(5), 959–973. 11

Buck, W. R., Lavier, L. L., & Poliakov, A. N. (2005). Modes of faulting at mid-ocean ridges. *Nature*, *434*(7034), 719–723. 8, 10

Calvert, A. (1995). Seismic evidence for a magma chamber beneath the slow-spreading Mid-Atlantic Ridge. *Nature*, *377*(6548), 410–414. 10

Cann, J., Blackman, D., Smith, D., McAllister, E., Janssen, B., Mello, S., Avgerinos, E., Pascoe, A., & Escartin, J. (1997). Corrugated slip surfaces formed at ridge–transform intersections on the Mid-Atlantic Ridge. *Nature*, *385*(6614), 329–332. 8, 11

Cannat, M., Briais, A., Deplus, C., Escartın, J., Georgen, J., Lin, J., Mercouriev, S., Meyzen, C., Muller, M., Pouliquen, G., Rabain, A., & da Silva, P. (1999). Mid-Atlantic Ridge–Azores hotspot interactions: along-axis migration of a hotspot-derived event of enhanced magmatism 10 to 4 Ma ago. *Earth and Planetary Science Letters*, *173*(3), 257–269. 3

Cannat, M., Sauter, D., Mendel, V., Ruellan, E., Okino, K., Escartin, J., Combier, V., & Baala, M. (2006). Modes of seafloor generation at a melt-poor ultraslow-spreading ridge. *Geology*, *34*(7), 605–608. 3, 8, 9, 13, 16

Carbotte, S. M., & Scheirer, D. S. (2004). Variability of ocean crustal structure created along the global mid-ocean ridge. *Hydrogeology of the oceanic lithosphere*, (pp. 59–107). 3

Chen, Y., & Morgan, W. J. (1990). Rift valley/no rift valley transition at mid-ocean ridges. *Journal of Geophysical Research: Solid Earth*, *95*(B11), 17571–17581. 8

Chian, D., Keen, C., Reid, I., & Louden, K. E. (1995). Evolution of nonvolcanic rifted margins: New results from the conjugate margins of the Labrador Sea. *Geology*, *23*(7), 589–592. 4

Christeson, G., Goff, J., & Reece, R. (2019). Synthesis of oceanic crustal structure from two-dimensional seismic profiles. *Reviews of Geophysics*, *57*(2), 504–529. 3, 6

Cowie, P. A., & Karner, G. D. (1990). Gravity effect of sediment compaction: Examples from the North Sea and the Rhine Graben. *Earth and Planetary Science Letters*, *99*(1-2), 141–153. 5

Dannowski, A., Grevemeyer, I., Phipps Morgan, J., Ranero, C. R., Maia, M., & Klein, G. (2011). Crustal structure of the propagating TAMMAR ridge segment on the Mid-Atlantic Ridge, 21.5° N. *Geochemistry, Geophysics, Geosystems*, *12*(7). 23

Dannowski, A., Grevemeyer, I., Ranero, C. R., Ceuleneer, G., Maia, M., Morgan, J. P., & Gente, P. (2010). Seismic structure of an oceanic core complex at the Mid-Atlantic Ridge, 22 19' N. *Journal of Geophysical Research: Solid Earth*, *115*(B7). 23

Dannowski, A., Morgan, J. P., Grevemeyer, I., & Ranero, C. R. (2018). Enhanced mantle upwelling/melting caused segment propagation, oceanic core complex die off, and the death of a transform fault: The Mid-Atlantic Ridge at 21.5 n. *Journal of Geophysical Research: Solid Earth*, *123*(2), 941–956. 23

De Charpal, O., Guennoc, P., Montadert, L., & Roberts, D. (1978). Rifting, crustal attenuation and subsidence in the Bay of Biscay. *Nature*, *275*(5682), 706–711. 22

Dean, S. L., Sawyer, D. S., & Morgan, J. (2015). Galicia Bank ocean–continent transition zone: New seismic reflection constraints. *Earth and Planetary Science Letters*, *413*, 197–207. 13

Delescluse, M., Funck, T., Dehler, S. A., Louden, K. E., & Watremez, L. (2015). The oceanic crustal structure at the extinct, slow to ultraslow Labrador Sea spreading center. *Journal of Geophysical Research: Solid Earth*, *120*(7), 5249–5272. 23

Dick, H. J., Lin, J., & Schouten, H. (2003). An ultraslow-spreading class of ocean ridge. *Nature*, *426*(6965), 405–412. 3, 16

Dick, H. J., Tivey, M. A., & Tucholke, B. E. (2008). Plutonic foundation of a slow-spreading ridge segment: Oceanic core complex at Kane Megamullion, 23 30' N, 45 20' W. *Geochemistry, Geophysics, Geosystems*, *9*(5). 11

Dick, H. J. B., Natland, J. H., Alt, J. C., Bach, W., Bideau, D., Gee, J. S., Haggas, S., Hertogen, J. G. H., Hirth, G., Holm, P. M., Ildefonse, B., Iturrino, G. J., John, B. E., Kelley, D. S., Kikawa, E., Kingdon, A., LeRoux, P. J., Maeda, J., Meyer, P. S., Miller, D. J., Naslund, H. R., Niu, Y.-L., Robinson, P. T., Snow, J., Stephen, R. A., Trimby, P. W., Worm, H.-U., & Yoshinobu, A. (2000). A long in situ section of the lower ocean crust: Results of ODP Leg 176 drilling at the Southwest Indian Ridge. *Earth and planetary science letters*, *179*(1), 31–51. 11

Escartín, J., & Canales, J. (2011). Detachments in oceanic lithosphere: Deformation, magmatism, fluid flow, and ecosystems. 11, 14

Escartín, J., & Cannat, M. (1999). Ultramafic exposures and the gravity signature of the lithosphere near the Fifteen-Twenty Fracture Zone (Mid-Atlantic Ridge, 14–16.5 N). *Earth and Planetary Science Letters*, *171*(3), 411–424. 11

Gouiza, M., & Paton, D. A. (2019). The role of inherited lithospheric heterogeneities in defining the crustal architecture of rifted margins and the magmatic budget during continental breakup. *Geochemistry, Geophysics, Geosystems*, *20*(4), 1836–1853. 23

Hamilton, W. B. (1988). Detachment faulting in the Death Valley region, California and Nevada. *Geologic and hydrologic investigations of a potential nuclear waste disposal site at Yucca Mountain, southern Nevada: US Geological Survey Bulletin*, *1790*, 51–85. 11

Harrison, C. (1976). Magnetization of the oceanic crust. *Geophysical Journal International*, *47*(2), 257–283. 7

Johnson, H. P., & Tivey, M. A. (1995). Magnetic properties of zero-age oceanic crust; A new submarine lava flow on the Juan de Fuca Ridge. *Geophysical research letters*, *22*(2), 175–178. 5, 7

Kahle, R. L., Tilmann, F., & Grevemeyer, I. (2016). Crustal structure and kinematics of the TAMMAR propagating rift system on the Mid-Atlantic Ridge from seismic refraction and satellite altimetry gravity. *Geophysical Journal International*, *206*(2), 1382–1397. 23

Karson, J. A. (1998). Internal structure of oceanic lithosphere: A perspective from tectonic windows. *Geophysical Monograph-American Geophysical Union*, *106*, 177–218. 6

Keen, C. (1987). Some important consequences of lithospheric extension. *Geological Society, London, Special Publications*, *28*(1), 67–73. 16

Larson, R. L., & PITMAN III, W. C. (1972). World-wide correlation of Mesozoic magnetic anomalies, and its implications. *Geological Society of America Bulletin*, *83*(12), 3645–3662. 5

Le Pichon, X., & Barbier, F. (1987). Passive margin formation by low-angle faulting within the upper crust: The northern Bay of Biscay margin. *Tectonics*, *6*(2), 133–150. 22

Lister, G., Etheridge, M., & Symonds, P. (1986). Detachment faulting and the evolution of passive continental margins. *Geology*, *14*(3), 246–250. 4

Lister, G., Etheridge, M., & Symonds, P. (1991). Detachment models for the formation of passive continental margins. *Tectonics*, *10*(5), 1038–1064. 16

Louden, K., & Chian, D. (1999). The deep structure of non–volcanic rifted continental margins. *Philosophical Transactions of the Royal Society of London. Series A: Mathematical, Physical and Engineering Sciences*, *357*(1753), 767–804. 2

Lowrie, W. (1997). Fundamentals of Geophysics. *ISBN*, *521467284*, 368. 7

Macdonald, K. C. (1982). Mid-ocean ridges: Fine scale tectonic, volcanic and hydrothermal processes within the plate boundary zone. *Annual Review of Earth and Planetary Sciences*, *10*(1), 155–190. 3, 8, 10

MacLeod, C. J., Escartin, J., Banerji, D., Banks, G., Gleeson, M., Irving, D. H. B., Lilly, R., McCaig, A., Niu, Y., Allerton, S., *et al.* (2002). Direct geological evidence for oceanic detachment faulting: The Mid-Atlantic Ridge, 15 45' N. *Geology*, *30*(10), 879–882. 11

MacLeod, C. J., Searle, R., Murton, B., Casey, J., Mallows, C., Unsworth, S., Achenbach, K., & Harris, M. (2009). Life cycle of oceanic core complexes. *Earth and Planetary Science Letters*, *287*(3-4), 333–344. 11, 15

Maus, S., Barckhausen, U., Berkenbosch, H., Bournas, N., Brozena, J., Childers, V., Dostaler, F., Fairhead, J. D., Finn, C., von Frese, R. R. B., Gaina, C., Golynsky, S., Kucks, R., Lühr, H., Milligan, P., Mogren, S., Müller, R. D., Olesen, O., Pilkington, M., Saltus, R., Schreckenberger, B., Thébault, E., & Caratori Tontini, F. (2009). EMAG2: A 2–arc min resolution Earth Magnetic Anomaly Grid compiled from satellite, airborne, and marine magnetic measurements. *Geochemistry, Geophysics, Geosystems*, *10*(8). 23

McKenzie, D. (1978). Some remarks on the development of sedimentary basins. *Earth and Planetary science letters*, *40*(1), 25–32. 2, 4

McKenzie, D., & Bowin, C. (1976). The relationship between bathymetry and gravity in the Atlantic Ocean. *Journal of Geophysical Research*, *81*(11), 1903–1915. 5, 7

Mendel, V., Sauter, D., Parson, L., & Vanney, J.-R. (1997). Segmentation and morphotectonic variations along a super slow-spreading center: the Southwest Indian Ridge (57 E - 70 E). *Marine Geophysical Researches*, *19*(6), 505–533. 3, 16

Meyer, B., Saltus, R., & Chulliat, A. (2017). EMAG2 Version 3-Update of a two arc-minute global magnetic anomaly grid. In *EGU General Assembly Conference Abstracts*, (p. 10614). 23

Michael, P., Langmuir, C., Dick, H., Snow, J., Goldstein, S., Graham, D., Lehnert, K., Kurras, G., Jokat, W., Mühe, R., *et al.* (2003). Magmatic and amagmatic seafloor generation at the ultraslow-spreading Gakkel ridge, Arctic Ocean. *Nature*, *423*(6943), 956–961. 16

Montadert, L., de Charpal, O., Roberts, D., Guennoc, P., & Sibuet, J.-C. (1979). Northeast Atlantic passive continental margins: Rifting and subsidence processes. *Deep drilling results in the Atlantic Ocean: Continental margins and paleoenvironment*, *3*, 154–186. 17

Morgan, W. J. (1968). Rises, trenches, great faults, and crustal blocks. *Journal of Geophysical Research*, *73*(6), 1959–1982. 8

Okino, K., Matsuda, K., Christie, D. M., Nogi, Y., & Koizumi, K.-i. (2004). Development of oceanic detachment and asymmetric spreading at the Australian-Antarctic Discordance. *Geochemistry, Geophysics, Geosystems*, *5*(12). 10

Oufi, O., Cannat, M., & Horen, H. (2002). Magnetic properties of variably serpentinized abyssal peridotites. *Journal of Geophysical Research: Solid Earth*, *107*(B5), EPM–3. 5, 7

O'Neill, H. S. C., & Jenner, F. E. (2012). The global pattern of trace-element distributions in ocean floor basalts. *Nature*, *491*(7426), 698–704. 3

Pariso, J. E., & Johnson, H. P. (1991). Alteration processes at deep sea drilling project/ocean drilling program hole 504B at the Costa Rica rift: Implications for magnetization of oceanic crust. *Journal of Geophysical Research: Solid Earth*, *96*(B7), 11703–11722. 7

Pariso, J. E., & Johnson, H. P. (1993). Do layer 3 rocks make a significant contribution to marine magnetic anomalies? In situ magnetization of gabbros at Ocean Drilling Program Hole 735B. *Journal of Geophysical Research: Solid Earth*, *98*(B9), 16033–16052. 7

Parker, R. (1973). The rapid calculation of potential anomalies. *Geophysical Journal International*, *31*(4), 447–455. 5

Parsons, B., & McKenzie, D. (1978). Mantle convection and the thermal structure of the plates. *Journal of Geophysical Research: Solid Earth*, *83*(B9), 4485–4496. 2

Pockalny, R., Smith, A., & Gente, P. (1995). Spatial and temporal variability of crustal magnetization of a slowly spreading ridge: Mid-Atlantic Ridge (20–24 N). *Marine Geophysical Researches*, *17*(3), 301–320. 8

Pockalny, R. A., Gente, P., & Buck, R. (1996). Oceanic transverse ridges: A flexural response to fracture-zone–normal extension. *Geology*, *24*(1), 71–74. 8

Sauter, D., Cannat, M., Rouméjon, S., Andreani, M., Birot, D., Bronner, A., Brunelli, D., Carlut, J., Delacour, A., Guyader, V., MacLeod, C. J., Manatschal, G., Mendel, V., Ménez, B., Pasini, V., Ruellan, E., & Searle, R. (2013). Continuous exhumation of mantle-derived rocks at the Southwest Indian Ridge for 11 million years. *Nature Geoscience*, *6*(4), 314–320. 3, 9

Sauter, D., Carton, H., Mendel, V., Munschy, M., Rommevaux-Jestin, C., Schott, J.-J., & Whitechurch, H. (2004). Ridge segmentation and the magnetic structure of the Southwest Indian Ridge (at 50 30' E, 55 30' E and 66 20' E): Implications for magmatic processes at ultraslow-spreading centers. *Geochemistry, Geophysics, Geosystems*, *5*(5). 18

Searle, R. (2013). *Mid-ocean ridges*. Cambridge University Press. 7, 9

Sengör, A. C., & Burke, K. (1978). Relative timing of rifting and volcanism on Earth and its tectonic implications. *Geophysical Research Letters*, *5*(6), 419–421. 2

Singh, S. C., Crawford, W. C., Carton, H., Seher, T., Combier, V., Cannat, M., Canales, J. P., Düsünür, D., Escartin, J., & Miranda, J. M. (2006). Discovery of a magma chamber and faults beneath a Mid-Atlantic Ridge hydrothermal field. *Nature*, *442*(7106), 1029–1032. 14

Sinton, J. M., & Detrick, R. S. (1992). Mid-ocean ridge magma chambers. *Journal of Geophysical Research: Solid Earth*, *97*(B1), 197–216. 10

Sleep, N. H. (1971). Thermal effects of the formation of Atlantic continental margins by continental break up. *Geophysical Journal International*, *24*(4), 325–350. 2

Sleep, N. H., & Biehler, S. (1970). Topography and tectonics at the intersections of fracture zones with central rifts. *Journal of Geophysical Research*, *75*(14), 2748–2752. 8

Smith, D. K., & Cann, J. R. (1992). The role of seamount volcanism in crustal construction at the Mid-Atlantic Ridge (24°–30° N). *Journal of Geophysical Research: Solid Earth*, *97*(B2), 1645–1658. 3

Smith, D. K., Escartin, J., Cannat, M., Tolstoy, M., Fox, C. G., Bohnenstiehl, D. R., & Bazin, S. (2003). Spatial and temporal distribution of seismicity along the northern Mid-Atlantic Ridge (15°–35° N). *Journal of Geophysical Research: Solid Earth*, *108*(B3). 23

Smith, D. K., Escartìn, J., Schouten, H., & Cann, J. R. (2008). Fault rotation and core complex formation: Significant processes in seafloor formation at slow-spreading mid-ocean ridges (Mid-Atlantic Ridge, 13-15 N). *Geochemistry, Geophysics, Geosystems*, *9*(3). 10, 11, 14

Standish, J. J., & Sims, K. W. (2010). Young off-axis volcanism along the ultraslow-spreading Southwest Indian Ridge. *Nature Geoscience*, *3*(4), 286–292. 19

Steckler, M., & Watts, A. (1982). Subsidence history and tectonic evolution of Atlantic-type continental margins. *Dynamics of Passive Margins. AGU Geodyn. Ser*, *6*, 184–196. 2

Straume, E. O., Gaina, C., Medvedev, S., Hochmuth, K., Gohl, K., Whittaker, J. M., Abdul Fattah, R., Doornenbal, J. C., & Hopper, J. R. (2019). Globsed: Updated total sediment thickness in the world's oceans. *Geochemistry, Geophysics, Geosystems*, *20*(4), 1756–1772. 23

Tivey, M. A., & Johnson, H. P. (1987). The central anomaly magnetic high: Implications for ocean crust construction and evolution. *Journal of Geophysical Research: Solid Earth*, *92*(B12), 12685–12694. 3

Tucholke, B. E., Behn, M. D., Buck, W. R., & Lin, J. (2008). Role of melt supply in oceanic detachment faulting and formation of megamullions. *Geology*, *36*(6), 455–458. 9, 12

Tucholke, B. E., & Lin, J. (1994). A geological model for the structure of ridge segments in slow spreading ocean crust. *Journal of Geophysical Research: Solid Earth*, *99*(B6), 11937–11958. 10

Tucholke, B. E., Lin, J., & Kleinrock, M. C. (1998). Megamullions and mullion structure defining oceanic metamorphic core complexes on the Mid-Atlantic Ridge. *Journal of Geophysical Research: Solid Earth*, *103*(B5), 9857–9866. 11

Wernicke, B. (1985). Uniform-sense normal simple shear of the continental lithosphere. *Canadian Journal of Earth Sciences*, *22*(1), 108–125. 2, 4, 11

White, N., Thompson, M., & Barwise, T. (2003). Understanding the thermal evolution of deep-water continental margins. *Nature*, *426*(6964), 334–343. 16, 20, 21

White, R. (1984). Atlantic oceanic crust: Seismic structure of a slow-spreading ridge. *Geological Society, London, Special Publications*, *13*(1), 101–111. 8

White, R., & McKenzie, D. (1989). Magmatism at rift zones: The generation of volcanic continental margins and flood basalts. *Journal of Geophysical Research: Solid Earth*, *94*(B6), 7685–7729. 2

Chapter 2

Characterising different types of spreading by observing the directionality of shipboard multibeam bathymetry

Abstract

The shapes and directionality of the oceanic crust at slow-spreading ridges are key to understanding its magmatic or tectonic emplacement. At slow spreading ridges, magmatic terrain is marked by linearly fault-bounded abyssal hills, while tectonic terrain is marked by long-lived detachment faults forming sporadic massifs termed Oceanic Core Complexes (OCCs). However, the quantitative description of these crustal regimes is still limited. Interpretation of shipborne multibeam bathymetry data over the years has been attempted by eye based on the shapes and sizes of the features. In this chapter, I develop a novel automatic terrain classification technique based on the parameterisation of the shape, directionality, and curvature of the seafloor. The algorithm is tested at 12.5°-15.5° N on the Mid-Atlantic Ridge (MAR), where the two distinct modes of spreading occur. The weighted eccentricity of the horizontal eigenvalues, or the slope-weighted eccentricity (SWE), is computed to represent the general directionality of the seafloor and reveal its magmatic or tectonic regimes. The application of this new technique yields results consistent with those from qualitative interpretation. Thus, it provides both new insights into the mid-oceanic ridge spreading and the potential to automate such mapping at other slow-spreading ridge regions.

2.1 Introduction

Parts of slow-spreading ridges have been characterised with typical magmatic accretion where fault-bounded abyssal hills form symmetrically at both flanks of the spreading axis (Macdonald, 1982). On the other parts, asymmetric accretion is observed, where volcanic flows form at one flank and detachment faults form at the opposing flank (Rona *et al.*, 1987; Smith, 2013). These atypical, curved faults form a dome-shaped seafloor, termed oceanic core complexes (OCCs), in which lower-crustal and mantle rocks are exhumed (Blackman *et al.*, 2009; Cann *et al.*, 1997; Dannowski *et al.*, 2010; MacLeod *et al.*, 2002). These exposures of deep-seated rocks have been a topic of interest since they show a potentially large amount of tectonic extension at slow-spreading ridge segments (Smith *et al.*, 2006, 2008). This type of morphology contrasts with the typical linearly fault-bounded abyssal hills resulting from a typical magmatic accretion (Mutter & Karson, 1992; Sinton & Detrick, 1992), hence indicating the complex interaction between the magmatic and tectonic regime over the area (Escartín & Cannat, 1999).

The formation of an OCC is initiated when the magmatic accretion at the ridge axis falls between 30% and 50%, or when the fraction of the plate of separation rate, M, falls between 0.3 and 0.5 (Tucholke *et al.*, 2008). As the magmatic accretion wanes, the main locus of the plate separation jumps to one side of the ridge (MacLeod *et al.*, 2009). The local waning triggers the thinning of the crustal layer that allows the formation of secondary hydrous minerals such as talc and serpentine, which in turn causes weakening of the lithosphere along the axis (Escartin *et al.*, 1997, 2001). Some areas then experience strain localisation from this lithosphere weakening, triggering the creation of a fault. The footwall is then rotated parallel-outward to the ridge axis, resulting in a long-lived fault, often with corrugation parallel to the spreading direction (Buck, 1988; Cann *et al.*, 1997; Reston & Ranero, 2011). This rotation forms a low-angle and curved fault as a response to the flexural unloading during extension (Buck, 1988; Lavier *et al.*, 1999; Tucholke *et al.*, 2008). Mantle lithosphere is then brought up to shallower levels following the rotation, marking a sharp discontinuity between the exhumed mantle rocks and the surrounding upper-crust rocks, hence the term ‘detachment mode’ or generally the ‘tectonic’ spreading (e.g., Cann *et al.*, 2015).

The OCCs are initially considered to form at the inside corners of a ridge-transform interaction, e.g., the Atlantis Massif in the vicinity of the Atlantis fracture zone (Cann *et al.*, 1997). Gradually, OCCs are identified at places away from the ridge-transform interaction (Cann *et al.*, 2015; Smith *et al.*, 2008). The discoveries postulate questions over their general distribution and their forming patterns. However, identifications over the years have been attempted based on qualitative observation of shipboard multibeam bathymetry, often paired with rock sampling through dredging, drilling, and sample collecting using submersible vehicles (e.g., Cannat *et al.*, 1992; Lagabrielle *et al.*, 1998; Schroeder *et al.*, 2007) as well as other geophysical surveys such as gravity, magnetic, and seismic surveys (e.g., Dannowski *et al.*, 2010; Pockalny *et al.*, 1995; Tivey & Dyment, 2010). This study aims to aid the identification by developing a tool to automate the magmatic and tectonic crust classification through a series of quantitative terrain characterisation, or the geomorphometry, of the magmatic and tectonic seafloor. We introduce the use of an algorithm termed 'slope-weighted eccentricity' (SWE) as a novel geomorphometric technique that can be applied in slow-spreading ridges to further characterise the interplay between the magmatic and tectonic regimes in the region.

The first comprehensive overview of marine geomorphometry efforts carried out to date is presented in Lecours *et al.* (2016). According to the review, the development and application of geomorphometry in the marine environment is still forming with many concepts, methods, and applications, as the number of marine applications of geomorphometry are more recent and less numerous than in the terrestrial environment. Geomorphometry characterisation in the marine environment have been developing quite rapidly in recent years thanks to the increasing availability and accessibility of shipboard multibeam bathymetry data sets. Seabed feature identification such as pockmarks (Gafeira *et al.*, 2012; Harrison *et al.*, 2011), submarine canyons (Green & Uken, 2008; Ismail *et al.*, 2015; Micallef *et al.*, 2012), and terraces (Passaro *et al.*, 2011) have been made available from the derivation and statistical characterisation of the multibeam bathymetry data.

In the mid-ocean ridges, seabed characterisation have been attempted for example by Smith & Shaw (1989), Goff *et al.* (1995), and Chakraborty *et al.* (2001). Specifically, a quantitative characterisation of magmatic abyssal hills have been attempted by Goff *et al.* (1995) by describing the multibeam data into three physical parameters, namely the rms (root-mean-square) height, characteristic width, and plan view aspect ratio (Goff & Jordan, 1988). The study manage to characterise the relation between the resulting morphology of the abyssal hills with the thickness of the crust derived from the residual mantle Bouguer anomaly (RMBA), where lower-relief, narrower, and more lineated abyssal hills are formed when the crust is thickner, while higher, wider, less lineated abyssal hills are formed when the crust is thinner. However, the characterisation have not taken into account if a certain region is dominated either by an extensional tectonic or an accretional magmatic processes. The formation of OCCs through detachment faulting have not been explained by the time of the publication of the study, hence strengthening the potential application of our established algorithm.

The algorithm is built based on three of the four main types of terrain attributes described in Wilson *et al.* (2007), which are the slope, orientation, and curvature of the seafloor. We exploit the slope and orientation to describe the plunge and azimuth of the features of interest, respectively, and examine their distribution in the form of a spherical distribution (Watson, 1965; Woodcock, 1977) and a simplified form of azimuth rose termed azimuth ellipse. While the spherical distribution gives us the three-dimensional distribution of the examined terrain patch, the azimuth ellipse gives us a simplified view of the two-dimensional distribution, where a patch of terrain dominated by bidirectional dipping slopes is identified by an ellipse with high eccentricity, while a patch of terrain dominated by omnidirectional dipping slopes is identified by an ellipse with low eccentricity. The dominating orientation (bidirectional or omnidirectional) gives us the information of the spreading mode of the respective terrain, whether the terrain is dominated by an accretionary magmatic or an extensional tectonic forces, as magmatic mode tends to form the bidirectional fault-bounded abyssal hills and tectonic mode tends to form long-lived detachment faults resulting in the omnidirectional dipping sporadic massifs (e.g., Smith *et al.*, 2008).

From our observation, we classify the terrain characterisation into three types of terrain, namely the magmatic, extended, and tectonic terrain (Cann *et al.*, 2015). The extended terrain represents an area where both bidirectional and omnidirectional dipping slopes exist, showing the transition between the two crustal regimes. Furthermore, we exploit the curvatures of the seafloor to identify individual OCCs using a mask created from a Laplacian-of-Gaussian-filtered (LoG-filtered) bathymetry. The automatically classified seafloor and the identified individual OCCs will then act as a novel means to provide insights on the processes that occurs in a slow-spreading ridge through time. The SWE algorithm itself has been tested is ready to be applied at different sections of the spreading ridges.

2.2 Study area

As a case study, I select an area with shipboard multibeam bathymetry data over ∼5 Ma between the Marathon and Fifteen-Twenty FZs (12.5°-15.5° N). The extent of the area can be seen in Figure 2.1. The gridded bathymetry is provided by Deborah K. Smith through personal contact, and is a combination of shipboard multibeam surveys carried out by Escartín & Cannat (1999) along the Fifteen-Twenty fracture zone (∼15° 20’ N) and its two adjacent ridge axes, by Fujiwara *et al.* (2003) from ∼14° N up to the Fifteen-Twenty FZ, and by Smith *et al.* (2006) from ∼14° N down to the Marathon FZ (∼12° 40’ N). The original combined bathymetry was gridded with the cell size of 200 m. The area represents a complex history of magmatism and tectonism since the movement of the North American (NA), South American (SA), and African (AF) plates (e.g., Bonatti, 1996; Müller & Smith, 1993). The site has been speculated as a potential location of the NA-SA-AF triple junction (Escartín *et al.*, 2003).

Seismicity in the area has been recorded by an array of autonomous hydrophones moored on the flanks of the MAR between 15° N and 35° N (Smith *et al.*, 2003, 2002). The locations of the seismic activities, or earthquakes, are derived from the peak amplitudes of the tertiary waves (or T-waves) observed in the vicinity of the hydrophones. The derived locations may coincide with earthquake epicentres, but factors such as morphology, the velocity structure of the crust, and the depth of the earthquake below the seafloor may bias the calculation. Hence, the derived locations are not termed ‘epicentres’ but rather ‘T-wave source locations’ (Fox *et al.*, 2001).

The distribution of the observed seismicity reflects the tectonism in the area, where continuous seismicity is found close to the bounding FZs while a seismic gap is found in the middle of the area, or around 14° N (Escartín *et al.*, 2003). The seismic gap at the segment is consistent with a continuous zone of high acoustic backscatter as well as a magmatically-robust morphology, marked by the presence of long abyssal hills parallel to the spreading axis. In contrast, the continuous seismicity at the segment ends (13° N and 15° N) occurred in a terrain with much rougher topography where sporadic massifs are in place (Smith *et al.*, 2008). Furthermore, the observation is consistent with the indication of brittle rupture at depths up to 10-12 km below the seafloor near the ends of spreading segments by means of teleseismic and microearthquake studies (Bergman & Solomon, 1990; Kong *et al.*, 1992; Wolfe *et al.*, 1995).

The abundant samples of ultramafic rocks close to the massifs at both 13° N and 15° N segments (Cannat *et al.*, 1997; MacLeod *et al.*, 2009; Rona *et al.*, 1987) demonstrate the domination of the OCC formation specifically in these two segments (Smith *et al.*, 2008). The formation is accommodated through prolonged slip on a detachment fault during a long-lived phase of relatively amagmatic extension at segment ends (Tucholke *et al.*, 1998). The magmatic and amagmatic phase of spreading is then described as the factor M, or the fraction of the plate of separation rate accommodated by magmatic emplacement (Buck *et al.*, 2005). Tucholke *et al.* (2008) experimented with models with a variation of M values and found that detachment faults may initiate when $\sim 0.3 \leq M \leq 0.5$. The faulting geometry itself varies along the ridge axis, where normal faults are predicted to form adjacent to the detachment fault where $M > 0.5$, forming fault-bounded abyssal hills (Howell *et al.*, 2019). The study provides consistent correlation with an observed OCC at 13° 20’ N (Parnell-Turner *et al.*, 2017), where the presence of dense microseismicity at the termination of the OCC correlates well with the modelled M factor of $\sim$0.5. The distinct morphology of both magmatic and tectonic modes of spreading within the 12.5°-15.5° N segments makes it a suitable site to assess the automated classification algorithm.

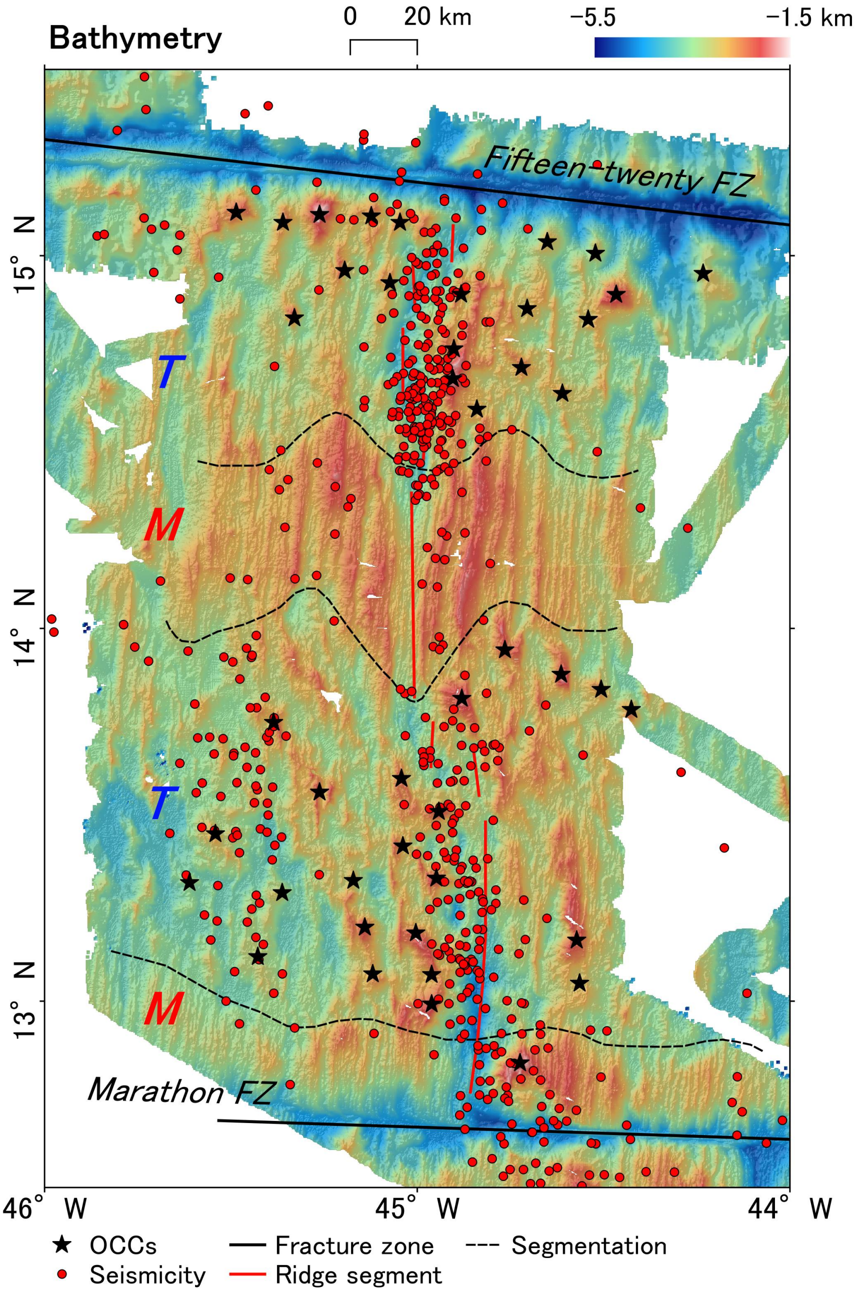

Figure 2.1: Bathymetric map of the study area. The combined data is obtained from cruises documented in Escartín & Cannat (1999), Fujiwara *et al.* (2003), and Smith *et al.* (2006). Segmentation (black dashed lines) is inferred by Smith *et al.* (2008), dividing the area into tectonic (T) and magmatic (M) terrain. Black stars: inferred OCCs (Smith *et al.*, 2008). Red dots: T-wave origin seismicity (Smith *et al.*, 2003). Black lines: fracture zones. Red lines: ridge segments.

2.3 Slope-weighted eccentricity

Slope-weighted eccentricity (SWE) is an algorithm created to obtain the numerical description of both magmatic and tectonic crust through a series of calculation based on the distribution of the azimuth and plunge observed in the seafloor morphology. The distribution of these two parameters indicates the general shape and directionality of the seafloor. The calculation is applied to a set of gridded multibeam bathymetry through a moving window, starting from the top-left corner down to the bottom-right corner of the grid. In this section, I will explain the fundamental theories in which the calculation is based on, starting from the description of spherical distribution, eigenvalues and its graphical representation, eccentricity as means of describing the horizontal pattern of a terrain patch, and the introduction of slope as a weight matrix. In addition, I include the use of the Laplacian-of-Gaussian (LoG) filter to define the curvatures of the seafloor. The defined curvatures will serve as means to highlight the concave-downward morphology of both magmatic abyssal hills and OCCs and mask out the concave-upward morphology as a means to identify individual OCCs.

2.3.1 Spherical distribution

The gridded multibeam bathymetry comprises data cells, each described as longitude, latitude, and height (lon, lat, h). From the gridded dataset, I compute the azimuth (α) and plunge (θ) of each cell using the built-in `aspect` and `slope` functions in `MATLAB` (e.g., used in Trauth (2007)), respectively. In the functions, azimuth is calculated by considering the horizontal deviation of dip relative to the north (0°), while the plunge is calculated by analysing the depth gradient of each cell of a gridded surface relative to a plane surface. It is important to notice that in this function, the plunge is described as positive down ($+\theta$ down) from the horizon down to the nadir ($+0°$ to $+90°$). Therefore, to match with the spherical description (Figure 2.2), the sign is reversed ($-\theta$) so the values are all $\leq 0°$.

Having the gridded bathymetry described as its azimuth and plunge values, we can sample a patch of terrain and describe each cell in terms of the Cartesian coordinates (x, y, z) of the end point of a unit vector, starting from (0,0,0), where (0,0,0) is the centre of the cell, by:

$$\begin{aligned} x &= \sin\alpha\cos(-\theta) \\ y &= \cos\alpha\cos(-\theta) \\ z &= \sin(-\theta) \end{aligned} \tag{2.1}$$

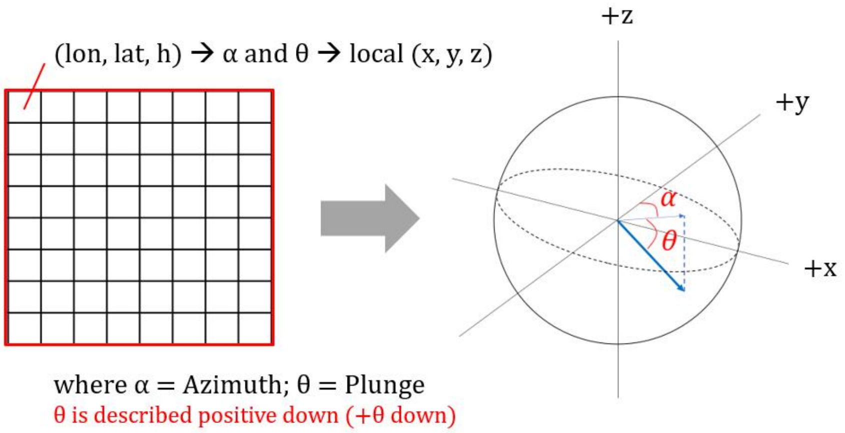

Figure 2.2: Illustration of how a patch of terrain with cells described as (lon, lat, h) is converted into a spherical distribution form. Firstly, the terrain patch is transformed into two separate patches of azimuth (α) and plunge (θ) using the built-in `slope` and `aspect` functions in `MATLAB`, respectively. Afterwards, the plunge and azimuth are then used to compute the local Cartesian coordinates (x, y, z) of each cell within each terrain patch.

By plotting the (x, y, z) into a spherical distribution form, we can see approximately where the moments of inertia are distributed and about which axis they are maximised (Watson, 1965; Woodcock, 1977). In other words, we can observe how the mass of the sampled crust is distributed within the terrain patch, whether the mass is maximised about the x, y, or the z axes. This distribution can be numerically described by computing the eigenvalues of the three axes.

2.3.2 Eigenvalues on a unit sphere

Prior to computing the eigenvalues, we need to describe a matrix B, which mimics the orientation tensor matrix defined by Scheidegger (1965) and Woodcock (1977) as:

$$B = \begin{bmatrix} \sum x_i^2 & \sum x_i y_i & \sum x_i z_i \\ \sum y_i x_i & \sum y_i^2 & \sum y_i z_i \\ \sum z_i x_i & \sum z_i y_i & \sum z_i^2 \end{bmatrix} \div n \tag{2.2}$$

Each of the matrix elements is the summation of the local Cartesian coordinates (x, y, z) of a number of points (n) over a terrain patch, each regarded as a point of unit mass on a sphere. The eigenvalues of this matrix B are then computed using the `eig` function in `MATLAB`, to represent the general patterns of vectors on the unit sphere. These patterns are useful to visualise the shapes and strength of a fabric, as well as tracing its progressive deformation (Woodcock, 1977). Several of the patterns can be seen in Figure 2.3. The three eigenvalues are defined in ascending order $(\lambda_1, \lambda_2, \lambda_3)$, each represents the moment tensor on a Cartesian axis, where the smallest value is defined as λ_1. Having the axis with the smallest eigenvalue defined, the axis of λ_2 is defined perpendicular to λ_1 and λ_3 following the right-hand rule. For instance, in Figure 2.3, the moment tensor is minimised about the z-axis. The Cartesian (x, y, z) axes are then described as $(\lambda_2, \lambda_3, \lambda_1)$.

Woodcock (1977) generalised the classification patterns by graphing logs of ratios of the eigenvalues, defined as:

$$K = \frac{\ln(\lambda_1/\lambda_2)}{\ln(\lambda_2/\lambda_3)} \tag{2.3}$$

where K is the number defining the general ratios of the eigenvalues on the unit sphere. The Woodcock classification can be seen in Figure 2.4. However, the range of the plunge is naturally incomparable to the range of the azimuth (0° to 90° and 0° to 360°, respectively). This argument will be explored later in the algorithm building section, in which the spherical distribution visualisation will be applied to a real-world dataset. Considering this assumption, if we use the K ratio to describe the general morphology, the computed value will mainly represent the pattern observed in the horizontal axis, almost neglecting the vertical component. In addition, there is no known upper limit to the K-ratio, limiting the re-applicability of the algorithm at different settings as the range of the value is not fixed. Therefore, another way of describing the patterns observed on each unit sphere is needed.

2.3.3 Eigenvalue ellipse and horizontal eccentricity

To observe the general pattern created by the point masses, I separate the computation into two steps, in which the first one focuses on the horizontal distribution of the point masses and another focuses on the vertical distribution. The pattern constructed by the point masses at the horizontal axes is described by its horizontal eigenvalues. As previously discussed, λ_1 is where the moment of inertia is minimised, while λ_2 is perpendicular to λ_1 and λ_3 following the right-hand rule of Cartesian coordinates. In the algorithm building section we shall see that the moment of inertia is always minimised about the z-axis, depicting the narrow range of the plunge values. Therefore, in the following computations, the eigenvalues of the (x, y, z) axes will each be described as $(\lambda_2, \lambda_3, \lambda_1)$.

The 3-dimensional spherical distribution is then simplified into a 2-dimensional eigenvalue ellipse, in which the horizontal lambda values (λ_3 and λ_2) represents the semi-major and the semi-minor axes (a and b, respectively). The illustration of how the spherical distribution is projected into an ellipse can be seen in Figure 2.5.

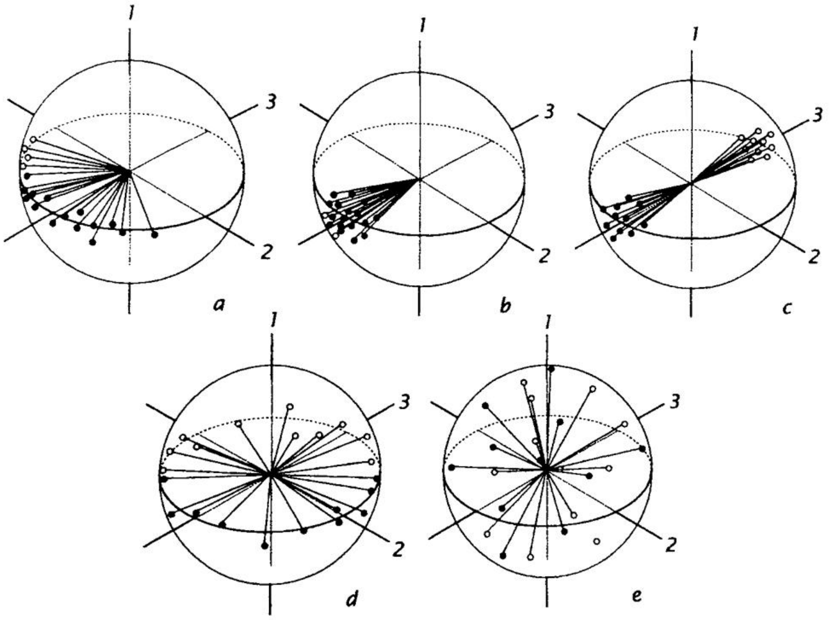

Figure 2.3: Patterns of vectors on the unit sphere, after Davis (1986). (a) Partial girdle pattern in the plane containing λ_2 and λ_3. (b) Unimodal distribution of vectors around λ_3. (c) Bimodal distribution of vectors around λ_3. (d) Complete girdle plane containing λ_2 and λ_3. Their eigenvalues are identical or nearly so. (e) Uniform distribution. Eigenvalues are all approximately equal.

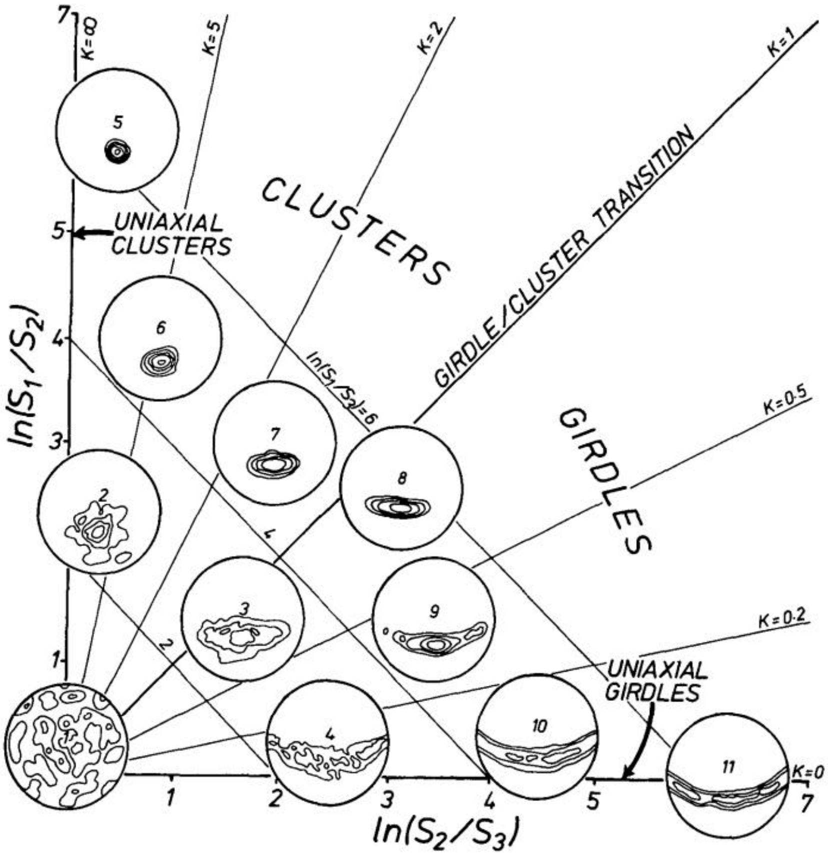

Figure 2.4: Classifications of patterns of vectors on the unit sphere, according to the logarithms of the ratios of their eigenvalues, after Woodcock (1977).

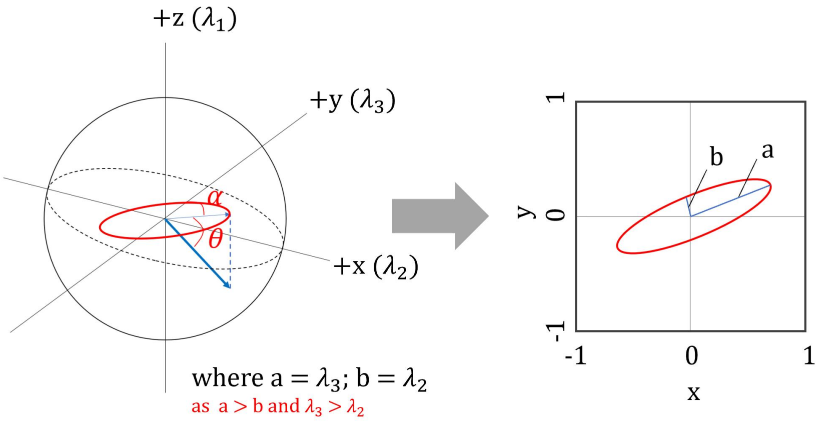

Figure 2.5: Illustration of how the 3-dimensional spherical distribution is projected into a 2-dimensional ellipse. The semi-major and semi-minor axes of the ellipse (a and b, respectively) is described as λ_3 and λ_2, respectively.

Mathematically, the shape of an ellipse can be characterised by a unique number termed eccentricity. In general, eccentricity is computed based on the values of the semi-major and semi-minor axes. In particular, the eccentricity of an ellipse falls between $0 < e < 1$, where the $e = 0$ represents the eccentricity of a circle. Therefore, we can characterise the horizontal pattern of the terrain patch using the eccentricity equation, described as:

$$e = \sqrt{1 - \frac{b^2}{a^2}} = \sqrt{1 - \frac{{\lambda_2}^2}{{\lambda_3}^2}} \tag{2.4}$$

The eccentricity value of a terrain patch then describes the general pattern of the point mass in its horizontal axes. For instance, a terrain patch with a high eccentricity value describes a bi-directional pattern of azimuths commonly found at magmatic terrain, as the faults are slipping parallel to each other. On the other hand, a terrain patch with a low eccentricity value describes a more omnidirectional pattern of azimuth, which might indicate the presence of a detachment fault or an OCC. Having the horizontal components defined, we need to introduce the computation of the vertical component to have a full numerical description of the seafloor morphology. The vertical component will be introduced as a weight matrix to the computed horizontal eccentricity.

2.3.4 Introducing slope as a weight matrix

The vertical distribution of the point masses can be described by the plunge (θ) parameter over a patch of terrain. As discussed in 2.3.1., the plunge is calculated by analysing the depth gradient of each cell of a gridded surface relative to a plane surface using the `slope` function in `MATLAB`. This depth gradient can be viewed as a proxy of the fault planes over both magmatic and tectonic terrain, in which normal faults indicate the presence of magmatic terrain and detachment faults indicate the latter. From the computed slopes, we can generate a weight matrix that resembles the range of the eccentricity numbers computed in the previous subsection ($0 < e < 1$). The simplest way to achieve it is by computing the sine of the slope ($\sin\theta$), as the sine of $0° \leq \theta \leq 90°$ is $0 \leq \sin\theta \leq 1$.

However, it is important to note that the high-angle normal faults over the magmatic terrain might be depicted as having gentler slopes compared to the long-lived detachment faults. In magmatic terrain, the horizontal offset, or the heave of the normal faults, is naturally much narrower than the heave of the footwall of the detachment faults in tectonic terrain. For instance, in a patch of a normal fault-bounded magmatic terrain, there will be many fewer cells being processed in one single fault compared to those at a single detachment fault. As a result, the gradient of the normal fault will be described as a few cells having much gentler slopes compared to the many more cells detected at the detachment fault, favouring a higher value of gradient in each cell. This argument will be explored more in the algorithm building section.

In 2.3.3, we have learned that the eccentricity equation favours magmatic terrain with higher values compared to the tectonic terrain. Therefore, the weight matrix must be built to favour magmatic terrain with higher values as well. Considering the argument that magmatic terrain tends to be described as having gentler slopes than tectonic terrain, the weight matrix W is introduced as:

$$W = 1 - \sin\theta \tag{2.5}$$

By introducing Equation 2.5 as a weight matrix to Equation 2.4, the 'slope-weighted eccentricity' or SWE can be defined as:

$$SWE = e \times W = \sqrt{1 - \frac{(\lambda_2/2)^2}{(\lambda_3/2)^2}} \times (1 - \sin\theta) \tag{2.6}$$

Following the original ranges of e and $(1 - \sin\theta)$, the SWE will always fall between $0 < SWE < 1$, making it applicable to any multibeam dataset.

Having both the horizontal and vertical parameters included in the algorithm, it is now possible to distinguish the two types of terrain. However, the SWE technique is still insufficient to identify individual OCCs, as it has not taken into account the curvatures of the seafloor. For instance, the numerical description of an OCC is similar to an identical-sized local basin, as both features are characterised with omnidirectional dipping slopes without considering if it is a concave-downward or a concave-upward feature. For that reason, we need to create a mask to filter out the concave-upward features, or the bathymetric lows from the whole grid.

2.3.5 Defining curvatures with Laplacian-of-Gaussian filter

The bathymetric lows can be masked by determining the zero-crossing of each slope from the bathymetry using the Laplacian filter (Marr & Hildreth, 1980). This space-domain filter uses curvature to discriminate long- and short-wavelength anomalies by delineating their zero-crossing points. This filter can be used to observe the general directionality and, at times, shapes and patterns of the observed signals. The two-dimensional filter can be expressed in many ways. One of them is described by Rosenfeld & Kak (1982), where the filter is expressed as the linear differential operator approximating the second derivative for a function (grid/image) $f(x, y)$ of two variables, given by:

$$\bigtriangledown^2 f = \frac{\partial^2 f}{\partial x^2} + \frac{\partial^2 f}{\partial y^2} \tag{2.7}$$

where x and y are the horizontal coordinates of each cell. However, if the filter is applied directly to the original gridded bathymetry, too many edges will be detected, as a slight change of slope will be defined as new zero-crossing. In the same study, Marr & Hildreth (1980) suggested the use of a smoothing filter before running the edge detection; hence the term Laplacian-of-Gaussian (LoG) mask (e.g., Huertas & Medioni, 1986). The Gaussian filter itself is a fixed bell-shaped response curve that is essentially a space-domain low-pass filter from a specified cut-off wavelength, which is useful to mask out noise and high-frequency features that might affect further operations and interpretations. The use of Gaussian filters has been appealing for many grid/image processing purposes as the Fourier transform of this filter is also inferring its capability in averaging the data set without neglecting its original distribution. The two-dimensional filter can be expressed in many ways. One of them is described by Deng & Cahill (1993) as:

$$G(x, y) = \frac{1}{\sqrt{2\pi\sigma}} exp(-(x^2 + y^2)/2\sigma^2) \tag{2.8}$$

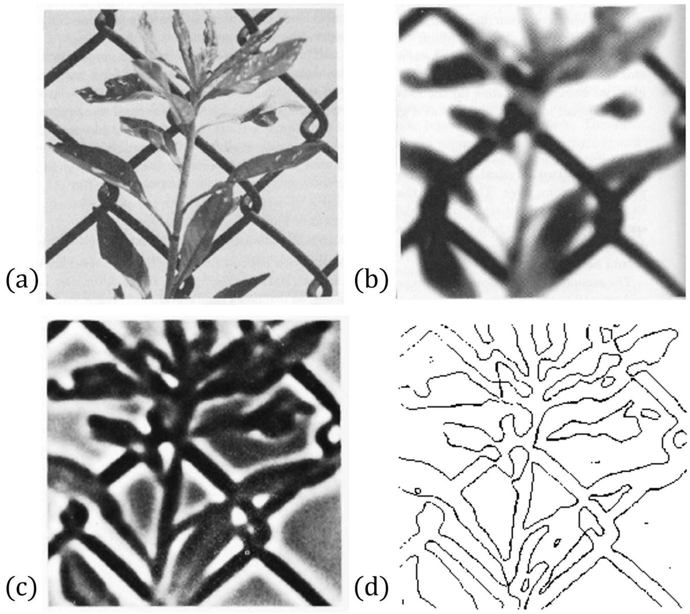

Figure 2.6: Illustration of Laplacian-of-Gaussian (LoG) filter, after Marr & Hildreth (1980). (a) Sample image as a data input. (b) Gaussian-filtered data. Each cell/pixel is smoothed at a specific wavelength. (c) LoG-filtered data. Edges are detected from the smoothed data. (d) LoG mask. The mask is used to distinguish the positive and negative values computed from the LoG filter.

where σ^2 is the variance of Gaussian filter, and the size of the filter kernel l $(-l \leq x, y \leq l)$ is often determined by omitting values lower than five percent of the maximum value of the kernel. The application of the combination of these two filters can be seen in Figure 2.6. Accordingly, a cut-off wavelength for the Gaussian filter must be specified to optimise the identification of OCCs within the study area.

2.4 Algorithm building

The SWE algorithm is built to obtain the numerical description of the magmatic and tectonic crust through a series of calculation based on the distribution of the azimuth and plunge observed in the seafloor morphology. The calculation will be applied to a set of gridded multibeam bathymetry through a moving window, starting from the top-left corner down to the bottom-right corner of the grid. In this section I will explain the steps of the algorithm building, starting by sampling several OCC and magmatic terrain patches to examine its general spherical distribution, followed by determining the most optimum window size that will best capture the morphology of an OCC without much interference from the surroundings, and ended by constructing a grid that consists of an appropriate weight matrix.

2.4.1 Calculating terrain eccentricity from the horizontal eigenvalues

To observe the general pattern of the two types of spreading, I selected 10 different patches of OCC and magmatic terrain (MTR), guided by the interpretation of (Smith *et al.*, 2008). For this trial, I sampled the terrain patches with a window size of 8' (~14.8 km), following the general size of OCCs found in the MAR (e.g., Cann *et al.*, 1997, 2015; Smith *et al.*, 2008). A more thorough sensitivity test on the window size determination will be discussed in the next subsection. The selected terrain patches are shown in Figure 2.7. From the original gridded cell size (200 m), the terrain patches are resampled into having a 15" (~462 m) cell size to optimise the computing time while maintaining quality. The resampling is carried out through the `grd2xyz` and `surface` functions in GMT.

Firstly, the general pattern of the terrain is observed from its plunge and azimuth. By computing these two parameters, we can see that the edges of an OCC are depicted as having steeper slopes compared to its surroundings, and dipping in an omnidirectional form (Figure 2.8). On the other hand, the fault planes over a magmatic terrain are also depicted as having steeper slopes compared to their surroundings, but not as steep as those found at the edges of an OCC. These slopes indicate the steep yet narrow scarps bounding the abyssal hills, which alternate in a bi-directional form (Figure 2.9). The general directionality of each terrain patch can also be viewed in the form of azimuth roses (Figure 2.8d and 2.9d). We can see that the azimuth is distributed more equally in the OCC compared to a more clustered distribution in the magmatic terrain.

Secondly, we can plot the local (x, y, z) coordinates of each cell in the form of spherical distribution. From Figure 2.8 and 2.9, we can see that in general, the variation in the vertical axis is not comparable to those in the horizontal axes as the plunge values computed in the study area never surpass 30°. To prove this argument, I calculate the eigenvalues of each terrain patch, which results can be seen in Table 2.1. From the table, we can see that the values of λ_1 is extremely small compared to the other two eigenvalues. This confirms the argument in 2.3.2, in which the vertical axis will always be described as λ_1, with λ_2 and λ_3 axes described consecutively following the right-hand rule. Furthermore, we can already see a pattern of directionality in the ratio between λ_2 and λ_3 over both types of terrain. In the OCCs, the ratio between these two horizontal eigenvalues is not as drastic as the ratio found in the magmatic terrain. This observation simplifies the directionality previously observed in the azimuth grid and azimuth rose.

Finally, we can describe the general directionality of each patch of terrain in one single number by computing the eccentricity of a ‘horizontal ellipse,’ where λ_3 and λ_2 are defined as its semi-major and semi-minor axes, respectively (Figure 2.8f and 2.9f). In Table 2.1, we can already see that OCCs generally have lower value of eccentricity compared to the magmatic terrain. These results confirmed the efficacy of the algorithm in sampled terrain patches and is ready to be applied to the whole grid.

2.4.2 Determining optimal window size

The main feature that characterises the tectonic mode of spreading is the presence of the OCCs. The OCCs are varying in shape and size, depending in which side of the ridge they are emplaced and their proximity to fracture zones or non-transform offsets. Therefore, the application of the established algorithm to the whole bathymetric grid must be preceded by determining the most effective window size that will best capture the morphology of an OCC without much interference from the surroundings.

Over the selected OCC terrain patches, I carried out a sensitivity test by creating windows with varying widths, ranging from 4’ (∼7.4 km) to 16’ (∼29.6 km) with the interval of 2’ (∼3.7 km) and testing the algorithm over the terrain sampled with these varying window sizes. The general results of the sensitivity test can be seen in Figure 2.10. The figure shows that that the 8’ (∼14.8 km) window is the best fit window size as it generally computes the lowest value of eccentricity with the narrowest range of values. A few detailed samples of the process can be seen in Figure 2.11 and and 2.12. In the figures, we can see how the eigenvalue ellipses (Equation 2.4) are computed over the OCC-02 and OCC-09 terrain patches using the varying window sizes. As can be seen in Figure 2.11, the lowest value of eccentricity is computed when the window size is 16’ (∼14.8 km). However, as can be seen in the index map of the figure, we can see that the computation is largely affected by the extreme change of depth north of the OCC, implying uncertainty to the computed eccentricity value. Therefore, I computed the resultant (R) of the eigenvalues ($\lambda_1, \lambda_2, \lambda_3$) to have the overall description of the terrain directionality, defined as:

$$R = \sqrt{{\lambda_1}^2 + {\lambda_2}^2 + {\lambda_3}^2} \tag{2.9}$$

In Figure 2.11g, we can see that although the eccentricity is minimised at 16’, the eigenvalue resultant is relatively large compared to the other computed eccentricity ellipses. Another set of results is shown in Figure 2.12, where the eccentricity and resultant eigenvalue are both minimised at 6’ (∼11.1 km). This test is carried out on all 10 sampled OCCs and the results are compiled in Figure 2.10. From the distribution summarised in the boxplot, I decided to use 8’ as the window size to run the algorithm to the whole gridded multibeam data as it consistently computes low SWE values with the narrowest range of data.

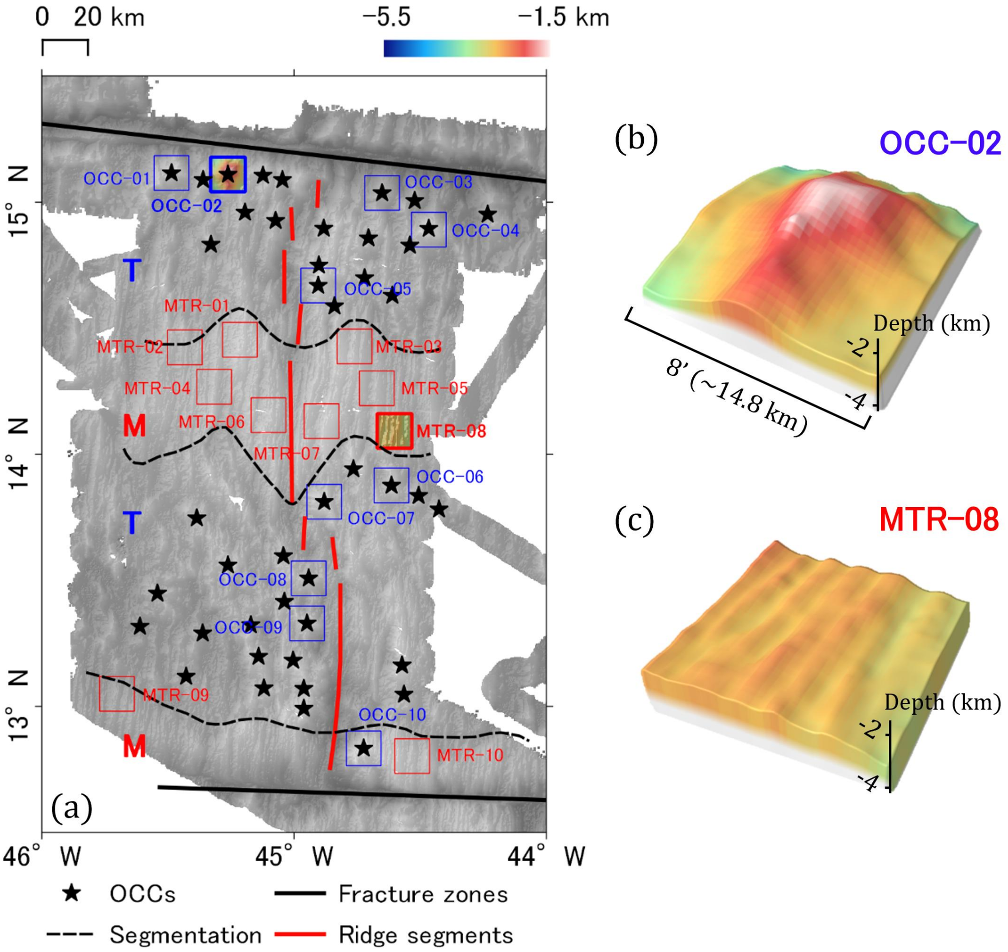

Figure 2.7: Distribution of sampled OCC and magmatic terrain patches. (a) Study area with the distribution of sampled OCC (blue squares) and magmatic terrain (red squares) which will be used throughout the study. Inferred OCCs and segmentation Smith *et al.* (2008), fracture zones, and ridge segments are identified as in Figure 2.1. (b) A three-dimensional visualisation of an OCC terrain patch. (c) A three-dimensional visualisation of a magmatic terrain patch. The terrain patches shown are sampled with 8’ × 8’ window and 15” cell size. From both terrain patches, we can see that the OCC tend to have steeper slope than the magmatic terrain.

.

Table 2.1: Eigenvalues $(\lambda_1, \lambda_2, \lambda_3)$ and eccentricity (e) of the sampled terrain patches

Patch ID	λ_1	λ_2	λ_3	e
Oceanic core complex (OCC)				
OCC-01	0.04	0.42	0.54	0.63
OCC-02	0.05	0.42	0.53	0.62
OCC-03	0.02	0.43	0.55	0.63
OCC-04	0.04	0.40	0.56	0.70
OCC-05	0.04	0.31	0.65	0.88
OCC-06	0.04	0.33	0.63	0.80
OCC-07	0.04	0.40	0.56	0.72
OCC-08	0.03	0.41	0.56	0.67
OCC-09	0.05	0.42	0.53	0.61
OCC-10	0.06	0.42	0.52	0.60
Magmatic terrain (MTR)				
MTR-01	0.01	0.26	0.73	0.94
MTR-02	0.01	0.17	0.82	0.98
MTR-03	0.02	0.23	0.75	0.95
MTR-04	0.02	0.17	0.81	0.98
MTR-05	0.01	0.18	0.81	0.98
MTR-06	0.02	0.18	0.80	0.97
MTR-07	0.03	0.17	0.80	0.98
MTR-08	0.01	0.20	0.79	0.97
MTR-09	0.01	0.27	0.72	0.93
MTR-10	0.01	0.26	0.73	0.94

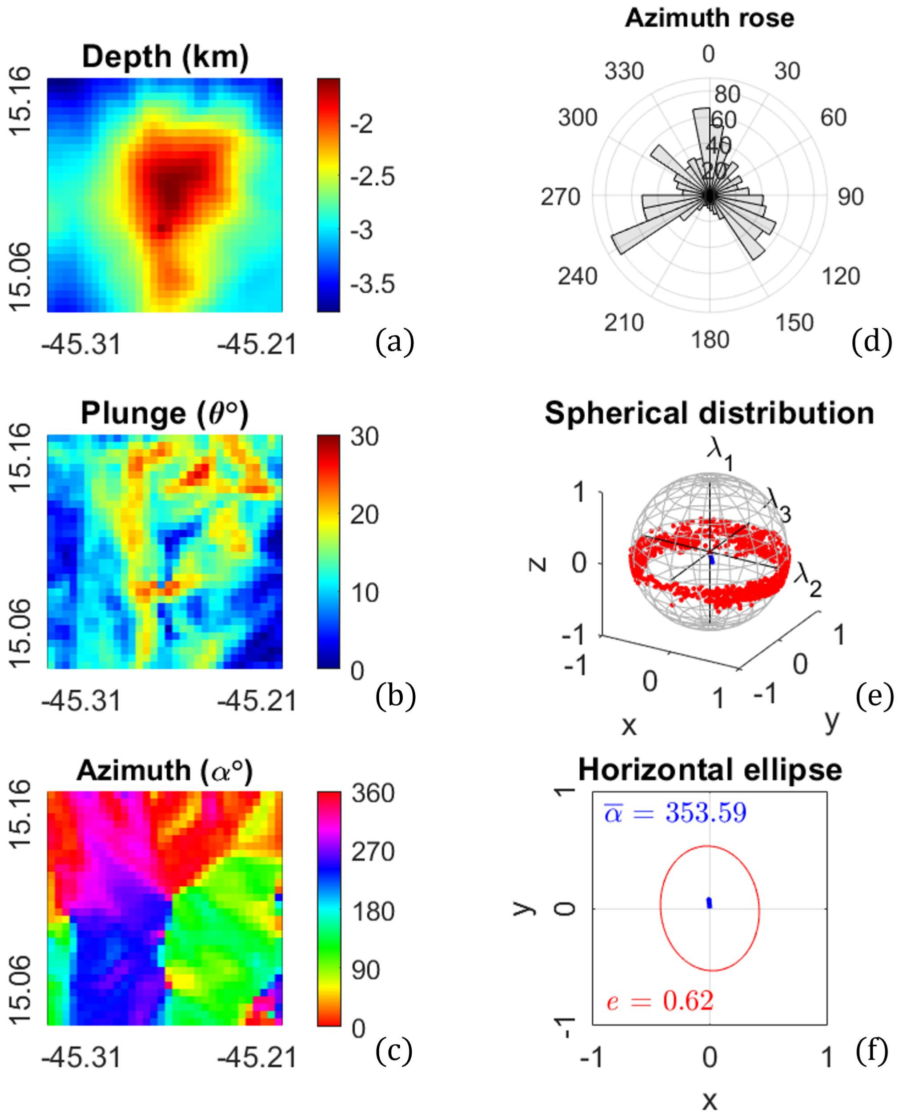

Figure 2.8: Directionality of OCC-02 terrain patch. (a) Depth in km. (b) Plunge, or θ in degrees. The edges surrounding the OCC are depicted as having steeper slopes up to $\sim 30°$. (c) Azimuth, or θ in degrees. The OCC is depicted as an omnidirectional feature centred at the peak of the massif. (d) Azimuth rose. (e) Spherical distribution. We can see that variation in the vertical axis is incomparable to those in the horizontal axes, confirming the argument in 2.3.2. (f) Horizontal ellipse. The mean azimuth, $\bar{\alpha}$, depicts the resultant of the whole point masses and the eccentricity, e, describes the directional trend observed over the terrain patch.

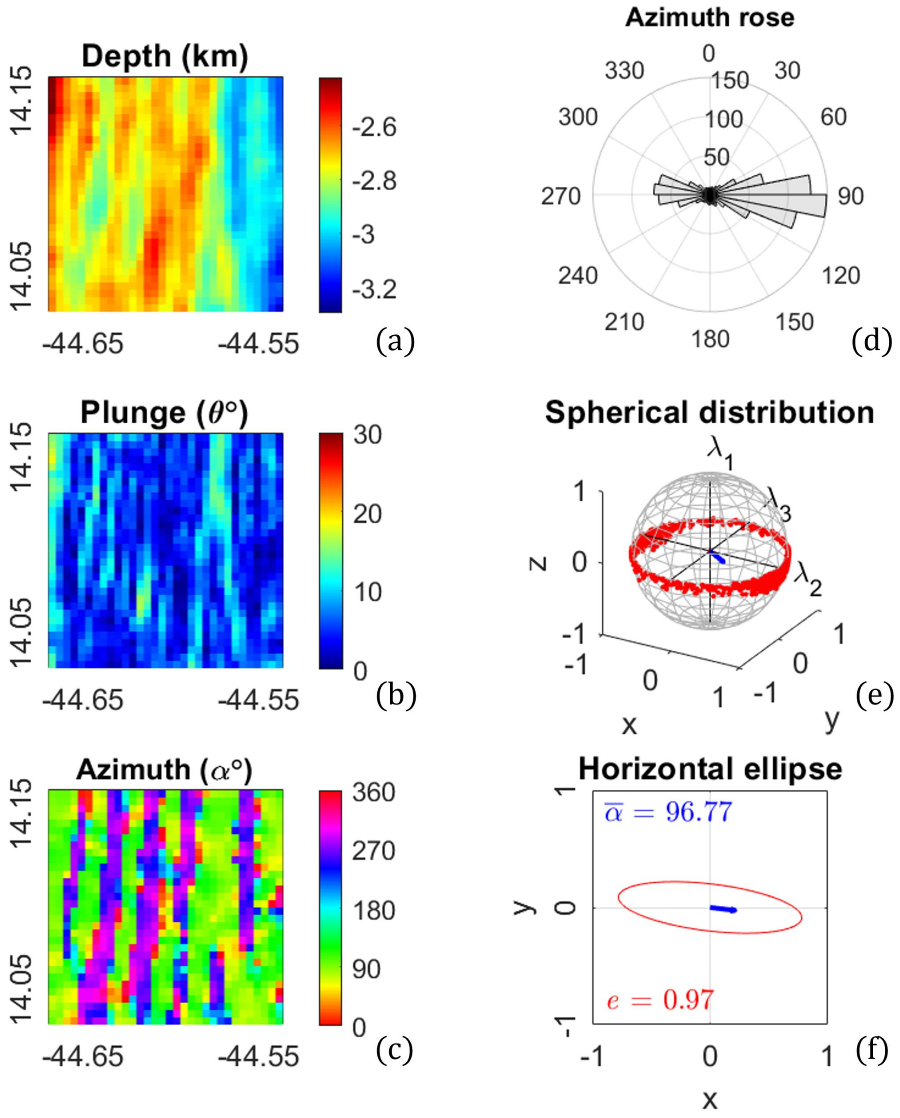

Figure 2.9: Directionality of MTR-08 terrain patch. (a) Depth in km. (b) Plunge, or θ in degrees. The edges of the abyssal hills are depicted as having gentler slopes compared to the OCC terrain patch. (c) Azimuth, or θ in degrees. The terrain patch is depicted as consecutive bi-directional features. (d) Azimuth rose. (e) Spherical distribution. We can see that variation in the vertical axis is still incomparable to those in the horizontal axes. (f) Horizontal ellipse. The mean azimuth, $\bar{\alpha}$, depicts the resultant of the whole point masses and the eccentricity, e, describes the directional trend observed over the terrain patch. We can see that the eccentricity value of this terrain patch is higher than in the OCC.

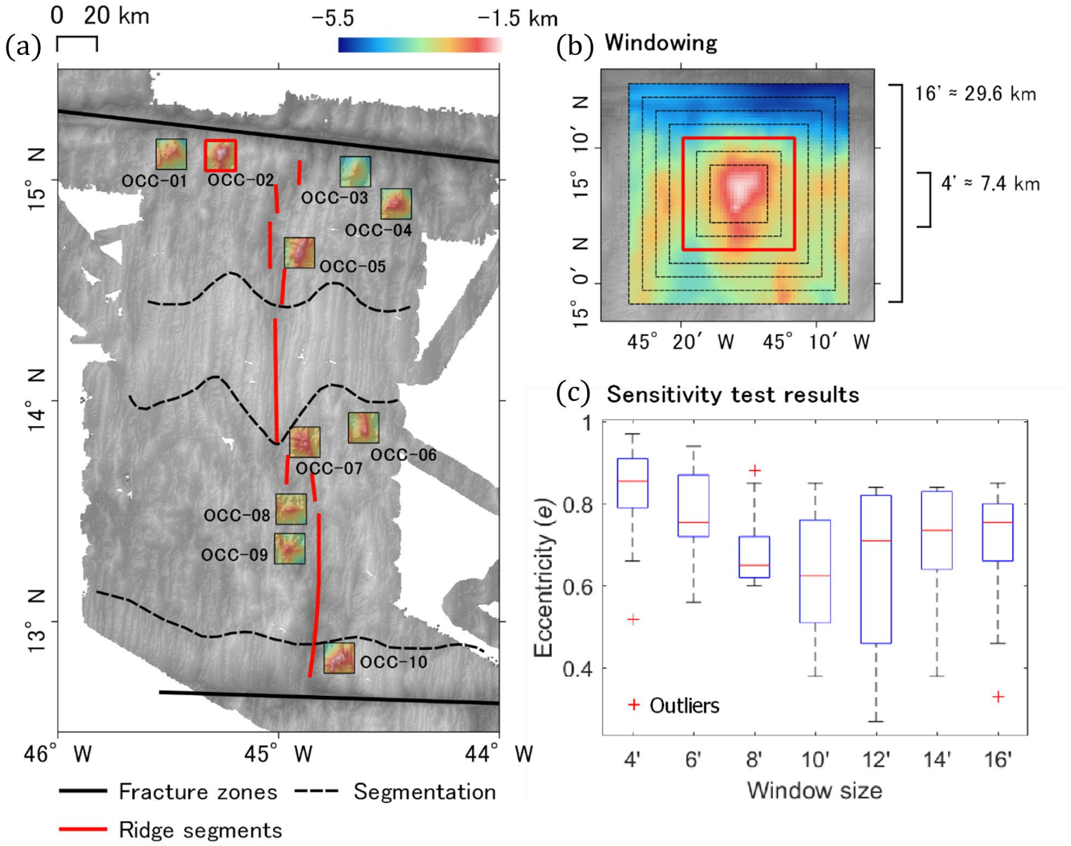

Figure 2.10: Sensitivity test to determine the optimum window size. (a) The 10 OCCs selected for the sensitivity test. The selection is aided by the interpretation of Smith *et al.* (2008). (b) Illustration of OCC windowing. The window size varies from 4' (∼7.4 km) to 16' (∼29.6 km). Dashed square: windows with varying sizes. Red square: best-fit window. (c) Sensitivity test result, each with the sample size of 10 OCCs. Each window size is presented as a 'box and whisker' plot. The red line in each 'box and whisker' plot is the median eccentricity value of each window size, the 'box' shows the interquartile range of the eccentricity values (from Q1, or lower quartile, to Q3, or upper quartile), and the 'whiskers' the minimum and maximum eccentricity values. It can be seen from the plot that the window size of 8' (∼14.8 km) is the best fit as it delivers the smallest range of eccentricities.

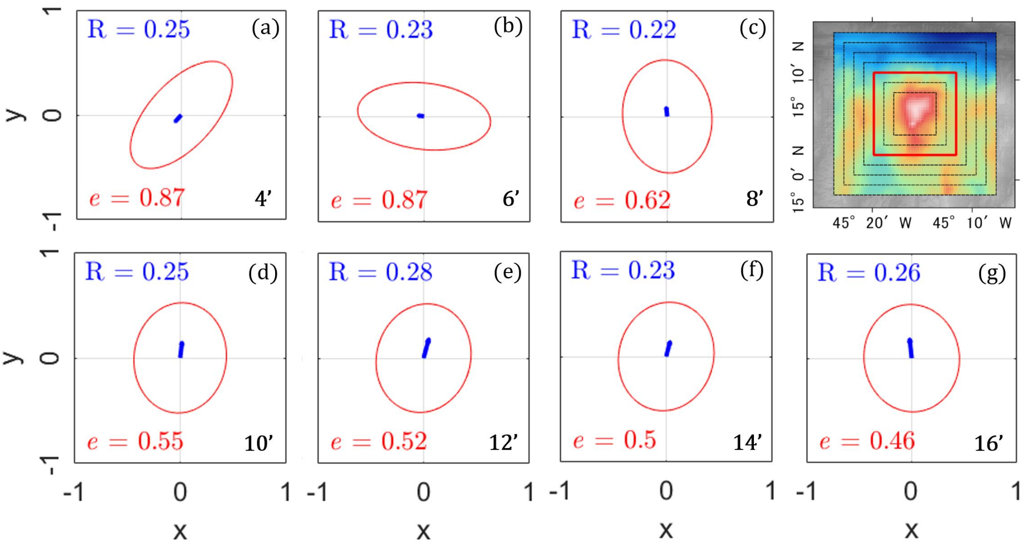

Figure 2.11: Windowing over the OCC-02 terrain patch. Figures (a) to (g) are eigenvalue ellipses with window sizes varies from 4’ (∼7.4 km) to 16’ (∼29.6 km), illustrated in the index map (top-right corner). Although the 8’ (∼14.8 km) window size (c) does not return the lowest eccentricity value on this OCC, it returns a relatively consistent range of eccentricity values when applied to the other OCCs as it computes the directional component of the OCC without much interference from the surroundings. For instance, the 16’ window (g) computation is significantly affected by the extreme change of depth at the north, depicted in its relatively large eigenvalue resultant, R compared to the other windows. See Figure 2.12 for another set of results.

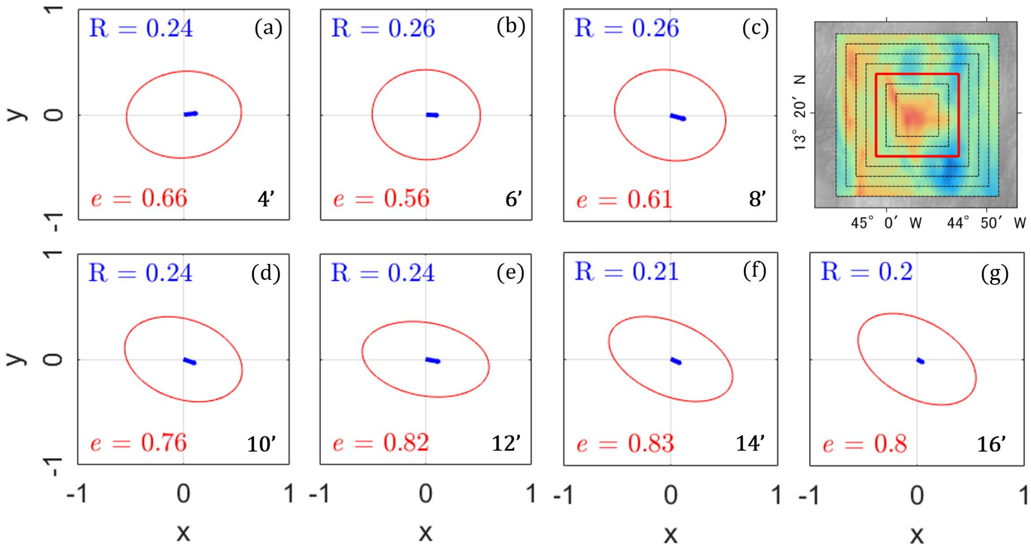

Figure 2.12: Windowing over the OCC-09 terrain patch. Figures (a) to (g) are eigenvalue ellipses with window sizes varies from 4' (∼7.4 km) to 16' (∼29.6 km), illustrated in the index map (top-right corner). Compared to the results in Figure 2.11, the best fit window identification for this OCC can be identified more clearly, as the 6' (∼11.1 km) window returns both the lowest eigenvalue resultant, R, and eccentricity, e. Figure 2.10 compiles all the resulting eccentricities and shows that the 8' (∼14.8 km) is the best fit to run in this study area as it generally captures the morphology of OCC as a whole without much interference from the surrounding terrain.

2.4.3 Building the weight matrix

Having the optimum window size defined, I can now build a weight matrix to quantify the vertical components of the sampled terrain. As discussed in 2.3.4 I define the weight matrix using Equation 2.5, in which the defining parameter is the `slope` values computed from the bathymetry. In this subsection, I will explain how the equation is defined and how the weight matrix can give consistent terrain classification with the eccentricity calculation carried out in 2.4.1.

In 2.3.4, I presume that the high-angle normal faults over the magmatic terrain might be depicted as having gentler slopes compared to the long-lived detachment faults, as the horizontal offsets are naturally much narrower than those observed at the footwall of the detachment faults. To prove this hypothesis, I compute the slopes of all the sampled OCCs and magmatic terrain and show their distribution in the form of frequency histograms. In Figure 2.13, we can see that the slopes observed over an OCC falls between 0° and 30°. A gradual change is observed between one frequency bin to another. This might depict the moderate change of slope forming the domed-shape feature. The mean values of the slope histograms fall between 9.1° and 14°. On the other hand, we can see in Figure 2.14 that the range of the slopes observed over the magmatic terrain is generally narrower than those observed in the OCC. In addition, we can see a more extreme change between one frequency bin to another, specifically starting at slopes over 5°-10°. The mean values of the slope histogram falls between 5.2° and 8.1°, which is lower than the mean slope values at the OCCs and hence confirming the presumed hypothesis.

We can also examine the histogram by computing each histogram's skewness and kurtosis values (Table 2.2). The skewness and kurtosis values allow us to characterise the symmetry and the tails respectively of the slope distribution in a windowed terrain. For instance, a perfectly domed OCC will be defined with the skewness and kurtosis values closest to the reference values, as the slope distribution will mimic a Gaussian normal distribution. As a reference, the skewness value of a perfectly symmetrical normal distribution is zero. An increase of skewness value depicts the increase of asymmetricity of a slope distribution. Meanwhile, the tails of a normal distribution are defined with a reference kurtosis value of three. A decrease of kurtosis value depicts heavier tails, while an increase depicts lighter tails.

In Table 2.2, we can see that the slope distribution of the windowed OCCs is characterised by the skewness and kurtosis values closer to the reference values than the magmatic terrain, which indicates little domination of any specific slope values compared to the highly skewed and light-tailed slope distribution in the magmatic terrain. The highest skewness value in the slope distribution of a windowed OCC is found in OCC-07. In this particular OCC, the breakaway zone is indicated by a steep-dipping slope facing away from the axis, increasing the asymmetry of the histogram. Meanwhile, the lowest skewness value in the slope distribution of a windowed magmatic terrain is found in MTR-10. The proximity of this patch of magmatic terrain to an OCC decreases the asymmetry of the histogram. We can also see that in the windowed terrain, a high skewness value correlates with the kurtosis value that is the furthest from the reference, while a low skewness value correlates with the kurtosis value the closest to the reference. This observation validates the use of slope as one of the main parameters in characterising the types of terrain in our study area.

To observe the spatial extent of the weight matrix, I computed the slopes of the OCC-02 and MTR-08 terrain patches, which results can be seen in Figure 2.15b and 2.16b. In the figures, we can see that the slopes surrounding the OCC are computed as steeper slopes compared to those bounding the abyssal hills in the magmatic terrain. However, the eccentricity calculation favours magmatic terrain with higher values compared to the OCC, as high eccentricity values represent a bi-directional trend of dipping slopes. Therefore, the consequent weight matrix must be built based on the early classification obtained from the eccentricity of the horizontal eigenvalues. Lower weight must be assigned to terrain patches containing potential OCCs. From this understanding, Equation 2.5 is defined and its application can be seen in Figure 2.15c and 2.16c.

In Figure 2.15c, we can see how the computed weight (W) allows an identification of the OCC, as the steep slopes surrounding the OCC are converted into cells with lower W values. In addition, we can see from the frequency histogram Figure 2.15d) that the W values are distributed quite normally, following a normal Gaussian distribution. The histogram hence represents the general distribution of the vertical component of the sampled terrain, where the slopes observed over an OCC tend to vary gradually following the domed structure. On the other hand, as magmatic terrain is governed by sparse, parallel, and gentle dipping slopes, Equation 2.5 allows the ‘background’ values to be computed as cells with higher W values (Figure 2.16c). In contrast with the OCC, the frequency histogram shows a skew, representing an extreme number of cells defined as higher W values (Figure 2.16d). Having the weight matrix defined, we can now run the complete SWE algorithm to the whole dataset.

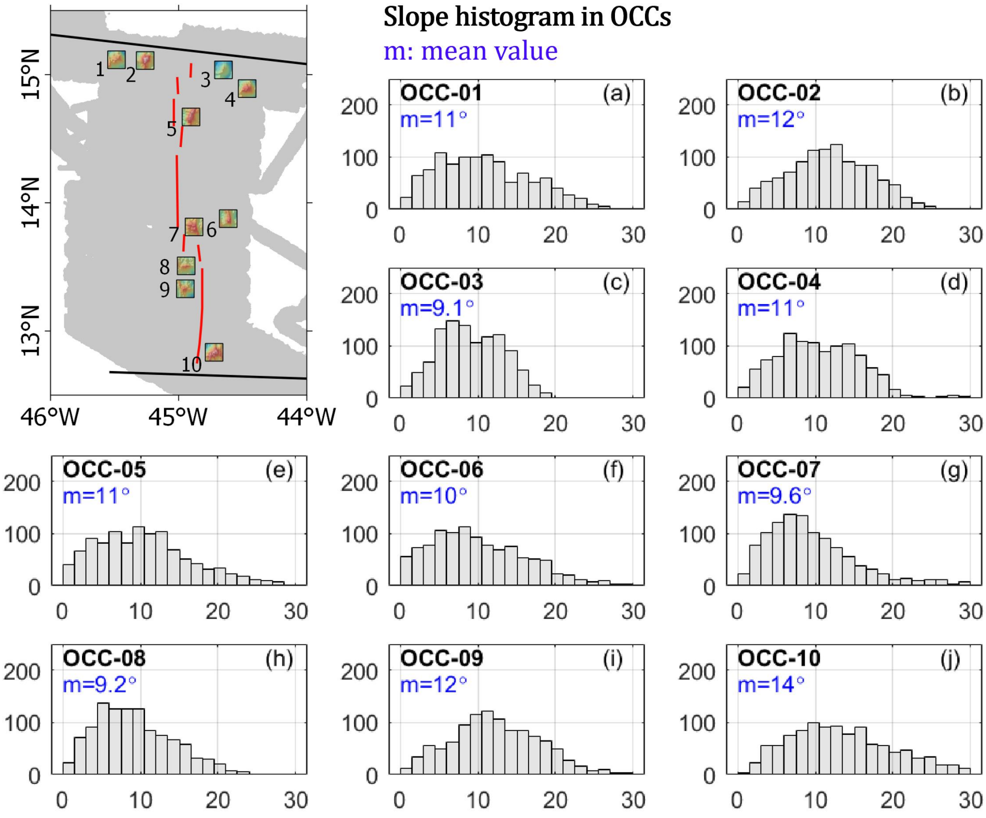

Figure 2.13: Slope histogram of the sampled OCCs. Frequency histogram of the slopes observed on OCC-01 to OCC-10 are depicted in (a) to (j) with locations depicted in the inset. The x-axis of each histogram is the value of the slope in degrees and the y-axis is the frequency, or number of slopes in each bin. In general, we can see a gradual change between one frequency bin to another, depicting the moderate change of the omnidirectional slopes observed on an OCC. A bell-shaped distribution mimicking the Gaussian normal distribution is observed at OCC-02 as the size of the OCC matches quite well with the size of the window and the shape of this particular OCC mimics the shape of a dome centred within the windowed area. Skewed distribution is mainly found at OCC-05 to OCC-08 as the breakaway zone of these OCCs is indicated by a steep-dipping slope, facing the opposite direction of the axis. The mean value of the slopes observed over these OCCs falls between 9.2° and 14°.

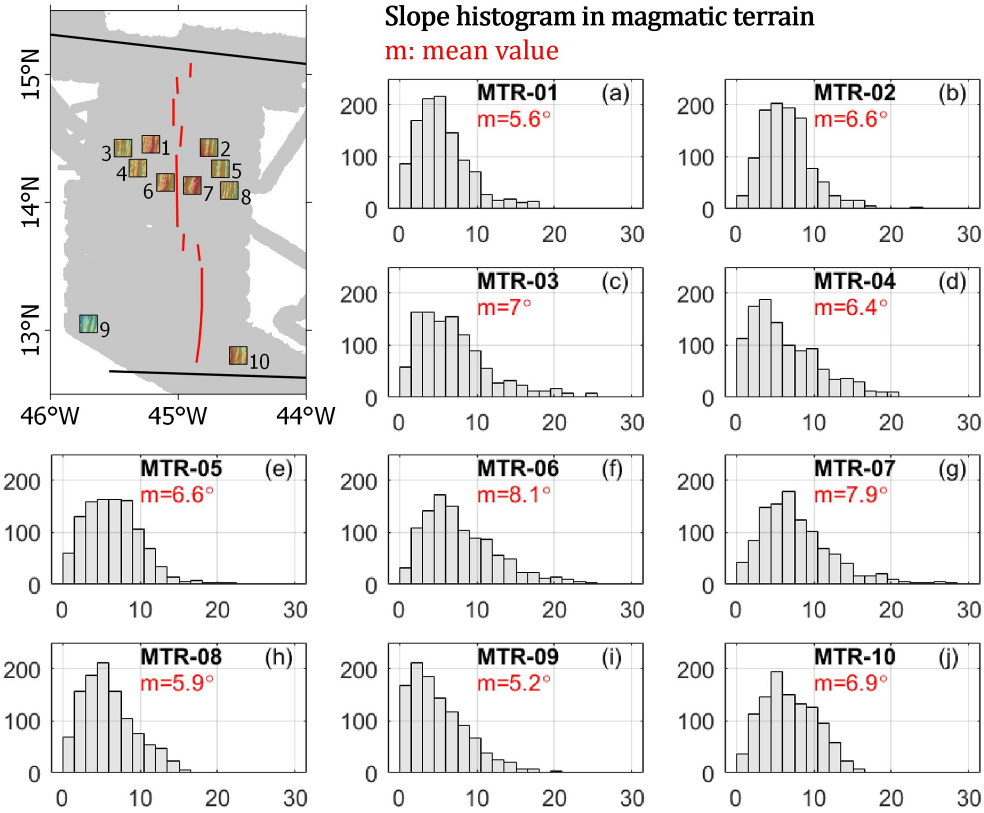

Figure 2.14: Slope histogram of the sampled OCCs. Frequency histogram of the slopes observed on MTR-01 to MTR-10 are depicted in (a) to (j) with locations depicted in the inset. The x-axis of each histogram is the value of the slope in degrees and the y-axis is the frequency, or number of the slope in each bin. In general, we can see a more extreme change between one frequency bin to another, specifically starting from around 5°-10°. This extreme change depicts the sparsity of the steep slopes over this type of terrain. The largely skewed distribution depicts the domination of the ‘background’ or the ‘flat’ values compared to the steep-dipping slopes. The mean value of the slopes observed over these OCCs falls between 5.2° and 8.1°, which is lower than the mean slope values at the OCCs.

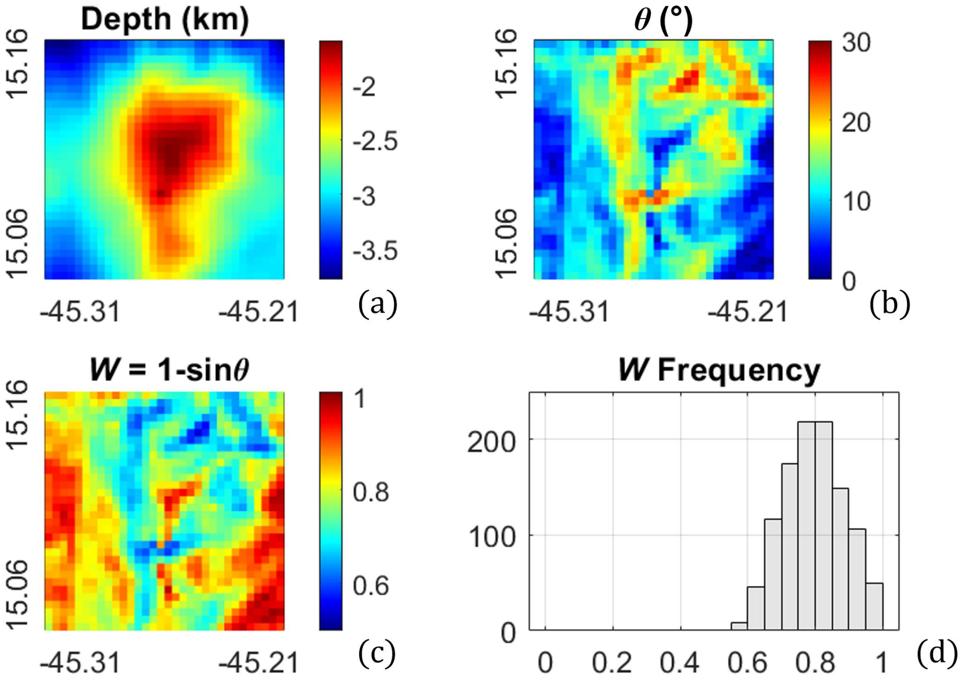

Figure 2.15: Computing the weight matrix over an OCC. (a) The bathymetry (depth) of OCC-02, gridded at 15" with 8' window size. (b) Computed slope (θ). We can see that the OCC is surrounded by omnidirectional steep-dipping slope. (c) Computed weight matrix (W). The OCC is indicated by cells with lower W values. (d) The frequency histogram of the W matrix over an OCC. Skewness: 0.00. Kurtosis: 2.39. Mean: 0.80. Standard deviation: 0.09. The skewness value depicts the omnidirectional dipping slopes characterising the OCCs in tectonic terrain. The kurtosis value imply that the histogram closely resembles a perfectly Gaussian distribution, for which the kurtosis value is 3.

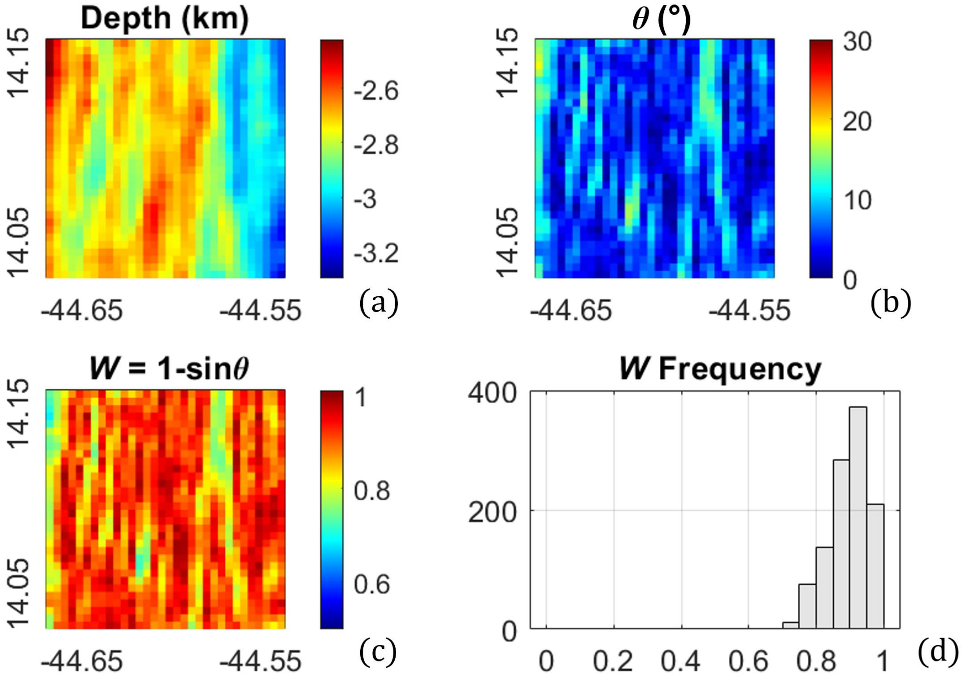

Figure 2.16: Computing the weight matrix over MTR-08. (a) The bathymetry (depth) of the sampled magmatic terrain, gridded at 15" with 8' window size. (b) Computed slope (θ). We can see that the magmatic terrain is characterised by sparse, parallel, gentle dipping slopes scattered over the sampled area. (c) Computed weight matrix (W). The magmatic terrain is indicated by cells with higher W values. (d) The frequency histogram of the W matrix over a sampled magmatic terrain. Skewness: -0.67. Kurtosis: 2.95. Mean: 0.90. Standard deviation: 0.06. The negative skew distribution occurs as the W is confined to values $0 \leq W \leq 1$. It is impossible for the 'tail' of the distribution to be symmetric about its mode as the greatest value computed by the equation in (c) is 1. The kurtosis value imply that the histogram closely resembles a perfectly Gaussian distribution, for which the kurtosis value is 3.

Table 2.2: Skewness and kurtosis values of each slope histogram in the windowed OCC and magmatic terrain. SD: Standard deviation.

Oceanic core complex (OCC)			Magmatic terrain (MTR)		
Terrain ID	Skewness	Kurtosis	Terrain ID	Skewness	Kurtosis
OCC-01	0.43	2.49	MTR-01	1.09	4.29
OCC-02	0.04	2.41	MTR-02	1.17	5.40
OCC-03	0.12	2.30	MTR-03	1.26	4.63
OCC-04	0.53	3.46	MTR-04	0.98	3.49
OCC-05	0.66	3.14	MTR-05	0.94	4.75
OCC-06	0.74	3.31	MTR-06	1.36	5.73
OCC-07	1.20	4.58	MTR-07	1.24	5.02
OCC-08	0.55	2.74	MTR-08	0.69	2.99
OCC-09	0.49	3.40	MTR-09	1.17	4.61
OCC-10	0.71	3.59	MTR-10	0.37	2.54
Mean	0.55	3.14	Mean	1.03	4.34
SD	0.33	0.69	SD	0.30	1.03

2.5 Characterising the different types of spreading

To assess the performance of the established algorithm, it is applied to the whole bathymetric grid in the study area. The grid is resampled into 15" (∼462 m) cell size, following the tests over the sampled terrain patches. The resampling is carried out through the `grd2xyz` and `surface` functions in GMT. In this section, I will discuss the performance of the algorithm and how the resulting SWE numbers can aid automated identification of the oceanic crust formed by different types of spreading.

Figure 2.17 shows a general result of how the eccentricity, weight matrix, and SWE calculation works. In 2.17b, we can see how areas dominated with omnidirectional dipping slopes are quantified as having lower eccentricity numbers (e.g., areas in proximity to the bounding fracture zones), while areas dominated with bi-directional dipping slopes are quantified as having higher eccentricity numbers (e.g., the area in the middle of the 13°-15° N ridge segment). Afterwards, Figure 2.17c shows how the weight matrix assigns lower weight to areas that is dominated by faults with substantial horizontal offset. Specifically, we can see the areas in proximity to the bounding fracture zones are assigned with lower weight, in line with the definition resulting from the eccentricity calculation. Finally, the complete SWE grid is presented in Figure 2.17d, in which the weight matrix is assigned to the computed eccentricity. The figure shows how the SWE can classify the types of spreading by assigning cells with certain values based on the parameterisation that have been carried out in the sampled terrain patches.

In this section, I will discuss how we can further examine the resulting SWE grid and how specific ranges of SWE values can be determined to have the terrain classified into crusts formed specific types of spreading. I will start by examining the distribution of the SWE values both in the sampled OCC and magmatic terrain, defining the ranges of values determining specific types of spreading from the sampled terrain examination, and compare the final results to the terrain interpretation from previous studies.

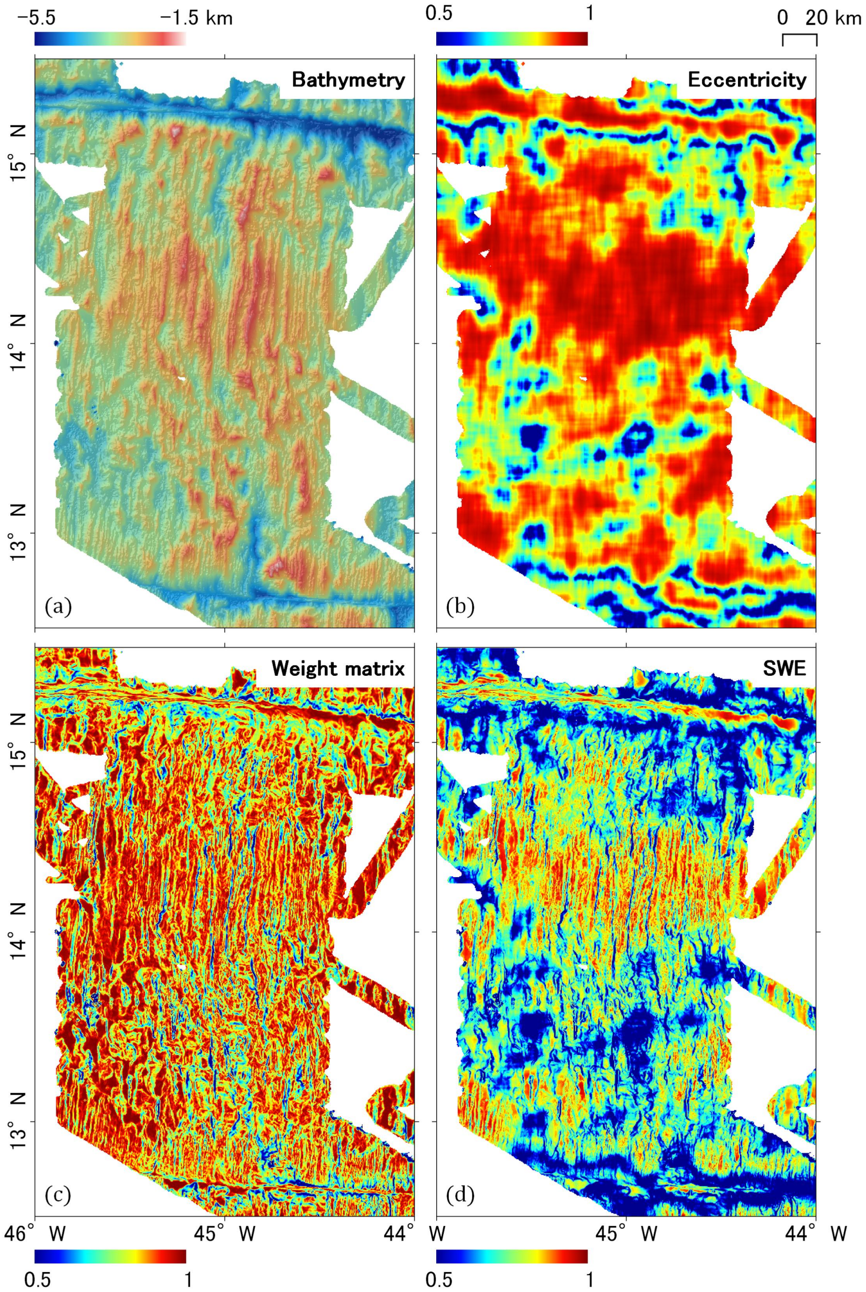

Figure 2.17: From bathymetry to SWE. (a) Bathymetry gridded in 15” cell size. (b) Eccentricity computed from the two horizontal eigenvalues. Lower eccentricity values indicate areas composed of omnidirectional dipping slopes. (c) Weight matrix (W) computed from the slope values. Lower W values indicate cells with relatively steep slope compared to its surrounding. (d) Slope-weighted eccentricity values (SWE), computed by assigning the weight matrix to the eccentricity grid. The general classification of the terrain can already be seen where tectonic terrain is indicated by lower SWE values. The boundary between the tectonic and magmatic types of spreading will be examined in Figure 2.18, 2.19, and 2.20.

2.5.1 SWE in sampled terrain patches

From the SWE grid shown in Figure 2.17d, I examine the distribution of the SWE values in the 10 sampled patches of OCC and magmatic terrain (Figure 2.18 and 2.19). In Figure 2.18, we can see that the SWE values in OCCs are generally distributed in a bell-shaped curve following a Gaussian normal distribution, in which the mean value lies approximately in the median of the histogram. The approximately normal distribution implies the gradual change of slope surrounding the dome-shaped/concave-downward OCCs. The mean SWE values of each sampled OCC fall between 0.45 and 0.68. The highest value is found at OCC-05 as the size of the OCC is slightly bigger than the size of the window used in the SWE algorithm. This in turn limits the performance of the SWE algorithm, as the window only captures a fragment of OCC-05 in which the detected slopes are dipping in a more bi-directional fashion. The remaining slopes at the northern and southern part of OCC-05 have been cut-off by the window. Despite this issue, all the histograms generally give consistent information on both the distribution and the range of SWE values that characterises tectonic terrain.

On the other hand, we can see that the SWE values in magmatic terrain are generally skewed towards the higher SWE values. The skewed distribution implies the domination of areas with high eccentricity values, indicating the presence of highly bi-directional dipping slopes that characterise the fault-bounded magmatic terrain. The mean SWE values of each sampled magmatic terrain fall between 0.80 and 0.85. The high SWE values also implies the sparsity of faults with substantial horizontal offset in the sampled terrain patch, leaving the areas with little to no slopes dominating the calculation of the weight matrix (Equation 2.5).

The obtained mean SWE values over the sampled OCC and magmatic terrain will be used to define the boundaries of the oceanic crust formed by the different types of spreading, which will be explained in the following subsection.

2.5.2 Spreading mode classification

From the observation in Figure 2.18 and 2.19, can define the bounding values of the tectonic and magmatic terrain. The observation can be simplified in the form of boxplots, shown in Figure 2.20. From the boxplots, we can see that the SWE values in the sampled OCCs are generally lower than those observed in the sampled magmatic terrain. The variation of SWE values is higher in the OCC samples compared to the magmatic terrain. From the distribution, I select the highest mean SWE value from the sampled OCCs as the uppermost boundary of the tectonic terrain (T). The value of this boundary is 0.68 with the standard deviation of ± 0.09. The standard deviation is computed from the SWE values in the consecutive terrain patch, i.e., the OCC-05. Another boundary is defined by the lowest mean SWE value from the sampled magmatic terrain, which will act as the lowermost boundary of the magmatic terrain (M). The value of this 0.80 with the standard deviation of ± 0.07. The standard deviation is also computed from the consecutive terrain patch, i.e., the MTR-10. Having these boundaries defined, the remaining terrain is defined as the extended terrain (E), where $0.68 < \text{SWE} < 0.80$. The extended terrain represents a buffer zone where both omnidirectional and bidirectional dipping slopes/faults exist, showing the transition from tectonic to magmatic spreading or vice versa. The SWE values of this buffer zone also lies within the standard deviation of the uppermost limit of the tectonic terrain and the lowermost limit of the magmatic terrain.

Having the ranges quantified, we can simplify the colour bar of the SWE grid in Figure 2.17d into three different classes: tectonic terrain ($\text{SWE} \leq 0.68$), extended terrain ($0.68 < \text{SWE} < 0.8$), and magmatic terrain ($\text{SWE} \geq 0.8$). The resulting grid is shown in Figure 2.21. In the figure, we can see how the algorithm manage to classify the terrain based on the parameterisation of the seafloor morphology. The results is then compared to the seismicity documented in Smith *et al.* (2003) and the visual interpretation of Smith *et al.* (2008). We can see that the tectonic terrain defined by the SWE algorithm correlates well with areas previously interpreted as tectonic terrain, where higher number of seismicity is observed as well as where the interpreted OCCs are in place. However, a complex alteration between the magmatic and tectonic terrain is observed in the southernmost segment. The observation improves the previous interpretation, where the southernmost segment was defined as being dominated by magmatic terrain. The results also shows the efficacy of the algorithm, at least when applied in this particular study area.

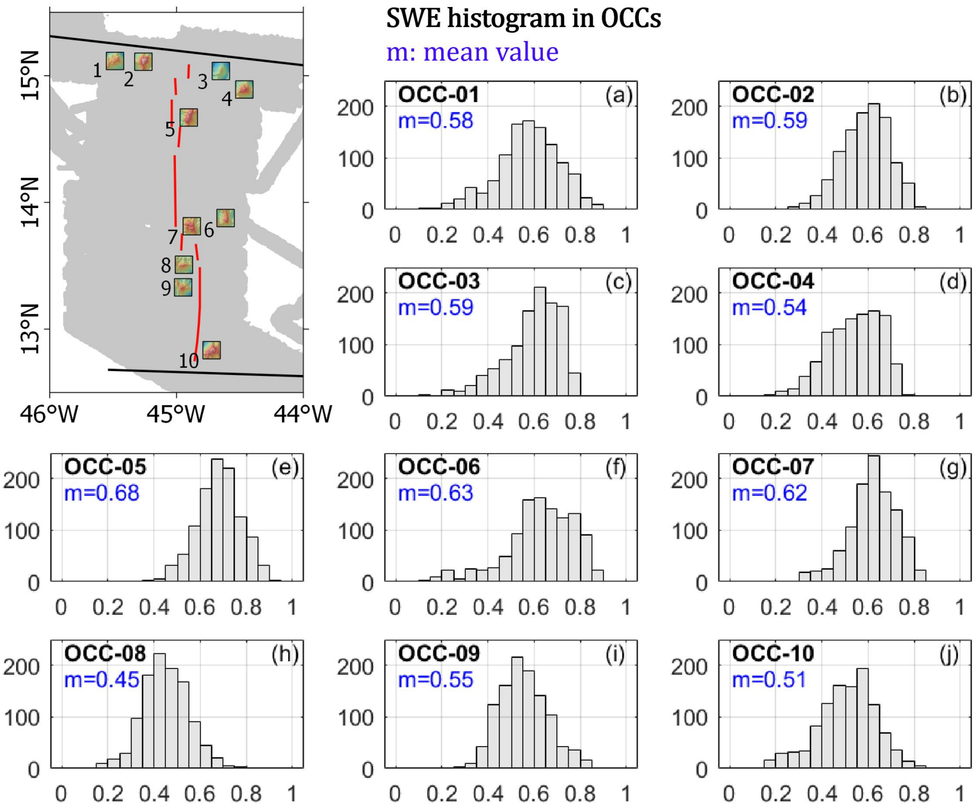

Figure 2.18: SWE histogram of the sampled OCCs. Frequency histogram of the SWE values computed on OCC-01 to OCC-10 are depicted in (a) to (j) with locations depicted in the inset. In general, we can see that most of the histograms mimic the bell-shape of a Gaussian normal distribution, in which the mean value lies approximately in the median of the histogram. The approximately normal distribution implies the gradual change of slope, both horizontally and vertically, surrounding the dome-shaped/concave-downward OCCs. It also implies that the window has manage to sample the terrain with the peak of the OCC centred in the middle of the window. The mean SWE value over these OCCs falls between 0.45 and 0.68.

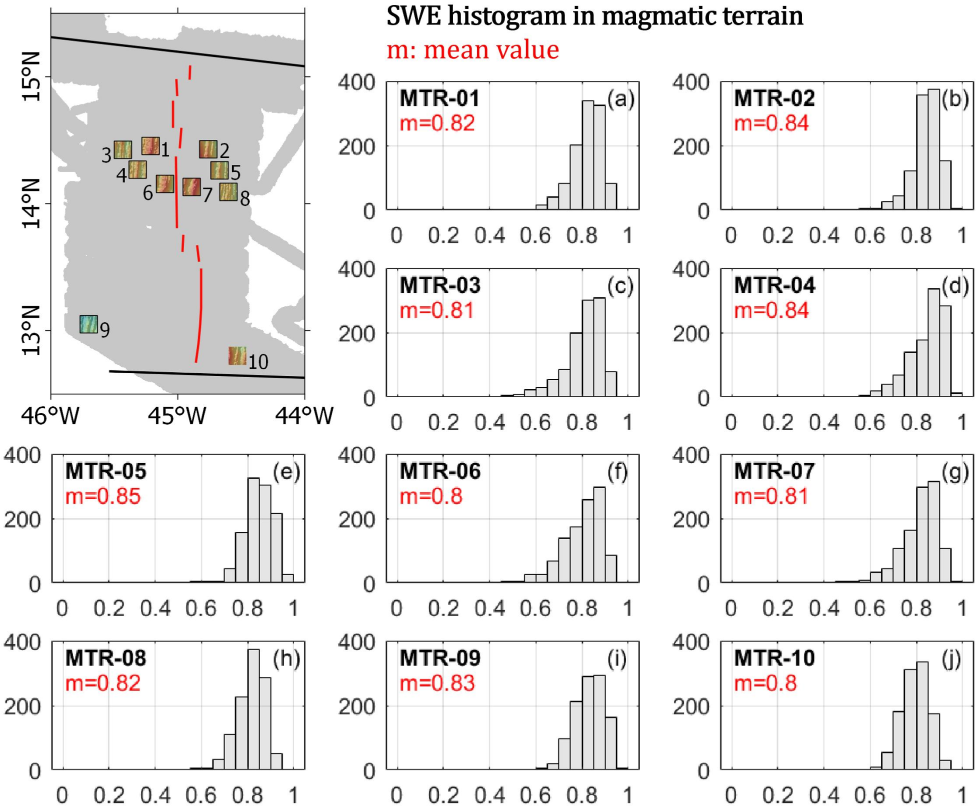

Figure 2.19: SWE histogram of the sampled magmatic terrain. Frequency histogram of the SWE values computed on MTR-01 to MTR-10 are depicted in (a) to (j) with locations depicted in the inset. In general, we can see that most of the histograms are skewed towards the higher SWE values. This implies the domination of areas with high eccentricity values, indicating highly bi-directional dipping slopes commonly found in the fault-bounded magmatic terrain. The high SWE values also implies areas with little to no slopes, as well as depicting the sparsity of faults with substantial horizontal offset. The mean SWE value over these sampled magmatic terrain falls between 0.8 and 0.85.

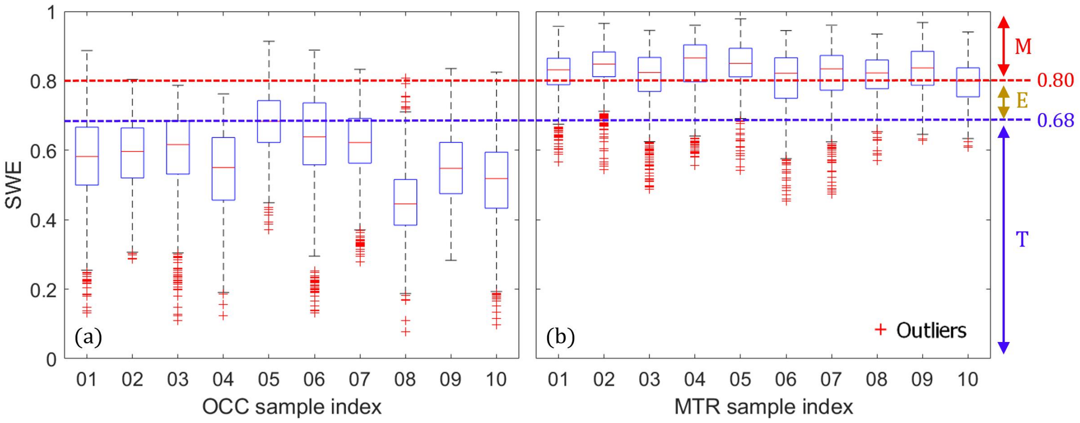

Figure 2.20: Terrain classification based on the SWE values computed in the sampled terrain patches. The SWE values in the sampled OCCs (a) are generally lower than those observed in the sampled magmatic terrain (b). Based on the distribution, I selected the highest mean SWE value at the sampled OCCs as the uppermost boundary of the tectonic terrain (T = SWE $\leq$ 0.68) and the lowest mean SWE value at the lowermost boundary of the magmatic terrain (M = SWE $\geq$ 0.80). The standard deviation of these bounding values is then computed from the SWE values in the consecutive terrain patches, i.e., the OCC with the highest mean SWE values (OCC-05) and the magmatic terrain with the lowest mean SWE values (MTR-10). The resulting standard deviation is ± 0.09 for the uppermost boundary of the tectonic terrain and ± 0.07 for the magmatic terrain. SWE values between 0.68 and 0.80 is defined as extended terrain (E), in which the alteration from one type of spreading to another are commonly found.

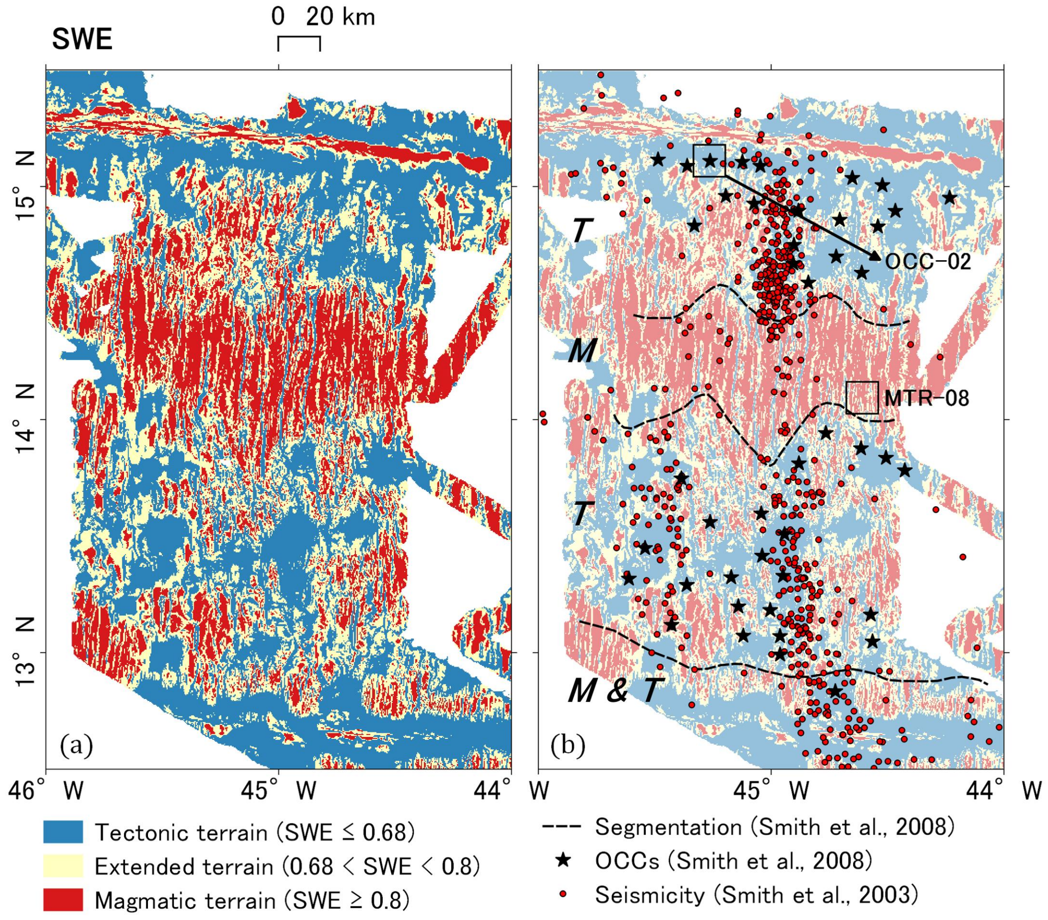

Figure 2.21: Terrain classification using the SWE algorithm. (a) The study area is classified based on the examination of the sampled OCC and magmatic terrain shown in Figure 2.20. Tectonic terrain is defined where SWE ≤ 0.68, extended terrain is defined where $0.68 <$ SWE < 0.8, and magmatic terrain is defined where SWE $\geq$ 0.8. (b) The SWE classification results is compared to the segmentation and OCCs interpreted by Smith *et al.* (2008) as well as seismicity documented in Smith *et al.* (2003). T: Tectonic terrain. M: Magmatic terrain. The tectonic terrain defined by the SWE algorithm correlates well with the areas close to the bounding fracture zones, where higher number of seismicity is observed as well as where OCCs inferred by Smith *et al.* (2008) are in place. A complex alteration between the magmatic and tectonic terrain is observed in the southernmost segment.

2.6 Identifying individual OCCs

In the previous section, I have assessed the performance of the SWE algorithm as well as defining the range of values to classify the study area into tectonic, extended, and magmatic terrain. However, the algorithm itself is not sufficient in identifying individual OCC as the curvatures of the seafloor has not been taken into account. For instance, local basins are described with SWE values similar to those computed over the OCCs, as the two distinct features are governed by a similar trend of directionality (Figure 2.22). Therefore, I created a mask aided by the Laplacian-of Gaussian (LoG) filter to eliminate concave-upward features which size and directionality mimics those found in OCCs.

Firstly, I applied a Gaussian filter with the window size of 8' (~14.8 km) to the gridded bathymetry, following the window size utilised in the SWE algorithm (Figure 2.23). As explained in 2.4.2, the window size also mimics the general size of OCCs found in the study area. From the filtered bathymetry, I applied the Laplacian filter to detect the zero crossing and separate the generalised morphology based on its curvatures. In the resulting LoG grid, the concave-downward features are defined as positive values (> 0), while the concave-upward features are defined as negative values. This grid is used as a mask to remove areas with concave-upward features from the SWE grid. The remaining area is shown in Figure 2.23c, in which the local basins have been removed from the SWE grid. Finally, we can highlight the individual OCCs by removing areas indicated as extended and magmatic terrain (Figure 2.23d). The results correlate quite well with the OCCs inferred by Smith *et al.* (2008) and potentially indicate other OCCs that have not been previously defined. This experiment shows that if the SWE algorithm is coupled with the application of the LoG filter, it can potentially be used not only to classify the different types of terrain, but also to aid the identification of individual OCCs within the tectonic terrain in the study area.

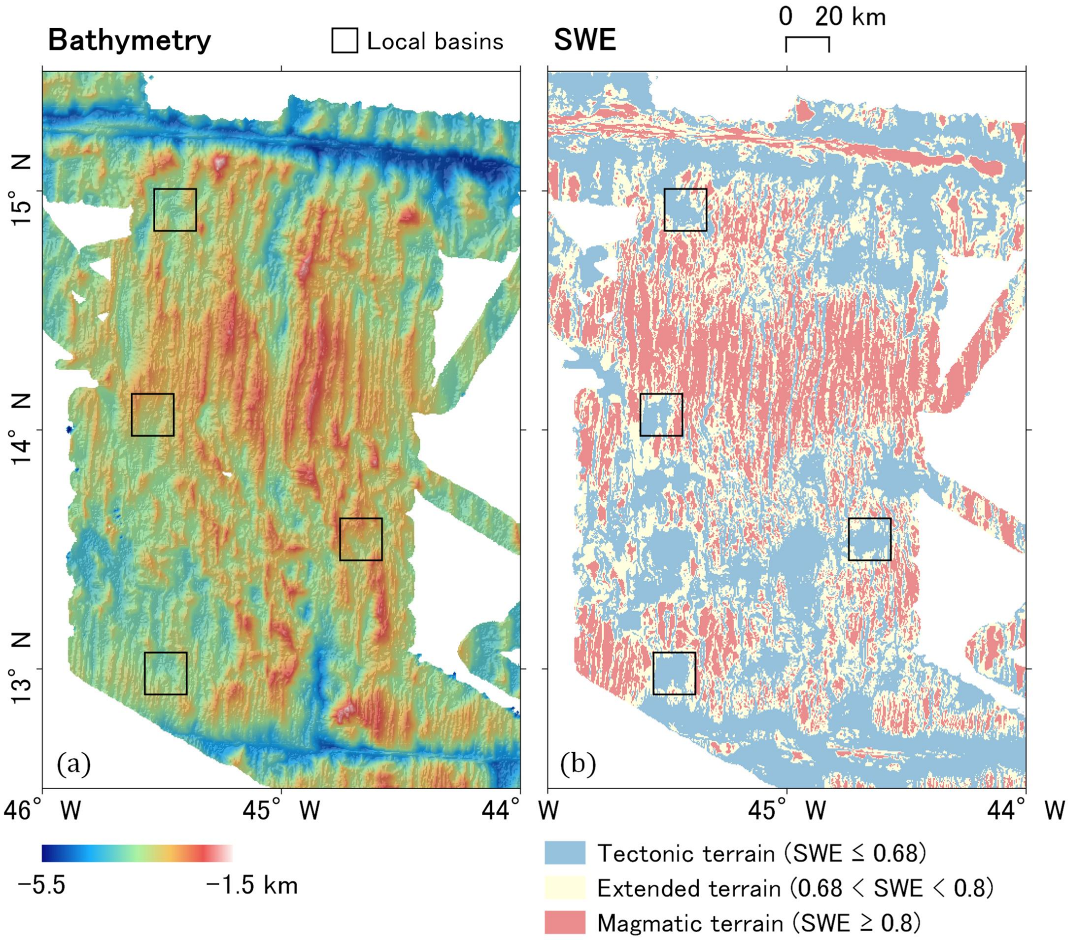

Figure 2.22: Local basins indicated in tectonic terrain (black squares). (a) Bathymetric grid. (b) SWE grid. The SWE values of the local basins is similar to those computed over the OCCs, as the two distinct features are governed by a similar trend of directionality and the curvatures of the seafloor has not been taken into account. To identify individual OCCs within the tectonic terrain, we need to mask out these concave-upward features from the SWE grid.

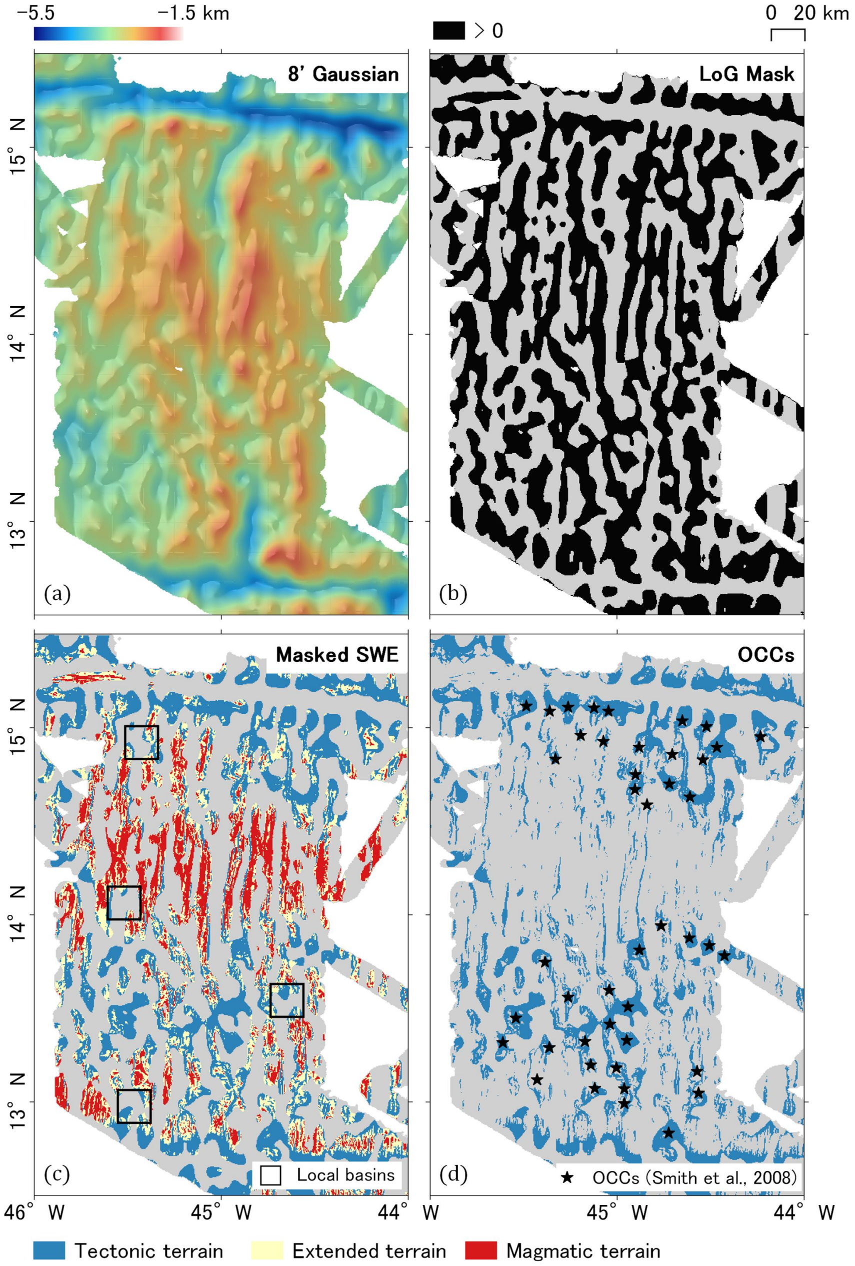

Figure 2.23: Identifying individual OCCs. (a) Gaussian-filtered bathymetry with 8' (∼14.8 km) window size, following the window size utilised in the SWE computation, which also mimics the general size of OCCs in the study area. (b) Laplacian-of-Gaussian (LoG) mask after the Gaussian-filtered bathymetry in (a). Areas with negative (< 0) LoG values are removed from the grid. The grid is used as a mask to remove SWE values over areas with concave-upward morphology. (c) Masked SWE grid. The local basins indicated in Figure 2.22 have been removed. (d) Individual OCCs highlighted by removing areas indicated as extended and magmatic terrain. The results corelate quite well with the OCCs inferred by Smith *et al.* (2008) and potentially indicate other OCCs that have not been previously defined.

2.7 Conclusions

I have developed a novel geomorphometric tool to automate terrain classification in slow-spreading ridges based on the shape, directionality, and curvature of a shipboard multibeam bathymetry data. The algorithm exploits the azimuth and plunge of the seafloor to compute the dimensionless SWE values which can be used to classify the crust dominated by either tectonic or magmatic regimes based on its governing morphology. The oceanic crust in the study is hereafter classified into:

1. Tectonic terrain, with SWE $\leq 0.68 \pm 0.09$,
2. Extended terrain, with $0.68 \pm 0.09 <$ SWE $< 0.80 \pm 0.07$, and
3. Magmatic terrain, with SWE $\geq 0.80 \pm 0.07$

These values are always fixed within the range of eccentricity values ($0 < e < 1$), implying the re-applicability of the algorithm into different grid sets. In general, the tectonic terrain hosts features governed by omnidirectional dipping slopes such as OCCs and local basins, while the magmatic terrain hosts features governed by bi-directional dipping faults. Between these two types, the extended terrain represents a buffer zone where both omnidirectional and bidirectional dipping slopes/faults exist, showing the transition from tectonic to magmatic spreading or vice versa. This buffer zone lies approximately within the standard deviations of the uppermost limit of the tectonic terrain and the lowermost limit of the magmatic terrain. The classification correlates well with published qualitative interpretation as well as the general distribution of seismicity observed from the peaks of the T-waves, where areas classified as tectonic terrain hosts most of the seismicity occuring within the region. Furthermore, when the SWE algorithm is coupled with the utilisation of LoG filter, it can potentially be used to aid the identification of individual OCCs within the study area, in addition to classifying the area into the different types of terrain. The results correlate well with the OCCs inferred by previous studies and potentially indicate other OCCs that have not been previously defined.

I suggest that the automated classification through SWE with an additional application of LoG filter can act as a novel and efficient means to provide insights on the magmatic and tectonic processes that occur in a slow-spreading ridge, at least where shipboard multibeam bathymetry exists. This technique also widens the use of geomorphometric techniques to automate terrain classification by deriving the statistical characteristics of available multibeam bathymetry data sets. The resulting classification will serve as a substantial first step to reveal the evolution of a slow-spreading ridge through time, hand-in-hand with a more thorough geophysical and geochemical studies through various different types of surveys, rock sampling, and laboratory analyses.

References

Bergman, E. A., & Solomon, S. C. (1990). Earthquake swarms on the Mid-Atlantic Ridge: Products of magmatism or extensional tectonics? *Journal of Geophysical Research: Solid Earth*, *95*(B4), 4943–4965. 37

Blackman, D. K., Canales, J. P., & Harding, A. (2009). Geophysical signatures of oceanic core complexes. *Geophysical Journal International*, *178*(2), 593–613. 34

Bonatti, E. (1996). Long-lived oceanic transform boundaries formed above mantle thermal minima. *Geology*, *24*(9), 803–806. 36

Buck, W. R. (1988). Flexural rotation of normal faults. *Tectonics*, *7*(5), 959–973. 34

Buck, W. R., Lavier, L. L., & Poliakov, A. N. (2005). Modes of faulting at mid-ocean ridges. *Nature*, *434*(7034), 719–723. 37

Cann, J., Blackman, D., Smith, D., McAllister, E., Janssen, B., Mello, S., Avgerinos, E., Pascoe, A., & Escartin, J. (1997). Corrugated slip surfaces formed at ridge–transform intersections on the Mid-Atlantic Ridge. *Nature*, *385*(6614), 329–332. 34, 48

Cann, J. R., Smith, D. K., Escartin, J., & Schouten, H. (2015). Tectonic evolution of 200 km of Mid-Atlantic Ridge over 10 million years: Interplay of volcanism and faulting. *Geochemistry, Geophysics, Geosystems*, *16*(7), 2303–2321. 34, 36, 48

Cannat, M., Bideau, D., & Bougault, H. (1992). Serpentinized peridotites and gabbros in the Mid-Atlantic Ridge axial valley at 15 37' N and 16 52' N. *Earth and Planetary Science Letters*, *109*(1-2), 87–106. 34

Cannat, M., Lagabrielle, Y., Bougault, H., Casey, J., de Coutures, N., Dmitriev, L., & Fouquet, Y. (1997). Ultramafic and gabbroic exposures at the Mid-Atlantic Ridge: Geological mapping in the 15 N region. *Tectonophysics*, *279*(1-4), 193–213. 37

Chakraborty, B., Schenke, H., Kodagali, V., & Hagen, R. (2001). Analysis of multibeam-Hydrosweep echo peaks for seabed characterisation. *Geo-Marine Letters*, *20*(3), 174–181. 35

Dannowski, A., Grevemeyer, I., Ranero, C. R., Ceuleneer, G., Maia, M., Morgan, J. P., & Gente, P. (2010). Seismic structure of an oceanic core complex at the Mid-Atlantic Ridge, 22 19' N. *Journal of Geophysical Research: Solid Earth*, *115*(B7). 34, 35

Davis, J. C. (1986). *Statistics and data analysis in geology*, vol. 646. Wiley New York et al. 42

Deng, G., & Cahill, L. W. (1993). An adaptive Gaussian filter for noise reduction and edge detection. In *1993 IEEE Conference Record Nuclear Science Symposium and Medical Imaging Conference*, (pp. 1615–1619 vol.3). 46

Escartín, J., & Cannat, M. (1999). Ultramafic exposures and the gravity signature of the lithosphere near the Fifteen-Twenty Fracture Zone (Mid-Atlantic Ridge, 14–16.5 N). *Earth and Planetary Science Letters*, *171*(3), 411–424. 34, 36, 38

Escartin, J., Hirth, G., & Evans, B. (1997). Effects of serpentinization on the lithospheric strength and the style of normal faulting at slow-spreading ridges. *Earth and Planetary Science Letters*, *151*(3-4), 181–189. 34

Escartin, J., Hirth, G., & Evans, B. (2001). Strength of slightly serpentinized peridotites: Implications for the tectonics of oceanic lithosphere. *Geology*, *29*(11), 1023–1026. 34

Escartín, J., Smith, D. K., & Cannat, M. (2003). Parallel bands of seismicity at the Mid-Atlantic Ridge, 12–14° N. *Geophysical Research Letters*, *30*(12). 36, 37

Fox, C. G., Matsumoto, H., & Lau, T.-K. A. (2001). Monitoring Pacific Ocean seismicity from an autonomous hydrophone array. *Journal of Geophysical Research: Solid Earth*, *106*(B3), 4183–4206. 37

Fujiwara, T., Lin, J., Matsumoto, T., Kelemen, P. B., Tucholke, B. E., & Casey, J. F. (2003). Crustal evolution of the Mid-Atlantic Ridge near the Fifteen-Twenty fracture zone in the last 5 Ma. *Geochemistry, Geophysics, Geosystems*, *4*(3). 36, 38

Gafeira, J., Long, D., & Diaz-Doce, D. (2012). Semi-automated characterisation of seabed pockmarks in the central North Sea. *Near Surface Geophysics*, *10*(4), 301–312. 35

Goff, J. A., & Jordan, T. H. (1988). Stochastic modeling of seafloor morphology: Inversion of sea beam data for second-order statistics. *Journal of Geophysical Research: Solid Earth*, *93*(B11), 13589–13608. 35

Goff, J. A., Tucholke, B. E., Lin, J., Jaroslow, G. E., & Kleinrock, M. C. (1995). Quantitative analysis of abyssal hills in the Atlantic Ocean: A correlation between inferred crustal thickness and extensional faulting. *Journal of Geophysical Research: Solid Earth*, *100*(B11), 22509–22522. 35

Green, A., & Uken, R. (2008). Submarine landsliding and canyon evolution on the northern KwaZulu-Natal continental shelf, South Africa, SW Indian Ocean. *Marine Geology*, *254*(3-4), 152–170. 35

Harrison, R., Bellec, V., Mann, D., & Wang, W. (2011). A new approach to the automated mapping of pockmarks in multi-beam bathymetry. In *2011 18th IEEE International Conference on Image Processing*, (pp. 2777–2780). IEEE. 35

Howell, S. M., Olive, J.-A., Ito, G., Behn, M. D., Escartin, J., & Kaus, B. (2019). Seafloor expression of oceanic detachment faulting reflects gradients in mid-ocean ridge magma supply. *Earth and Planetary Science Letters*, *516*, 176–189. 37

Huertas, A., & Medioni, G. (1986). Detection of intensity changes with subpixel accuracy using Laplacian-Gaussian masks. *IEEE Transactions on Pattern Analysis and Machine Intelligence*, (5), 651–664. 46

Ismail, K., Huvenne, V. A., & Masson, D. G. (2015). Objective automated classification technique for marine landscape mapping in submarine canyons. *Marine Geology*, *362*, 17–32. 35

Kong, L. S., Solomon, S. C., & Purdy, G. (1992). Microearthquake characteristics of a mid-ocean ridge along-axis high. *Journal of Geophysical Research: Solid Earth*, *97*(B2), 1659–1685. 37

Lagabrielle, Y., Bideau, D., Cannat, M., Karson, J. A., & MéVel, C. (1998). Ultramafic-Mafic Plutonic Rock Suites Exposed Along the Mid-Atlantic Ridge (10 N - 30 N) Symmetrical-Asymmetrical Distribution and Implications for Seafloor Spreading Processes. *GEOPHYSICAL MONOGRAPH-AMERICAN GEOPHYSICAL UNION*, *106*, 153–176. 34

Lavier, L. L., Roger Buck, W., & Poliakov, A. N. (1999). Self-consistent rolling-hinge model for the evolution of large-offset low-angle normal faults. *Geology*, *27*(12), 1127–1130. 34

Lecours, V., Dolan, M. F., Micallef, A., & Lucieer, V. L. (2016). A review of marine geomorphometry, the quantitative study of the seafloor. *Hydrology and Earth System Sciences*, *20*(8), 3207–3244. 35

Macdonald, K. C. (1982). Mid-ocean ridges: Fine scale tectonic, volcanic and hydrothermal processes within the plate boundary zone. *Annual Review of Earth and Planetary Sciences*, *10*(1), 155–190. 34

MacLeod, C. J., Escartin, J., Banerji, D., Banks, G., Gleeson, M., Irving, D. H. B., Lilly, R., McCaig, A., Niu, Y., Allerton, S., *et al.* (2002). Direct geological evidence for oceanic detachment faulting: The Mid-Atlantic Ridge, 15 45' N. *Geology*, *30*(10), 879–882. 34

MacLeod, C. J., Searle, R., Murton, B., Casey, J., Mallows, C., Unsworth, S., Achenbach, K., & Harris, M. (2009). Life cycle of oceanic core complexes. *Earth and Planetary Science Letters*, *287*(3-4), 333–344. 34, 37

Marr, D., & Hildreth, E. (1980). Theory of edge detection. *Proceedings of the Royal Society of London. Series B. Biological Sciences*, *207*(1167), 187–217. 46, 47

Micallef, A., Le Bas, T. P., Huvenne, V. A., Blondel, P., Hühnerbach, V., & Deidun, A. (2012). A multi-method approach for benthic habitat mapping of shallow coastal areas with high-resolution multibeam data. *Continental Shelf Research*, *39*, 14–26. 35

Müller, R. D., & Smith, W. H. (1993). Deformation of the oceanic crust between the North American and South American plates. *Journal of Geophysical Research: Solid Earth*, *98*(B5), 8275–8291. 36

Mutter, J. C., & Karson, J. A. (1992). Structural processes at slow-spreading ridges. *Science*, *257*(5070), 627–634. 34

Parnell-Turner, R., Sohn, R., Peirce, C., Reston, T., MacLeod, C., Searle, R., & Simão, N. (2017). Oceanic detachment faults generate compression in extension. *Geology*, *45*(10), 923–926. 37

Passaro, S., Ferranti, L., & de Alteriis, G. (2011). The use of high-resolution elevation histograms for mapping submerged terraces: Tests from the Eastern Tyrrhenian Sea and the Eastern Atlantic Ocean. *Quaternary International*, *232*(1-2), 238–249. 35

Pockalny, R., Smith, A., & Gente, P. (1995). Spatial and temporal variability of crustal magnetization of a slowly spreading ridge: Mid-Atlantic Ridge (20–24 N). *Marine Geophysical Researches*, *17*(3), 301–320. 35

Reston, T., & Ranero, C. R. (2011). The 3-D geometry of detachment faulting at mid-ocean ridges. *Geochemistry, Geophysics, Geosystems*, *12*(7). 34

Rona, P., Widenfalk, L., & Boström, K. (1987). Serpentinized ultramafics and hydrothermal activity at the Mid-Atlantic Ridge crest near 15° N. *Journal of Geophysical Research: Solid Earth*, *92*(B2), 1417–1427. 34, 37

Rosenfeld, A., & Kak, A. (1982). Edge detection. In *Digital picture processing*, vol. 2, (pp. 84–112). 46

Scheidegger, A. (1965). On the statistics of the orientation of bedding planes, grain axes, and similar sedimentological data. *United States Geological Survey Professional Paper*, *525*(C), 164–167. 40

Schroeder, T., Cheadle, M. J., Dick, H. J., Faul, U., Casey, J. F., & Kelemen, P. B. (2007). Nonvolcanic seafloor spreading and corner-flow rotation accommodated by extensional faulting at 15 N on the Mid-Atlantic Ridge: A structural synthesis of ODP Leg 209. *Geochemistry, Geophysics, Geosystems*, *8*(6). 34

Sinton, J. M., & Detrick, R. S. (1992). Mid-ocean ridge magma chambers. *Journal of Geophysical Research: Solid Earth*, *97*(B1), 197–216. 34

Smith, D. (2013). Mantle spread across the sea floor. *Nature Geoscience*, *6*(4), 247–248. 34

Smith, D. K., Cann, J. R., & Escartín, J. (2006). Widespread active detachment faulting and core complex formation near 13 N on the Mid-Atlantic Ridge. *Nature*, *442*(7101), 440–443. 34, 36, 38

Smith, D. K., Escartin, J., Cannat, M., Tolstoy, M., Fox, C. G., Bohnenstiehl, D. R., & Bazin, S. (2003). Spatial and temporal distribution of seismicity along the northern Mid-Atlantic Ridge (15°–35° N). *Journal of Geophysical Research: Solid Earth*, *108*(B3). 36, 38, 67, 71

Smith, D. K., Escartìn, J., Schouten, H., & Cann, J. R. (2008). Fault rotation and core complex formation: Significant processes in seafloor formation at slow-spreading mid-ocean ridges (Mid-Atlantic Ridge, 13-15 N). *Geochemistry, Geophysics, Geosystems*, *9*(3). 34, 36, 37, 38, 48, 50, 54, 67, 71, 72, 74

Smith, D. K., & Shaw, P. R. (1989). Using topographic slope distributions to infer seafloor patterns. *IEEE journal of Oceanic Engineering*, *14*(4), 338–347. 35

Smith, D. K., Tolstoy, M., Fox, C. G., Bohnenstiehl, D. R., Matsumoto, H., & J. Fowler, M. (2002). Hydroacoustic monitoring of seismicity at the slow-spreading Mid-Atlantic Ridge. *Geophysical Research Letters*, *29*(11), 13–1. 36

Tivey, M. A., & Dyment, J. (2010). The magnetic signature of hydrothermal systems in slow spreading environments. *Diversity of Hydrothermal Systems on Slow Spreading Ocean Ridges, Geophys. Monogr. Ser*, *188*, 43–65. 35

Trauth, M. H. (2007). *MATLAB Recipes for Earth Sciences – with text contributions by Gebbers, R. & Marwan, N.*, vol. 34. Springer. 39

Tucholke, B. E., Behn, M. D., Buck, W. R., & Lin, J. (2008). Role of melt supply in oceanic detachment faulting and formation of megamullions. *Geology*, *36*(6), 455–458. 34, 37

Tucholke, B. E., Lin, J., & Kleinrock, M. C. (1998). Megamullions and mullion structure defining oceanic metamorphic core complexes on the Mid-Atlantic Ridge. *Journal of Geophysical Research: Solid Earth*, *103*(B5), 9857–9866. 37

Watson, G. S. (1965). Equatorial distributions on a sphere. *Biometrika*, *52*(1/2), 193–201. 35, 40

Wilson, M. F., O'Connell, B., Brown, C., Guinan, J. C., & Grehan, A. J. (2007). Multiscale terrain analysis of multibeam bathymetry data for habitat mapping on the continental slope. *Marine Geodesy*, *30*(1-2), 3–35. 35

Wolfe, C. J., Purdy, G., Toomey, D. R., & Solomon, S. C. (1995). Microearthquake characteristics and crustal velocity structure at 29° N on the Mid-Atlantic Ridge:

The architecture of a slow spreading segment. *Journal of Geophysical Research: Solid Earth*, *100*(B12), 24449–24472. 37

Woodcock, N. (1977). Specification of fabric shapes using an eigenvalue method. *Geological Society of America Bulletin*, *88*(9), 1231–1236. 35, 40, 41, 43

Chapter 3

Asymmetric spreading at MARK 21-24° N Atlantic: a gravity and magnetic data investigation

Abstract

Asymmetric spreading has been characterised as the typical spreading mode over slow-spreading ridges and has been a subject of interest as it illustrates the underlying interplay between magmatic accretion and tectonic extension over time. In this study, I aim to investigate the evolution of the spreading asymmetry at the Mid-Atlantic Ridge at Kane (MARK) area, 21° -24° N Atlantic, by observing the evolution of spreading rate, crustal thickness, and the geometry of the tectonic fabric over 10 Ma. A regional view of the magmatic and tectonic setting of this study area found that at thinner crust, the resulting topography is a lot lineated compared to the ridge parallel topography found at thicker crust. The regional observation is followed by a more thorough analyses in the four spreading segments bounded by the Kane and southern fracture zones. Asymmetric spreading is mostly observed at the northernmost and southernmost segments, as the western flank of both these segments are formed as inside corners. The middle part of the study area experienced a lot more symmetrical spreading, with tectonic type of spreading occurred at the non-transform discontinuity resulting from the non-transform offsets between the ridge segments. Two volcanic locus are observed within the study area, one interpreted as a now depleted neovolcanic zone and one interpreted as an active neovolcanic zone propagating to the south. OCCs are emplaced in the inside corners of the non-transform offsets within the depleted neovolcanic zone, while the active neovolcanic zone seem to be cutting the now inactive southern fracture zone. From the study, I also found that thin crust seem to be formed at faster spreading rate. This early finding might enhance our understanding of the forming of the crust at slow-spreading ridge, in which faster spreading might not always result in thicker magmatic crust.

3.1 Introduction

Asymmetric spreading at slow-spreading ridges has been observed in the central Atlantic and has led to understanding of the interplay between the magmatic accretion and tectonic extension over the area (e.g., MacDonald, 1977). Studies have shown that this highly asymmetric spreading might relate to the segmentation of the magmatism at slow-spreading ridges. For instance, the magmatic segments are separated by transform faults and non-transform discontinuities or NTDs (Schouten *et al.*, 1985; Whitehead *et al.*, 1984). Migration of the ridge axis (Allerton *et al.*, 2000; Cormier & Sloan, 2019) and the accumulation of short-term asymmetries by detachment faulting (Okino *et al.*, 2004) are observed as key features characterising the asymmetric spreading ridges. This typical crustal accretion has been characterised at ridges with rates less than 40 mm/year (Smith, 2013), where volcanic flows are observed at one flank and detachment fault at the opposing flank. The asymmetry is even observed at the adjacent Canadian-Moroccan margin where faulting of oceanic lithosphere exists on the Canadian margin while magmatic emplacement is more common at the adjacent Moroccan margin (Biari *et al.*, 2017).

A comprehensive geophysical survey has been carried out at Mid-Atlantic Ridge at Kane (MARK) 21° -24° N Atlantic by Gente *et al.* (1995) exposing the geometry of the area as well as its crustal properties. The survey includes shipboard multibeam bathymetry, magnetic, and gravity surveys. This area is characterised by a rhomb-shaped magmatic area at the mid segment, marked by oblique non-transform discontinuities at both ridge flanks. The thermal evolution of this area has been studied by Gac *et al.* (2006) explaining the past evolution of the segmentation which directly control the resulting geometry of the seafloor.

The evolution of this area over 10 Ma has been studied by Cann *et al.* (2015) by observing the morphology of the seafloor depicted by the high-resolution bathymetry. As discussed in the previous chapter, they classified the area into three different types of crust: magmatic, extended terrain, and tectonic crusts. Areas classified as tectonic crust correspond well with outcrops of serpentinites sampled at places away from the axis (Cannat, 1993) and areas with thin crust computed from gravity anomaly studies (Cannat *et al.*, 1995; Maia & Gente, 1998). Mafic and ultramafic rocks at this area have been exposed through detachment faulting in thin crust, which was initiated by tectonic extension in an increasingly asymmetric ridge segment (Mutter & Karson, 1992). This morphology is in contrast to the abyssal hills of magmatic seafloors, bounded by steep normal faults facing towards the spreading axis (Kong *et al.*, 1988). The two different types of spreading alternate through time depending on the magmatic and tectonic state of the spreading axis through different periods. Therefore, this study intends to explore the periodicity of the spreading rate by observing the evolution of half-spreading rate at both flanks and how it relates to the mantle fertility.

The proximity to the centre of the magmatic segments leads to variation in crustal thickness, where thicker crust formed in areas closer to the centre of a magmatic segment. Therefore, it is important to calculate the regional crustal thickness over the area to delineate areas formed by one mode of spreading from another. Studies on the crustal thickness variation by means of gravity anomaly in this area are initated by Maia & Gente (1998). They compute the crustal thickness by converting the free-air anomaly (FAA) into Bouguer and mantle Bouguer anomaly (MBA), followed by removing the thermal effect from the lithospheric cooling. They decide to compute the thermal effect by filtering the long wavelengths of both the MBA and the bathymetry with a cutoff wavelength of 150 km, compared to generating a passive flow model (Morgan & Forsyth, 1988), commonly used in studies on determining crustal thickness variation in a mid-ocean ridge environment in more recent studies (e.g., Blackman *et al.*, 2008; Escartín & Cannat, 1999; Smith *et al.*, 2008). As a pioneering study in this area, the resulting crustal thickness have not been validated with any other types of data. Another method of thermal effect removal is employed by Kahle *et al.* (2016), focusing on the southernmost part of the same study area. The thermal effect approximation is divided into two steps. The first step is a 'thermal subsidence' removal from the bathymetry using a median filter with a window size of 100 km, followed by Bouguer anomaly calculation from the FAA using the median-filtered bathymetry. The resulting anomaly is termed the 'residual Bouguer gravity.' The second step is the removal of a 'very long-wavelength deep-seated gravity variations' using a high-pass filter with a cut-off wavelength of 750 km. The resulting crustal thickness is cross validated against Moho depth derived from an array of ocean bottom seismic (OBS) survey documented in the same study and yields a good fit within the location of the OBS array. Crustal thickness computation from OBS in this area have also been carried out by Dannowski *et al.* (2010), Dannowski *et al.* (2011), and Dannowski *et al.* (2018). However, these individual OBS studies have only been validated locally by forward modelling the Moho depth from the free-air gravity, and furthermore only by assigning parameters that could not depict the crustal thickness variation at a regional scale. Therefore, I introduce a development of the crustal thickness computation based on gravity anomalies and isostasy, results from which match well with existing seismic observations to date.

The alteration of the spreading mode through time by means of bathymetry, gravity, and magnetic observation will be presented as the final result of this study. What might cause these alterations? How was the rhomb-shaped magmatic area at the middle segment formed? Why did core complexes form in some parts but not others? To answer these questions, I divide the area into three segments: the northern, middle, and southern segments based on the rhomb-shape observed in the middle of the segment. By exploring the periodicity of the spreading in these segments, we will have a better understanding on the evolution of the asymmetric spreading at central Atlantic.

3.2 Fundamentals of geophysical data enhancements

In this study, various geophysical data enhancement methods are applied to the gridded bathymetry, gravity, and magnetic anomalies. To understand the nature of each method, the fundamental concepts and applications are explained in this section. The principles of gravity and magnetic data enhancements, denoted as transforms and geological filters, potential field derivatives, and semi-automated lineament tracking, are summarised from Fairhead (2015) and related articles. The potential field data enhancement operations are mostly conducted in `GETgrid` software v1.255 from `Getech, plc.` Afterwards, an automated crust classification developed in Chapter 2 termed slope-weighted eccentricity (SWE), will be summarised, and presented in the last sub-section.

3.2.1 Transforms and geological filters

Transforms can be defined as practices to change/modify the gridded data in specific ways, while geological filters usually separate the data to interpret features at different depths. The term 'geological filter' is used to imply that the filters is commonly used to aid the geological interpretation processes. In this chapter, I apply the reduction-to-pole (RTP) transform as well as the Gaussian and Laplacian filters. As the Gaussian and Laplacian filters have been explained in the previous chapter, specifically in 2.3.5, in this section I will only discuss the fundamental concepts of the RTP technique. While the Gaussian and Laplacian filters can be applied to either bathymetry, gravity, or magnetic dataset, the RTP operator is specifically used for magnetic data processing. Studies with other potential data enhancements such as upward/downward continuation and analytical signal have also been carried out. However, only those proven usedul for the case study is presented in this thesis.

Reduction-to-pole

RTP is an operator specifically used for magnetic data processing. The intention of using this operator is to remove the asymmetry of the observed magnetic anomaly caused by the inclination of the magnetic field in the corresponding magnetic latitude. The dipole nature of magnetic signatures causes progressive asymmetry the further it is from the magnetic poles, where the magnetic field is vertical (Figure 3.1). The RTP operator is built based on the Poisson's relation between magnetic and gravity anomalies (Baranov, 1957), illustrated in Figure 3.2. By applying the RTP operator, interpretation based on magnetic anomaly is made simpler as the ambient magnetisation has been shifted to the vertical of the anomalous magnetised bodies, as observed in the magnetic poles.

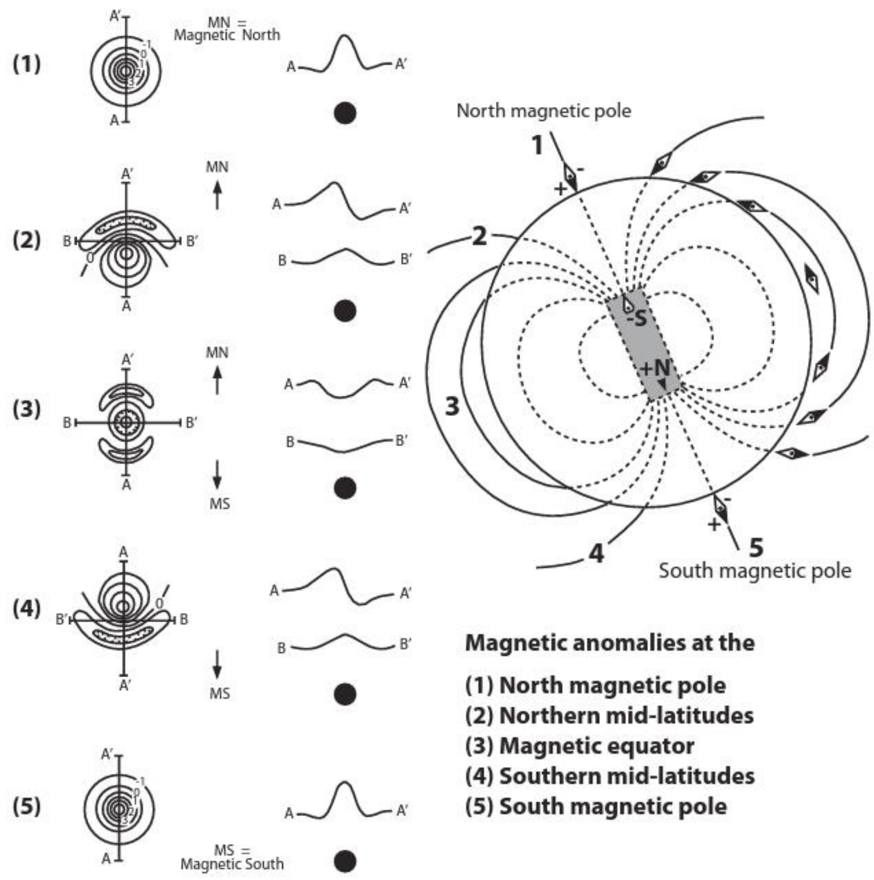

Figure 3.1: Magnetic anomaly maps and profiles for a dipole or equivalent spherical subsurface source (solid dot) with constant magnetisation intensity along zero declination and varying inclination between the magnetic north (MN) and south (MS) poles, and magnetic equator (ME), after Hinze *et al.* (2013), adapted from Breiner (1973).

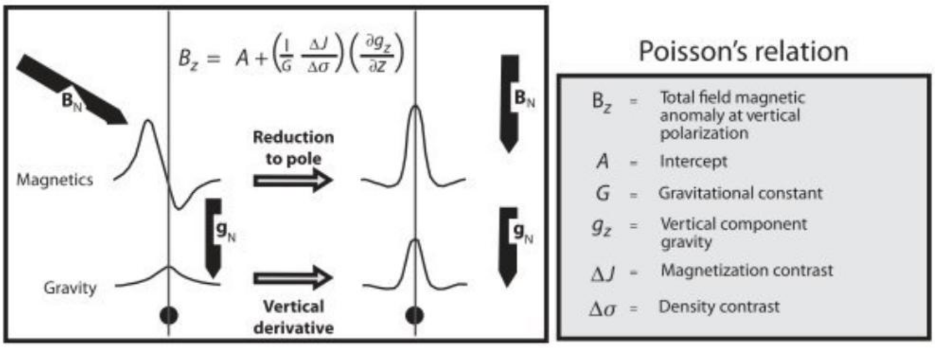

Figure 3.2: Poisson's relation between magnetic and gravity anomalies for a point source (dot) with positive density and magnetization contrast, after Hinze *et al.* (2013).

The RTP technique can be applied by transforming the observed anomaly data either in the wavenumber or space domain (e.g., Arkani-Hamed, 1988; Baranov, 1957; Gunn, 1995) using a constant geomagnetic field in the form of magnetic inclination and magnetic declination in a limited sized region, typically no more than a few hundred kilometres (Hinze *et al.*, 2013). One of the most common method is documented in Grant & Dodds (1972) and MacLeod *et al.* (1993), where the RTP operator $L(\theta)$ is expressed as:

$$L(\theta) = \frac{1}{[\sin(I) + i\cos(I)cos(D-\theta)]^2} \tag{3.1}$$

where θ is the wavenumber direction, I is the magnetic inclination, and D is the magnetic declination. The operator works best between 15° and 75° magnetic latitudes, as the operator is unstable below 15°, and the field is essentially RTP above 75° (Fairhead, 2015). Studies on stabilising the operator at low latitudes have been conducted, e.g., by Gunn (1995) and Swain (2000) using the Wiener design principle to minimise the mean square error between an actual and desired output or by introducing a pseudo-inclination into the denominator of the filter transfer function, which increased from the true inclination in order to reduce the amplification of north-south wavenumbers, respectively. An example of the application of this transform to a magnetic anomaly data set can be seen in Figure 3.3. Another alternative is to apply a reduced-to-equator or RTE operator at regions of low magnetic latitudes (e.g., Aina, 1986). However, this alternative is not thoroughly discussed in this chapter as the lowest latitude in the particular study area is 21.2° N, in which the RTP operator is still within the 'stable' range.

In any case, the RTP transformation is based on the assumption that the total magnetisation is all induced (e.g., Baranov, 1957), neglecting the remanent components. In the oceanic crust, the resulting magnetisation consists mostly of the thermoremanent magnetisation from the cooling of the newly formed crust below its Curie and blocking temperatures (Tauxe, 1998). Therefore, RTP application to the oceanic crust works by removing the asymmetry resulting from the different magnetic inclination, shifting the signature to vertically over to the anomalous bodies, yet leaving its original dipole character. The alternating pattern of the normal and reversed polarity of the oceanic floor magnetisation (Vine & Matthews, 1963) will remain without directly inferring information about the strength of the magnetisation. For instance, the magnetic signature of 200 nT might be comparable to those observed as -200 nT in the oceanic crust if each of them are observed during a normal and reversed polarity period, respectively (c.f. Figure 3.4). Hence, the application of RTP over oceanic crust is sometimes termed 'half RTP' but to simplify the nomenclature, it is termed RTP throughout this study.

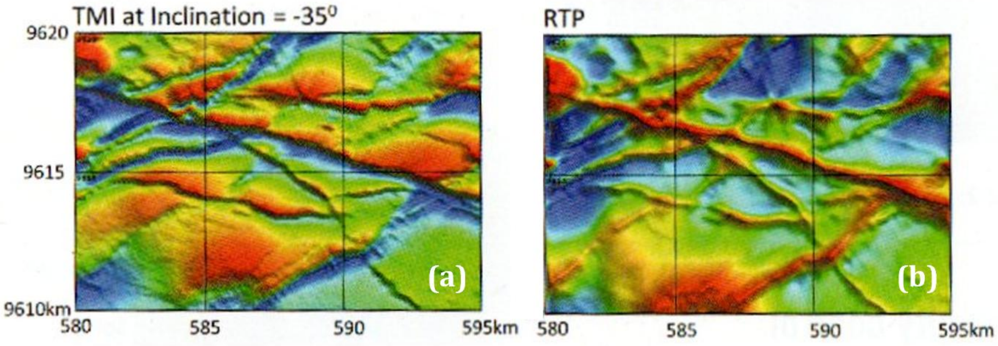

Figure 3.3: Total magnetic intensity (TMI) at −35° inclination before (a) and after RTP (b). Image is after Fairhead (2015). The asymmetric nature of a geomagnetic dipole complicates interpretation in (a), as the observed magnetisation is not centred directly vertically over the anomalous magnetic bodies. The RTP-transformed grid (b) simplifies interpretation as the magnetic signatures are shifted to be vertically over the anomalous magnetic bodies.

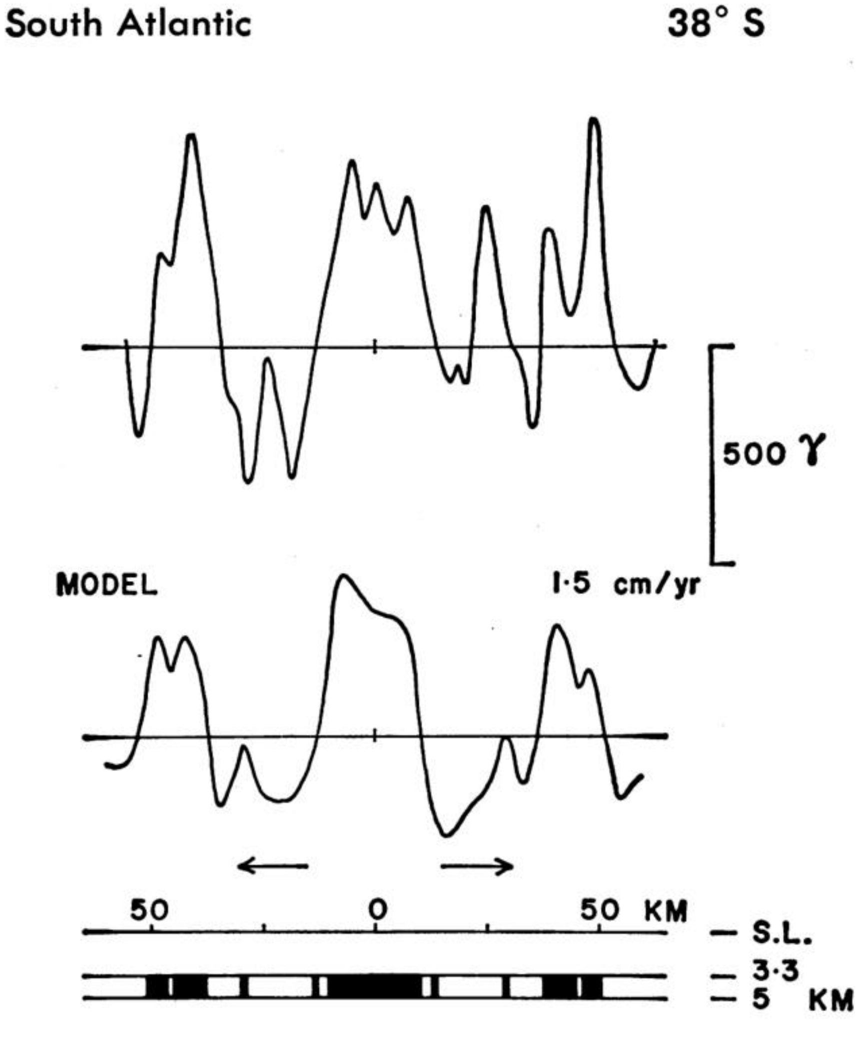

Figure 3.4: Observed and modelled magnetic profile at -38° South Atlantic taken from the Zapiola-2 profile of Heirtzler & Le Pichon (1965), after Vine (1966). The figure illustrates the alternating magnetic polarity through time in which positive values depict 'normal' magnetic polarity while negative values depict 'reversed' magnetic polarity.

3.2.2 Potential field derivatives

After the gridded data are conditioned through transforms and geological filtering, potential field derivatives can be can be applied as an attempt to delineate individual sources from potential field data as the observed signals tend to interfere with each other, masking bodies with smaller amplitudes, narrower shapes, and/or shallower depths. In this sub-section, the fundamental principle of the amplitude derivatives of total horizontal derivative (THDR) and vertical derivative (VDR) will be explained, followed by the tilt derivative (TDR) that is a phase derivative.

Total horizontal derivative (THDR)

THDR is useful for both gravity and magnetic data processing. It is a first order amplitude derivative of the full horizontal gradient, which delineates structural edges or contacts, described as:

$$THDR = \frac{\partial T}{\partial h} = \sqrt{\left(\frac{\partial T}{\partial x}\right)^2 + \left(\frac{\partial T}{\partial y}\right)^2} \tag{3.2}$$

where T is the potential field data, while x and y are the Cartesian coordinates of the corresponding field. The maxima of the THDR are normally close to the upper boundary of the structure causing the anomaly. Applying THDR to pseudo-gravity anomalies is also useful to remove edge multiples that might be generated from RTP transform of magnetic anomalies.

First vertical derivative (VDR)

VDR is useful for both gravity and magnetic data processing. It is a first order amplitude derivative of the vertical component, which is useful for resolving the location and edges of individual shallow structures, described as:

$$VDR = -\frac{\partial T}{\partial z} \tag{3.3}$$

where T is the magnetic anomaly field, and z is vertical Cartesian coordinate of the corresponding field. Due to its small gradient, VDR is least sensitive to regional and deep structures. The zero-crossing point of VDR closely coincides with the location of the structural edges (equivalent to the maxima of the THDR), and its positive anomalies are centred over the corresponding structure.

Tilt derivative (TDR)

TDR is useful for both gravity and magnetic data processing. First reported by Miller & Singh (1994), the TDR is a first order phase angle derivative, described as:

$$TDR = \theta = \tan^{-1}\left(\frac{\frac{\partial T}{\partial z}}{\frac{\partial T}{\partial h}}\right) \tag{3.4}$$

where θ has the range of ±90° resulting from the tangent function, $\frac{\partial T}{\partial h}$ is the THDR and $\frac{\partial T}{\partial z}$ is the VDR. The zero contours of the TDR coincide with the zero-crossing of the VDR, marking potential structural edges. To simplify interpretation processes, it is useful to remove all the negative TDR values to highlight the primary structures of the grid. Combined with THDR, TDR is potentially useful for mapping shallow basement structure Verduzco *et al.* (2004), as both operators exploit different parameters of potential field signals (TDR is independent of amplitude of magnetisation). The combined operation will be explained more thoroughly in the next sub-section.

3.2.3 Semi-automated lineated tracking

Recognizing the advantages of each grid enhancement operation, a combination of specific methods will result in a more robust interpretation. As discussed in 3.2.2, the maxima of the THDR generally coincide with the zero contour of the TDR, indicating contact edges. However, the zero TDR contours are generally formed in a continuous loop and the maxima of THDR can be multiply branched, causing complexity in interpreting the highlighted structures. Therefore, Cascone *et al.* (2017) introduced an automated coherency lineament analysis and selection (ACLAS) based on the coherency of the lineaments computed from the THDR and TDR of potential field anomaly data. In short, the method shows that only when the zero TDR contour overlies the significant maxima of the THDR can a fault or edge be confidently inferred. By detecting the places in which these two lineaments are close, the resulting lineament map will give a better approximation not only to the location of the contacts, but also their direction of strike. The ACLAS method is useful in both gravity and magnetic processes. However, it is important to note that the gravity field of a point source responds as $1/r^2$ while the magnetic field responds as $1/r^3$.

In order to obtain similar response from both types of data, we need to apply VDR to a set of gravity anomaly data before aplying ACLAS in order to have a point source respond as $1/r^3$ instead of $1/r^2$. Meanwhile, we can directly apply ACLAS to a set of magnetic anomaly data as the field already responds as $1/r^3$.

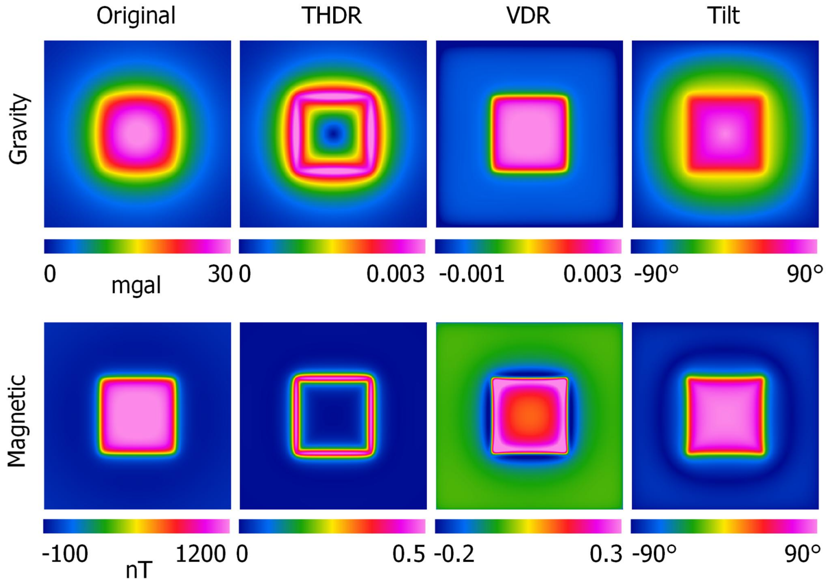

Figure 3.5: Gravity and magnetic signature of a squared synthetic source and its derivatives: Original, total horizontal derivative (THDR), first vertical derivative (VDR), and tilt derivative (TDR).

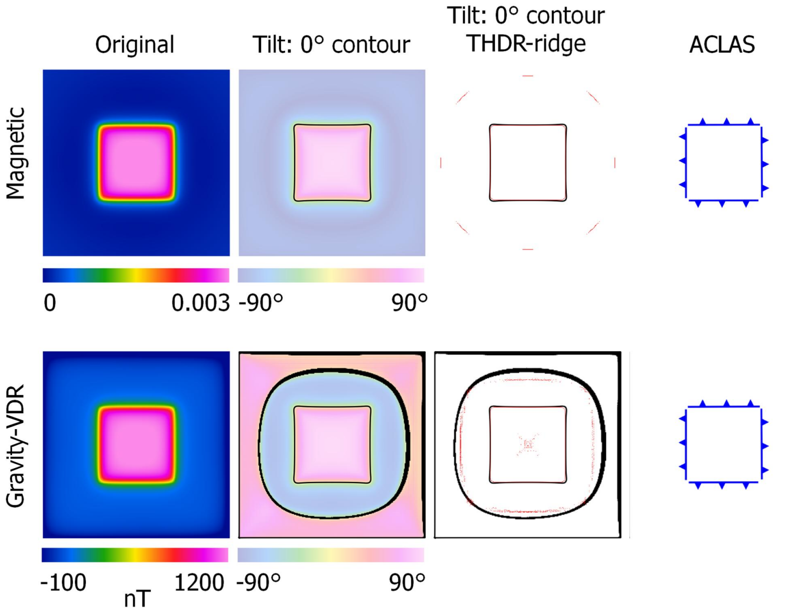

Figure 3.6: Illustration of the employment of the ACLAS technique to a squared synthetic source in its gravity and magnetic signatures: Original, total horizontal derivative (THDR), first vertical derivative (VDR), and tilt derivative (TDR).

3.2.4 Slope-weighted eccentricity (SWE) of directional data

In addition to applying the more well-known geophysical data enhancements, the newly-developed SWE operation (Chapter 2) is applied to the high-resolution bathymetry to reveal crustal types based on its shape, size, and directionality. Distinguishing the fault-bounded magmatic terrain from the long-lived detachment faults is key to understanding the pattern of mantle upwelling, ridge segmentation, and offsets (Shaw & Lin, 1993). The algorithm quantifies the characteristics of magmatic and detachment spreading a using an operator window which moves over the gridded data with a move along rate of one grid cell, explained thoroughly in Chapter 2.

SWE is based on the spherical distribution of the bathymetric terrain patch covered by each operator window, followed by computing the two most dominant eigenvalues (λ_2 and λ_3), describing the governing pattern in the horizontal plane. The governing pattern is simplified in term of its eccentricity, where the bi-directional pattern of magmatic crust will result in higher eccentricity than the detachment/tectonic crust. Another key parameter to the automated crust classification is the slope distribution, in which we can easily trace steep-dipping long-lived faults of detachment terrain, while the narrow faults of magmatic terrain are depicted by more gentle slopes following the number of imaged cells over the data grid. The key equation of SWE is described as:

$$SWE = e \times W = \sqrt{1 - \frac{(\lambda_2/2)^2}{(\lambda_3/2)^2}} \times (1 - \sin\theta) \tag{3.5}$$

where W is the weight matrix computed from the negative sine of the bathymetric slope $(1 - \sin\theta)$. The sine computation fixes the range of the weight into values between 0 and 1, identical with the range of eccentricity $(0 < e < 1)$, in which the magmatic crust will have higher values than the detachment crust. The crusts are finally distinguished using limiting values, where tectonic terrain is defined where SWE $\leq 0.68 \pm 0.09$, extended terrain defined where $0.68\ (\pm\ 0.09) <$ SWE $< 0.80\ (\pm\ 0.07)$, and magmatic terrain defined where SWE $\geq 0.80 \pm 0.07$.

3.3 Study Area

The Mid-Atlantic Ridge at Kane (MARK) area at 21-24° N Atlantic is selected as the study site based on its good coverage of ship-borne high-resolution bathymetry, gravity, and magnetic surveys. In addition, records of hydrophone seismicity are also available in this area to aid further interpretation (Smith *et al.*, 2003, 2002). The segment is bounded by the Kane Fracture Zone (KFZ) and an unnamed fracture zone to the south, which in this study is denoted as Southern Fracture Zone (SFZ). Several identified Oceanic Core Complexes (OCCs) are in place within the segment, e.g., the corrugated Kane Megamullion (Dick *et al.*, 2008), the OCCs described by Dannowski *et al.* (2010), several non-corrugated OCCs described by Cann *et al.* (2015), and several extinct OCCs described by Dannowski *et al.* (2018).

T-wave seismicity at the spreading axis (Smith *et al.*, 2003) indicates areas with high seismicity, where long-lived detachment faults and OCCs are expected. In general, higher seismicity is observed west of the ridge in the northern part of the segment, specifically at the inside corner of the KFZ. In the south, lower seismicity is observed, indicating a more magmatic regime which is also marked by symmetric elevated bathymetry. The seismicity is more pronounced again between 22° 15' N and 22° 45' N, marked by a more chaotic oceanic crust texture and dip distribution, then less seismicity is found down to the V-shaped abyssal hills that seem to propagate and cut the SFZ (Dannowski *et al.*, 2018). Otherwise, seismicity not captured by these studies could still be present within the study area.

Shipboard multibeam bathymetry, gravity, and magnetic anomalies from various survey periods are collected from the GMRT MapTool (www.gmrt.org/GMRTMapTool), LDEO's IEDA database (app.iedadata.org/databrowser), and NOAA's NCEI Trackline Geophysical data browsers (maps.ngdc.noaa.gov/viewers/geophysics).

3.3.1 Bathymetry and ship-borne survey coverage

A composite of high-resolution bathymetry over the MARK up to 10 Ma of age is obtained from the GMRT MapTool. The gravity and magnetic anomaly grids are created from the six available shipboard geophysical surveys conducted over the area. The list of the geophysical surveys is presented in Table 3.1 and the general ship-borne coverage including seismic lines is presented in Figure 3.7. In this study, the high-resolution bathymetry is resampled into 200-m and 30" ($\sim$1 km) resolution using the `grd2xyz` and `surface` functions in GMT. The higher resolution will be used for qualitative observation, while the latter will be used for geophysical processes to optimize computing time while maintaining quality.

A number of seismic surveys have also been carried out at the MARK area since the early studies of the KFZ (e.g., Cormier *et al.*, 1984; Detrick Jr & Purdy, 1980; Purdy & Detrick, 1986). However, in this study I only include the most recent Ocean Bottom Seismic (OBS) surveys that were carried out from the mid-segment of the area (∼23° N) to the south, also depicted in Figure 3.7. The list of the seismic lines is presented in Table 3.2.

Table 3.1: List of ship-borne geophysical surveys over MARK 21-24° N Atlantic

Code	**Year**	**Grav**	**Mag**	**Bat**	**Reference/lead**
74010907	1980	✓	✓	✗	Hussong, D. M. (HIG)
A2092L02	1982	✓	✓	✗	Purdy, G. (WHOI)
AKU20	1985	✓	✗	✗	Kogan, M. G. (IFZ AN SSSR)
RC2511	1984	✓	✓	✓	MGDS (1984)
RC3001	1989	✓	✗	✓	MGDS (1989)
SEADMA	1991	✓	✓	✓	Gente *et al.* (1995)

Table 3.2: List of seismic lines over MARK 21-24° N Atlantic

Code	**Reference**
K16	Kahle *et al.* (2016)
P02	Dannowski *et al.* (2011)
P04	Dannowski *et al.* (2018)
P05	Dannowski *et al.* (2018)
P08	Dannowski *et al.* (2010)

3.3.2 Gravity anomalies

A composite of gravity anomalies, in the form of Free-Air Anomaly (FAA), was created from the geophysical expeditions listed at Table 3.1. All the signals are levelled and interpolated in `QGIS 2.18.24` and `GMT 5.4.3` respectively. The interpolation is carried out using adjustable tension continuous curvature splines, or the `surface` function in GMT, with a resolution of 1' (∼1.85 km). To prevent extrapolation, a masking grid is created by interpolating the signals using `nearneighbor` function with a search radius of 10 km to cover the whole survey area. From the surface grid, data extrapolated outside the survey area are then masked out.

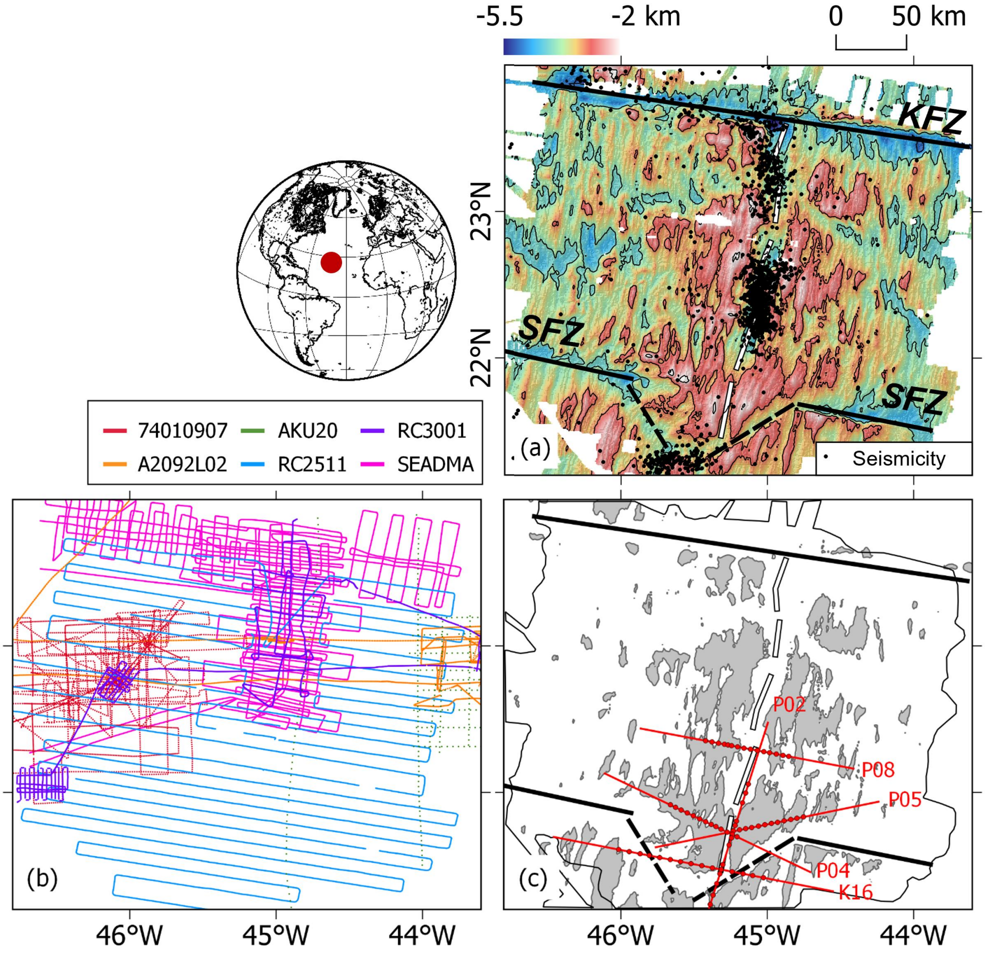

Figure 3.7: General coverage of geophysical survey at MARK 21-24° N Atlantic. (a) Shipboard multibeam bathymetry from the GMRT MapTool. KFZ: Kane Fracture Zone. SFZ: Southern Fracture Zone (inactive). Earthquakes are after Smith *et al.* (2003); (b) General coverage of geophysical survey of the MARK area, and; (c) Seismic lines from OBS surveys. Red dots: Shot points. Each data source is explained in Table 3.1 and 3.2.

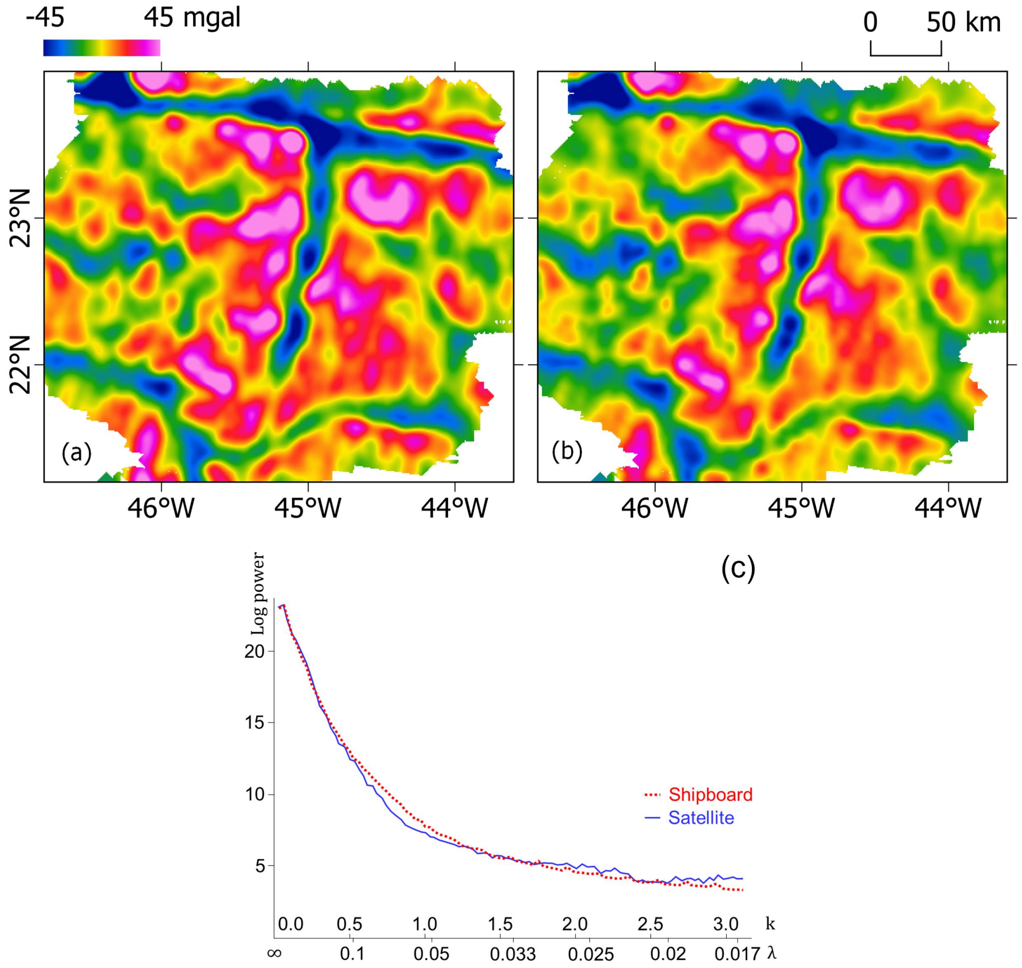

Figure 3.8: Free-air gravity at MARK. (a) Satellite-derived free-air gravity anomaly after Sandwell *et al.* (2014), masked by the extent of the available shipboard gravity data; (b) Composite grid of shipboard free-air gravity anomaly. The data is gridded into 30" × 30" cell size (∼1 × 1 km) using the `surface` function in GMT and masked by the extent created using the `nearneighbor` function in GMT with the same cell size and search radius of 10 km; (c) Spectral analysis of both grids (shipboard: dashed red line; satellite-derived: solid blue line). We can see how the power spectra are very similar in each of the wavenumber (k).

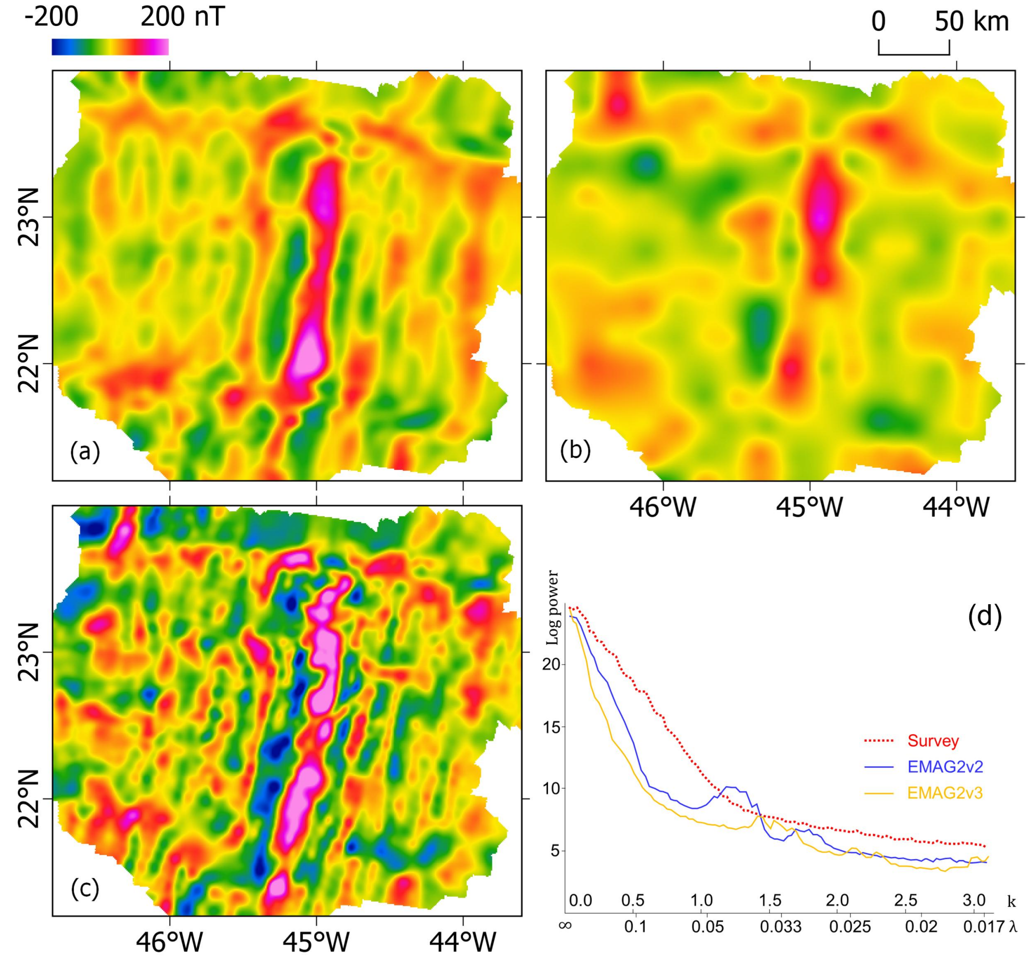

Figure 3.9: Magnetic anomaly at MARK. (a) Magnetic anomaly from EMAG2 v2, after (Maus *et al.*, 2009), masked by the extent of the available shipboard magnetic data; (b) Magnetic anomaly from EMAG2 v3, after (Meyer *et al.*, 2017), masked by the extent of the available shipboard magnetic data; (c) Composite grid of shipboard magnetic anomaly. The data is gridded into 30" × 30" cell size (~1 × 1 km) using the `surface` function in GMT and masked by the extent created using the `nearneighbor` function in GMT with the same cell size and search radius of 10 km; (d) Spectral analysis of the three grids (shipboard/survey: dashed red line; EMAG2 v2: solid blue line; EMAG2 v3: solid yellow line). We can see how the power spectrum of the surveyed data are a lot higher in smaller wavenumbers (k). The power spectra of EMAG2 v2 is relatively higher than the others specifically between $1.0 < k < 1.5$, and another peak followed in between $1.5 < k < 2.0$. This trend is also observed in EMAG2 v3, although with lower power spectrum. The peaks are found in between $1.25 < k < 1.75$ and $2.0 < k < 2.5$.

The resulting grid is used to assess the quality of the gravity signatures observed by the satellites, i.e. the satellite-derived gravity (Sandwell *et al.*, 2014) and the comparison can be seen in Figure 3.8. In the study area, we can see that both sets of data show similar anomalies and spatial trend, allowing satellite-derived data to be used at this scale and location. From the spectral analyses, we can also see how the power spectra from both shipboard and satellite data are comparable in each of the wavenumber (k). Considering the homogeneity of the gravity anomaly product compared to the shipboard in this area, as well as the comparability of the satellite-derived data compared to the shipboard data, I decided to use the satellite-derived free-air gravity for the following processes in this chapter.

3.3.3 Magnetic anomalies

A composite of magnetic anomalies (MA) was created using the same interpolation and masking method as used in 3.3.2. Afterwards, I assess the quality of the global magnetic signatures synthesized in EMAG2 v2 (Maus *et al.*, 2009) and EMAG2 v3 (Meyer *et al.*, 2017) by comparing it with the gridded shipboard magnetic anomaly data (Figure 3.9). According to the EMAG2 v3 release, EMAG2 v2 grid relied on known or idealized local geology to interpolate anomalies into non-existent data areas, while EMAG2 v3 relies solely on the available data. Nevertheless, it is evident that both EMAG2 v2 and v3 data do not show the same anomaly patterns nor spatial trend compared to the shipboard survey gridded data, making them unfit for further geophysical processes in this thesis. We can also see in the spectral analysis (Figure 3.9) that the power spectra of both EMAG2 v2 and EMAG2 v3 are not consistent with the shipboard magnetic anomaly data. In the shorter wavelengths ($0 < k < 1.0$) , we can observe a greater power spectra in the shipboard magnetic anomaly data compared to either of the EMAG2 data. In both EMAG2 data, we can observe two peaks of power spectrum, which are not observed in the shipboard magnetic anomaly data. In EMAG2 v2, the peaks are observed between $1.0 < k < 1.5$ and $1.5 < k < 2.0$, while in EMAG2 v3, the peaks are observed more subtlely between $1.25 < k < 1.75$ and $2.0 < k < 2.5$.

3.4 Bathymetry, magnetic, and gravity data processing

The spreading asymmetry over this study site will be observed based on its tectonic fabric and spreading mode classification, the distances of each geomagnetic polarity reversal to the current spreading axis, the evolution of crustal thickness, and testing the ACLAS method to interpret tectonic structures in an area with good high-resolution bathymetry coverage. The details of each method will be introduced in this section.

3.4.1 Tectonic fabric and spreading mode classification

The tectonic fabric of the seafloor is generally observed by qualitatively interpreting the high-resolution bathymetry grid (i.e. by eye). However, this mode of interpretation is limited to the experience and subjective perception of the interpreter. As in the previous chapter, I use the Laplacian-of-Gaussian filters to quantitatively analyse the available grid before tracing the tectonic fabric that is seen as object of interest. I choose to employ a 5-km low-pass Gaussian filter to the bathymetric grid as I would only like to see the fabric represented within this wavelength range, followed by applying the Laplacian filters to separate the convex upward and convex downward structures. From the interpretation, we can see the tectonic fabric, indicating the style of faulting at each segment (Figure 3.10).

Besides examining the tectonic fabric from the bathymetry, I employ the SWE algorithm to classify the modes of spreading that have been experienced by the terrain within the study area. According to the classification given in Chapter 2, the terrain can be classified into three types of terrain, which are:

1. Tectonic terrain, with $\mathrm{SWE} \leq 0.68 \pm 0.09$,
2. Extended terrain, with $0.68 \pm 0.09 < \mathrm{SWE} < 0.80 \pm 0.07$, and
3. Magmatic terrain, with $\mathrm{SWE} \geq 0.80 \pm 0.07$

The results can be seen in Figure 3.11. These results can be compared to other geophysical and geological surveys that have been carried out in the study area. For instace, comparing the classification results with the T-wave seismicity (Smith *et al.*, 2003), we can see that within the spreading axis, areas indicated as tectonic terrain are consistent with areas indicated with high seismicity. We can also observe an area of tectonic terrain forming a ‘triangle’ in northwestern flank. This ‘triangular’ area is consistent with an area of core complex terrain inferred by Cann *et al.* (2015), and this interpretation is strengthened by the various sampled gabbros and ultramafic rocks within that specific area. We can also see how in various places, the tectonic terrain classified by the SWE correlates well with sampled gabbros and ultramafic rocks. In addition, we can see how the fracture zones are accentuated at the north, as well as the inactive fracture zone at the south. A band of continuous tectonic terrain is also observed at the southwestern flank, marking a continuous tectonic stretching at the southwestern flank since the inactivity of the southern fracture zone. The youngest terrain at the south is shown as magmatic terrain, depicting a neo-volcanic zone migrating to the south.

Having the area classified as tectonic, extended, and magmatic terrain using the SWE algorithm, we can further indicate individual OCCs by applying LoG filters to the bathymetry and creating a mask out of it (SWE-LoG). As explained in Chapter 2, the idea of creating a bathymetry-based mask using the LoG filters is to eliminate concave upward features (e.g., local basins and non-transform discontinuities) and highlight concave downward features (e.g., OCCs). The results can be seen in Figure 3.12. From the results, we can see how the SWE-LoG can aid the identification of individual OCCs within the study area.

The evolution of the modes of spreading as well as the development of these OCCs can then be explored by observing its magnetic signatures. The alternating magnetic polarity through time can act as a proxy of a geological timescale of both tectonic and magmatic events within the study area.

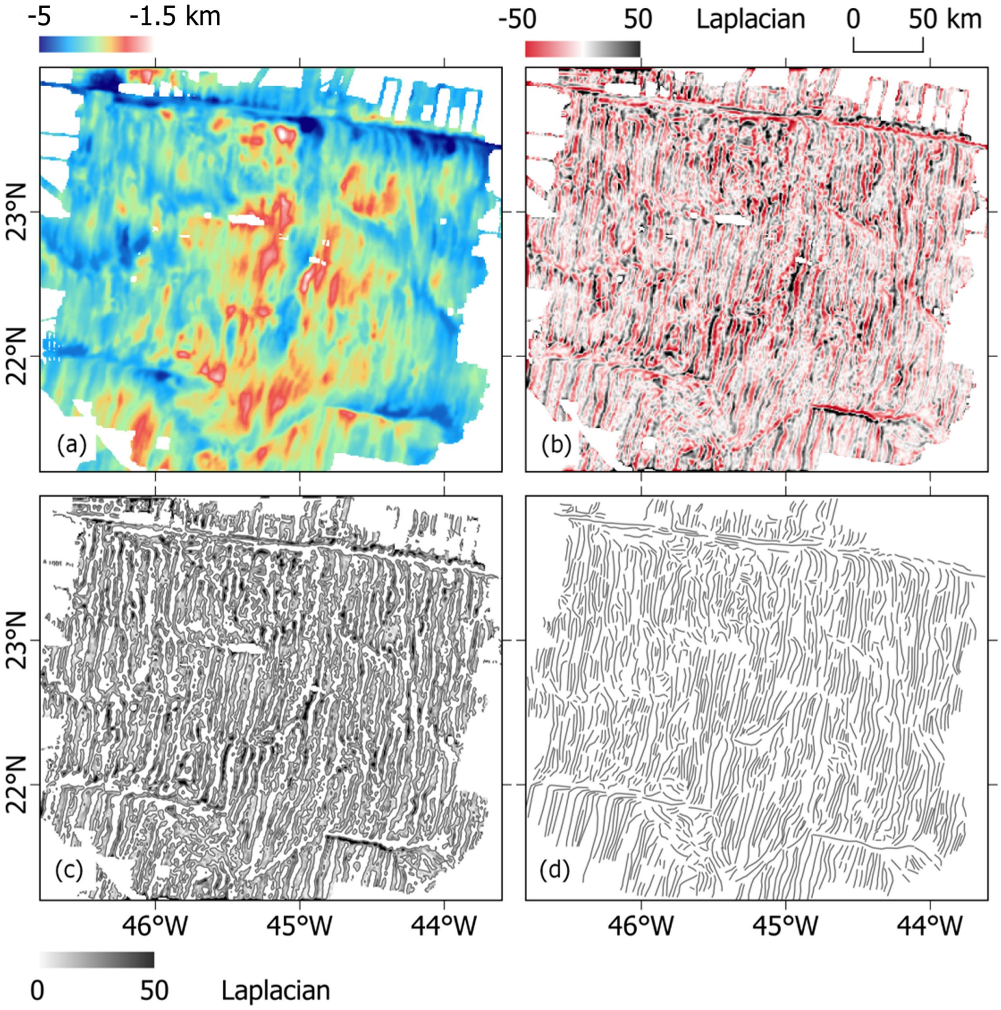

Figure 3.10: Tectonic fabric from bathymetry. (a) High-resolution bathymetry filtered with a 5-km Gaussian filter to generalise the morphology; (b) Laplacian-of-Gaussian-filtered (LoG-filtered) bathymetry; (c) Positive values of the LoG-filtered bathymetry depicting terrain curvatures, and; (d) Lineaments picked from the edges of the LoG-filtered bathymetry (c) depicting the tectonic fabric of the area. We can see that the majority of the lineaments are parallel to the spreading axis. Areas with lineaments that are not parallel to the spreading axis are interpreted as having experienced tectonic extension.

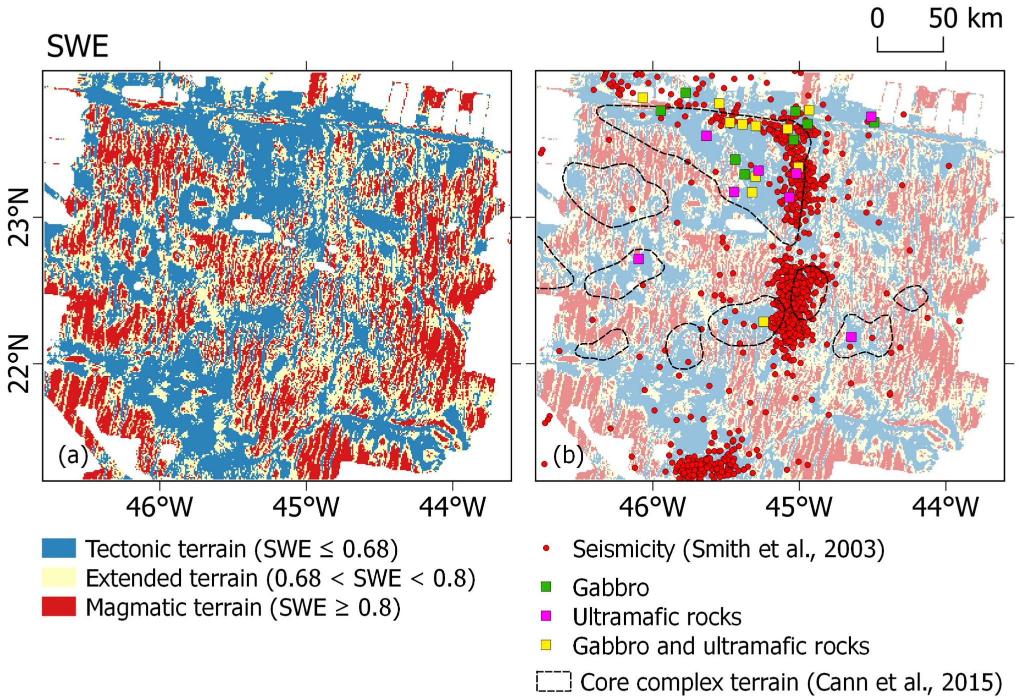

Figure 3.11: Terrain classification at MARK using the SWE algorithm. (a) The study area is classified based on the SWE algorithm. Tectonic terrain is defined where SWE ≤ 0.68, extended terrain is defined where $0.68 < \text{SWE} < 0.8$, and magmatic terrain is defined where $\text{SWE} \geq 0.8$. (b) The SWE classification results compared to the core complex terrain inferred by Cann *et al.* (2015) in areas bounded by dashed black lines, with T-wave seismicity of Smith *et al.* (2003), and with sampled rocks from various studies, documented e.g., in Cannat (1993).

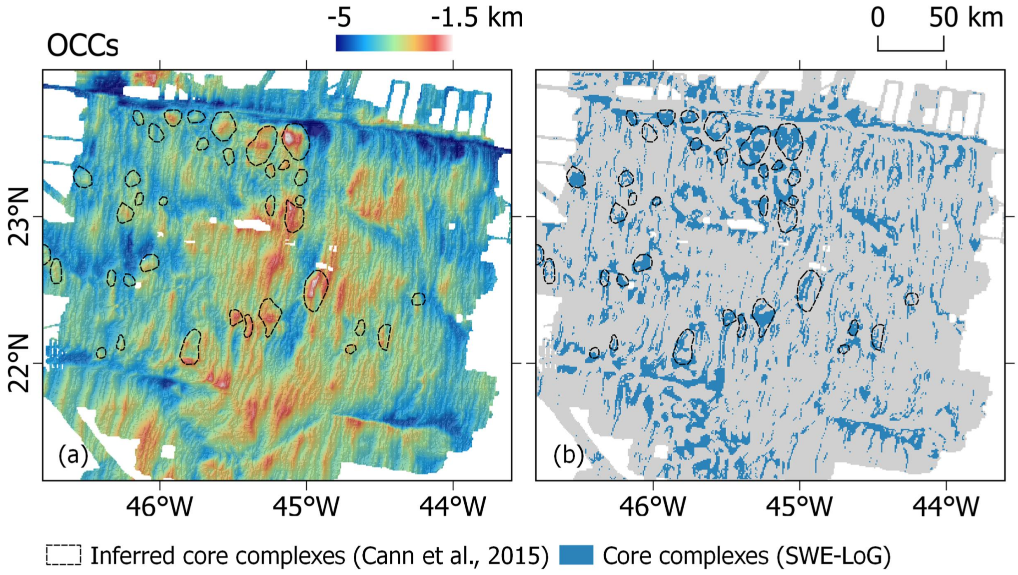

Figure 3.12: Inferred OCCs from SWE. (a) OCCs or core complexes inferred by Cann *et al.* (2015) shown in areas bounded by dashed black lines. (b) OCCs inferred from the SWE-LoG algorithm, overlaid by OCCs inferred by Cann *et al.* (2015). Areas with SWE $\leq$ 0.68 are masked with a grid created using an 8' ($\sim$14.8 km) low-pass LoG filters, eliminating concave upward features. The remaining highlighted (blue) areas are inferred OCCs.

3.4.2 Picking magnetic reversals

The cooling of the oceanic crust generates a thermoremanent magnetisation (TRM), recording the geomagnetic field variation at the time the crust was created (Vine, 1966). The latest pattern of the geomagnetic polarity reversals is documented by Walker *et al.* (2013) in the GSA Geologic Time Scale version 5.0. The reversals are marked by normal and reverse polarity chrons (short for 'isochrons') with preceding nomenclatures indicating their general period on the geological time scale (e.g., C-sequence is short for 'Cenozoic'). Within the magnetic anomalies, normal chrons are depicted as positive values, while reversed chrons are depicted as negative values.

To pick out the observable chrons, I apply the RTP operator to the shipboard magnetic anomalies to ensure that the signatures are centred over the causative body. Using the magnetic field calculator of the Natural Resources Canada website (geomag.nrcan.gc.ca/calc/mfcal-en.php), I calculate the magnetic inclination and declination of the four corners and the centre of the study area (c.f. Table 3.3). We can see that the variation in the magnetic inclination is around 3.5° and around 0.2° in the magnetic declination. Hence, applying the RTP operator with constant inclination and declination values (i.e., the centre point of the study area) is still appropriate within the size of the study area. The results can be seen in Figure 3.13.

Table 3.3: Magnetic inclination and declination of the four corners and centre of the study area. Lat: Latitude. Lon: Longitude. *I*: Inclination. *D*: Declination.

Point location	Lat (°)	Lon (°)	I (°)	D (°)
Top-left corner	24	-46.8	44.6	-17.7
Top-right corner	24	-43.6	42.8	-17.5
Centre	22.6	-45.2	41.9	-17.7
Bottom-left corner	21.2	-46.8	41.1	-17.7
Bottom-right corner	21.2	-43.6	44.6	-17.7

In Figure 3.13a, the 'Brunhes' or the C1r (0.78 Ma) anomaly is observed in the centre of the axis, with a short-wavelength low magnetic anomaly observed at its western flank. The signature indicates that the magnetic anomaly in the study area is still acting as a dipole, which signature greatly depends on its magnetic latitude. After applying the RTP operator of the centre point of the study area, we can see in Figure 3.13b that the 'dipolar' effect is no longer present, leaving a more 'centred' anomaly both in the spreading axis (depicted by the 'Brunhes' anomaly), the western flank, and the eastern flank. The other magnetic reversals are then picked out up to the edge of the last observed reversed anomaly, or the C5r: 10.94 Ma (Figure 3.13c) with the geomagnetic polarity as a guide (Figure 3.13d).

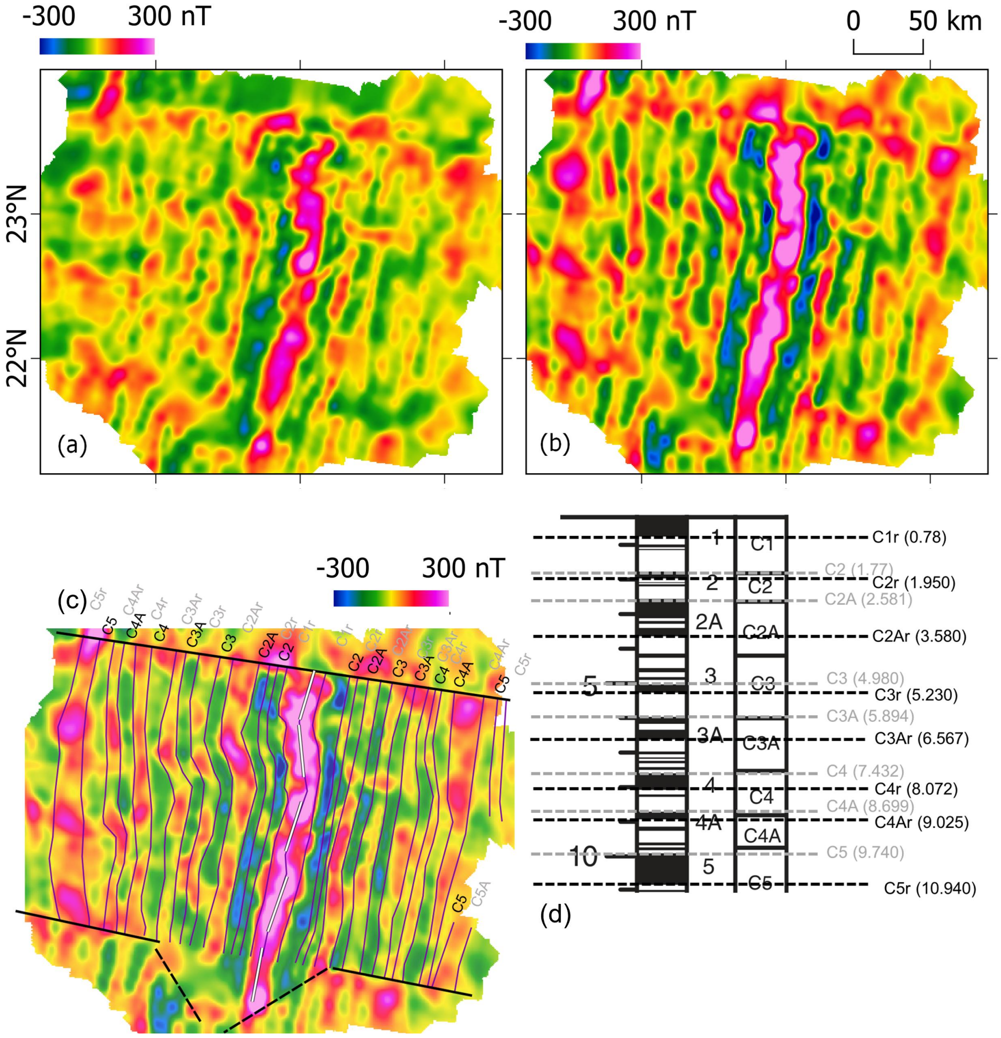

Figure 3.13: Picking magnetic chrons. (a) Gridded shipboard magnetic anomalies; (b) RTP of shipboard magnetic anomalies (RTP-MA); (c) RTP-MA picked on the edges of the indicated magnetic reversals, from C1r (0.78 Ma) to C5r (10.94 Ma); (d) Geomagnetic polarity up to C5r (10.940 Ma) as a guide, after the GSA Geologic Time Scale version 5.0 (Walker *et al.*, 2013). The geomagnetic reversals are marked by C1r, C2, C2r, C2A, up to C5r. All the numbers in the brackets are in million years (Ma).

3.4.3 Crustal thickness computation inferred from isostatic mantle Bouguer anomaly (IMBA)

The gravity anomalies observed over the study site reflect the sum of the total density contrast from the sea surface down to the upper mantle. As the study is intended to focus on the density variation in the crust, we need to remove from the FAA the gravity response from the water-crust interface using Parker (1973), resulting in Bouguer anomaly (BA). According to Ewing *et al.* (1973), in general, sediments are absent, or at best a very thin veneer, out to about 10-50 km from the ridge axis. The first thickening observed within that range of distances only range about 30-40 m. Based on this information, the water-sediment interaction is not considered in the computation over the study area.

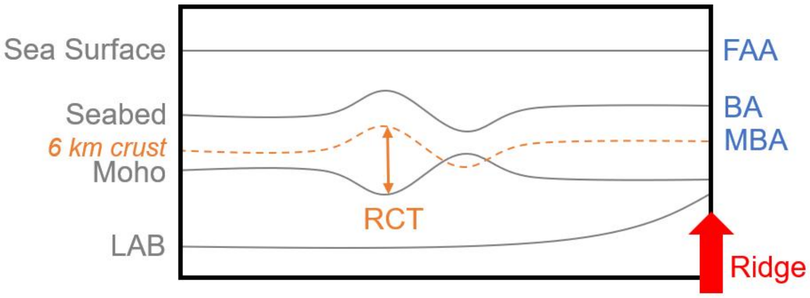

Figure 3.14: Illustration of the layers taken into account in the gravity and crustal thickness computation. LAB: Lithosphere-Asthenosphere Boundary. RCT: Residual Crustal Thickness. FAA: Free-Air Anomaly. BA: Bouguer anomaly. MBA: Mantle Bouguer Anomaly.

Prior to conducting the Bouguer correction, I applied a 20-km Gaussian filter to the shipboard multibeam bathymetry to simplify the signals and convert them to similar wavelengths as the FAA, as conducted e.g., in Goff (1991). The mantle Bouguer anomaly (MBA) can then be computed by removing the attraction of the crust-mantle interface using the same method, assuming a homogeneous 6 km thick crust, following the average oceanic crust thickness in the study of Christeson *et al.* (2019). The MBA can then enable us to see the "bullseye" pattern of gravity anomaly lows over the spreading centres (e.g., Kuo & Forsyth, 1988; Lin *et al.*, 1990), depicting the high temperature, low density, mantle upwelling at the ridge axis. This prominent pattern, caused by the crust-upper mantle density contrast, need to be removed in order to interpret the anomalies observed solely in the crustal layer.

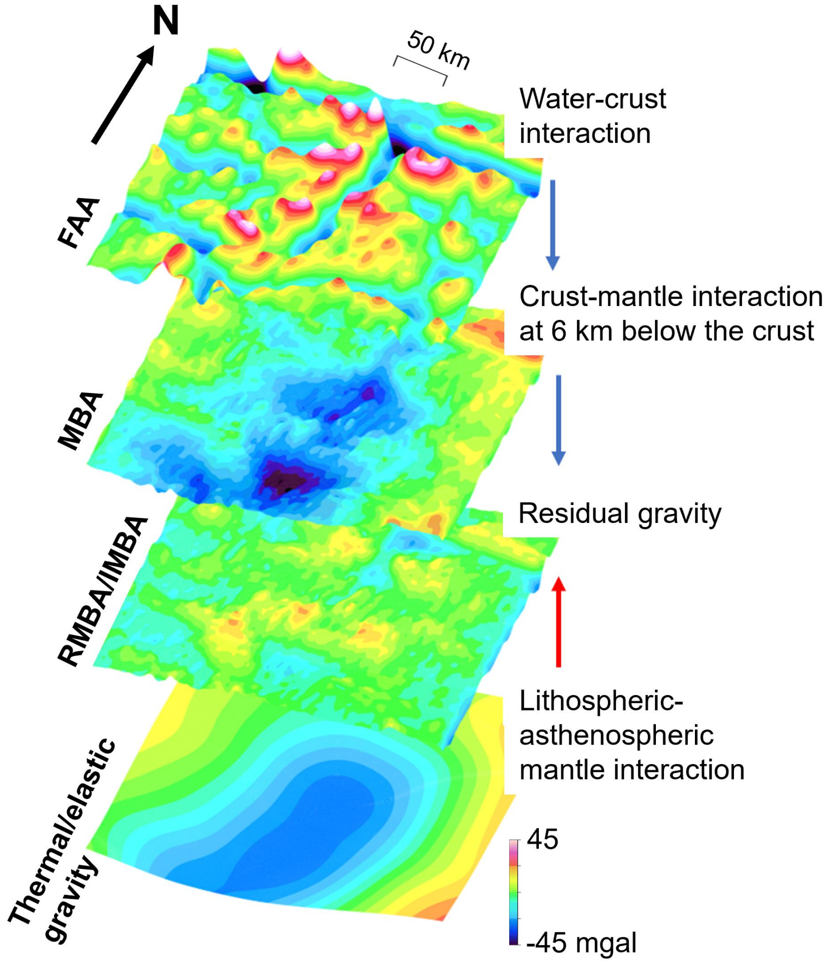

Figure 3.15: Gravity anomaly residual illustration. The free-air gravity anomaly (FAA) mostly depicts the water-crust interaction. Hence, in the oceanic crust, the FAA generally mimics the long-wavelength of the bathymetry in the consecutive area. The mantle Bouguer anomaly (MBA) is computed to observe the crust-mantle interaction at 6 km below the crust, assuming a homogeneous crust with constant thickness. The "bullseye" pattern is observed in the MBA, depicting the passive mantle upwelling in the study area. This pattern can be eliminated by reducing the effect from the lithospheric-asthenospheric mantle interaction. This gravity effect can be computed either from the thermal or the elastic gravity models, explained in the text. The final product will be the residual gravity, in the form of residual mantle Bouguer anomaly (RMBA) or the isostatic mantle Bouguer anomaly (IMBA).

One common approach to estimate this effect is by modelling the cooling of the lithosphere using a plate model equation (e.g., Morgan & Forsyth, 1988; Turcotte & Schubert, 2002), computing the gravity effect it causes, and removing this effect from the MBA resulting in a residual mantle Bouguer anomaly (RMBA). The illustration of the residual processes can be seen in Figure 3.15. To obtain the lithospheric cooling model, I use the plate model equation of Turcotte & Schubert (2002), described as:

$$T = (T_i - T_0) \times erf\left(\frac{y}{2\sqrt{\kappa t}}\right) + \frac{(T_{i+1} - T_i)}{2} \times \left\{ erf\left(\frac{y-b}{2\sqrt{\kappa t}}\right) + erf\left(\frac{y+b}{2\sqrt{\kappa t}}\right) \right\} + T_0 \quad (3.6)$$

where T is the temperature at depth b and time t, T_i is the temperature at $t = i$, T_0 is the temperature at $t = 0$, y is the maximum crustal thickness, $\sqrt{\kappa t}$ is the characteristic thermal diffusion distance, and b is the depth of the computed cell. Afterwards, the gravity anomaly of the lithospheric cooling model T can be computed based on the density contrast. I picked the ages of the lithosphere from the magnetic anomalies to construct the time t grid. Using a thermal expansion coefficient (Kuo & Forsyth, 1988), thermal gravity anomalies can be computed by expressing the density contrast (Chappell & Kusznir, 2008) in each 1-km layer, described as:

$$\Delta T = T_i - T_m \times \frac{z_i}{y} \quad (3.7)$$

$$\Delta g = -\alpha \rho_m \Delta T \quad (3.8)$$

The total gravity anomaly is the sum of the Δg from each 1-km layer. I set the lithosphere depth by following the lithosphere-asthenosphere boundary at 1350^{o}C from the ridge out to its spreading direction. The depth will flatten when it reached the defined maximum plate thickness. The parameters used in the modelling process can be seen in Table 3.4 and the resulting model can be seen in Figure 3.16.

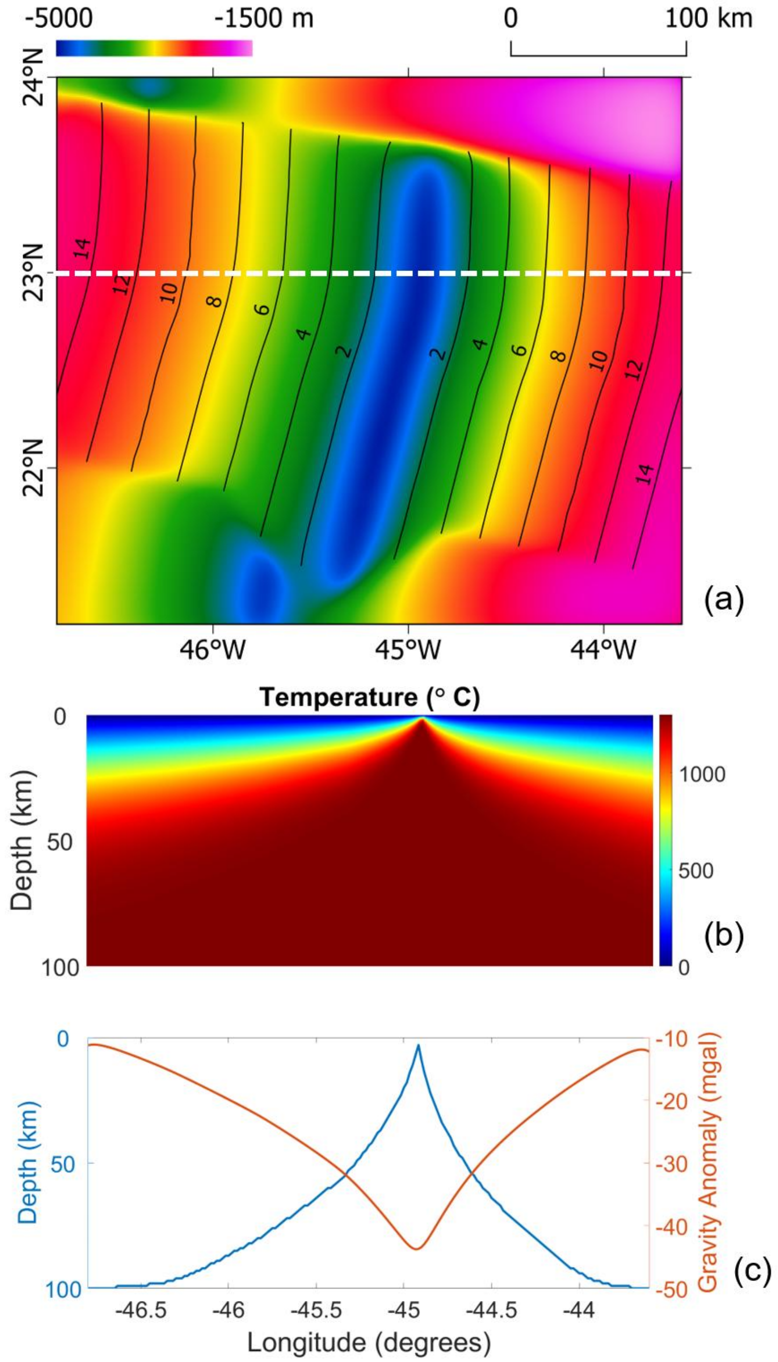

Figure 3.16: Lithospheric cooling model at MARK. (a) Gridded depth to lithosphere modelled from the plate model computation. Black lines are modelled age contours marked each 2 Ma; (b) Cross-profile of the temperature distribution at 23

Table 3.4: Parameters used to build the lithospheric cooling model

Symbol	Parameter	Value and Unit
T_0	Surface temperature	0 ^{o}C
T_m	Mantle asthenosphere temperature	1350 ^{o}C
y	Lithosphere plate thickness	100 km
κ	Coefficient of thermal conductivity	10^{-6} Wm^{-1}K^{-1}
b	Depth spacing	1 km
α	Coefficient of thermal expansion	3×10^{-5} ^{o}C^{-1}
ρ_m	Mantle density	3.30×10^3 kg m^{-3}

By subtracting this thermal gravity model from the MBA, we can now observe the remaining residual gravity anomalies, or the RMBA (Figure 3.17). However, we can see from the figure that the forward modelling approach of the thermal gravity anomalies generally overestimates the temperature of the lithosphere at the younger ages and underestimates the gravity effects at the older ages. This is evident in Figure 3.17d, in which the thermal gravity model managed to reduce the appearance the "bullseye" pattern at the centre of the axis, yet the remaining gravity signatures further than 100 km from the spreading axis cannot give much information about the crustal structure variation beneath the crust. In addition, the model can only run with several couples of symmetrical spreading rates. Therefore, in this study I attempted to remove the long-wavelength "bullseye" pattern by examining the regional isostasy of the study area, which result is denoted here as the isostatic mantle Bouguer anomaly (IMBA).

Similar to the widely used RMBA, this method employs the concept of Airy isostasy, assuming infinite slabs of homogeneous water, crust, and mantle layers (Figure 3.15). The main difference between the IMBA and RMBA methods is in the calculation of the gravity responses at the lithospheric-asthenospheric mantle interaction. Instead of forward modelling the gravity effects from the cooling of the oceanic lithosphere, I compute the Moho gravity effect of an elastic plate using the Wessel (2001) approximation through the `gravfft` function on `GMT 5.4.3`. The computation is controlled by the Airy isostatic factor A, described as:

$$A = \frac{\rho_c - \rho_w}{\rho_m - \rho_c} \tag{3.9}$$

where ρ_c, ρ_w, and ρ_m, are the densities of the crust, water, and mantle, and by the flexural rigidity D, described as:

$$D = \frac{E{T_e}^3}{12(1 - v^2)} \tag{3.10}$$

where E is the Young's modulus and is the Poisson's ratio. The parameters that are used in this calculation are listed in Table 3.5. The T_e value of 6 km is chosen based on the studies of Blackman & Forsyth (1991) and Cannat (1996).

Table 3.5: Parameters used in isostatic computation

Symbol	Parameter	Value and unit
ρ_c	Crust (load) density	2.80×10^3 kg m^{-3}
ρ_w	Water density	1.03×10^3 kg m^{-3}
ρ_m	Mantle density	3.30×10^3 kg m^{-3}
E	Young's modulus	1011 Pa
Te	Elastic plate thickness	6 km
v	Poisson's ratio	0.25

From Figure 3.17c and 3.18c, we can see that the values of the elastic gravity anomaly more resemble the longer wavelength observed at the MBA than the forward-modelled thermal gravity anomaly. Hence, by removing the elastic anomalies from the MBA, we get the IMBA which depicts the isostatic response of the crust-mantle interaction without the effect of the cooling of the lithosphere (Figure 3.18d). The density variation observed at IMBA is confined to the crustal layer, hence it will act as a good proxy for the crustal thickness approximation and the following crustal features interpretation.

The IMBA can then treated as an expression of the crustal thickness variation over the area, where high residual is indicative of thin crust. Furthermore, the residuals will allow us to compute the depth to the Moho, followed by computing the crustal thickness variation over the area. The crustal thickness variation in this study is observed by computing the depth to the Moho, i.e., the top of the residual gravity contact. Using the infinite slab principle, we can calculate the depth to the Moho by:

$$h = \frac{\Delta_g}{2\pi G \Delta_\rho} \tag{3.11}$$

where Δ_g is the observed anomaly, G is the gravitational constant (6.674×10^{-11} N kg^{-2} m^2), and Δ_ρ is the density contrast considered at the selected anomalies.

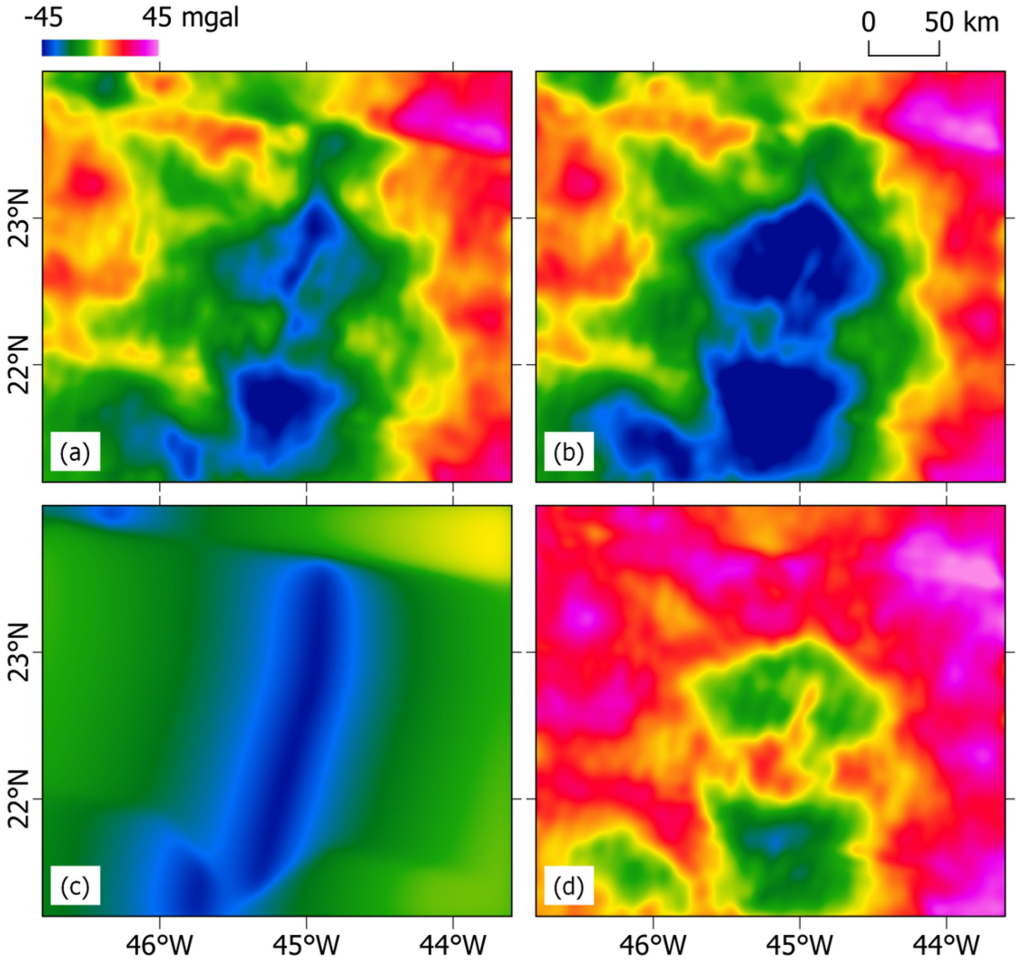

Figure 3.17: Computed gravity values at MARK, reduced by the thermal gravity model. (a) Bouguer anomaly; (b) Mantle Bouguer anomaly with two apparent "bullseye" patterns in the middle of two segments of the spreading axis; (c) Thermal gravity anomaly. We can see along the axis that the resulting thermal gravity anomaly values are similar to the gravity anomaly values found in the locus of the two apparent "bullseye" patterns in the MBA; (d) Residual mantle Bouguer anomaly (RMBA). We can now see more variations in the gravity anomaly signatures, specifically those located closest to the spreading axis. However, the reduction fails to give us information on the crustal structure variation at areas further than 100 km from the spreading axis. Colour schemes are scaled at the same rage for each figure.

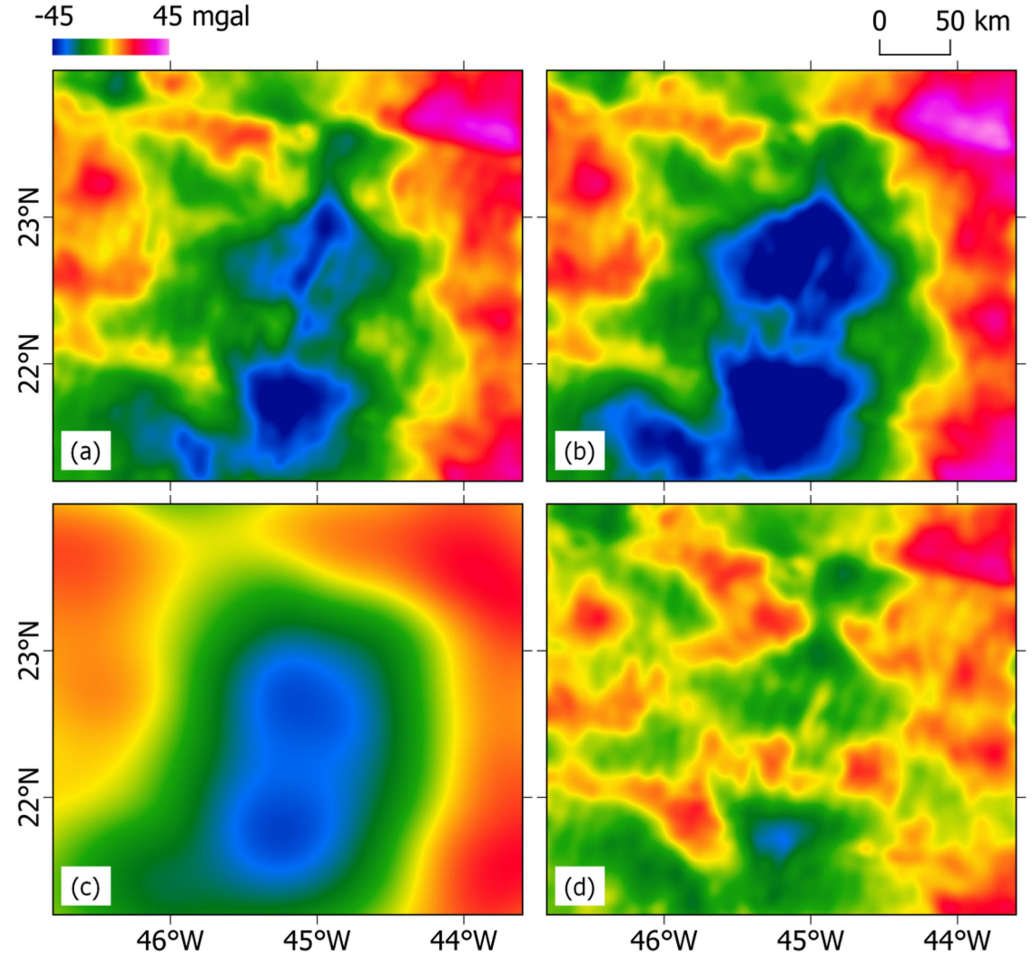

Figure 3.18: Computed gravity values at MARK, reduced by the elastic gravity model. (a) Bouguer anomaly; (b) Mantle Bouguer anomaly with two apparent "bullseye" patterns in the middle of two segments of the spreading axis; (c) Elastic gravity anomaly. We can see that two locuses with low gravity anomaly values that resemble the "bullseye" pattern observed in the RMBA. (d) Isostatic mantle Bouguer anomaly (IMBA). We can now see the variation in the gravity anomaly signature throughout the study area, as the "bullseye" pattern have been successfully removed. Unlike in the RMBA, the variation is still observable at areas further than 100 km from the spreading axis. The IMBA grid will then be used to compute the crustal thickness variation in the study area.

The resulting IMBA is cosine-tapered between the wavelengths of 25 and 35 km (low pass and high pass, respectively) before the infinite slab computation is carried out. Afterwards, the resulting depth variation is subtracted from the Moho with constant 6 km thick crust to get the regional depth to Moho. The depth to Moho computation processes can be seen in Figure 3.19. The resulting depth to Moho is then compared with the available seismic lines in the area. The cross-profile comparison can be seen in Figure 3.20 and the 3-dimensional plot of the cross-profiles can be seen in Figure 3.21. From the figures, we can see that the computed depth to Moho matches quite well with the observed Moho, except in P08 where the observed Moho is systematically shallower by on the order of 0-2 km. We can also see that the middle section of the P08 profile is generally more elevated compared to the other observed Moho profiles. This discrepancy might occur as a result of the 2-dimensional seismic profile processing and interpretation, as opposed to the 1-dimensional depth to Moho computation from Δ_g using Equation 3.11. As the P08 profile is parallel to the direction of the detachment faulting of an OCC, out-of-the-plane reflection might be captured as sideswipes. The average discrepancy between the computed and observed Moho in each of the profiles can be seen in Table 3.6.

3.4.4 Tectonic structures from potential field data

Another way to interpret the tectonic fabric is by examining the lineaments of the available potential data, both gravity and magnetic, using the ACLAS technique explained in 3.2.3. Firstly, I computed the THDR of the RTP-magnetic anomaly grid, followed by creating a ridge grid to trace the local peaks of the THDR. Afterwards, I computed a separate grid, which is the tilt derivative of the magnetic anomalies. From the tilt derivative, I created a zero-contour map, and traced where the second-, third-, and fourth- order of the THDR ridge (Blakely & Simpson, 1986) overlays the zero-contour of the tilt derivative (Figure 3.22). For the gravity grid, as explained in 3.2.3, it is important to apply VDR to the grid before applying any other operations to convert the gravity field response $1/\mathrm{r}^2$ into $1/\mathrm{r}^3$. In this study, I use the computed IMBA as the gravity input as it depicts the density contrast solely within the crust (water-crust and crust-mantle density contrasts have been removed). The results can be seen in Figure 3.23. The ACLAS technique will be useful especially in places where detailed bathymetry is not available. Hence, it is a good way to check how well it works over an area with good coverage of bathymetry.

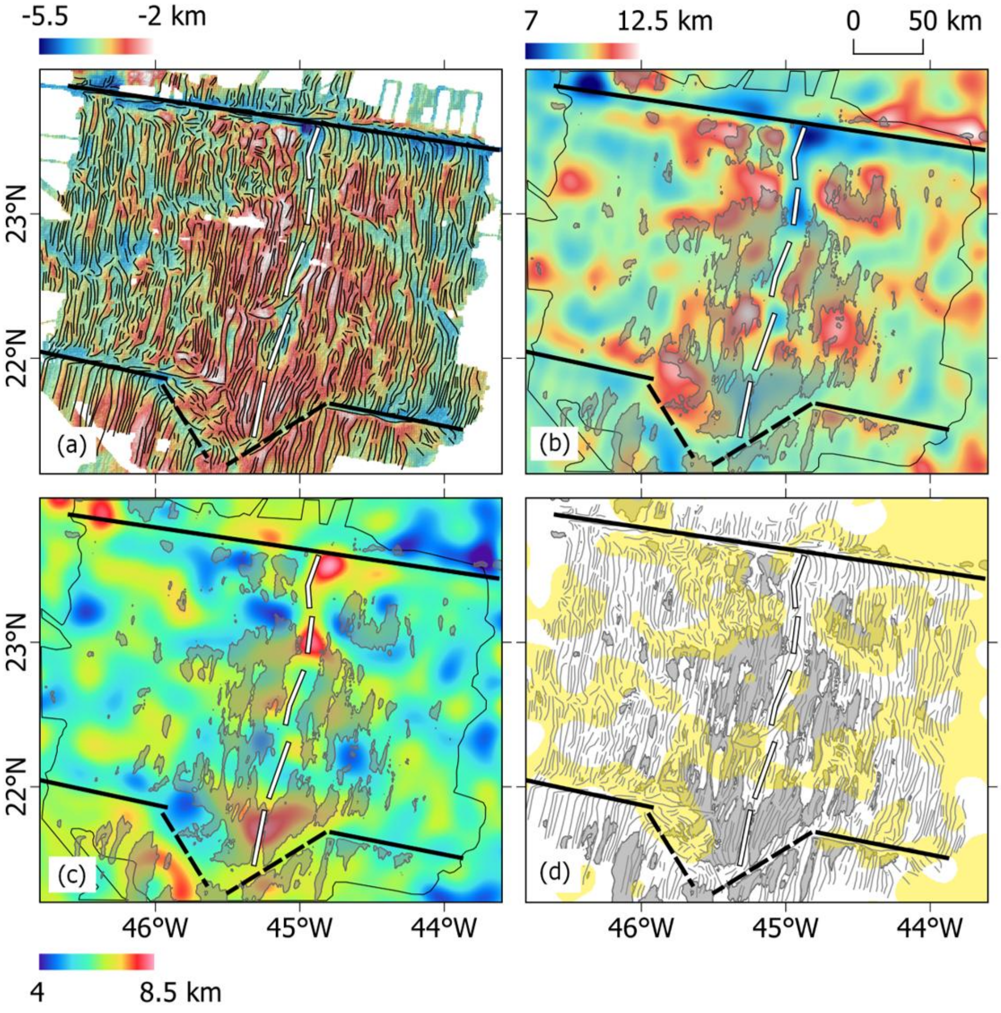

Figure 3.19: Bathymetry, depth to Moho, and crustal thickness. (a) Bathymetry overlaid with 500 m contours and major features; (b) Depth to Moho computed from IMBA. Depths are computed relative to sea level. Transparent grey: Area with depths shallower than 3 km. Thin solid line: Area with available high-resolution bathymetry; (c) Crustal thickness, and (d) Interpreted bathymetry overlaid with classified crustal thickness. Yellow: Area with < 6 km crust (thin crust). Thick black lines: fracture zones. Dashed thick black lines: non-transform discontinuity depicting the migration of the neo-volcanic zone to the south. Bordered white lines: spreading axis segments.

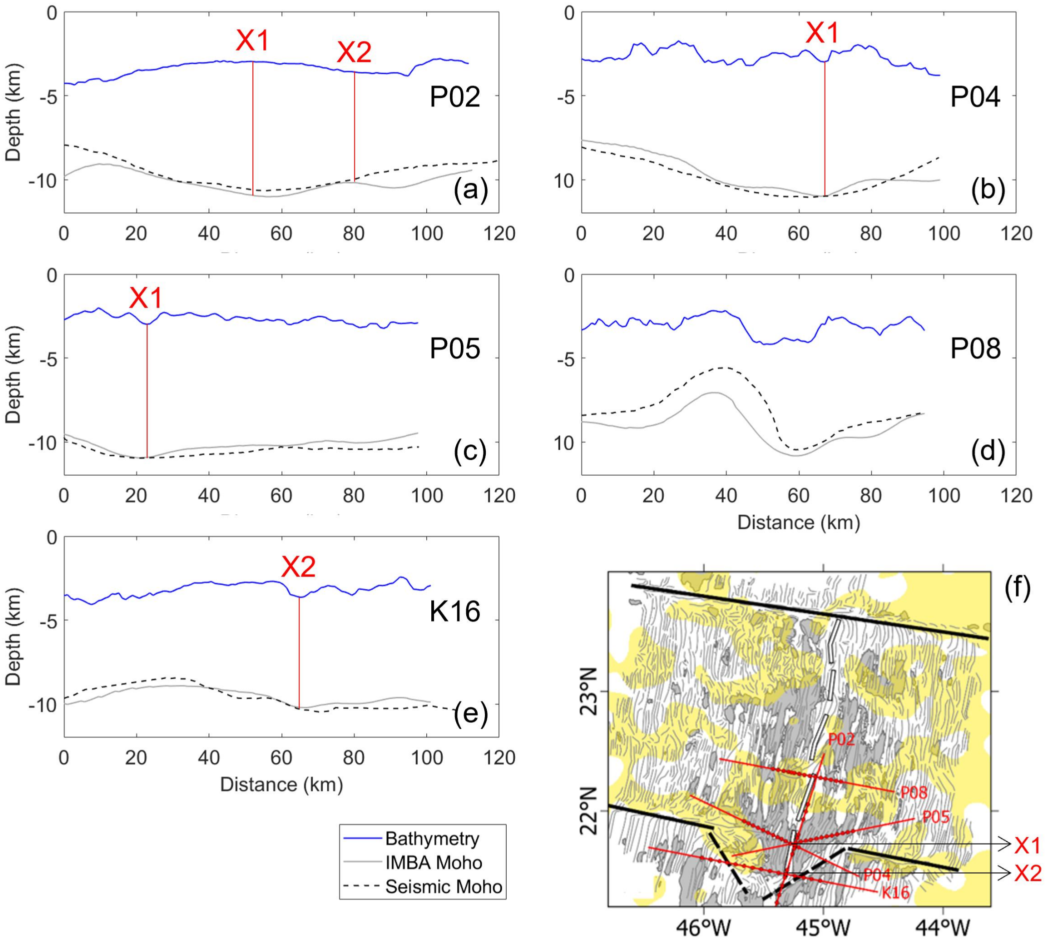

Figure 3.20: Comparison between the depth to Moho from IMBA and from seismic tomography as explained in Table 3.2. Solid blue line: bathymetry. Solid grey line: Moho computed from IMBA. Dashed black line: Moho from seismic tomography. (a) to (e) are cross-profiles at P02, P04, P05, P08, and K16, respectively. The crossing of the profiles are marked as X1 and X2.

Table 3.6: The discrepancy between computed and observed Moho. SD: Standard deviation.

Line	Mean discrepancy (km)	SD (km)
P02	0.61	0.36
P04	0.38	0.27
P05	0.33	0.19
P08	0.90	0.68
K16	0.35	0.13
Mean	0.51	0.44

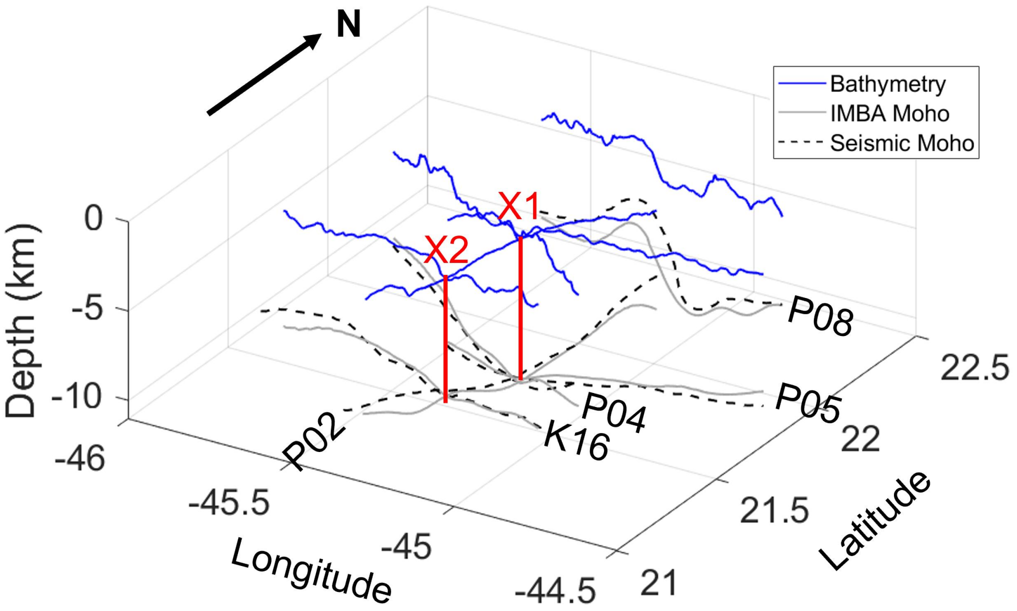

Figure 3.21: Three-dimensional plot of the cross-profiles. Solid blue line: bathymetry. Solid grey line: Moho computed from IMBA. Dashed black line: Moho from seismic tomography. Red solid line: Crossing points.

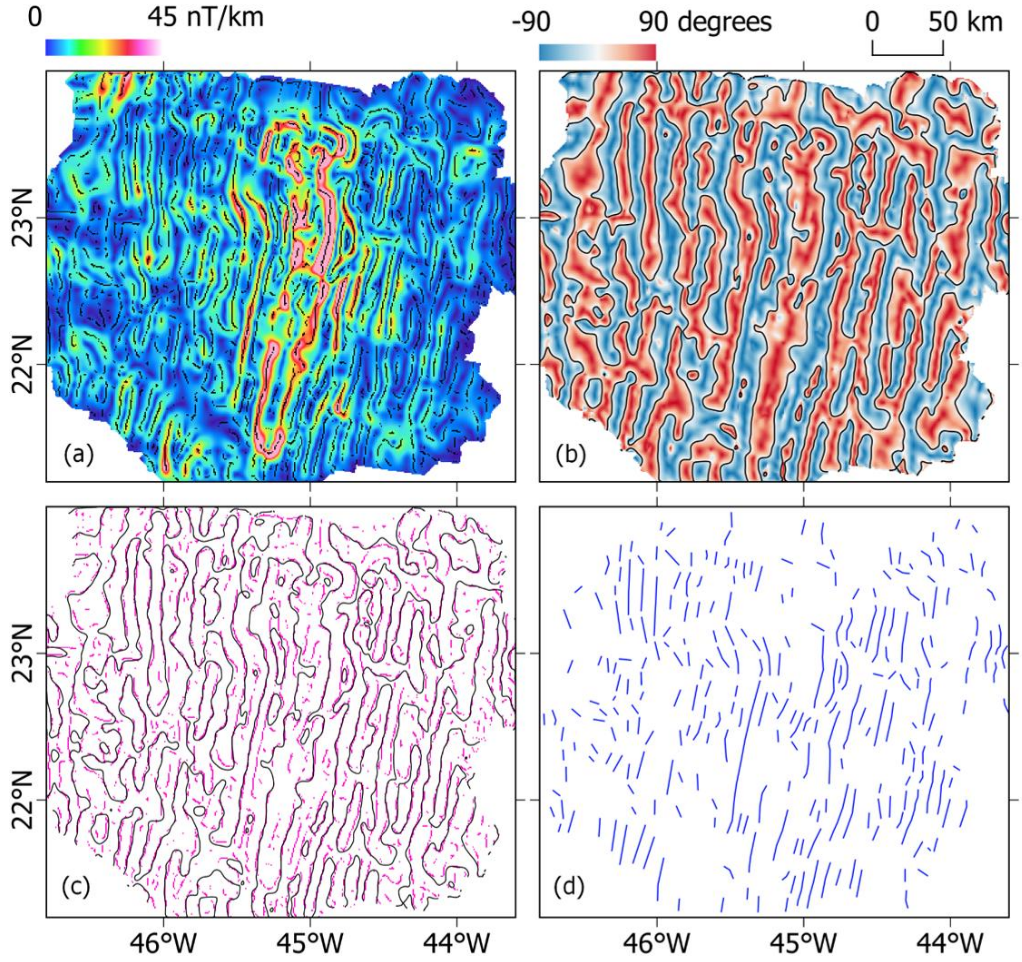

Figure 3.22: Tectonic interpretation using ACLAS: Magnetic. (a) Total horizontal derivative of reduced-to-pole magnetic anomalies (THDR-MA);(b) Tilt derivative of reduced-to-pole magnetic anomalies (TDR-MA); (c) Zero-contour of TDR-MA overlaid with the second, third, and fourth order of the ridge from THDR-MA; (d) Lineaments from reduced-to-pole magnetic anomalies.

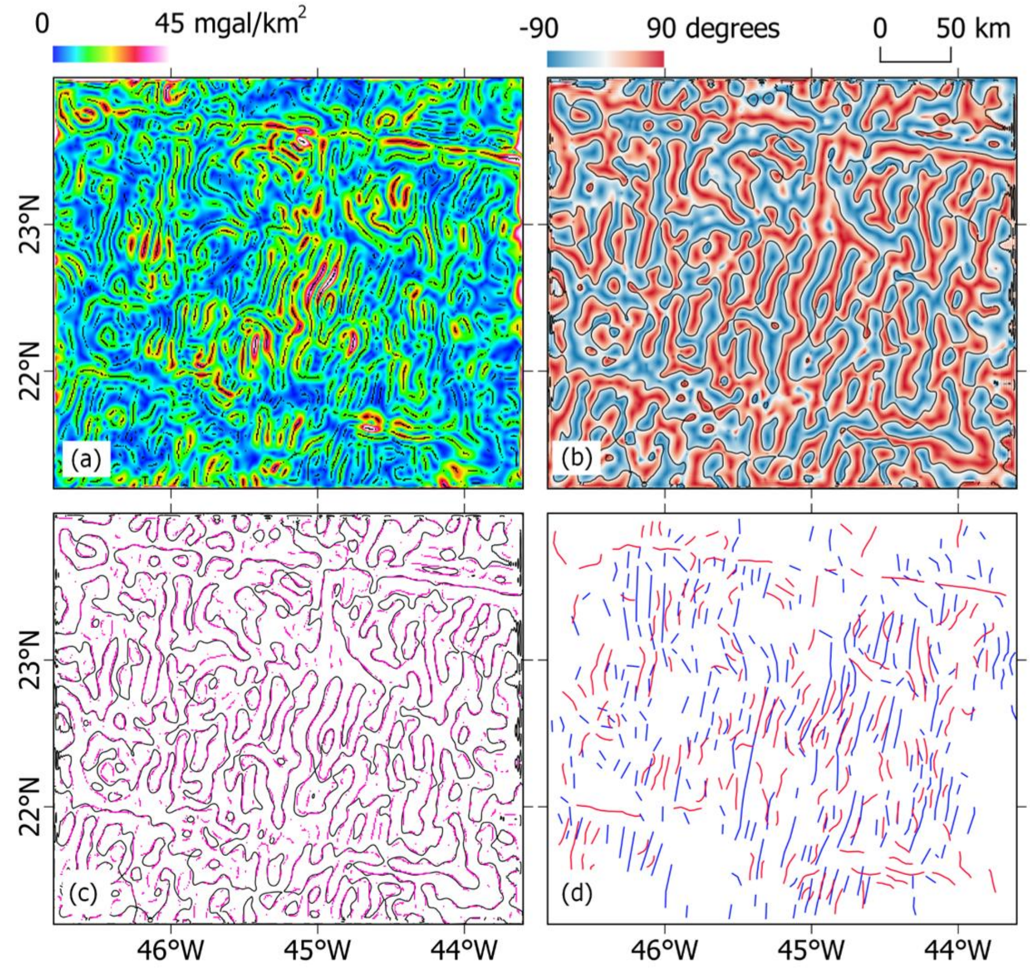

Figure 3.23: Tectonic interpretation using ACLAS: Gravity. (a) Total horizontal derivative of the vertical derivative of IMBA (THDR-VDR-IMBA); (b) Tilt derivative of the vertical derivative of IMBA (TDR-VDR-IMBA); (c) Zero-contour of TDR-VDR-IMBA overlaid with the second, third, and fourth order of the ridge from THDR-VDR-IMBA; (d) Lineaments from IMBA (red) and reduced-to-pole magnetic anomalies (blue). Fewer lineaments are generally found in detachment areas.

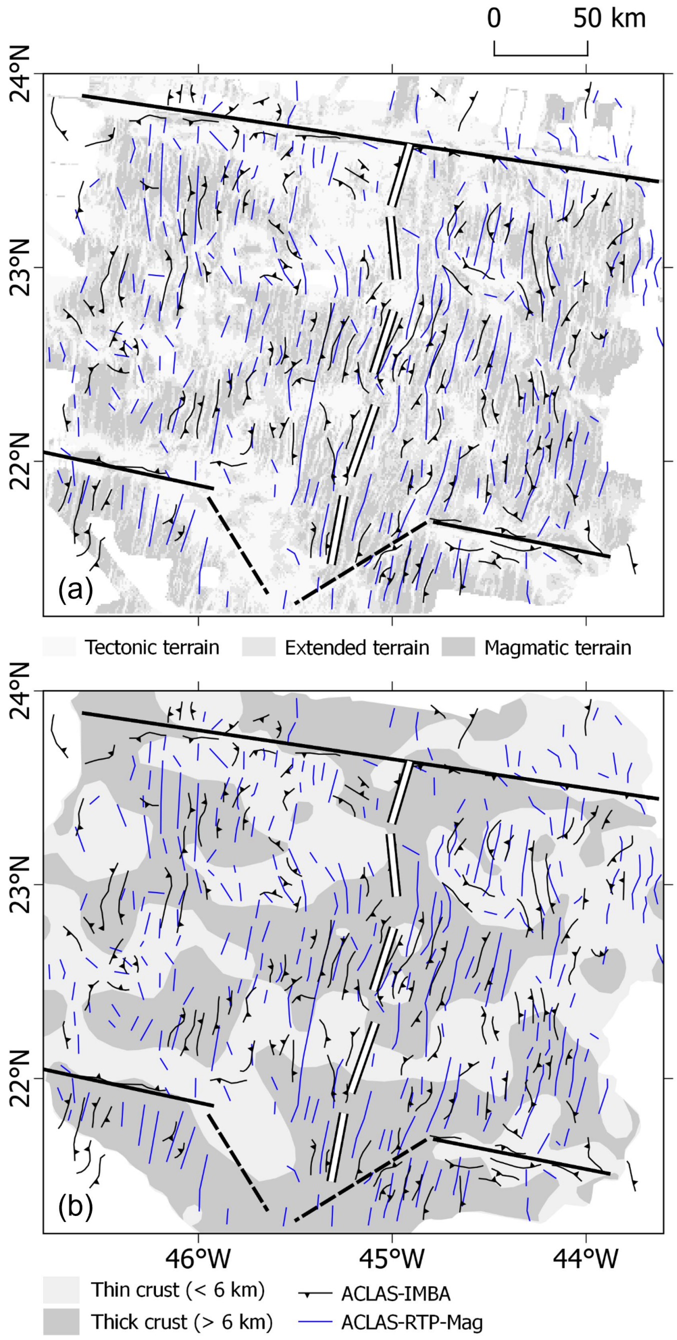

Figure 3.24: Lineaments interpreted from gravity and magnetic anomaly data sets using the ACLAS technique. (a) Interpreted lineaments over SWE-classified terrain. Lineaments parallel to the spreading axis are observed in the magnatic terrain and omnidirectional-dipping lineaments are observed in the extended and tectonic terrain. Less lineaments are observed in the tectonic terrain. (b) Interpreted lineaments over thickness-classified terrain. Lineaments parallel to the spreading axis are observed in the thick crust and omnidirectional-dipping lineaments are observed in the thin crust. Less lineaments are observed in the thin crust.

3.5 Results

In this section, I will examine the evolution of spreading rate, crustal thickness, and tectonic style by comparing observations of these parameters at both axis flanks over time, marked by the interpreted magnetic chrons. I divided the study area into four segments, each following the flowlines starting from the youngest crust at the spreading axis out to the oldest magnetic chrons at both flanks. Each of these segments is divided into five sections of flowlines, except for Segment 1 which is only divided into four sections (Figure 3.25).

Each segment provides different characteristic of crustal morphology along its flowline. For instance, in Segment 1 we observe the forming of numerous OCCs at the western flank. We can also observe that from around 8 Ma, the crust is generally thinner at the western flank compared to the eastern flank. In Segment 2, we observe quite a lot of axis rotation through time. At the western flank, thin crust is observed at around 8 Ma until around 2 Ma. At the youngest ages, the crust is thinner at the western flank compared to the eastern flank. In Segment 3, we observe a relatively thin crust at the older ages before it became thicker at around 6 Ma. We observe the forming of OCCs at both flanks at the youngest ages and thinner crust at the eastern flank compared to the western flank at these ages. Finally, in Segment 4, we observe the forming of a neo-volcanic zone at the youngest ages. Several OCCs are found specifically at the western flank until around 4-5 Ma. Thick symmetrical crust is observed at the northernmost end of the segment.

3.5.1 Evolution of spreading rates

In Figure 3.26, I compare the distances between each magnetic chron in the western flank and the spreading axis with the distances between each magnetic chron in the eastern flank and the spreading axis. In Segment 1, as the distances between chrons are generally greater in the western flank compared to the eastern flank, we can interpret that the crust was spreading faster to the western flank compared to the eastern flank. This asymmetry already occurred at the oldest chron (C5r: 10.94 Ma), followed by an increase of spreading velocity at the western flank until around 7 Ma, then it slowed down and became more symmetrical at around 4 Ma. Thereinafter, the eastern flank spread slightly faster than the western flank. In general, the northernmost section (1-2) is the most asymmetrical, in which the crust spreads faster to the eastern flank and the southernmost section (1-5) is the most symmetrical.

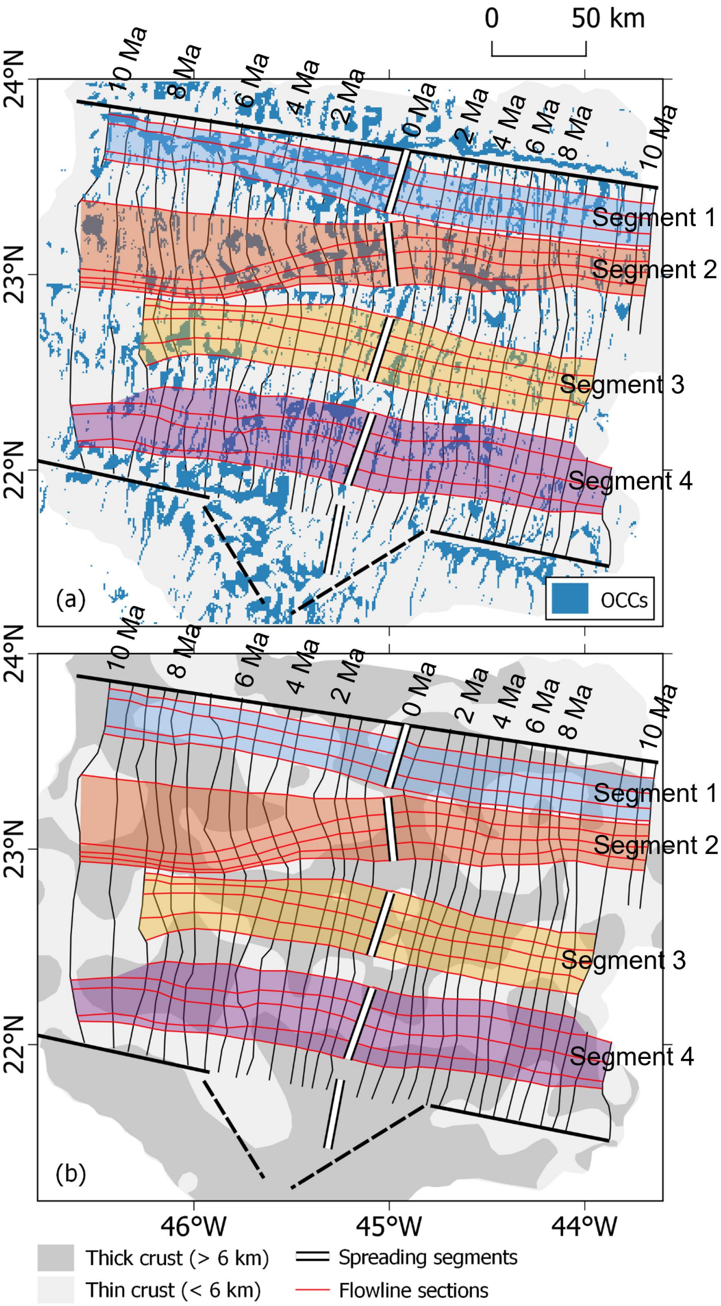

Figure 3.25: Segmentation within the study area based on the interpreted spreading axes. (a) Interpreted OCCs over the study area overlaid by the spreading segments (dark transparent area) and flowline sections (red lines). (b) Crustal thickness variation in the study area overlaid by the spreading segments and flowline sections. Dark grey: thick crust (> 6 km). Light grey: thin crust (< 6 km). Bordered white lines: spreading segments. Thick black lines: fracture zones. Thick dashed black lines: non-transform discontinuity. Thin black lines: interpreted magnetic chrons.

In Segment 2, the trend is more or less similar to those observed in Segment 1. The western flank generally spreads faster compared to the eastern flank since the oldest chron. The asymmetricity decreases until around 8.5 Ma, followed by an increase of spreading velocity until around 8 Ma, then it slowed down and becase more symmetrical at around 3.5 Ma. As observed in Segment 1, the eastern flank thereinafter spread slightly faster than the western flank. It is interesting to see that at around 6.5 Ma, all of the segments have similar distance ratio between the western and the eastern flank.

In Segment 3, we observe more variation in each of flowline sections, specifically between 8.5 and 6 Ma, where the northernmost section (3-1) spreads a lot faster to the western flank compared to the more or less symmetrical trend observed in the southernmost section (3-5). In contrast to Segment 1 and 2, we can see a general trend in which each of the flowline sections evolved to be more symmetrical towards 0 Ma. A much different trend is observed in Segment 4, where the relatively wide variation of the distance ratio observed at the oldest chron decreases until around 8 Ma. Thereinafter, the variation of the distance ratio increases until around 4 Ma. The wide variation is still observed until 2 Ma. In this segment, we can see that the centre of the segment (4-3) is the most symmetrical compared to the other flowline sections.

Having the evolution of crustal spreading observed in each of the segments, I computed the average distance ratio in each to compare how the evolution of each of the segments compared to one another (Figure 3.27). From the figure, we can see a trend where the spreading gets more symmetrical to the south. Another thing we can observe is how Segment 2 was spreading the fastest to the western flank compared to the other segments from the oldest chron until around 10 Ma. From around 9 Ma, Segment 1 was spreading the fastest to the western flank before being replaced by Segment 3 at around 3 Ma. Thereinafter, all of the segments are more or less symmetrical.

The evolution of spreading rate can also be observed by computing the half-spreading rate during each magnetic reversal at both flanks (Figure 3.28). As observed in Figure 3.26a and 3.26b, a similar trend is observed between Segment 1 and 2, where the crust was spreading faster to the western flank compared to the eastern flank up until around 4 Ma. From Figure 3.28a and 3.28b, we can observe a jump of spreading rate at around 2.5 Ma before it decreases until 0 Ma.

In Segment 3, the crust was still spreading faster to the western flank than the eastern flank, but the velocity at both flanks decreased faster than those observed in Segment 1 and 2. The lowest spreading rate is observed at around 4.5 Ma, followed by an increase of spreading rate at both flanks. The spreading rate is very similar at around 2.5 Ma, which is consistent with the symmetry observed in Figure 3.28c at this age. Thereinafter, the spreading rate at both flanks varies and ended with an increase of spreading rate in the eastern flank compared to the western flank.

Compared to the other segments, Segment 4 is the experienced the most symmetrical spreading as can be observed in the comparison between the half-spreading rate at both segments through time. The largest asymmetry is observed at around 2 Ma and 4.5 Ma. The lowest spreading rate is observed just after 2 Ma, followed by an increase of spreading rate at both flanks. From the evolution of the half-spreading rate at each segment, we can see that in general, the greatest half-spreading rate is observed at the northernmost segment (Segment 1) and the least is observed at the southernmost segment (Segment 4).

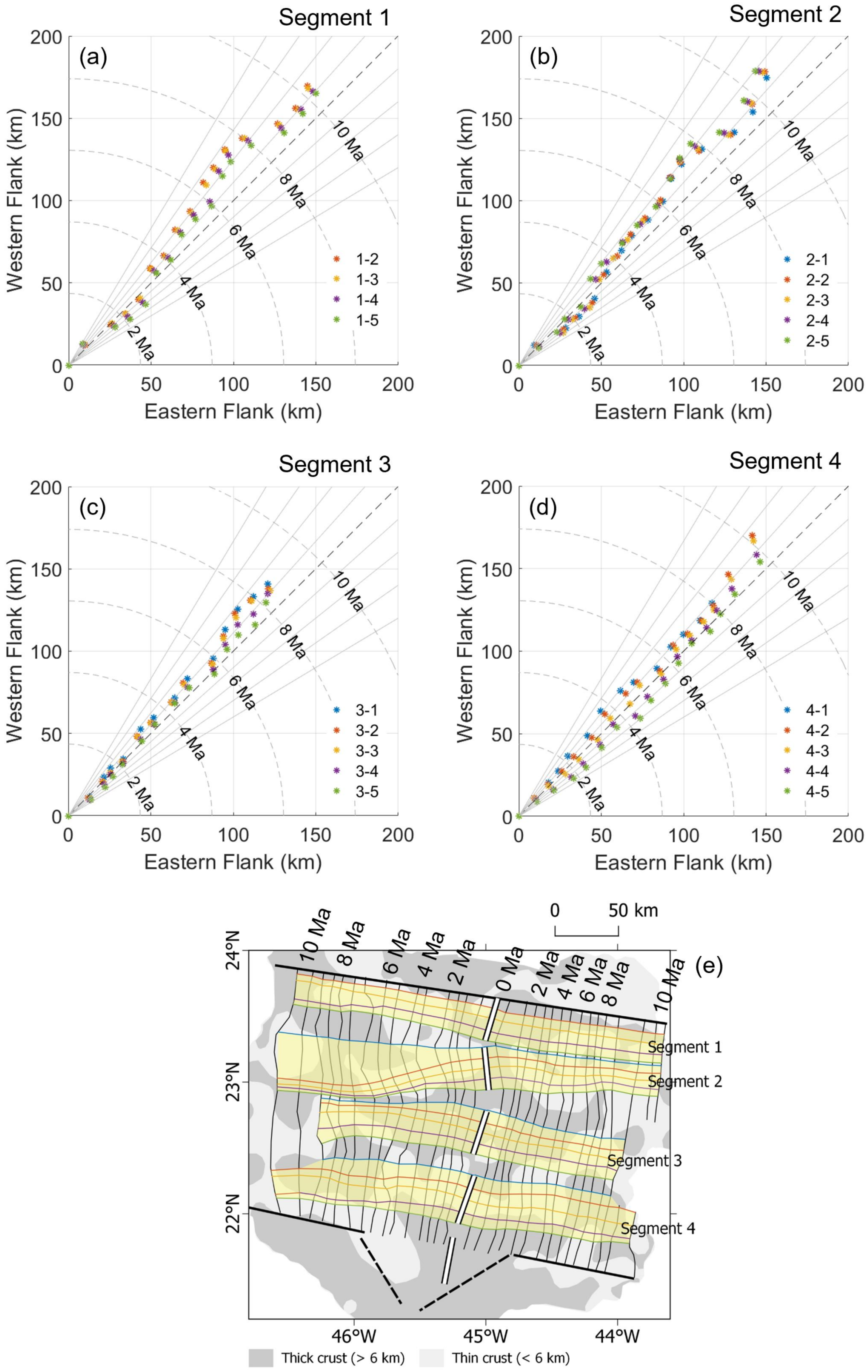

Figure 3.26: Distance ratio between each magnetic chron in the western flank and the eastern flank. The distance ratio depicts the symmetricity of each segment through time. (a) At Segment 1. In this segment, only four flowline sections are created and observed. (b) At Segment 2. (c) At Segment 3. (d) At Segment 4. (e) Index map. In general, we can see that Segment 4 experienced the most symmetrical spreading compared to the other segments.

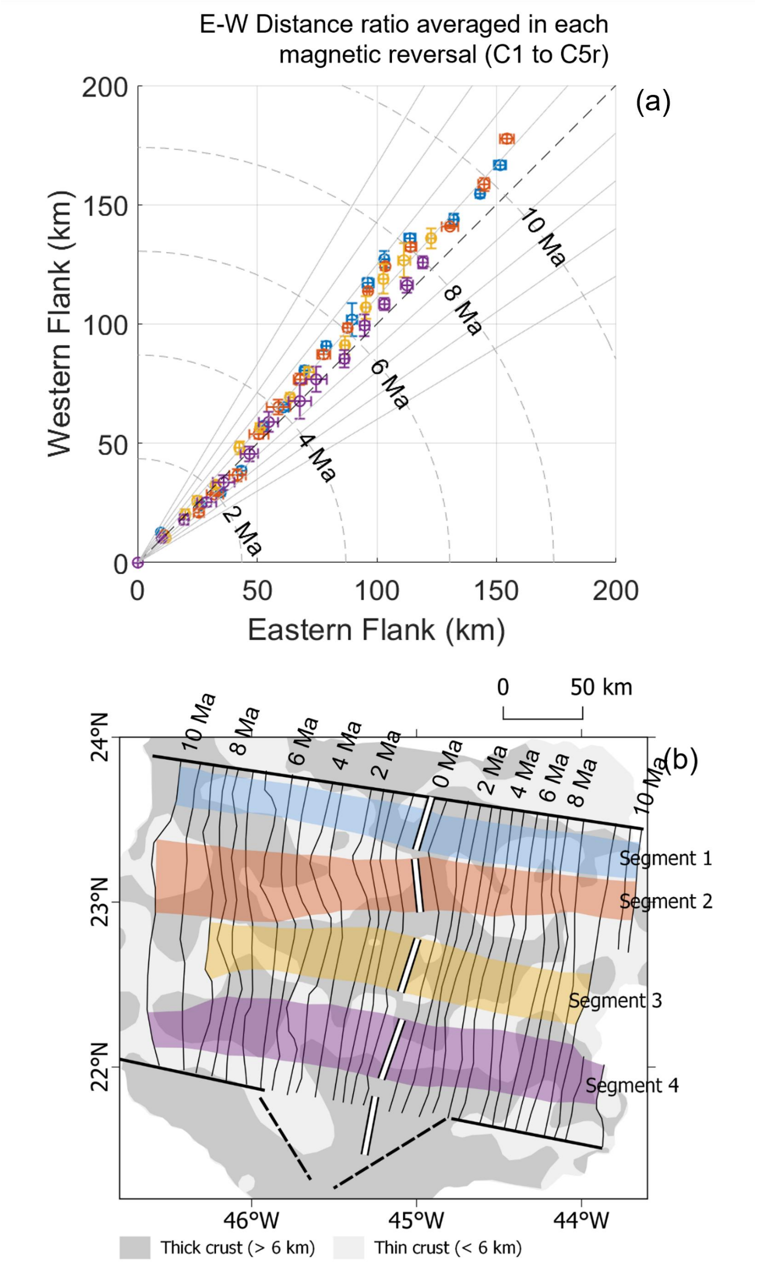

Figure 3.27: (a) Average distance ratio between each magnetic chron in the western flank and the eastern flank. The 'whiskers' depict standard deviation of the mean distances in the western and eastern flanks. In general, the southernmost segment (Segment 4) experienced the most symmetrical spreading through time compared to the other segments. At the oldest magnetic chron (C5r: 10.94 Ma), Segment 2 spreads the faster towards the western flank, before being replaced by Segment 1 at around 8 Ma. At around 3 Ma, Segment 3 became the fastest segment that spreads towards the western flank. (b) Index map.

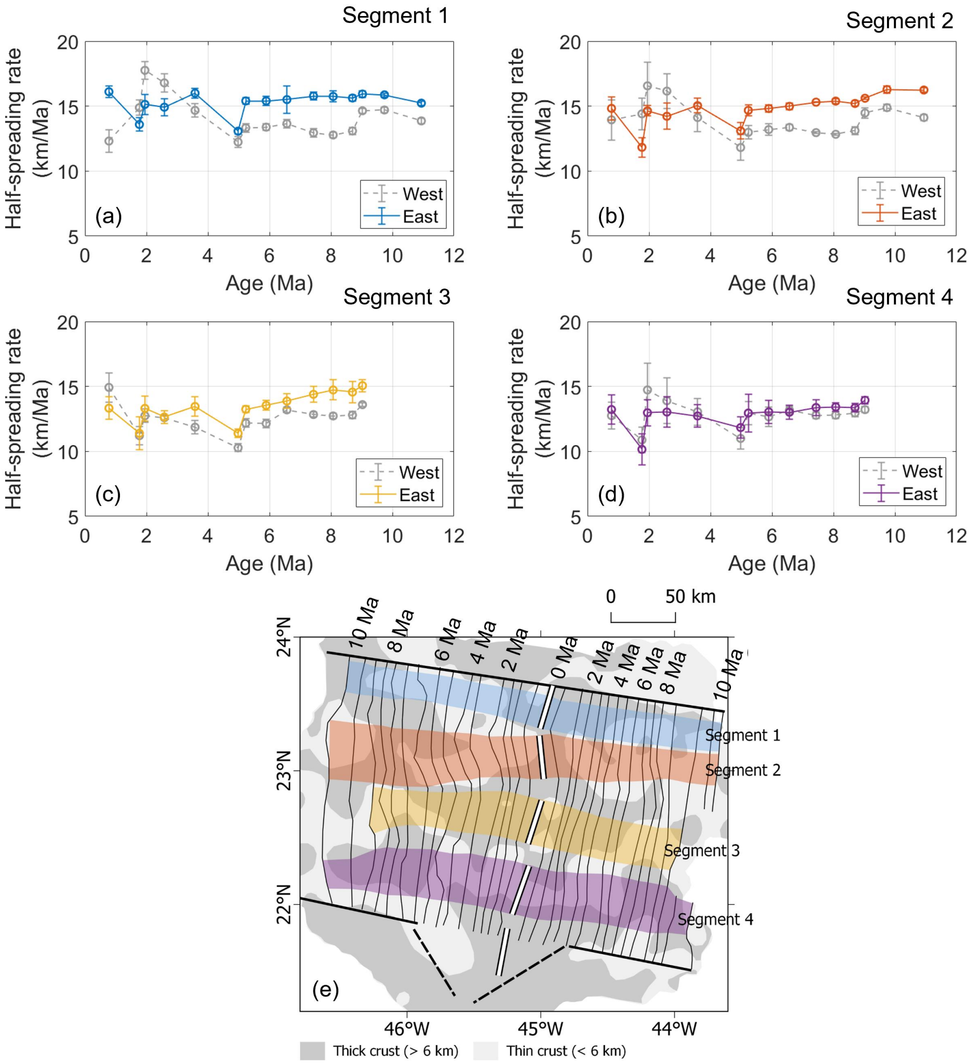

Figure 3.28: Evolution of average half-spreading rates at each segment along with its uncertainty bounds plotted as 'whiskers'. (a) Segment 1. (b) Segment 2. (c) Segment 3. (d) Segment 4. (e) Index map. In general, we can see that the southernmost segment (Segment 4) spreads the slowest compared to the other segments. Segment 1, 2, and 3 are generally spreading faster towards the western flank compared to the eastern flank, while Segment 4 experienced the most symmetrical spreading through time. Uncertainty bounds are relatively larger at the younger ages (from 2.58 Ma to the youngest observable chron, 0.78 Ma) of Segment 2 and 4.

3.5.2 Evolution of crustal thickness

To examine the evolution of crustal thickness, I sampled the bathymetry, computed depth to Moho, and the resulting crustal thickness along the flowlines of Section 1-3, 2-3, 3-4, 4-1, and 4-5. The five flowlines are chosen as they represent various tectonic styles over time. OCCs are found in Section 1-3, 3-4, 4-1, and at the older crust of Section 4-5, while a thick magmetic crust is found at Section 2-3 (Figure 3.28).

At Section 1-3, we can observe that at the oldest age (C5r: 10.94 Ma), the crust is thicker at the western flank compared to the eastern flank (Figure 3.28a and b). The thick crust at the western flank experienced thinning up to around 3 Ma (from ~7 km to ~4 km), while the crust at the eastern flank remained constant up to around 5 Ma before it was thickened up to present (from ~6 km to ~ 8 km). At the bathymetry and Moho plots, we can observe a bathymetric high which lies relatively close to the Moho (< 6 km). This observation indicates the presence of an OCC, supported by the presence of thin crust. We can compare this observation with the crustal thickness ratio plot in Figure 3.29a. At the oldest age, we can see that the crust is thicker at the western side (~7 km compared to ~6 km). After around 9.025 Ma (C4Ar), the crust tends to be formed thinner at the western side.

A much different morphology is observed in Section 2-3, where an approximately consistent 6 km crust was formed at the oldest age (C5r: 10.94 Ma) to around 2 Ma (Figure 3.28c and d). At 2 Ma, the crust experienced a slight thinning before forming a deep Moho at around 1 Ma, which indicates that the crust is getting thicker up to around 7.5 km. This slight thinning and the thickening that follows can also be observed in Figure 3.29b. From the figure, we can see that the thinning and thickening are not as symmetrical as expected. For instance, we can observe a thick crust (~7.25 km) at the eastern flank just before the present (C1r: 0.78 Ma) which is paired with a thin crust (~ 5.25 km) at the western flank. However, this observation might occur due to the misinterpretation of the ridge axis.

In Section 3-4, we can see that the crust is generally getting thicker from the oldest age (C4Ar: 9.025 Ma) up to around 2 Ma (Figure 3.28e and f). Afterwards, the eastern flank experienced thinning, which is also indicated by a bathymetric high underlied with a shallow Moho. Hence, we can interpret this bathymetric high as an OCC. The evolution of this section can be seen in Figure 3.29c, where the crustal thickness is relatively symmetric up to around 2.581 Ma, then becomes thicker at the western flank.

A unique morphology and Moho depth is observed in Section 4-1, where a shallow Moho is observed at around 5 Ma at both the eastern and western flank, and around 2 Ma at the western flank (Figure 3.28g). As the shallow Moho at around 5 Ma is not overlain by a bathymetric high, we can interpret these features as thin crust formed as an effect of the non-transform discontinuity instead of OCCs. Hence, the thin crust found at around 2 Ma at the western flank which is overlaid with a bathymetric high can be interpreted as an OCC. We can see a fluctuation of thinning and thickening overtime at this section, in which the thickest crust (∼7 km) is formed at the present age (Figure 3.28h). This fluctuation can also be observed at the crustal thickness ratio plot (Figure 3.29d), where the crustal thickness was approximately symmetrical at the oldest age (10.94 Ma), experienced asymmetrical thinning and thickening through time with the variation of around 4.5-7.1 km until it became symmetrical at the youngest ages.

Finally, in Section 4-5 we observe another fluctuation in thinning and thickening of the crust at the oldest ages (C5r: 10.94 Ma) up to around 5 Ma (Figure 3.28i and j). After 5 Ma, the crustal thickness tends to be consistent at both flanks (∼7 km) with a slight thickening at around 2 Ma at the eastern flank. In the crustal thickness ratio plot (Figure 3.29e), we can observe that the crust at this section is consistently thicker at the eastern side compared to the western side. This phenomenon mirrors what we have observed in Section 1-3, specifically from around 9.025 Ma up to the present. Looking at the general tectonic setting of the spreading segments, we can see that the eastern flanks at both Segment 1 and 4 are formed as the outside corner of the spreading axis, while the western flanks are formed as the inside corner. This explains the presence of a generally thicker crust at the eastern flank compared to the western flank at these two northernmost and southernmost segments.

Having the knowledge of the evolution of the crustal thickness, we can then observe the evolution of the tectonic style by examining the spreading mode classification through time.

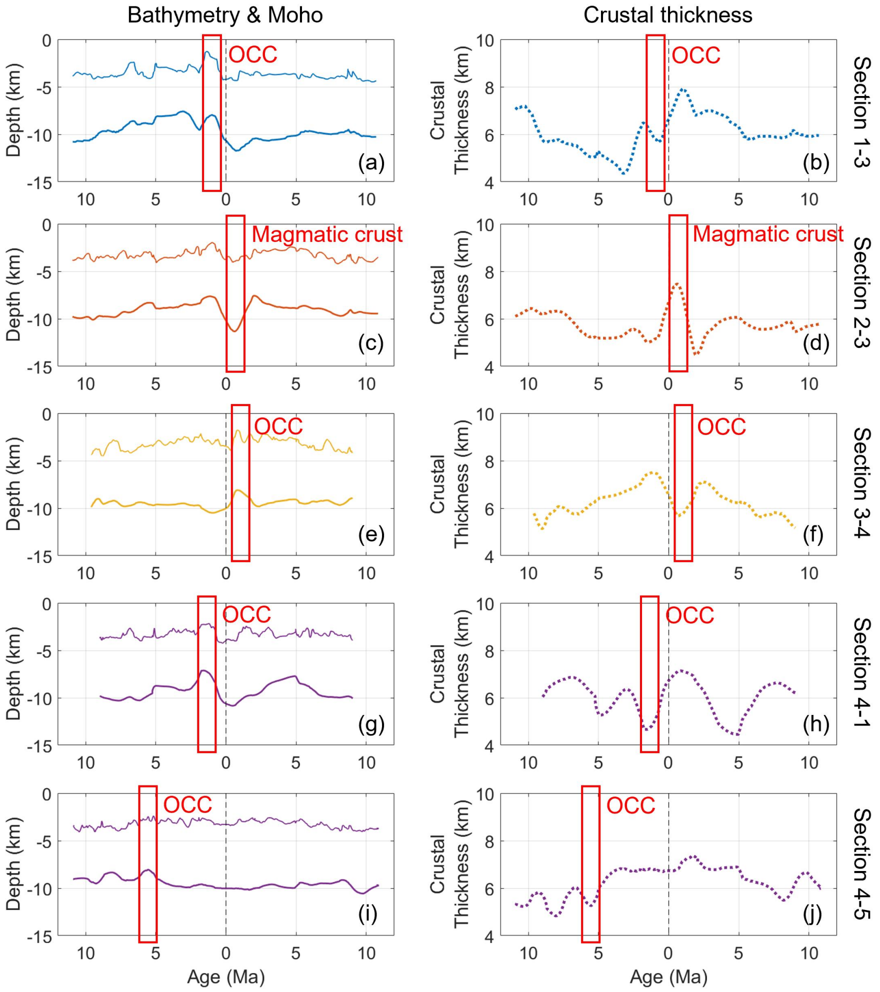

Figure 3.29: Bathymetry, depth to Moho, and crustal thickness variation profiles along selected flowlines. Elevated morphology underlied with elevated Moho is found at the youngest crust of the western flank at Section 1-3 (a and b), depicting the presence of OCC. In Section 2-3 (c and d), bathymetric low underlied with deep Moho is found at the youngest crust of the eastern flank, depicting the presence of a highly magmatic and thick crust. Similar morphology to what is observed at the western flank of Section 1-3 is found at the eastern flank of Section 3-4 (e to g), depicting the presence of OCC. Another OCC is observed at the western flank of the older crust of Section 4-5.

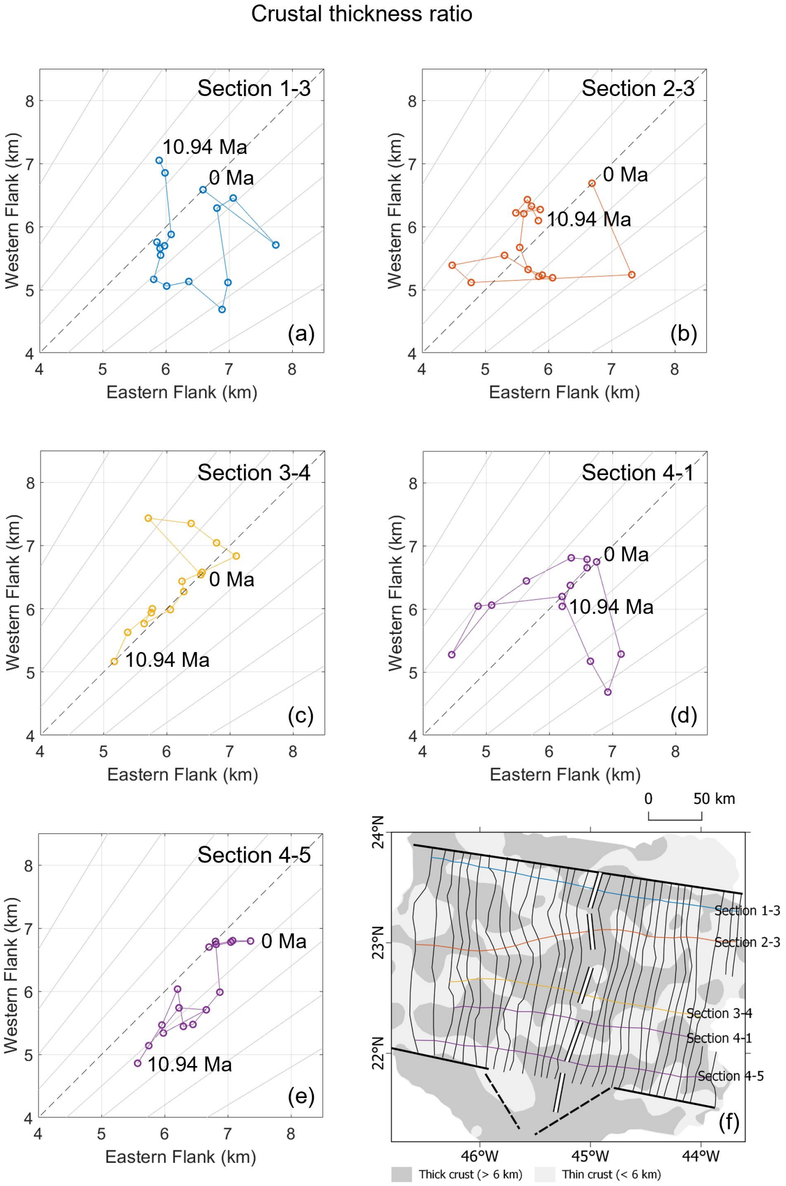

Figure 3.30: Crustal thickness ratio along selected flowlines. Highly asymmetric crust is found in Section 1-3 (a), where thicker crust dominates the eastern flank. A more identical crustal thickness is found in Section 2-3 up to around 1.77 Ma (b) and in Section 3-4 up to 2.58 Ma (c). After 1.77 Ma, thicker crust is formed at the eastern flank of Section 2-3, as well as the western flank of Section 3-4 after 2.58 Ma. The crustal thickness ratio varies along Section 4-1 through time (d), while a similar trend as observed in Section 1-3 is found at Section 4-5 (e) where thicker crust dominates the eastern flank.

3.5.3 Evolution of tectonic style

The evolution of tectonic style in the study area can be observed by comparing the SWE map to the crustal thickness map, interpreted tectonic fabric, and T-wave seismicity (Figure 3.31). From the figure, we can observe that in general, areas defined as tectonic terrain by the SWE are areas defined as thin crust by the gravity computation. T-wave seismicity is also present over these areas. On the other hand, areas defined as magmatic terrain are areas defined as thick crust by the gravity computation, with less to no presence of T-wave seismicity.

To examine the evolution of tectonic style in each spreading segment, I sampled the SWE along the same flowlines as in 3.5.4 and compare them with the sampled crustal thickness along those flowlines (Figure 3.32). The sampled SWE values are smoothened using a Gaussian filter to enable an easier cross-profile interpretation of each flow line.

In Section 1-3, we can see a fluctuation of the SWE value at the western flank from the oldest age to present (Figure 3.32a and b). The highest SWE value is found at the eastern flank, at an approximately similar location as the thickest crust. The OCC is indicated as low SWE value ($\sim$0.5), though not the lowest at the western flank. A similar fluctuation is found at the western flank of Section 2-3, with less fluctuation at the eastern flank (Figure 3.32c). The SWE value experienced a decrease from the oldest age up to around 2 Ma, where the SWE value became more similar to those found at the eastern flank. It is interesting to observe that the eastern flank is indicated by the SWE algorithm as highly magmatic crust, while the crustal thickness is quite consistent at around 6 km at this flank (Figure 3.32d).

A much different trend is observed at Section 3-4 (Figure 3.32e and f). We can see a general increase of the SWE value from the oldest age up to around 1 Ma, which is similar to the thickening observed in the sampled crustal thickness. After around 1 Ma, the eastern flank experienced a crustal thinning, which is also observed by the SWE as a relatively low value indicating a more tectonic terrain. Extremely low SWE values ($<$0.5) are found at both Section 4-1 and 4-5 over the indicated OCCs (Figure 3.32g and 3.32i).

To further observe the relation between the SWE classification with the crustal thickness classification derived from gravity signatures, I carried out a simple spatial relation between the two maps using the matrix defined in Table 3.7 Areas with low SWE values ($<$0.68) with thin crust ($<$6 km) are defined as tectonic terrain, while areas with high SWE values ($>$0.80) with thick crust ($>$6 km) are defined as magmatic terrain. In between these extremes, areas defined as extended terrain ($0.68 < \text{SWE} < 0.80$) with thin crust are defined as extended-tectonic terrain, while areas defined as extended terrain ($0.68 < \text{SWE} < 0.80$) with thick crust are defined as extended-magmatic terrain. Outside of these four classes, the terrain is defined as 'not-a-number' or 'NaN' to avoid misinterpretation.

Table 3.7: Comparative matrix between SWE-derived terrain classification and gravity-derived crustal thickness variation

		SWE		
		< 0.68	0.68-0.80	> 0.80
Crustal thickness	< 6 km	Tectonic terrain	Extended-tectonic terrain	NaN
	> 6 km	NaN	Extended-magmatic terrain	Magmatic terrain

The results can be seen in Figure 3.33. Although there are still around 10-15% of the terrain that are defined as NaN, we can see that the majority of the tectonic terrain are defined where the crust is thinner and the majority of the magmatic terrain are defined where the crust is thicker. Having the terrain types defined, we can now compare the symmetricity of the spreading through time following the five flowlines (Figure 3.34). The terrain types are indicated as magmatic terrain (MT), extended-magmatic terrain (EM), extended-tectonic terrain (ET), and tectonic terrain (TE). The terrain types comparison plots the types of terrain along each section at both flanks.

In Section 1-3 (Figure 3.34a), specifically from around 10 Ma to 8 Ma, we can see that the eastern flank tend to have magmatic spreading (MT and EM) while the eastern flank tend to have a more tectonic spreading (ET and TE). We can define this phenomenon as an example of highly asymmetric spreading. In contrast, the terrain became more symmetrical up to around 4 Ma, where both flanks experienced a more tectonic spreading (ET and TE). The asymmetricity reoccur from around 4 Ma to around 0.5 Ma.

In Section 2-3 (Figure 3.34b), the highly asymmetric spreading occurred from the oldest age up to around 7 Ma, where the eastern flank experienced a more tectonic spreading while the western flank experienced a more magmatic spreading. Between 7 and 5 Ma, both flanks experienced a more tectonic spreading, which might represent the presence of the non-transform discontinuity. Between 5 and 4 Ma, we can see that the western flank experienced a more tectonic spreading while the eastern flank experienced a slightly tectonic spreading. I define this phenomenon as slightly asymmetric spreading. The spreading became symmetrical between 4 and 2 Ma, with both flanks experienced a more tectonic spreading before it finally experienced a slightly asymmetric spreading up to the present.

Compared to Section 1-3 and 2-3, Section 3-4 experienced the most symmetrical spreading through time, where both flanks experienced tectonic spreading from around 9 to 6 Ma followed by magmatic spreading from around 6 to 2 Ma (Figure 3.34c). Similar to what is found at Section 2-3, the tectonic terrain represents the presence of non-transform discontinuity. Asymmetric spreading only occurred slightly after 2 Ma up to the present, resulting in the forming of an OCC at the eastern flank, where the crust experienced a more tectonic spreading.

Section 4-1 also experienced an approximately symmetrical spreading through time, where both flanks experienced magmatic spreading from around 9 to 5 Ma followed by tectonic spreading from around 5 to 3 Ma (Figure 3.34d). The tectonic terrain also represents the presence of a non-transform discontinuity. Asymmetric spreading occurred slightly after 3 Ma up to the present, resulting in the forming of an OCC at the western flank, where the crust experienced a more tectonic spreading.

A unique evolution is observed in Section 4-5, where the crust was spreading asymmetrically at the oldest age up to around 8.5 Ma, where tectonic spreading occurred at the western flank and magmatic spreading occurred at the eastern flank (Figure 3.34e). Symmetrical tectonic spreading occurred from around 8.5 to 7.5 Ma, depicting the presence of the non-transform discontinuity. The asymmetric spreading reoccur from around 7.5 to 4.5 Ma, where tectonic spreading occurred at the western flank and magmatic spreading occurred at the eastern flank. Finally, a symmetrical magmatic spreading occurred from 4.5 Ma up to the present, indicating the forming of a neovolcanic zone. Comparing the phenomenon to the classification map (Figure 3.34f), we can see that the neovolcanic zone propagates to the south.

3.6 Discussions: Asymmetric spreading over 10 Ma

3.6.1 Regional magmatic and tectonic setting

Based on general observation of the shipboard multibeam bathymetry, we can infer that the study area experienced a complex history of magmatism and tectonism. For instance, the tips of the western flank of the whole study area are formed as inside corners, resulting in thinner crust compared to the opposing flank. Within this thinner crust, we can observe a more irregularly faulted morphology with a lot less lineated topography, while ridge parallel topography and faults are a lot more commonly found at the outside corners (Figure 3.31b). Irregular morphology is only found at areas defined as thin crust, specifically at non-transform discontinuities and the inside corners of the non-transform offset between the ridge axis segments. Crooked morphologies are common at the northern outside corner, indicating the active tectonic interaction between the seafloor spreading north and south of the Kane fracture zone. Following the direction of the crooked morphology, we can infer that the crust in the study area spreads faster compared to the crust north of the Kane fracture zone. This crooked morphology is not found at the southern outside corner, indicating less to no tectonic interaction between the crust in the study area and south of the southern fracture zone.

Crooked morphology with similar direction is also common at the western flank, specifically south of the thin crust area created by Segment 1 and Segment 2. In general, we can also observe that the western flank spreads faster than the eastern flank. The crooked morphology might indicate that the northernmost part of the study area was spreading faster than the middle segments. As commonly found at the eastern flank, ridge parallel topography and faults are prominent in areas indicated as having thick crust.

From the crustal thickness map, we can observe two loci of high volcanic activities. One locus was constructed in the middle of the whole segments, forming the rhomb-shaped thick crust area. Observing the pattern constructed from around 5 Ma to the present, we can interpret that Segment 3 might be formed as a neo-volcanic zone, creating the rhomb-shaped thick crust in the middle of the segment as well as ridge-parallel faults and morphology. At around 2 Ma, the segment produced less melt, which allows the forming of an OCC at its western flank, followed by another forming of OCC at its eastern flank. Another locus is observed at the southernmost part of the study area. Observing the V-shaped feature which cuts off the southern fracture zone (Figure 3.31a) and a ‘band’ of tectonic thin crust at its west, the southernmost ridge axis might be formed as a neovolcanic zone at around 5 Ma, together with the neovolcanic zone at the middle of the study area. The neovolcanic zone formed a younger, thicker crust, propagated to the south, and finally cutting off the former southern fracture zone. This propagation, coupled with the westward crustal spreading, might cause the ‘band’ of tectonic thin crust to form.

Each of the four segments bounded by the Kane and southern fracture zones formed areas of non-transform discontinuities, where thin crust formed as a result of lower melt at the tip of each ridge segment. Non-transform discontinuity is prominent between Segment 1 and 2. We can also observe a non-transform discontinuity between Segment 3 and 4, which might now be propagated to the south and now located at Segment 4. Up to around 5 Ma, thin crust was formed continuously at the western flank of Segment 1, specifically those located the closest to the transform fault. This also occurred at the similar time at the western flank of Segment 4. Although the outside corner crust, has been formed generally thicker than those in the inside corner, several areas are still formed as thin crust. Observing the faulting and topographical pattern, most of the thin crust regions at the outside corners are not formed the way an OCC is supposed to be formed. Instead, they mostly represent the presence of non-transform discontinuities.

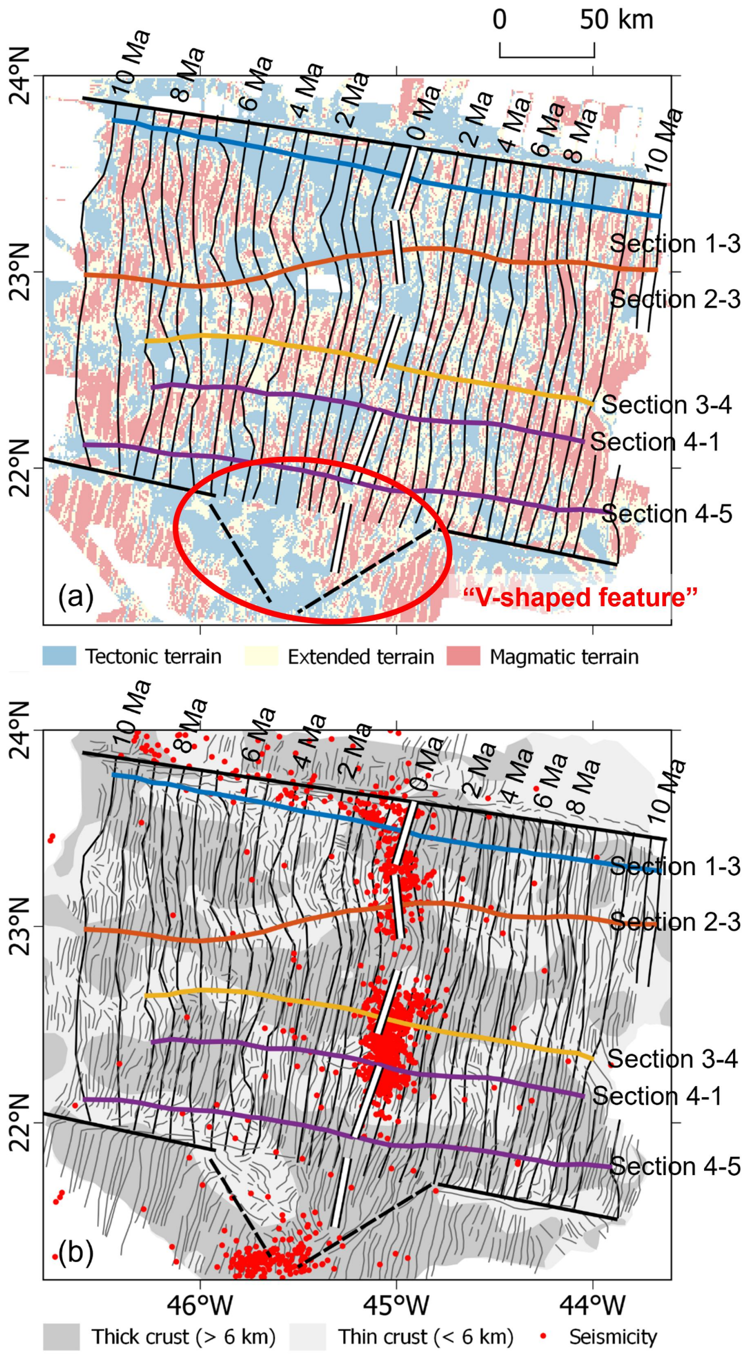

Figure 3.31: Regional tectonic setting and variation of crustal thickness in the study area. (a) Terrain classification resulted from employing the SWE technique to the shipboard multibeam bathymetry. Thin crust are found at the western flank, specifically at the northernmost and southernmost tips of the spreading axes. (b) Crustal thickness variation overlaid by tectonic fabric interpreted from the shipboard multibeam bathymetry and T-wave seismicity of Smith *et al.* (2003).

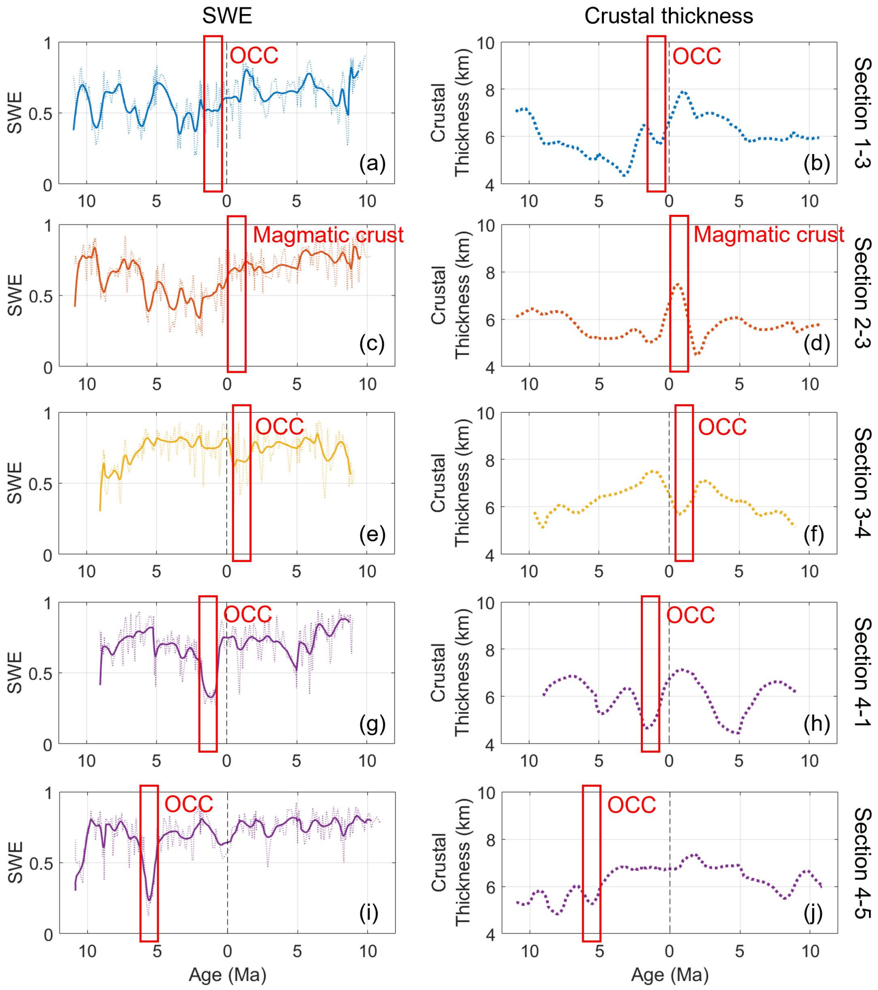

Figure 3.32: Gaussian-filtered SWE and crustal thickness variation profiles along selected flowlines. OCCs and magmatic crust at Section 1-3 and 2-3 cannot be not directly correlated to the crustal thickness (a to d), although the SWE numbers still match the general classification of tectonic and magmatic terrain. The relation between SWE number and crustal thickness are most prominent at the OCCs found in Section 3-4, 4-1, and 4-5, where strikingly low SWE number correlates well with low crustal thickness (e to j).

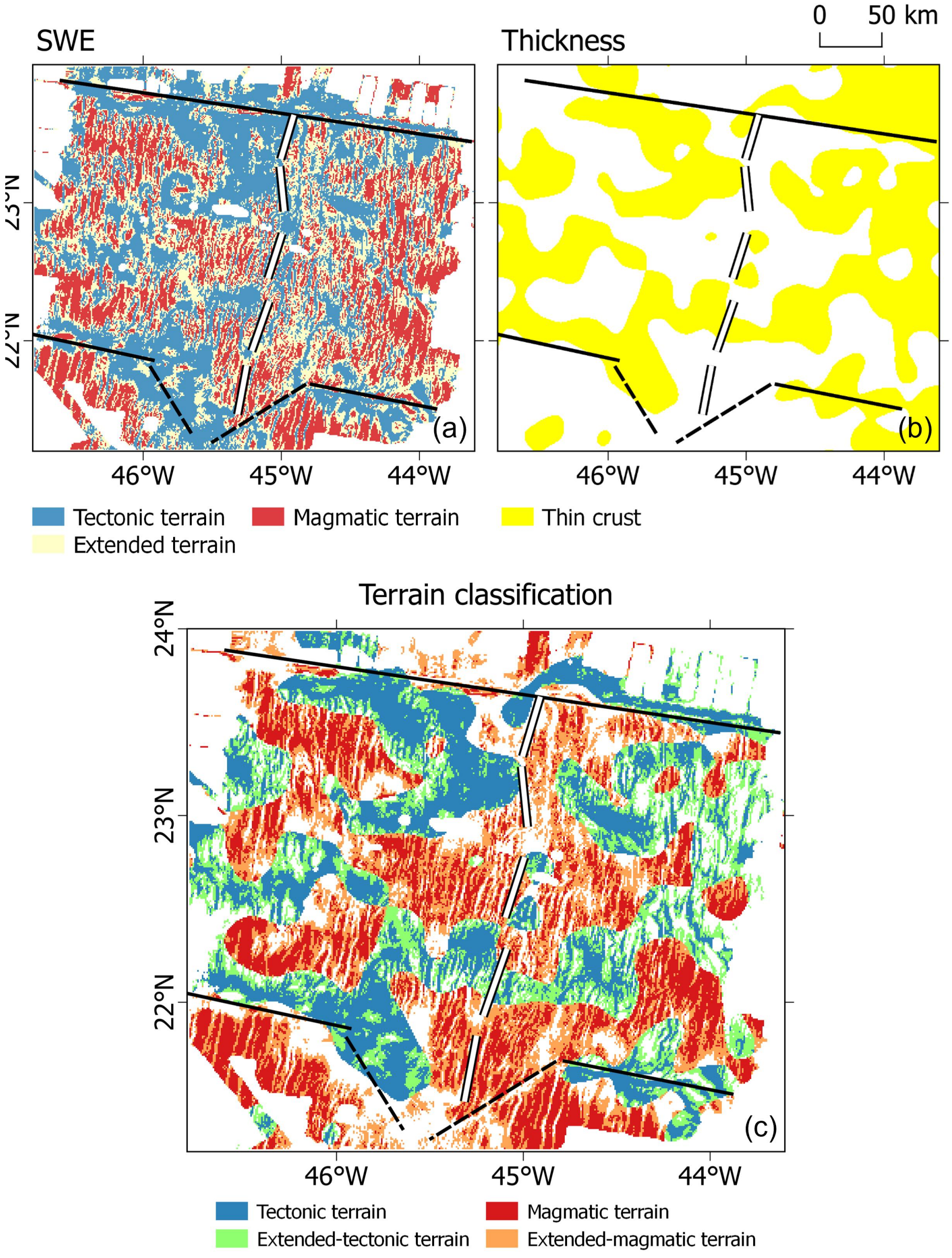

Figure 3.33: Compiling SWE-derived terrain classification (a) and gravity-derived crustal thickness variation (b). Based on these figures, most of the tectonic crust correlates well with thin crust. On the other hand, most of the magmatic crust also correlates well with thick crust. The terrain types are then classified into four types: tectonic terrain, extended-tectonic terrain, magmatic terrain, and extended-magmatic terrain (c).

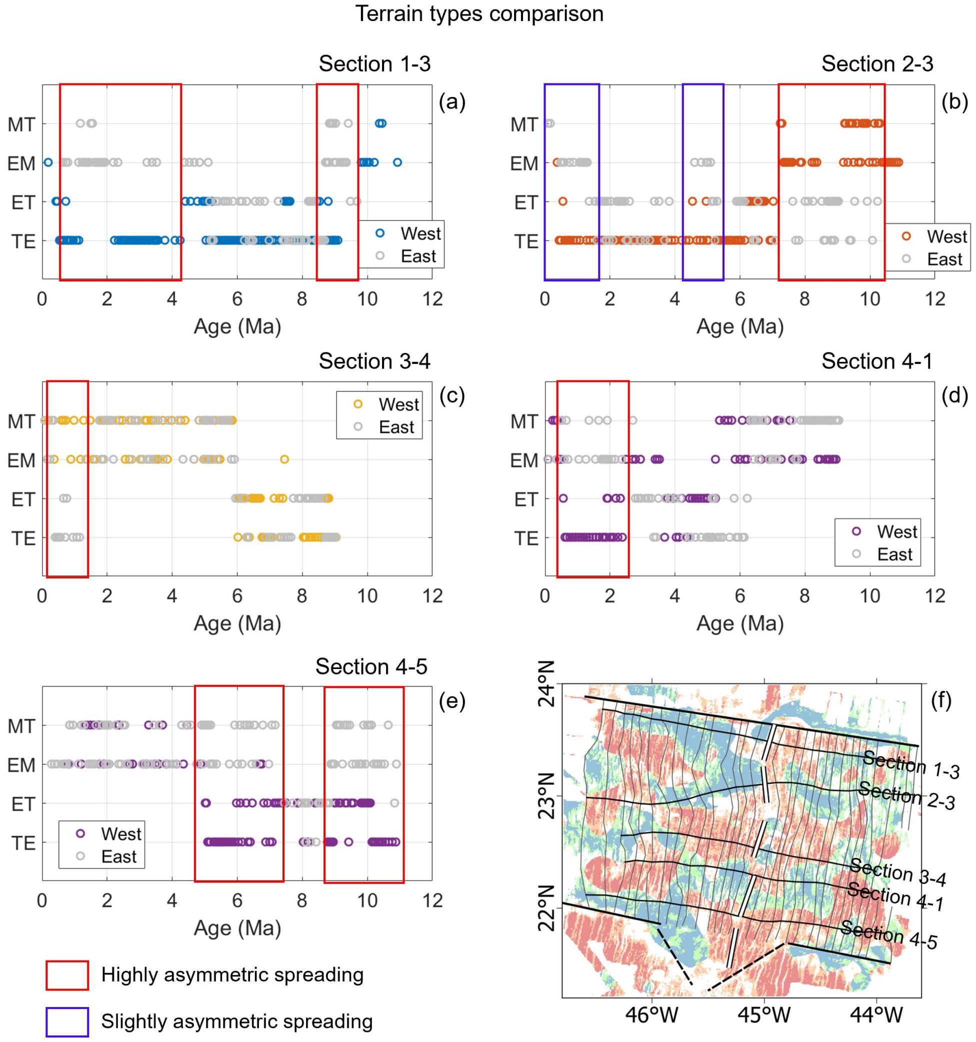

Figure 3.34: Terrain types comparison between the western and eastern flank. The terrain types are classified as magmatic terrain (MT), extended-magmatic terrain (EM), extended-tectonic terrain (ET), and tectonic terrain (ET). Highly asymmetric spreading is marked where magmatic terrain is observed at one flank and tectonic terrain is observed at the other flank (red rectangles), while slightly asymmetric spreading is marked where magmatic/extended-magmatic terrain is observed at one flank and tectonic/extended-tectonic terrain is observed at the other flank (blue rectangles). We can observe that Section 3-4 and 4-1 is dominated by a more identical terrain types through time (c and d), indicating the potential presence of symmetrical spreading.

3.6.2 Spreading mode evolution in relation to spreading rate

The magmatic and tectonic history of each segment can be explored by comparing the terrain classification resulted from bathymetric and gravity-derived analyses with the spreading rates computed from the interpreted magnetic reversals. In Segment 1, we can clearly see that tectonic terrain dominates the western flank of the ridge axis. This observation matches well with the spreading rate comparison, where the crust at the western flank generally spreads faster than those at the eastern flank. From around 9 to 5 Ma, the western flank spreads as much as twice as fast than the eastern flank. The faster spreading rate might relate to less magmatic emplacement coupled with blocky and irregularly faulted topography to accommodate the newly formed crust. These factors might induce the formation of several OCCs found at the western flank of this ridge axis segment.

Based on what is observed in Figure 3.31b, the older crust of Segment 2 is composed of well-lineated morphology. However, we can see a difference in classification between the western and eastern segment of these older crust, where the western flank is composed of thicker crust than the eastern flank. This finding is quite anomalous if compared to the half-spreading rate of Figure 3.28b. The figure depicts a similar trend to the half-spreading rate comparison between the western and eastern flank of the Segment 1 ridge axis, while resulting in a different trend. Hence, the interpretation of this segment might need to be carried out more carefully to enable a more robust observation of this segment. This segment is quite unique as the western flank mostly crosses the northern part of the non-transform discontinuity created by the non-transform offset between Segment 1 and 2 ridge axes.

In Segment 3, the western flank still spreads relatively faster than the eastern flank, although with a lot less difference. The morphological trend is quite straightforward, where thin crust dominates both flanks at the older crust up to 6 Ma, depicting the presence of a non-transform discontinuity and replaced by thicker crust as a result of the newly formed neo-volcanic zone locus in the midde of this segment. Comparing the spreading rate to the resulting morphology, it is interesting to see that the slower spreading results in a more symmetrical morphology. At places with faster spreading rate (from around 9 to 5 Ma), tectonic spreading occurred at both flanks and a more magmatic spreading occurred when the half-spreading rate falls to around 14 km/Ma at the western flank and around 12.5 km/Ma at the eastern flank. A jump of half spreading rate just after 2 Ma results in an asymmetric spreading, where the western flank experienced a more magmatic spreading while the eastern flank experienced a more tectonic spreading. Around this time, an OCC is formed at the eastern flank of this spreading axis, which happens to be the inside corner of the non-transform offset between Segment 3 and 4.

Similar to what is observed in Segment 3, the spreading in Segment 4 also seems to be a lot more symmetrical compared to that observed in Segment 1 and 2. The oldest crust is composed of thicker crust with ridge parallel topography while the younger crust is predominantly thinner, with a more irregular topography. Most of these younger crusts can be interpreted as non-transform discontinuities. However, in contrast to the non-transform discontinuity created by the non-transform offset between Segment 1 and 2, this non-transform discontinuity seems to be created by the non-transform offset between Segment 3 and 4, but got propagated to the south as an effect of the strengthening of the neovolcanic zone of Segment 3. We can also observe that a prominent OCC was formed recently at the western inside corner of the non-transform offset between Segment 3 and 4. Comparing the observed morphology to the evolution of spreading rate, it is interesting to see that the average comparison between the half-spreading rate between the western and eastern flanks of this segment is the most identical compared to the other segments. The identical spreading rate supports the symmetrical spreading through time. At the northern tip of this segment, asymmetrical spreading was only found at the last 2 Ma, indicated by the forming of the western inside corner OCC. However, at the southern tip, asymmetrical spreading occurred twice. The first one occurred at the oldest crust up to around 8.5 Ma, with tectonic thin crust dominates the western flank of this segment. This phenomenon might be identical to what was occurring at Segment 1, where both of these segments were affected by the tectonic forces occurring at inside corners. Another asymmetrical spreading occurred at around 7.5 to 4.5 Ma, which also results in thin tectonic crust at the western flank. In contrast to the northern tip of this segment, symmetrical magmatic spreading occurred at this tip from around 4.5 Ma to the present, resulting in thicker crust.

From the comparison between the evolution of spreading rate and the resulting crustal thickness and morphology, I can infer that slower spreading rates tend to result in thicker magmatic crust in a slow-spreading environment. Faster spreading might occur due to the tectonic forces acting on the crust, compensating for a lower magmatic emplacement. This observation is interesting as in general, faster spreading normally relates to a more magmatic emplacement, resulting in thicker crust as in the East Pacific Rise. Within a slow-spreading environment, as in the Mid-Atlantic Ridge, faster spreading is apparently induced by a more tectonic type of spreading, marked by thinner crust and emplacement of lower crust and upper mantle rocks in the form of OCCs.

3.7 Conclusions

Asymmetric spreading at MARK 21-24° N Atlantic can be observed from the available shipboard multibeam bathymetry, gravity, and magnetic anomaly data sets. The SWE technique developed in Chapter 2 was applied to the shipboard multibeam bathymetry to obtain the spreading mode classification in the study area, coupled with the tracing of tectonic fabric indicated by applying the Laplacian filters to the bathymetry. Multiple gravity and magnetic surveys were collated to enable a thorough identification, specifically to identify the evolution of the half-spreading rate at both flanks by tracing the apparent geomagnetic polarity reversals and to compute the variation of crustal thickness from the gravity anomaly.

The magnetic reversals were picked after applying RTP to the compiled dataset, ensuring that the signatures are centred over the causative source. The crustal thickness is inferred from the isostatic mantle Bouguer anomaly, or IMBA, computed by removing the water-crust from the bathymetry, followed by removing the crust-mantle interaction at 6 km below the crust as well as removing the potential lithospheric-asthenospheric mantle interaction, also derived from the bathymetry. Hence, the remaining signature represents the crustal thickness variation in the study area. The depth to Moho computed from this remaining signature correlates well with the depth to Moho inferred from five available OBS arrays.

In addition to the picked magnetic reversals and the modelled crustal thickness variation, seafloor lineaments are also interpreted from both gravity and magnetic anomaly data sets using the ACLAS technique. Based on the comparison between the interpreted lineaments and the SWE-classified terrain as well as the resulting crustal thickness variation, we can observe that far fewer lineaments are found at areas defined as tectonic or thin crust. Should lineaments be found at these tectonic or thin crust, their orientations are a lot more irregular compared to the ridge parallel lineaments found at magmatic or thick crust. This interpretation matches well with the resulting tectonic fabric interpreted from the shipboard multibeam bathymetry.

To observe the evolution of the whole study area, I divided up the area based on the four spreading axis segments bounded by the Kane and southern fracture zones. The evolution of spreading rate at each segment affected the forming of the NTDs and OCCs, as a response to the friction created by the different spreading rates at different time periods. Segment 1 experienced the most asymmetric spreading with the highest half-spreading rate at both flanks. Faster half-spreading rate at the western flank coincides with the forming of thinner crust, which is also indicated by the presence of irregular morphology. The thinner crust at the western flank might induce the forming of an OCC through detachment faulting while the eastern flank consistently forms thicker magmatic crust. Segment 2 is interpreted as the most oblique segment compared to the other segments. The flowlines at the western flank mostly follow the non-transform discontinuity formed by the non-transform offset between Segment 1 and 2. Compared to Segment 1 and 2, Segment 3 experienced a slower spreading at both of its flanks. The older crust seems to depict the formation of the southern non-transform offset, bounding the rhomb-shaped thick crust in the middle of this segment. This rhomb-shaped thick crust might be formed as a neo-volcanic zone at around 5 Ma, which experienced less melt at around 2 Ma, inducing the formation of an OCC at the eastern inside corner of the non-transform offset between Segment 3 and 4, followed by the formation of the latest OCC at the western inside corner of the same segments. Finally, Segment 4 represents two types of evolution. The northern tip of this segment mostly represents what Segment 3 also represents, which is mostly symmetrical spreading at both flanks, with variation of thickness depicting the presence of magmatic thick crust and non-transform discontinuities. In contrast, the older crust of the southern tip seems to depict a similar morphology to what is observed in Segment 1, where thinner crust was formed at the western flank compared to its opposing flank. The younger crust seems to depict the creation of a neovolcanic zone, propagating to the south, cutting the now inactive southern fracture zone.

This study reveals the relationship between the spreading modes, spreading rates, and crustal thickness derived from shipboard multibeam bathymetry, magnetic, and gravity data sets. High magmatism results in the creation of thick crust at both flanks of the ridge axis and commonly correlates with slower spreading rates. This is most prominent in the two loci located at the middle of the whole study area as well as at the southernmost segment. At the northernmost and southernmost tips, the spreading tends to become a lot more asymmetric, as tectonic extension is more likely to occur over the poorly accreted inside corners. The crust in the inside corner is commonly thinner, allowing detachment faults to form and exhume mantle rocks in the form of OCCs. It is interesting to see that these tectonic crusts are mostly evident where there is a faster spreading rate. This finding might enhance our current understanding of the magmatic and tectonic setting of slow-spreading ridges, which might differ to that commonly found at faster spreading ridges. Similar studies at other slow-spreading ridge segments, particularly in the Atlantic, might strengthen this observation and result in a more conclusive model of slow-spreading ridge morphology.

References

Aina, A. (1986). Reduction to equator, reduction to pole and orthogonal reduction of magnetic profiles. *Exploration Geophysics*, *17*(3), 141–145. 88

Allerton, S., Escartín, J., & Searle, R. C. (2000). Extremely asymmetric magmatic accretion of oceanic crust at the ends of slow-spreading ridge segments. *Geology*, *28*(2), 179–182. 84

Arkani-Hamed, J. (1988). Differential reduction-to-the-pole of regional magnetic anomalies. *Geophysics*, *53*(12), 1592–1600. 88

Baranov, V. (1957). A new method for interpretation of aeromagnetic maps: Pseudo-gravimetric anomalies. *Geophysics*, *22*(2), 359–382. 86, 88, 89

Biari, Y., Klingelhoefer, F., Sahabi, M., Funck, T., Benabdellouahed, M., Schnabel, M., Reichert, C., Gutscher, M.-A., Bronner, A., & Austin, J. (2017). Opening of the central Atlantic Ocean: Implications for geometric rifting and asymmetric initial seafloor spreading after continental breakup. *Tectonics*, *36*(6), 1129–1150. 84

Blackman, D. K., & Forsyth, D. W. (1991). Isostatic compensation of tectonic features of the Mid-Atlantic Ridge: 25–27° 30' S. *Journal of Geophysical Research: Solid Earth*, *96*(B7), 11741–11758. 113

Blackman, D. K., Karner, G. D., & Searle, R. C. (2008). Three-dimensional structure of oceanic core complexes: Effects on gravity signature and ridge flank morphology, Mid-Atlantic Ridge, 30 N. *Geochemistry, Geophysics, Geosystems*, *9*(6). 85

Blakely, R. J., & Simpson, R. W. (1986). Approximating edges of source bodies from magnetic or gravity anomalies. *Geophysics*, *51*(7), 1494–1498. 116

Breiner, S. (1973). *Applications manual for portable magnetometers*, vol. 395. Geometrics Sunnyvale, California. 87

Cann, J. R., Smith, D. K., Escartin, J., & Schouten, H. (2015). Tectonic evolution of 200 km of Mid-Atlantic Ridge over 10 million years: Interplay of volcanism and faulting. *Geochemistry, Geophysics, Geosystems*, *16*(7), 2303–2321. 84, 95, 101, 104, 105

Cannat, M. (1993). Emplacement of mantle rocks in the seafloor at mid-ocean ridges. *Journal of Geophysical Research: Solid Earth*, *98*(B3), 4163–4172. 84, 104

Cannat, M. (1996). How thick is the magmatic crust at slow spreading oceanic ridges? *Journal of Geophysical Research: Solid Earth*, *101*(B2), 2847–2857. 113

Cannat, M., Mevel, C., Maia, M., Deplus, C., Durand, C., Gente, P., Agrinier, P., Belarouchi, A., Dubuisson, G., Humler, E., *et al.* (1995). Thin crust, ultramafic exposures, and rugged faulting patterns at the Mid-Atlantic Ridge (22–24 N). *Geology*, *23*(1), 49–52. 84

Cascone, L., Green, C., Campbell, S., Salem, A., & Fairhead, D. (2017). ACLAS – A method to define geologically significant lineaments from potential-field data. *Geophysics*, *82*(4), G87–G100. 92

Chappell, A., & Kusznir, N. (2008). Three-dimensional gravity inversion for Moho depth at rifted continental margins incorporating a lithosphere thermal gravity anomaly correction. *Geophysical Journal International*, *174*(1), 1–13. 110

Christeson, G., Goff, J., & Reece, R. (2019). Synthesis of oceanic crustal structure from two-dimensional seismic profiles. *Reviews of Geophysics*, *57*(2), 504–529. 108

Cormier, M.-H., Detrick, R. S., & Purdy, G. M. (1984). Anomalously thin crust in oceanic fracture zones: New seismic constraints from the Kane fracture zone. *Journal of Geophysical Research: Solid Earth*, *89*(B12), 10249–10266. 96

Cormier, M.-H., & Sloan, H. (2019). Distinctive seafloor fabric produced near western versus eastern ridge-transform intersections of the northern Mid-Atlantic Ridge: Possible influence of ridge migration. *Geochemistry, Geophysics, Geosystems*, *20*(4), 1734–1755. 84

Dannowski, A., Grevemeyer, I., Phipps Morgan, J., Ranero, C. R., Maia, M., & Klein, G. (2011). Crustal structure of the propagating TAMMAR ridge segment on the Mid-Atlantic Ridge, 21.5° N. *Geochemistry, Geophysics, Geosystems*, *12*(7). 85, 96

Dannowski, A., Grevemeyer, I., Ranero, C. R., Ceuleneer, G., Maia, M., Morgan, J. P., & Gente, P. (2010). Seismic structure of an oceanic core complex at the Mid-Atlantic Ridge, 22 19' N. *Journal of Geophysical Research: Solid Earth*, *115*(B7). 85, 95, 96

Dannowski, A., Morgan, J. P., Grevemeyer, I., & Ranero, C. R. (2018). Enhanced mantle upwelling/melting caused segment propagation, oceanic core complex die off, and the death of a transform fault: The Mid-Atlantic Ridge at 21.5 n. *Journal of Geophysical Research: Solid Earth*, *123*(2), 941–956. 85, 95, 96

Detrick Jr, R. S., & Purdy, G. (1980). The crustal structure of the Kane fracture zone from seismic refraction studies. *Journal of Geophysical Research: Solid Earth*, *85*(B7), 3759–3777. 96

Dick, H. J., Tivey, M. A., & Tucholke, B. E. (2008). Plutonic foundation of a slow-spreading ridge segment: Oceanic core complex at Kane Megamullion, 23 30' N, 45 20' W. *Geochemistry, Geophysics, Geosystems*, *9*(5). 95

Escartín, J., & Cannat, M. (1999). Ultramafic exposures and the gravity signature of the lithosphere near the Fifteen-Twenty Fracture Zone (Mid-Atlantic Ridge, 14–16.5 N). *Earth and Planetary Science Letters*, *171*(3), 411–424. 85

Ewing, M., Carpenter, G., Windisch, C., & Ewing, J. (1973). Sediment distribution in the oceans: the Atlantic. *Geological Society of America Bulletin*, *84*(1), 71–88. 108

Fairhead, J. (2015). Generating a high-resolution global gravity model for oil exploration: Part 1 – Land data compilations. *The Leading Edge*, *34*(3), 326–330. 86, 88, 89

Gac, S., Tisseau, C., Dyment, J., & Goslin, J. (2006). Modelling the thermal evolution of slow-spreading ridge segments and their off-axis geophysical signature. *Geophysical Journal International*, *164*(2), 341–358. 84

Gente, P., Pockalny, R. A., Durand, C., Deplus, C., Maia, M., Ceuleneer, G., Mével, C., Cannat, M., & Laverne, C. (1995). Characteristics and evolution of the segmentation of the Mid-Atlantic Ridge between 20 N and 24 N during the last 10 million years. *Earth and Planetary Science Letters*, *129*(1-4), 55–71. 84, 96

Goff, J. A. (1991). A global and regional stochastic analysis of near-ridge abyssal hill morphology. *Journal of Geophysical Research: Solid Earth*, *96*(B13), 21713–21737. 108

Grant, F., & Dodds, J. (1972). MAGMAP FFT processing system development notes. *Paterson Grant and Watson Limited*, *230*. 88

Gunn, P. J. (1995). An algorithm for reduction to the pole that works at all magnetic latitudes. *Exploration Geophysics*, *26*(3), 247–254. 88

Heirtzler, J. R., & Le Pichon, X. (1965). Crustal structure of the mid-ocean ridges: 3. Magnetic anomalies over the Mid-Atlantic Ridge. *Journal of Geophysical Research*, *70*(16), 4013–4033. 90

Hinze, W. J., Von Frese, R. R., Von Frese, R., & Saad, A. H. (2013). *Gravity and magnetic exploration: Principles, practices, and applications*. Cambridge University Press. 87, 88

Kahle, R. L., Tilmann, F., & Grevemeyer, I. (2016). Crustal structure and kinematics of the TAMMAR propagating rift system on the Mid-Atlantic Ridge from seismic refraction and satellite altimetry gravity. *Geophysical Journal International*, *206*(2), 1382–1397. 85, 96

Kong, L. S., Detrick, R. S., Fox, P. J., Mayer, L. A., & Ryan, W. (1988). The morphology and tectonics of the MARK area from Sea Beam and Sea MARC I observations (Mid-Atlantic Ridge 23 N). *Marine Geophysical Researches*, *10*(1-2), 59. 84

Kuo, B.-Y., & Forsyth, D. W. (1988). Gravity anomalies of the ridge-transform system in the South Atlantic between 31 and 34.5 S: Upwelling centers and variations in crustal thickness. *Marine Geophysical Researches*, *10*(3-4), 205–232. 108, 110

Lin, J., Purdy, G., Schouten, H., Sempere, J., & Zervas, C. (1990). Evidence from gravity data for focused magmatic accretion along the Mid-Atlantic Ridge. *Nature*, *344*(6267), 627–632. 108

MacDonald, K. C. (1977). Near-bottom magnetic anomalies, asymmetric spreading, oblique spreading, and tectonics of the Mid-Atlantic Ridge near lat 37 N. *Geological Society of America Bulletin*, *88*(4), 541–555. 84

MacLeod, I., Vieira, S., & Chaves, A. (1993). Analytic signal and reduction-to-the-pole in the interpretation of total magnetic field data at low magnetic latitudes. In *3rd International Congress of the Brazilian Geophysical Society*, (pp. cp–324). European Association of Geoscientists & Engineers. 88

Maia, M., & Gente, P. (1998). Three-dimensional gravity and bathymetry analysis of the Mid-Atlantic Ridge between 20 N and 24 N: Flow geometry and temporal evolution of the segmentation. *Journal of Geophysical Research: Solid Earth*, *103*(B1), 951–974. 84, 85

Maus, S., Barckhausen, U., Berkenbosch, H., Bournas, N., Brozena, J., Childers, V., Dostaler, F., Fairhead, J. D., Finn, C., von Frese, R. R. B., Gaina, C., Golynsky, S., Kucks, R., Lühr, H., Milligan, P., Mogren, S., Müller, R. D., Olesen, O., Pilkington, M., Saltus, R., Schreckenberger, B., Thébault, E., & Caratori Tontini, F. (2009). EMAG2: A 2–arc min resolution Earth Magnetic Anomaly Grid compiled from satellite, airborne, and marine magnetic measurements. *Geochemistry, Geophysics, Geosystems*, *10*(8). 99, 100

Meyer, B., Saltus, R., & Chulliat, A. (2017). EMAG2 Version 3-Update of a two arc-minute global magnetic anomaly grid. In *EGU General Assembly Conference Abstracts*, (p. 10614). 99, 100

MGDS (1984). Multibeam Sonar Bathymetry Data collected aboard Robert D. Conrad (RC2511). NOAA National Centers for Environmental Information. 96

MGDS (1989). Multibeam Sonar Bathymetry Data collected aboard Robert D. Conrad (RC3001). NOAA National Centers for Environmental Information. 96

Miller, H. G., & Singh, V. (1994). Potential field tilt – A new concept for location of potential field sources. *Journal of applied Geophysics*, *32*(2-3), 213–217. 92

Morgan, J. P., & Forsyth, D. W. (1988). Three-dimensional flow and temperature perturbations due to a transform offset: Effects on oceanic crustal and upper mantle structure. *Journal of Geophysical Research: Solid Earth*, *93*(B4), 2955–2966. 85, 110

Mutter, J. C., & Karson, J. A. (1992). Structural processes at slow-spreading ridges. *Science*, *257*(5070), 627–634. 84

Okino, K., Matsuda, K., Christie, D. M., Nogi, Y., & Koizumi, K.-i. (2004). Development of oceanic detachment and asymmetric spreading at the Australian-Antarctic Discordance. *Geochemistry, Geophysics, Geosystems*, *5*(12). 84

Parker, R. (1973). The rapid calculation of potential anomalies. *Geophysical Journal International*, *31*(4), 447–455. 108

Purdy, G., & Detrick, R. S. (1986). Crustal structure of the Mid-Atlantic Ridge at 23° N from seismic refraction studies. *Journal of Geophysical Research: Solid Earth*, *91*(B3), 3739–3762. 96

Sandwell, D. T., Müller, R. D., Smith, W. H., Garcia, E., & Francis, R. (2014). New global marine gravity model from Cryosat-2 and Jason-1 reveals buried tectonic structure. *Science*, *346*(6205), 65–67. 98, 100

Schouten, H., Klitgord, K. D., & Whitehead, J. A. (1985). Segmentation of mid-ocean ridges. *Nature*, *317*(6034), 225–229. 84

Shaw, P. R., & Lin, J. (1993). Causes and consequences of variations in faulting style at the Mid-Atlantic Ridge. *Journal of Geophysical Research: Solid Earth*, *98*(B12), 21839–21851. 94

Smith, D. (2013). Mantle spread across the sea floor. *Nature Geoscience*, *6*(4), 247–248. 84

Smith, D. K., Escartin, J., Cannat, M., Tolstoy, M., Fox, C. G., Bohnenstiehl, D. R., & Bazin, S. (2003). Spatial and temporal distribution of seismicity along the northern Mid-Atlantic Ridge (15°–35° N). *Journal of Geophysical Research: Solid Earth*, *108*(B3). 95, 97, 101, 104, 138

Smith, D. K., Escartìn, J., Schouten, H., & Cann, J. R. (2008). Fault rotation and core complex formation: Significant processes in seafloor formation at slow-spreading mid-ocean ridges (Mid-Atlantic Ridge, 13-15 N). *Geochemistry, Geophysics, Geosystems*, *9*(3). 85

Smith, D. K., Tolstoy, M., Fox, C. G., Bohnenstiehl, D. R., Matsumoto, H., & J. Fowler, M. (2002). Hydroacoustic monitoring of seismicity at the slow-spreading Mid-Atlantic Ridge. *Geophysical Research Letters*, *29*(11), 13–1. 95

Swain, C. J. (2000). Reduction-to-the-pole of regional magnetic data with variable field direction, and its stabilisation at low inclinations. *Exploration Geophysics*, *31*(2), 78–83. 88

Tauxe, L. (1998). Magnetostratigraphy of Upper Paleocene-Lower Eocene Marine and Terrestrial Sequences. *Late Paleocene-Early Eocene Climatic and Biotic Events in the Marine and Terrestrial Records*, (p. 67). 89

Turcotte, D. L., & Schubert, G. (2002). *Geodynamics*. Cambridge university press. 110

Verduzco, B., Fairhead, J. D., Green, C. M., & MacKenzie, C. (2004). New insights into magnetic derivatives for structural mapping. *The leading edge*, *23*(2), 116–119. 92

Vine, F. J. (1966). Spreading of the ocean floor: New evidence. *Science*, *154*(3755), 1405–1415. 90, 106

Vine, F. J., & Matthews, D. H. (1963). Magnetic anomalies over oceanic ridges. *Nature*, *199*(4897), 947–949. 89

Walker, J. D., Geissman, J., Bowring, S., & Babcock, L. (2013). The Geological Society of America geologic time scale. *Bulletin*, *125*(3-4), 259–272. 106, 107

Wessel, P. (2001). Global distribution of seamounts inferred from gridded Geosat/ERS-1 altimetry. *Journal of Geophysical Research: Solid Earth*, *106*(B9), 19431–19441. 112

Whitehead, J. A., Dick, H. J., & Schouten, H. (1984). A mechanism for magmatic accretion under spreading centres. *Nature*, *312*(5990), 146–148. 84

Chapter 4

Basement structure classification based on gravity and magnetic observations over the Labrador Basin

Abstract

Basement structure classification at passive continental margins is key to understanding the crust-mantle interplay during lithospheric stretching, leading to full seafloor spreading. Studies have recognised at least two distinct types of spreading: (1) magmatic spreading, dominated by magmatic accretion over the freshly constructed oceanic crust, and; (2) tectonic spreading, dominated by tectonic extension, which results in varying modes of faulting and atypical oceanic crustal layers. However, the distinct morphology is not observable at passive continental margins, as most of these features have been buried by the sediments deposited from the continental crust. Therefore, gravity and magnetic data are selected as another identification tool as they correspond to specific physical properties of the basement, or the oceanic crust. In this chapter, I investigate the types of spreading recognized in the Labrador Basin by exploiting various gravity and magnetic derivative techniques, namely the automated coherency lineament analysis (ACLAS) technique, the pseudogravity of magnetic anomalies (PsGr-MA), and the finite local wavenumber (FLW) method to estimate the depth to the magnetic basement. I also employed the mantle Bouguer anomaly (MBA) technique to estimate the crustal thickness variation over the study area. Several of these techniques have been assessed in the previous chapter and yields results that would aid the crustal type characterisation. The results are consistent with previous published studies, where I indicate the presence of exhumed upper mantle rocks over a large area based on the thin crust derived from the MBA signatures. The finding support the theory that a large part of the Labrador Basin was emplaced by continuous tectonic extension as a response to the waning of the magma supply in an ultra-slow-spreading ridge.

4.1 Introduction

The Labrador Basin is part of the northwest (NW) Atlantic province (Abdelmalak *et al.*, 2019). Lithospheric stretching in the area started either in Early Cretaceous (Chalmers & Pulvertaft, 2001) or Late Jurassic time (Larsen *et al.*, 2009). The subsequent regional extension ended with a rift climax in Late Cretaceous/early Paleocene (Abdelmalak *et al.*, 2019), followed closely by full seafloor spreading (e.g., Chian *et al.*, 1995; Roest & Srivastava, 1989; Srivastava & Roest, 1999) which slowed down in Early Eocene at ∼48 Ma (Roest & Srivastava, 1989) and ceased in Oligocene time at ∼33 Ma (Hosseinpour *et al.*, 2013; Roest & Srivastava, 1989). During the full seafloor spreading stage, Abdelmalak *et al.* (2019) suggest that the majority of the volcanism in the NW Atlantic occurred between ∼62 and ∼58 Ma (Paleocene time), characterised by fast seafloor spreading with well-defined magnetic anomalies.

The subsequent decrease in spreading rate is related to the opening of the northeast (NE) Atlantic where the seafloor spreading distribution is divided between two spreading centres (Gaina *et al.*, 2009) and the waning of the magma supply in the Labrador Sea (Delescluse *et al.*, 2015). This decrease of spreading rate results in thinner than normal crustal thickness, where the volume of melt produced is restricted (Bown & White, 1994; Reid & Jackson, 1981), and enhanced exhumation and serpentinisation of the upper mantle rocks (Chian *et al.*, 1995). Seismic lines over the extinct ridge also indicate a tectonic extension of up to 70% compared to the waning magmatic accretion (Srivastava & Keen, 1995). The resulting overall crustal structure in this period is similar to active ultra-slow-spreading ridges like those found at the Southwest Indian Ridge (SWIR), with lower crustal velocities of 6.0-7.0 km/s (Delescluse *et al.*, 2015). Samples of serpentinised peridotites intruded by gabbro plutons are found in the vicinity of the active ultra-slow-spreading ridge axes of SWIR (Cannat, 1996). Finally, the fossil axial valley provides evidence of significant tectonic extension during the waning stage of the ridge axis (Delescluse *et al.*, 2015), which results in varying degrees of mantle serpentinisation resulting from various faulting and fluid circulation (Osler & Louden, 1995).

This study aims to classify the basement structure in the Labrador Basin based on available gravity and magnetic data. The classification is carried out mainly by computing the crustal thickness variation derived from processed gravity data, as well as observing the derivatives of both gravity and magnetic data resulting from various geophysical processing techniques. In this study, the main objective is to identify the presence of tectonic terrain that might host exhumed upper mantle rocks by detachment faulting, followed by the infiltration of seawater to the upper mantle rocks due to the insufficient melt supply at an ultraslow spreading ridge (e.g., Dick *et al.*, 2003). In addition, I also evaluate the performance of each technique and how far it could aid the basement structure classification, specifically in a sedimented and extinct slow- to ultra-slow-spreading ridge. The results of this study are compared with published and interpreted seismic profiles, both across and over the extinct spreading axis (Delescluse *et al.*, 2015) and across the basin from the hyperextended continental crust seaward to the extinct spreading ridge (Gouiza & Paton, 2019).

4.2 Fundamentals of geophysical data processing

In this chapter, I applied most of the geophysical data enhancement methods explained in Section 3.2 (e.g. reduction to pole of magnetic data, Gaussian filters, and various potential field derivatives). Methods that have been explained in the previous chapters will not be elaborated in this chapter. The section is divided into four subsections: transforms and filters, potential field derivatives, semi-automated lineament tracking, and tilt-depth.

For the moment, the slope-weighted eccentricity (SWE) technique developed in Chapter 2 is not ready to be applied to the available bathymetry, magnetic, and gravity data. The technique has only been tested on shipboard multibeam bathymetry data that reveals the morphology of the basement. Meanwhile, the bathymetry observed in the Labrador Basin represents the accummulated sediments over time, covering the extinct ridge axes. Applying the SWE technique to this type of bathymetry will return a much different result compared to what we have observed over an active spreading ridge, which has not been covered by sediments. Furthermore, application of this technique to available magnetic and gravity data requires a more careful assessment as these types of data represent a sum of physical variation observed from the top of the sediment layers down to the crust-mantle interaction. The technique has only been tested to represent what can be observed on the 'surface' instead of a sum of a multi-layered signatures.

4.2.1 Transforms and geological filters

The fundamental principles of several transforms and geological filters have been explained in 3.2.1, namely the reduction-to-pole (RTP) and the Gaussian filters. In addition to those techniques, I am applying the pseudogravity of the magnetic anomaly (PsGr-MA), which will be explained in this subsection.

Pseudo-gravity of the magnetic anomaly (PsGr-MA)

Similar to the application of RTP, pseudogravity is an operation used for magnetic data processing, assuming the fields of magnetisation are pointing to a similar direction. Hence, applying this transform to the oceanic crust needs to be followed by a careful interpretation process, as the magnetisation field alternates through its formation. In principle, pseudogravity is computed by exploiting Poisson's relation between magnetic and gravity signatures of an arbitrary volume based on the direction of magnetisation of the body (e.g., Baranov, 1957; Bott *et al.*, 1966). The magnetic inclination and declination are needed to correct the dipolar nature of the magnetic signature, thereby making sure that the effects are centred over the causative body. The resulting pseudogravity map can then later act as a proxy for density to susceptibility contrast ratio of the basement rock.

4.2.2 Potential field derivatives

The fundamental principle of several potential field derivatives has been explained in 3.2.2, namely the total horizontal derivative (THDR), vertical derivative (VDR), and the tilt derivative (TDR). In addition to those techniques, I am also applying the second vertical derivative (SVDR) and the local wavenumber K techniques, which will be explained in this subsection.

Second vertical derivative (SVDR)

The second vertical derivative is useful for both gravity and magnetic data processing. It is a second-order amplitude derivative of the field, which is useful in highlighting curvatures of the field, described as:

$$SVDR = \frac{\partial^2 T}{\partial z^2} \tag{4.1}$$

where T is the potential field and z is the vertical component. The second vertical derivative or the SVDR maps will reveal the nature of the gridded data, as the operation will generate maps that highlight small geological features as well as the line-spacing of the survey, interpolation method used, grid size, and overall data distribution. Hence, it is useful to separate the residual from the regional components as well as a qualitative metric to estimate the overall quality of the gridded data.

Local wavenumber K

Local wavenumber K is useful for both gravity and magnetic data processing. First reported by Thurston & Smith (1997), for profile data, the local wavenumber for a grid can be simplified as the total horizontal derivative of the tilt derivative (THDR or the TDR), defined as:

$$K = \frac{\partial \theta}{\partial h} = \sqrt{\left(\frac{\partial \theta}{\partial x}\right)^2 + \left(\frac{\partial \theta}{\partial y}\right)^2} \tag{4.2}$$

where $\frac{\partial \theta}{\partial x}$ and $\frac{\partial \theta}{\partial y}$ are the horizontal derivatives of the tilt derivative. The local wavenumber K provides a high-definition visualization of contacts that is independent of the inclination and declination of the magnetic field. It can also provide a proxy for the depth to contact, which will be explained more thoroughly in 4.2.4.

4.2.3 Semi-automated lineament tracking

In Chapter 3, I have applied the semi-automated lineament tracking approach known as automated coherency lineament analysis and selection (ACLAS) introduced by Cascone *et al.* (2017). The method shows that only where the zero-tilt derivative contour overlies significant maxima of the total horizontal derivative is a fault located. One of the advantages of this semi-automated lineament tracking is that it identifies not only the location of the contact but also the strike direction. The fundamental details of this technique have been explained in 3.2.3.

4.2.4 Extended tilt-depth using local wavenumber K

Besides mapping contact edges and the general structure based on lineaments, potential field data can be used to estimate the depth to the top of a magnetic body, i.e. depth to basement. A common method for computing these depths is the tilt-depth method, introduced in Salem *et al.* (2007). The development of the method to estimate the basement depth better will be explained in this section. The method was initially developed based on a model of an infinite-depth contact; it was extended to enable a more robust interpretation on high-resolution magnetic data using local wavenumber K, and finally redefined to apply to a finite-depth contact model.

Conventional infinite tilt-depth method

The conventional tilt-depth method is built based on the understanding that the zero contours of the TDR indicate the location of the source edges. Salem *et al.* (2007) showed that half the distance between the -45° and +45° contours provides an estimate of their depth. According to Nabighian (1972), the general expressions for the horizontal and vertical derivatives of the magnetic field over vertical contacts located at a horizontal location of $h = 0$ and at a contact depth of z_c, with the assumption of a vertical magnetic field (RTP) are:

$$\frac{\partial T}{\partial h} = 2kTc\frac{z_c}{h^2 + {z_c}^2} \tag{4.3}$$

$$\frac{\partial T}{\partial z} = 2kTc\frac{h}{h^2 + {z_c}^2} \tag{4.4}$$

where k is the susceptibility contrast at the contact, T the magnitude of the magnetic field, $c = 1 - \cos^2(i)\sin^2(A)$, A the angle between the positive h-axis and magnetic north, and i the ambient field inclination. Substituting these equations into the TDR equation 3.4 in Chapter 3, Salem *et al.* (2007), showed that the tilt angle θ could be written as:

$$\theta = \tan^{-1}\left(\frac{h}{z_c}\right) \tag{4.5}$$

which indicates that the tilt derivative above the contact is 0° and the distance between 0° and 45° or 0° and -45° contours is $h = z_c$. Hence, the depth can be described as half the horizontal distance between the ± 45° contours. Alternatively, Blakely *et al.* (2016) simplified mapping of the depths of the sources by describing the gradient of equation 4.5:

$$\frac{\partial \theta}{\partial h} = \frac{z}{(h^2 + {z_c}^2)} \tag{4.6}$$

and, by substituting wavenumber K for $\frac{\partial \theta}{\partial h}$ (equation 4.5) at $x = 0$, we get:

$$z = \left(\frac{\partial \theta}{\partial h}\right)^{-1} = K^{-1} \tag{4.7}$$

where the values of K^{-1} along the zero contours of θ will aid the depth estimation to the top of the magnetic contact. Interpolating these values will give us a grid of the depth to basement. However, it is important to note that these depths are computed on an infinite-depth contact model, which at the oceanic crust may result in underestimating the basement depths. Refining the computation with a finite-depth contact model will introduce a limit to the computation, resulting in a more robust approximation of the basement depths.

Redefining tilt depth method using finite-depth contact model and local wavenumber K

According to Salem *et al.* (2014), the basement depth resulting from the tilt-depth of an infinite depth contact model is generally underestimated at the oceanic and continental margin regions. Hence, introducing a proxy of depth to Moho (e.g. from gravity data) will refine the computation based on:

$$K_{(h=0)} = \frac{1}{z_t} + \frac{1}{z_b} \tag{4.8}$$

where $K_{(h=0)}$ is the value of K over the vertical contact, z_t is the depth to basement computed from the tilt-depth of the magnetic anomalies, and z_b is the depth to the bottom of the magnetic source. In this study, z_t is defined from the conventional infinite tilt-depth method, and z_b is defined from gravity inversion assuming an infinite slab of flexural isostasy.

4.2.5 Gravity attraction of sediments

At the ocean-continent transition, we need to take into account the gravity attraction of the accumulating sediment deposits from the continent. In this study, I use the exponential density-depth curve (Cowie & Karner, 1990; Wang *et al.*, 2011) to assign specific density at several classes of depths, as can be seen in Figure 4.1. The specified density values are used to remove the gravity response from each layer of sediment from the free-air gravity anomaly (FAA). The gravity attractions for each layers are computed using Parker (1973), as applied in Chapter 3. The computation is carried out from the top-most water-sediment boundary down to the bottom-most sediment-crust boundary, resulting in a Bouguer anomaly grid.

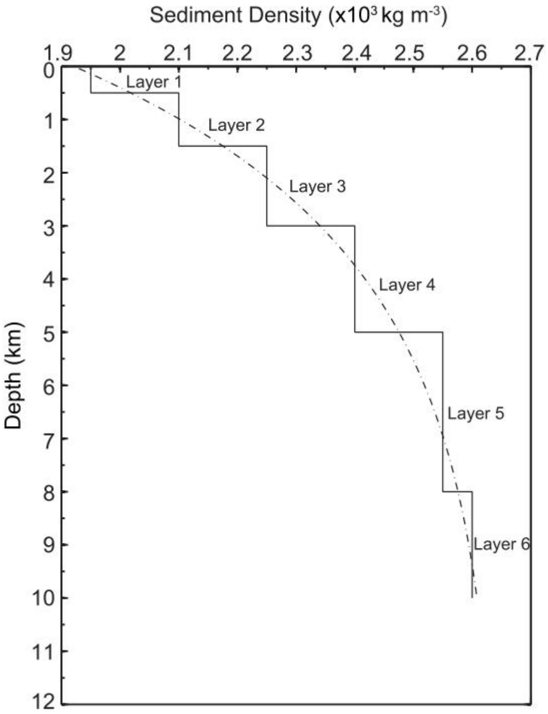

Figure 4.1: Exponential density-depth curve, after Wang *et al.* (2011). Dotted-dashed line: Density-depth curve of Cowie & Karner (1990). Solid line: classes of density-depth ranges that are used to calculate the gravity effect of each layer of sediment. The layer thicknesses and boundaries are arbitrarily chosen by Wang *et al.* (2011), while still honouring the published density-depth curve, and increase in thickness with depth, to honour semi-quantitatively the distance-decay of their gravity expression.

4.3 Study area

The Labrador Basin is selected as a study area based on its good coverage of shipborne and airborne magnetic anomaly data. In addition, the area covers the whole process from rifting, full seafloor spreading, to the extinction of the slow- to ultra-slow-spreading axes. Studies also found areas where mantle rocks are exhumed, as well as the presence of a shallow high-velocity mantle, interpreted as an oceanic core complex or OCC by Delescluse *et al.* (2015). Several types of seismic surveys have also been conducted both with ocean-bottom seismometers (OBS) close to the ridge, employing wide-angle refraction seismic (Delescluse *et al.*, 2015), and with multichannel reflection seismic, acquired by TGS of which several of the survey lines are interpreted and published by Gouiza & Paton (2019). In this study, I use the gridded bathymetry, gravity, and magnetic signatures provided by Getech, plc. I also digitized several interpreted seismic lines, especially where the top of the basement and the Moho are pictured. To compute the gravity effects of sediments in different layers, I use a global synthesized model of sediment thickness. The details of each sets of data will be explained in this section.

4.3.1 Bathymetry and seismic survey coverage

A composite of post-processed bathymetry is provided by Getech, plc. with 2 km cell size. The composite incorporates post-processed satellite-derived bathymetry as well as available shipborne sounding lines over the study area. The bathymetry is resampled to 1' (∼1.85 km) using the `grd2xyz`, `blockmean`, and surface functions in GMT 5.4.5 to make the cell size similar to the available gravity and magnetic data sets. The composite data set is selected based on the poor coverage of available high-resolution bathymetry in the Labrador Basin, both at the GMRT Synthesis (https://www.gmrt.org/GMRTMapTool/) and the NCEI-NOAA Multibeam Bathymetry Mosaic data repositories (https://maps.ngdc.noaa.gov/viewers/bathymetry/). The coverage of GMRT multibeam synthesis can be seen in Figure 4.2b. The synthesis consists of shipboard multibeam bathymetry from multiple survey periods, with sounding lines labeled in the figure.

In the bathymetry of Sandwell *et al.* (2014), we can see the similar sounding lines within the data set (Figure 4.2a), indicating that the grid is composed of both satellite-derived bathymetry and sounding lines from multiple survey periods. Meanwhile, the sounding lines have been made less visible in Getech's bathymetry (Figure 4.2c). The data is visually smoother, specifically at the Canadian ocean-continent transition. The discrepancy between the bathymetry of Sandwell *et al.* (2014) and Getech's bathymetry can be seen in Figure 4.2d. We can see that most of the differences are found near at the Canadian ocean-continent transition, as well as the inner part of the Greenland ocean-continent transition. Offshore, most of the differences are found over the sounding lines. From the comparison, we can imply that Getech's bathymetry has incorporated both satellite-derived and shipboard multibeam data but with further processes to make both data sets more homogeneous, with fewer artefacts and less noise.

A number of seismic surveys have also been carried out in the Labrador Basin. Several of which have been interpreted and published in (Gouiza & Paton, 2019) and (Delescluse *et al.*, 2015), as listed in Table 4.1. In this study, I included two interpreted OBS-refraction lines in the proximity of the extinct ridge (Delescluse *et al.*, 2015) and five interpreted reflection lines covering the ocean-continent transition on the Canadian side (Gouiza & Paton, 2019). The seismic refraction lines were acquired in 2009 during the SIGNAL cruise (Seismic Investigations off Greenland, Newfoundland, and Labrador) onboard CCGS Hudson, surveying both across and along the extinct spreading axis, while the reflection lines were acquired by TGS offshore the Labrador-Newfoundland margin.

Over the bathymetry, I also included the ocean-continent boundary (OCB) defined by Hosseinpour *et al.* (2013) based on a full-fit reconstruction of the Labrador Sea and Baffin Bay, as well as my own OCB interpretation following those already defined (bold white lines and dashed white lines in the Figure 4.2, respectively). The OCB will be used throughout this chapter to separate areas defined as oceanic crust from the continental crust and the ocean-continent transition zone.

Table 4.1: List of interpreted seismic lines over the Labrador Basin

Code	**Type**	**Reference**
GP19_A to GP19_F	Reflection	Gouiza & Paton (2019)
BGR77-17	OBS-Refraction	Delescluse *et al.* (2015)
GEUS2003-4	OBS-Refraction	Delescluse *et al.* (2015)

4.3.2 Gravity anomaly

A composite of post-processed free-air anomaly (FAA) is provided by Getech, plc. with 2 km cell size. The composite is derived from satellite gravity data. Similarly to the previous dataset, the FAA is resampled into a 1' (~1.85 km) grid. Compared to the satellite-derived FAA of Sandwell *et al.* (2014), Getech's FAA is visually very similar with a difference between those grid of up to ± 5 mgal (Figure 4.3). Although there is not much of a difference between these two gravity data sets, I will be using Getech's free-air gravity anomaly data set to have a comprehensive view of this area using all types of data given by the same data provider.

4.3.3 Magnetic anomaly

A composite of global magnetic anomaly is provided by Getech, plc. with 2 km cell size. The MA is also resampled into a 1' (∼1.85 km) grid. In contrast to the FAA, compared to the global dataset of EMAG2 v2 (Maus *et al.*, 2009) and EMAG2 v3 (Meyer *et al.*, 2017), we can already see that the data provided by Getech more resembles a composite of airborne/shipborne magnetic surveys. As explained in 3.3.3, the EMAG2 v2 and v3 do not fall into the same order, spatial trend, resolution, nor amplitudes compared to the composite shipborne/airborne magnetic survey. For example, we can see in Figure 4.4a that EMAG2 v2 data look forcefully extrapolated to fit the 'idealised' geology of the area. On the other hand, while EMAG2 v3 already provides a better dataset by only interpolating observed data instead of fitting it to the 'idealised' geology, the detail is still not comparable to Getech's dataset (Figure 4.4b). The potential coverage of shipborne magnetic surveys in the Labrador Basin can be seen by computing from the reduced-to-pole magnetic anomaly (RTP-MA) its second vertical derivative, in which the artefacts resulting from shipborne/airborne magnetic surveys can be observed. The subsequent studies are carried out with Getech's data set as it represents magnetic signatures sensed from dedicated shipborne/airborne magnetic surveys.

4.3.4 Sediment thickness

To calculate the gravity attraction caused by sediments in various depths, I use NCEI-NOAA's Total Sediment Thickness of the World's Oceans and Marginal Seas Version 3, or the GlobSed (Straume *et al.*, 2019). The sediment thickness is also used to define the initial depth to basement, i.e. the top of the oceanic crust. These grids can be seen in Figure 4.5. From the initial depth to basement, we can already see that the sediment thickness is greatly extrapolated from the isopachs of various sets of seismic surveys. We can see the varying details of each area along the ridges, for instance, the 'crosses' observed at the northern-most part of the ridge (Figure 4.5b), depicting where seismic surveys might have taken place (dashed white lines). Meanwhile, at the southern-most part of the ridge, we observe very smooth contours with little detail, which might depict the lack of seismic surveys in that area.

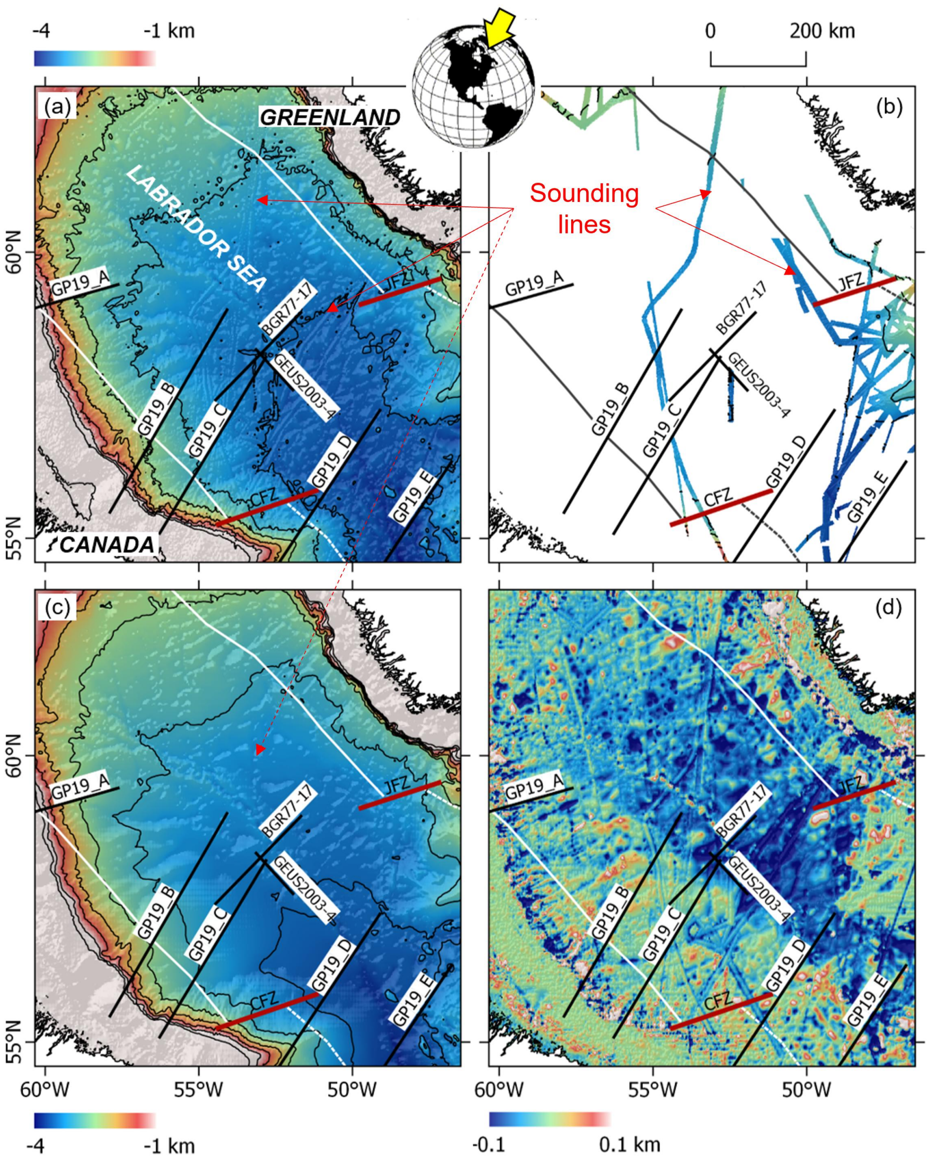

Figure 4.2: Study area with inset. (a) Satellite-derived bathymetry from Sandwell *et al.* (2014), with visual sounding lines labeled (red arrow). Black lines: seismic lines. Bold white lines: the ocean-continent boundary defined by Hosseinpour *et al.* (2013). Dashed white lines: the ocean-continent boundary defined in this study following the predefined line, the base of the continental shelf, and apparent across axis offset. CFZ: Cartwright fracture zone. JFZ: Julianehaab fracture zone; (b) High-resolution bathymetry coverage from the GMRT MapTool; (c) Getech's bathymetry. The sounding lines are less visual in this data set (dashed red arrow); (d) The discrepancy grid between Sandwell's and Getech's bathymetry. Most of the differences are found at the Canadian and Greenland ocean-continent transition. Offshore, most differences are found over the sounding lines.

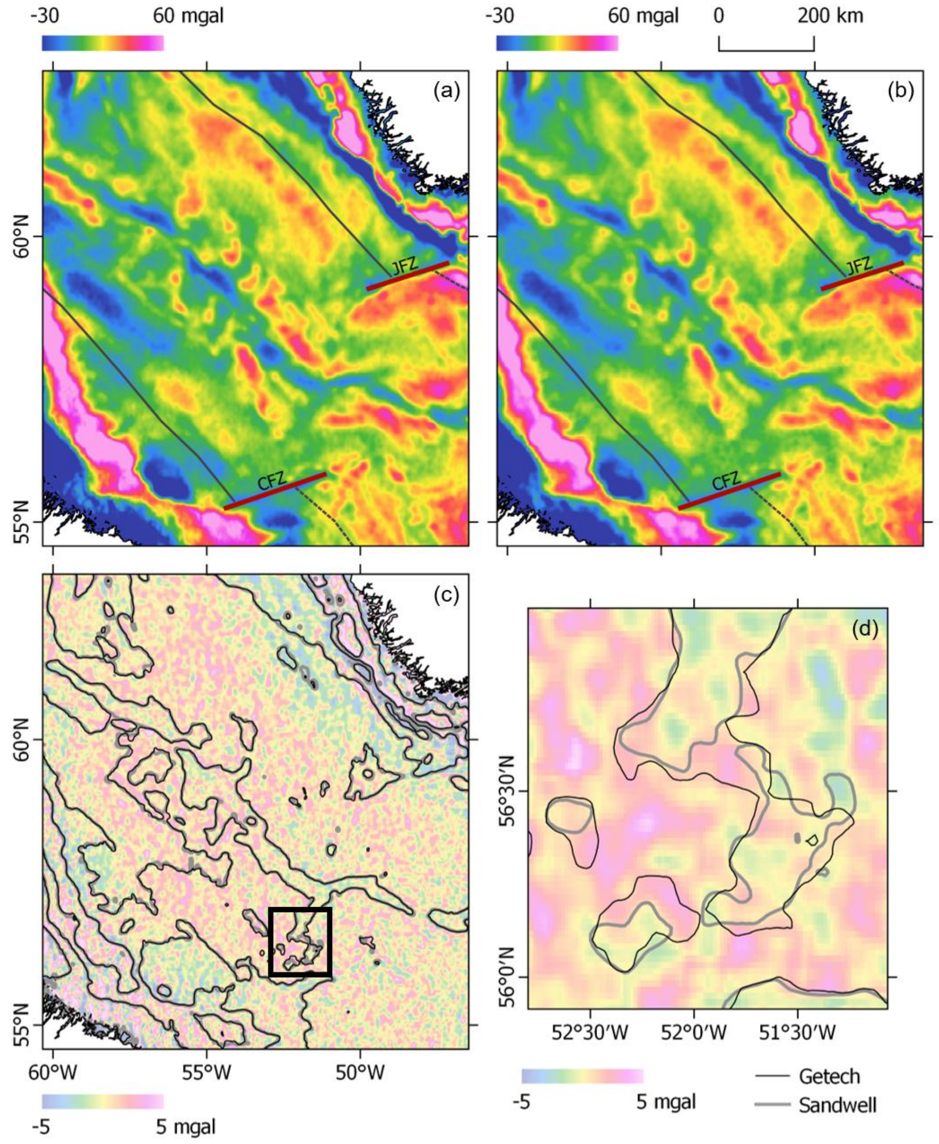

Figure 4.3: Free-air gravity anomaly (FAA) over the Labrador Basin. (a) Satellite-derived FAA of Sandwell *et al.* (2014); (b) FAA provided by Getech, plc.; (c) The discrepancy between Sandwell's and Getech's FAA; (d) A sample area in which we can see how Getech's contours are produced from a smoother surface with simplified textures. Black lines: Getech's FAA 50-mgal contours. Grey lines: Sandwell's FAA 50-mgal contours.

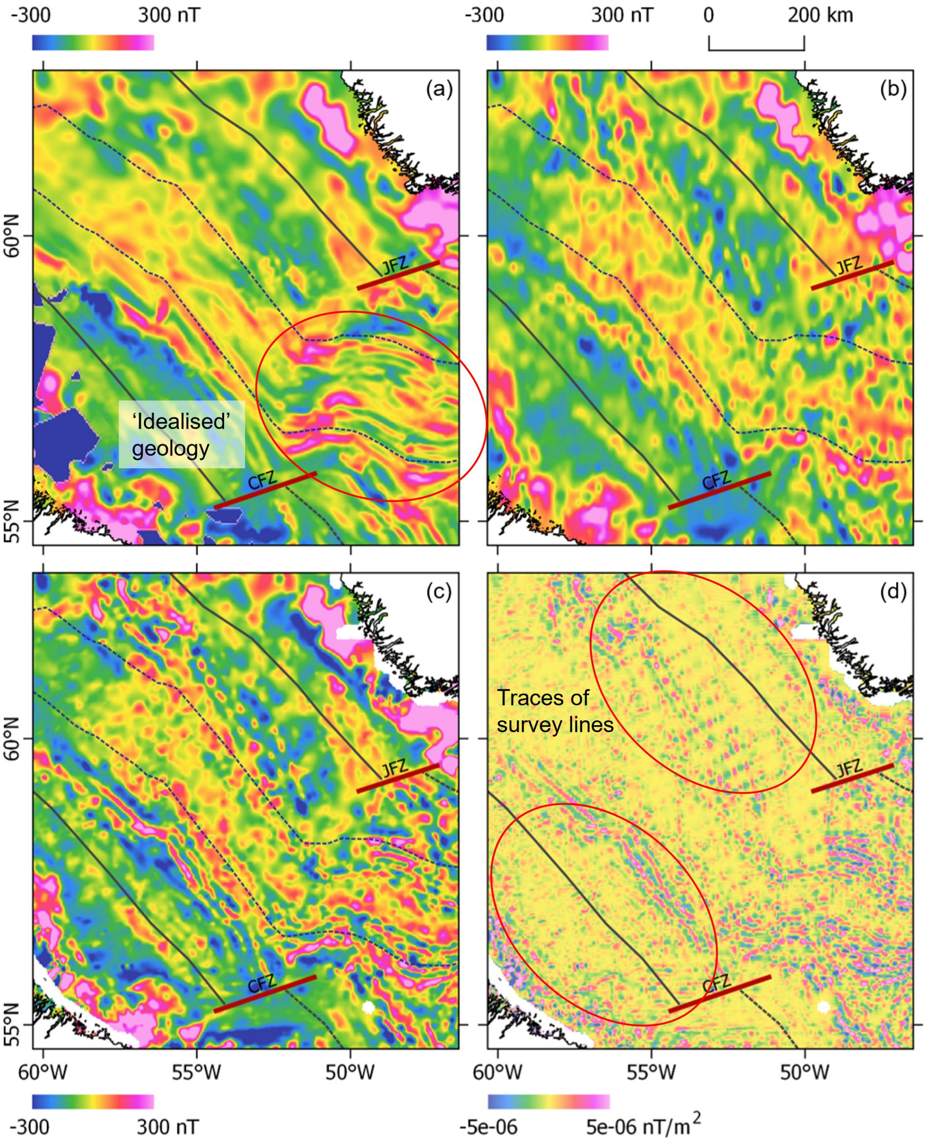

Figure 4.4: Magnetic anomaly over the Labrador Basin. (a) Magnetic anomaly from EMAG2 v2 (Maus *et al.*, 2009); (b) Magnetic from EMAG2 v3 (Meyer *et al.*, 2017); (c) Composite grid of magnetic anomaly provided by Getech, plc.; (d) Second vertical derivative of Getech's reduced-to-pole magnetic anomaly. Artefacts from shipborne/airborne surveys can be seen mostly perpendicular to the ridge. Dashed line: 50 Ma contour from Müller *et al.* (2008).

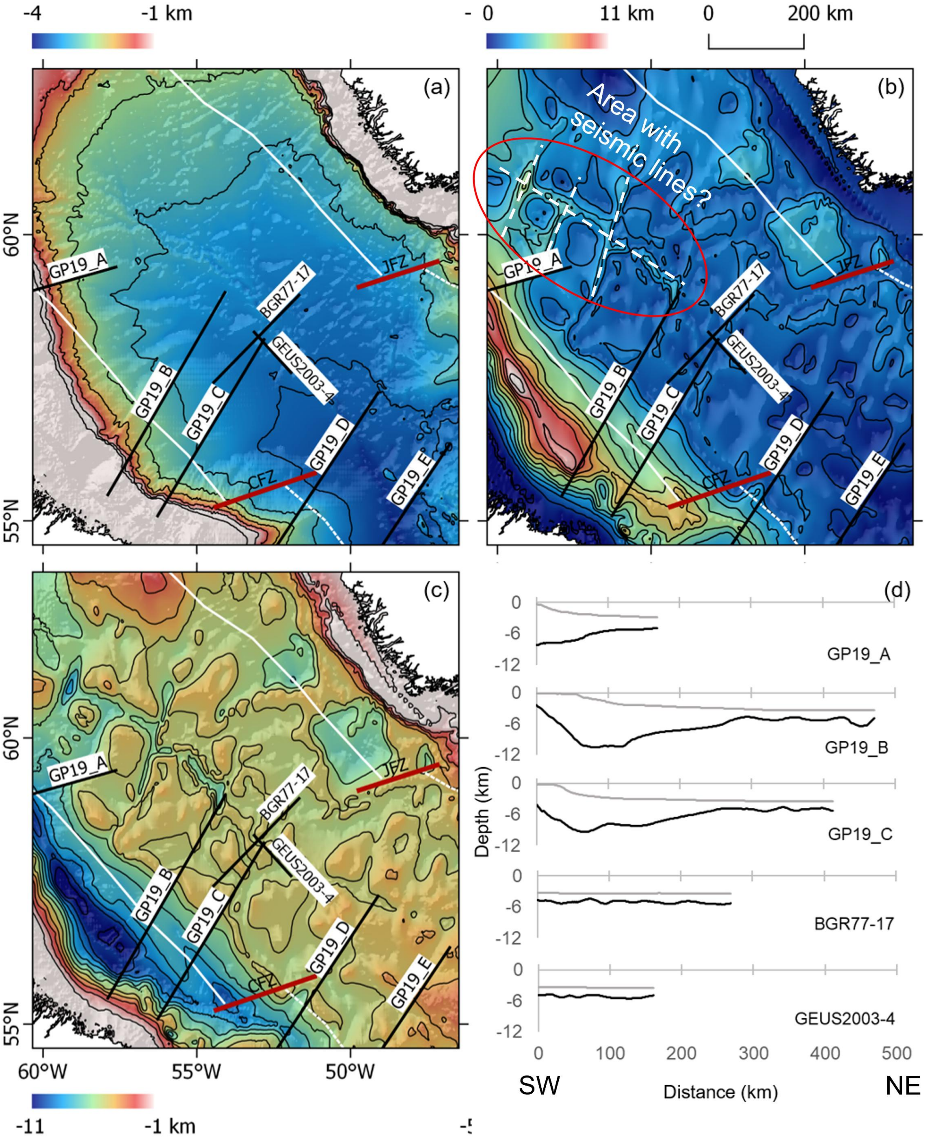

Figure 4.5: Bathymetry and sediment thickness. (a) Getech's bathymetry;(b) GlobSed sediment thickness from NCEI-NOAA (Straume *et al.*, 2019). Area where seismic surveys might have taken place is labelled by red ellipse, with implied seismic lines labelled by dashed white lines; (c) Initial depth to basement, computed by subtracting the GlobSed sediment thickness from the bathymetry; (d) SW-NE cross-profiles of bathymetry (grey) and initial depth to basement (black) at several seismic lines.

4.4 Gravity and magnetic data processing

The basement features in the Labrador Basin will be observed by describing its tectonic structures using derivatives and ACLAS on both gravity and magnetic data. To obtain the crustal type classification, I compute the depth to Moho using the mantle Bouguer anomaly (MBA) technique explained in 3.4.3. The depth to basement is computed using the finite local wavenumber (FLW) method on the magnetic anomaly. The result is compared to the initial depth to basement computed by subtracting the modelled global sediment thickness from the bathymetry.

4.4.1 Tectonic structures implied from gravity and magnetic anomalies

To describe the tectonic structure of the basement, we first need to define the sizes of the features we would like to observe. In this study, I applied a 100-km low-pass Gaussian filter to the FAA to observe the major tectonic features such as ridges, transforms, and fracture zones (FZs). Afterwards, I applied the vertical derivative to the low-passed FAA (termed here as VDR-FAA) and interpret the identified features from the resulting grid. In Figure 4.6a we can already see an oblique semi-continuous gravity low in the middle of the area, indicating a characteristic of an ultra-slow-spreading ridge. We can also observe two smaller oblique gravity lows close to the Canadian and Greenland margins, respectively. I interpret the gravity low in the middle of the area as the extinct ridge, which I divided into eight segments, separated by perpendicular transforms to simplify the ridge-ridge transform geometry occurred over the area. It is important to note that the segments are geometrically simplified in order to accommodate a standard perpendicular geometry between spreading axis and transform faults over a slow-spreading axis. Hence, the spreading axes may not necessarily be drawn right over the existing extinct valleys, as naturally occurs over ultra-slow-spreading ridges, specifically at Segments 2 to 5, where the spreading direction is oblique compared to the other segments. I interpret the two smaller oblique gravity lows as fracture zones, named by previous studies (e.g., Delescluse *et al.*, 2015) as Cartwright fracture zone (CFZ) and Julianehaab fracture zone (JFZ). From the interpretation, we can see that both CFZ and JFZ are traces of ancient transform valleys formed at the time of the spreading of both the ridge beneath the Labrador Basin and the Mid-Atlantic Ridge. We can also see that the horizontal offset of each ridge segment varies along the axis, as each of the ridge segments is compensating the seafloor spreading with varying obliquity.

Afterwards, I applied the ACLAS technique to both the VDR-FAA and RTP-MA. The RTP-MA is computed using the inclination and declination of the centre of this area, 75° and -24°, respectively. As we would like to observe smaller features at the basement, I applied a 50-km low-pass Gaussian filter to both grids before conducting the technique. The ACLAS method locates lineaments in which the maxima of the THDR are in line with the zero-tilt (Figure 4.7c and Figure 4.8c). It is also interesting to see that the lineaments interpreted by the ACLAS method act as a proxy for the quality of the data, especially in a global composite dataset. We can see how the lineaments define the structure of the basement by overlaying it on top of the RTP-MA grid (Figure 4.9a). As observed in the figure, several lineaments correspond to the magnetic reversals, while the others might correspond with the structure of the basement. In general, areas with good magnetic survey coverage tend to have denser lineaments than interpolated areas.

To classify the areas based on their magnetic signatures, I applied the pseudogravity derivative to the magnetic anomaly (termed here as PsGr-MA) with the same inclination and declination used to compute the RTP-MA. In Figure 4.9b, we can see that the PsGr-MA patterns are a lot more continuous in areas with denser survey coverage (areas with dense magnetic lineaments). This limitation is important for the interpretation, for instance, in the northern-most part of Segment 1, where quite a significant area is defined as having an area of lower amplitude. We need to be very careful in defining this area, because the pseudogravity is computed based on the assumption that all the magnetic fields are in the same direction. Lower amplitudes observed in PsGr-MA can also mean that the area is high in magnetisation but governed by reversed polarity. To avoid this interpretation mistake, we can compare the resulting grid with a published geomagnetic timescale, for example the Geological Society of America (GSA) Geologic Time Scale version 5.0. In addition, based on the lineaments, the northern-most part of Segment 1 might not have a good survey coverage compared to those to its southeast. To complement the information needed for interpretation, the resulting PsGr-MA grid will be verified by comparing it to the processed gravity anomalies.

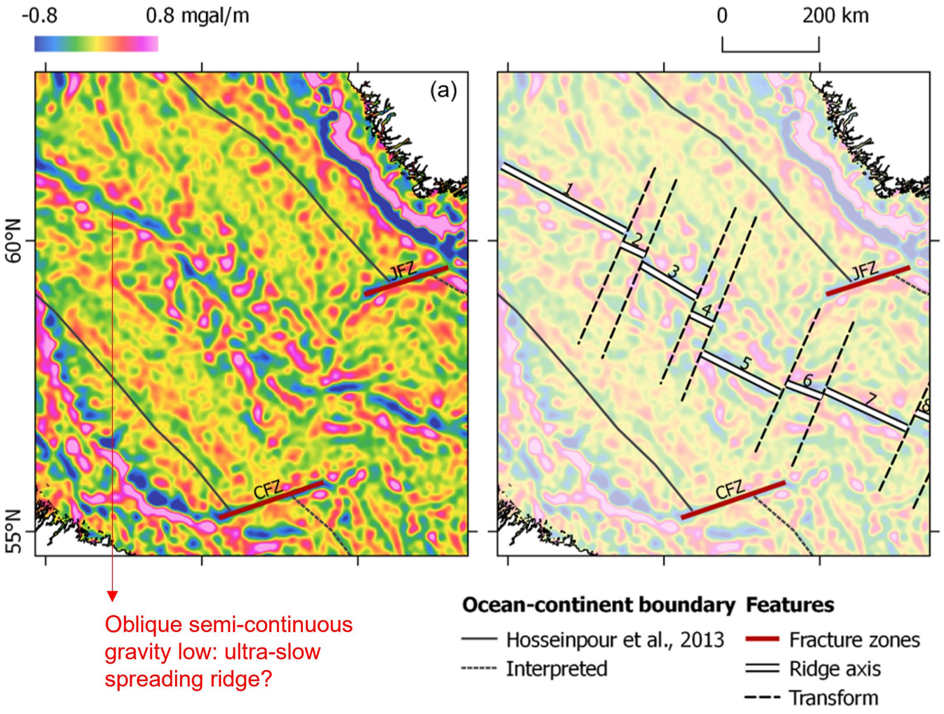

Oblique semi-continuous gravity low: ultra-slow spreading ridge?

Figure 4.6: Vertical derivative of low-pass filtered free-air gravity anomaly (VDR-FAA), and interpreted tectonic features. (a) VDR-FAA, where oblique semi-continuous gravity low is observed in the middle of the area. This semi-continuous structure is interpreted as extinct axes of ultra-slow-spreading ridges. (b) Interpreted tectonic structures. The oblique axis is divided into segments separated by transforms. CFZ: Cartwright fracture zone. JFZ: Julianehaab fracture zone.

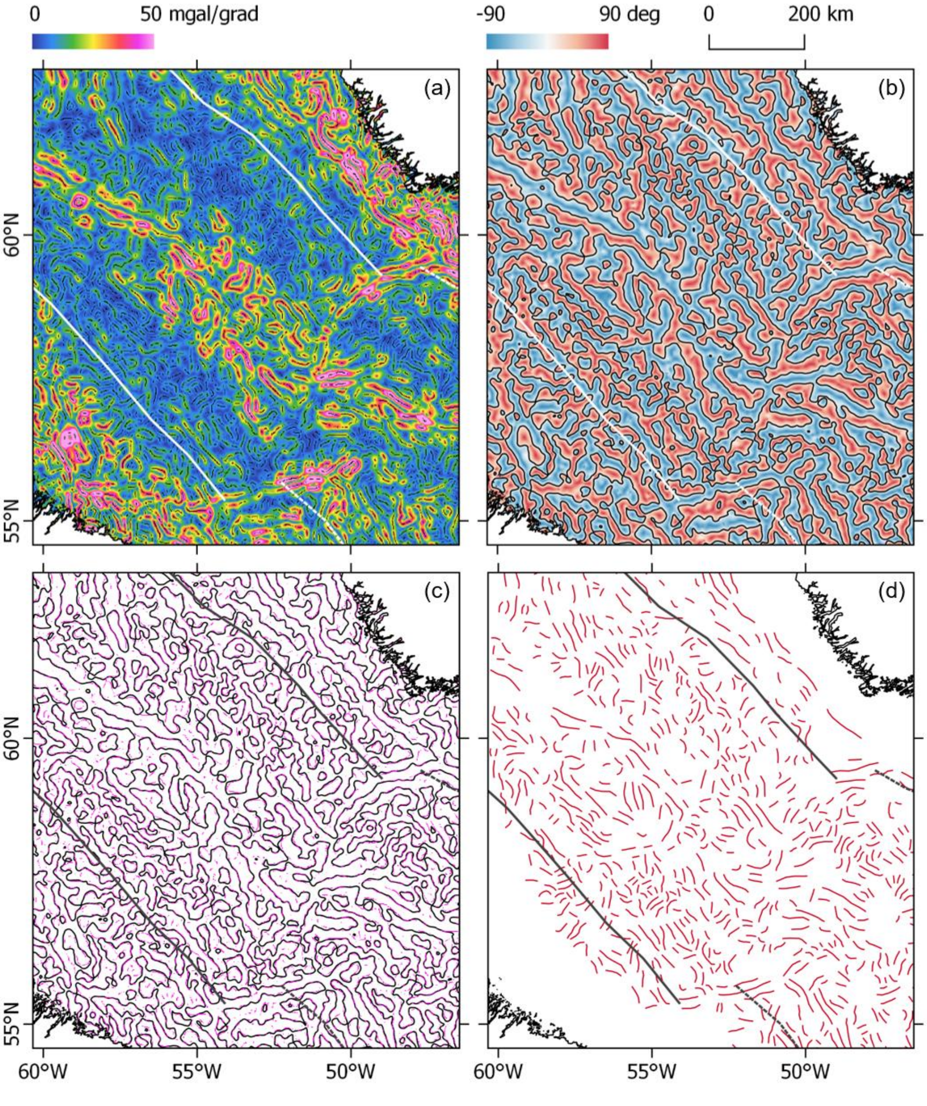

Figure 4.7: Tectonic interpretation using ACLAS on the first vertical derivative of the free-air gravity anomaly (VDR-FAA). The free-air gravity anomaly is low-pass-filtered at 50 km; (a) Total horizontal derivative of the VDR-FAA. (b) Tilt derivative of the VDR-FAA; (c) Zero-contour of tilt derivative of the VDR-FAA (black lines) overlaid with the second-, third-, and fourth-order of the ridge maxima of the total horizontal derivative of the VDR-FAA (magenta lines), and; (d) Lineaments from VDR-FAA.

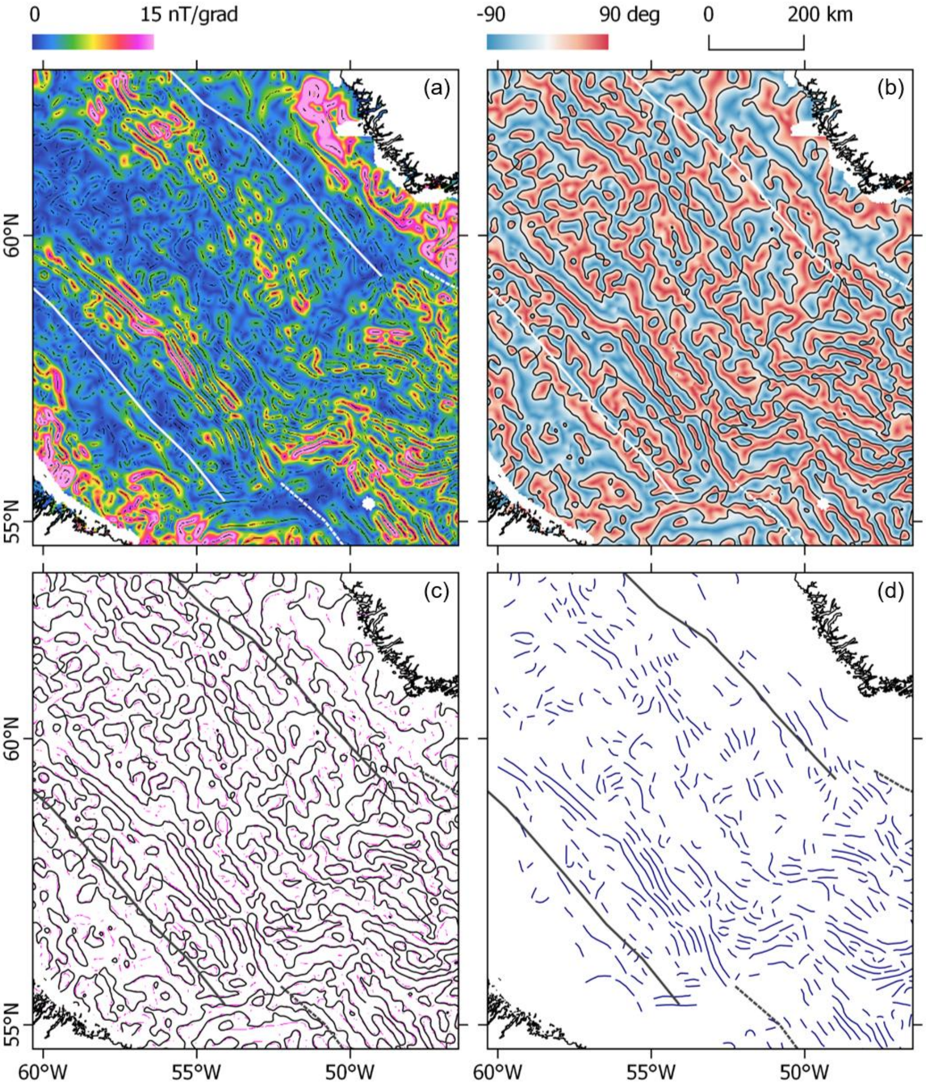

Figure 4.8: Tectonic interpretation using ACLAS on the reduced-to-pole magnetic anomaly (RTP-MA). The magnetic anomaly is low-pass-filtered at 50 km; (a) Total horizontal derivative of the RTP-MA. (b) Tilt derivative of the RTP-MA; (c) Zero-contour of tilt derivative of the RTP-MA (black lines) overlaid with the second-, third-, and fourth-order of the ridge maxima of the total horizontal derivative of the RTP-MA (magenta lines), and; (d) Lineaments from RTP-MA.

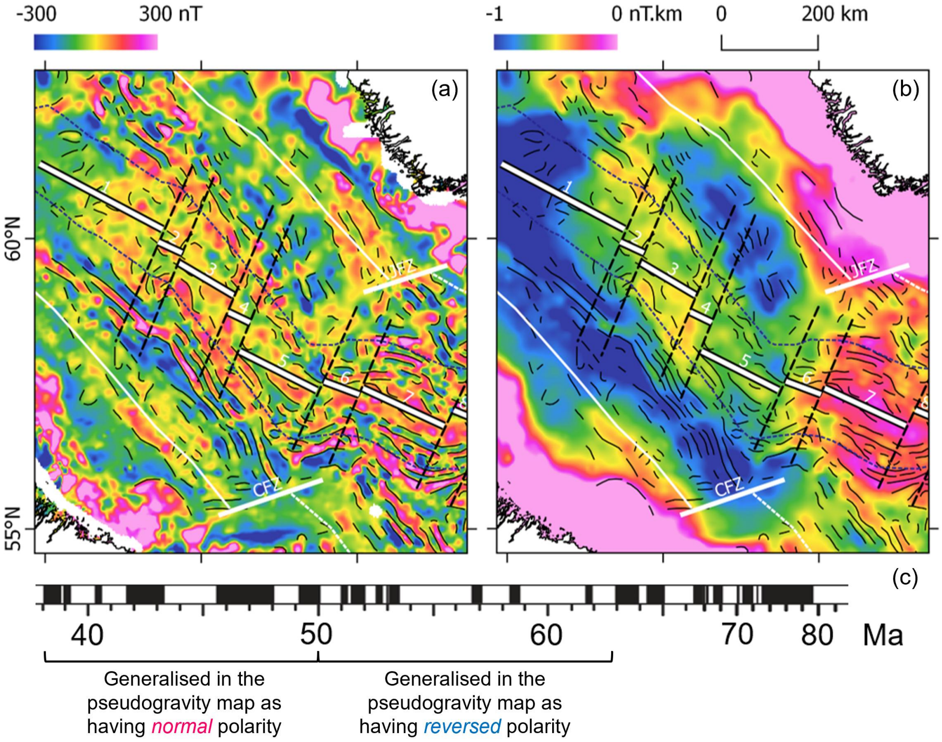

Figure 4.9: Reduced-to-pole magnetic anomaly (RTP-MA) and pseudogravity of the reduced-to-pole magnetic anomaly (PsGr-MA). (a) RTP-MA. (b) PsGr-MA. Magnetic anomalies are compared to the reversal scale from the GSA Geologic Time Scale v5.0 (c). Both grids are overlaid by magnetic lineaments derived from ACLAS (black lines), interpreted extinct ridge (bordered white lines), fracture zones (bold white lines), and continent-ocean boundary (solid and dashed white lines). The PsGr-MA grid is overlaid with thin black dashed lines, marking the 50 Ma contour from Müller *et al.* (2008) and can be compared to the reversal scale. Areas younger than 50 Ma is dominated by relatively higher values of PsGr-MA as they are dominated by normal magnetic polarity values.

4.4.2 Depth to Moho: Mantle Bouguer Anomaly (MBA)

To classify the crustal types over the study area, I compute a proxy of the crustal thickness using the MBA method as explained in 3.4.3. The lithospheric cooling effect is not taken into account in the gravity calculation as the ridge has been extinct since 33 Ma (Hosseinpour *et al.*, 2013; Roest & Srivastava, 1989). This consideration will be supported by the computed MBA values explained in this subsection. All the calculations and parameters used in this subsection are based on the equations and table of parameters presented in Table 3.5. However, as we are working on an area covered by sediment, we first need to remove the gravity effect of the sediment for each individual layer as explained in 4.2.5. Hence, I first create six layers of sediments with thicknesses based on the exponential density-depth curve in Figure 4.1. Each layer is assigned density defined by the curve and profile examples of these layers can be seen in Figure 4.10.

The gravity effects are then removed from the FAA by computing the gravity responses from the interaction of each layer, initially from the water-sediment boundary at the top-most layer down to the sediment-crust boundary at the bottom-most layer. These effects are computed using Parker (1973), resulting in the Bouguer anomaly, where the remaining anomalies are those observed from the top of the basement. Afterwards, a mantle Bouguer anomaly (MBA) is computed by reducing the attraction of the crust-mantle interaction assuming a 6 km deep crust as a reference. The homogenous crust is computed from the top of the initial depth to basement. From the MBA, we can see that this ridge does not have the unique “bulls-eye” pattern of gravity lows commonly found over spreading centres (e.g., Kuo & Forsyth, 1988; Lin *et al.*, 1990). This is consistent with the lack of activity observed over the ridge, where the spreading axes are now extinct. The computations are carried out using the *gravfft* function of GMT 5.4.5. From the MBA, I computed the residual crustal thickness (RCT) using the infinite slab equation presented in 3.4.3 (Eq. 3.11). Finally, the depth to Moho can be computed from the RCT, which can be used to estimate the crustal thickness variation in the study area. The resulting grids of the gravity processes can be seen in Figure 4.11.

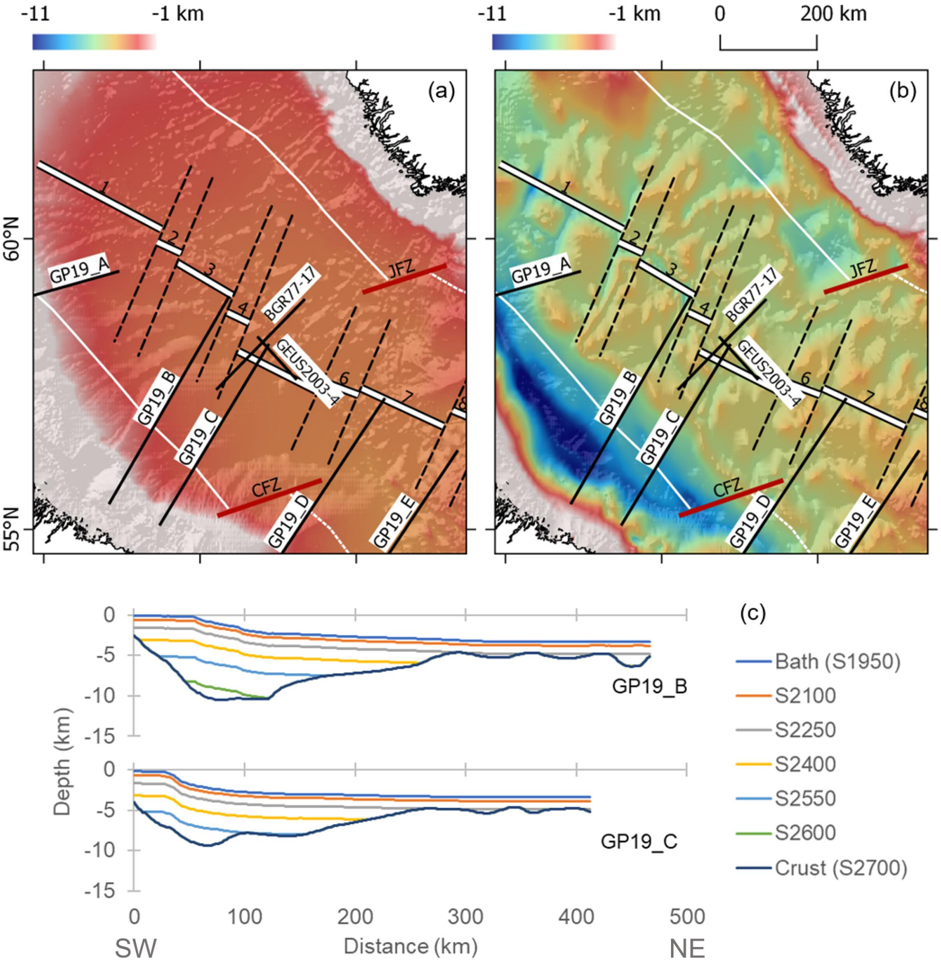

Figure 4.10: Sediment layers. (a) Bathymetry provided by Getech; (b) Initial depth to basement as explained in Figure 4.5c. (c) Sample of the top of each layer of sediment based on the graph in Figure 4.1. The top-most layer is the 500-m-thick sediment, in which the density is defined as 1950 kg/m^3. The bottom-most layer before the crust is sediment deeper than 8000 m, in which the density is defined as 2600 kg/m^3.

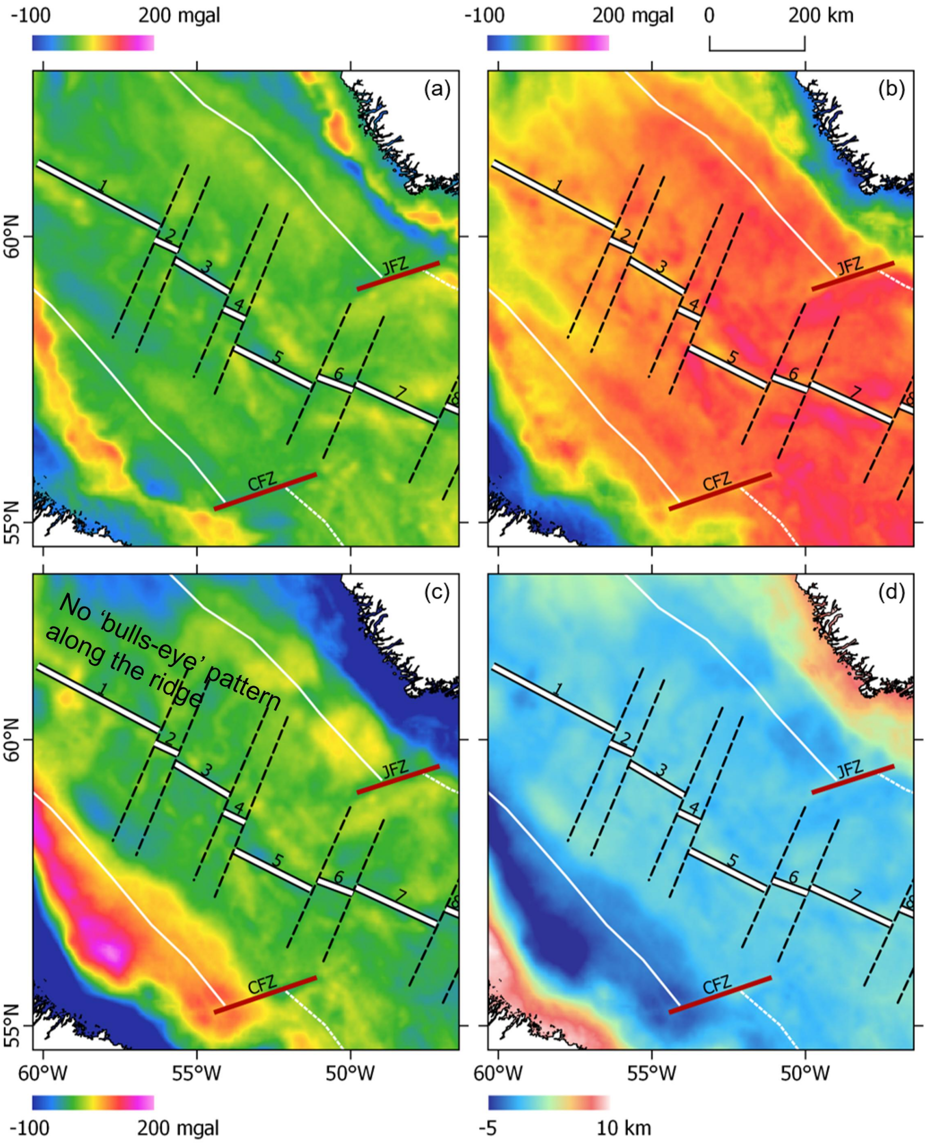

Figure 4.11: Gravity grids. (a) Getech's FAA; (b) Bouguer anomaly (BA); (c) Mantle Bouguer anomaly (MBA), computed by assigning a constant crustal thickness of 6 km from the top of the crust (Figure 4.10b);); (d) Residual crustal thickness (RCT) at the Moho, computed by inverting the remaining IMBA using the infinite slab formula.

4.4.3 Depth to basement: Finite local wavenumber (FLW)

The initial depth to basement has been defined by subtracting the sediment thickness of Globsed (Straume *et al.*, 2019) from the bathymetry. However, this initial depth to basement possesses a limitation as it seems to have been an interpolation of existing isopachs of the depth to basement acquired by seismic surveys. A detailed explanation of this has been covered in 4.3.4. In this subsection, I compute the depth to basement using the finite local wavenumber K (FLW) technique of Salem *et al.* (2014).

Firstly, I computed the depth to basement using the infinite tilt-depth technique, where I compute the tilt derivative (TDR) of the RTP-MA, as well as the local wavenumber K. The local wavenumber K can be approximated as the total horizontal derivative (THDR) of the TDR. From the local wavenumber K, we then compute the first proxy of the depth to basement by computing its inverse (K^{-1}), as explained in 4.2.4. I then sampled the K^{-1} along the zero-tilt contours of the RTP MA, followed by interpolating the points using the continuous curvature spline gridding through the *surface* function on GMT 5.4.5. However, the resulting depth to basement is highly variable, as the zero-tilt contours do not always represent the maxima of a structure, especially over their edges. In Figure 4.12a, we can see how the computed depths are most likely sensible at areas with relatively dense magnetic lineaments, or areas with good coverage of magnetic surveys and linear features to estimate depth from. Therefore, I resampled the K^{-1} over the defined lineaments and recomputed the depths. The resulting depth grid is generally smoother with less along- and across-axis variation. Nevertheless, the depths over areas with little to no magnetic lineaments are still highly underestimated. I thus introduce the depth to Moho, computed from MBA, to constrain the depth computation.

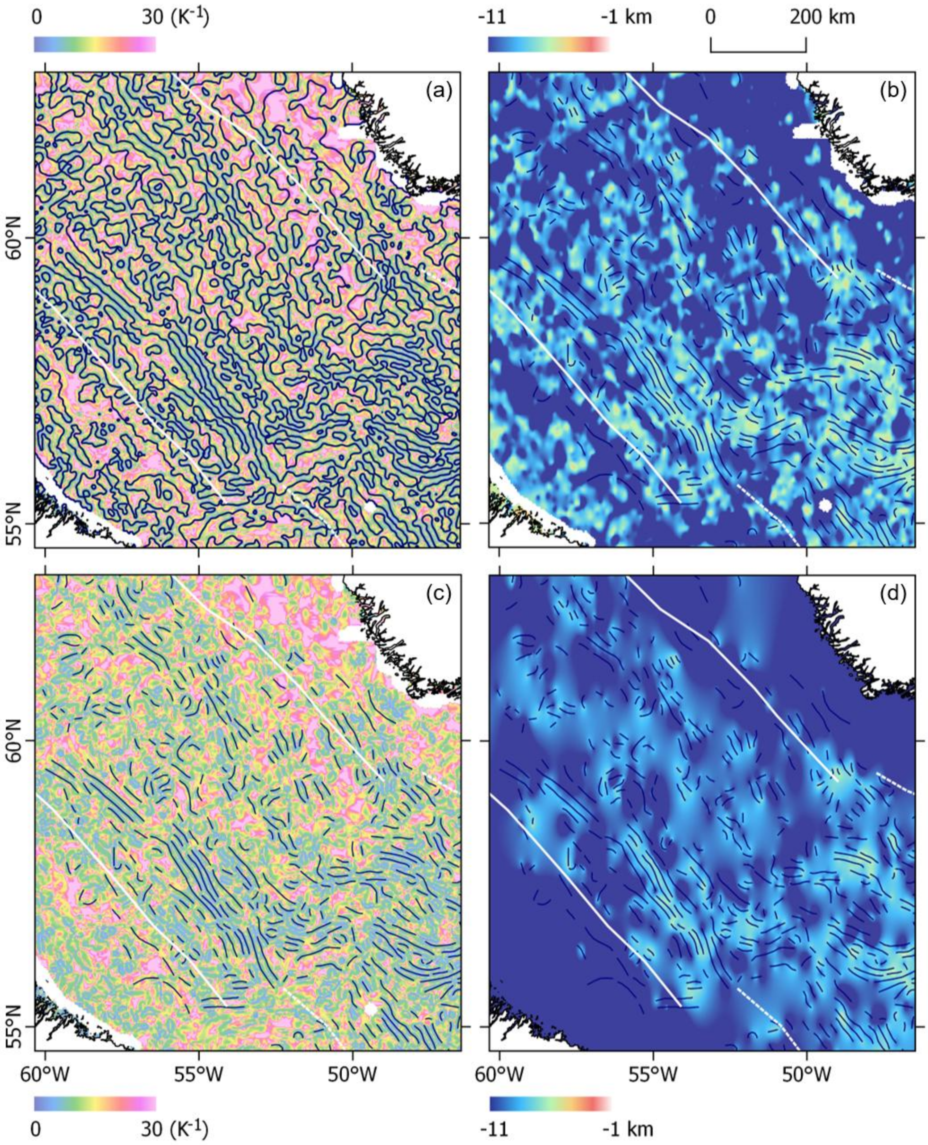

Figure 4.12: Depth to magnetic basement computation. (a) The inverse of local wavenumber (K^{-1}) overlaid by the zero-tilt contour of the RTP-MA (dark blue lines); (b) Depth to basement computed using the infinite local wavenumber technique, where depth values are sampled over the zero-tilt contour. Areas with good data coverage (marked by dense magnetic lineaments: dark blue lines) tend to give sensible depths while areas with sparse lineaments do not; (c) The inverse of local wavenumber (K^{-1}) overlaid by magnetic lineaments from ACLAS; (d) Depth to basement computed using the infinite local wavenumber technique, where depth values are sampled over areas with lineaments.

4.5 Basement structure and crustal type classification

4.5.1 General structure

To obtain the crustal thickness variation, I first compare the depth to Moho inferred from the MBA to those inferred from seismic surveys. In addition, I also compute the depth to Moho from an MBA that is cosine tapered at 25 km (low pass) and 135 km (high pass) at 11 km depth to see how the results change under this constraint. Both grids can be seen in Figure 4.13. The seismic, MBA, and cosine-tapered MBA Moho are then sampled across several seismic profiles, namely the BGR77-17 OBS-refraction line, the GEUS2003-4 OBS-refraction line, the GP19_B reflection line, and the GP19_D reflection line. The profiles of these lines can be seen in Figure 4.14 and the discrepancies between each computed models can be seen in Table 4.2.

The discrepancies are computed by resampling each set of data into a similar number of samples. In the spreading axis, the number of data sampled from the BGR77 and GEUS seismic lines is 167 and 73, respectively. Based on these numbers, I resampled the seismic, MBA, and cosine tapered MBA Moho in the BGR77 and GEUS seismic lines into 100 samples to compute the mean discrepancies in each line. In the continent-ocean transitions, the seismic lines are divided into the weakly thinned domain (WTD), necking domain (ND), hyperextended domain (HD), transitional domain (TD), and oceanic domain (OD) based on the interpretation of Gouiza & Paton (2019). Based on the number of data sampled from the GP19_B and GP19_D, I resampled the seismic, MBA, and cosine tapered MBA Moho in the weakly thinned, necking, and hyperextended domains into 50 samples, and 100 samples in the transitional and oceanic domains. The discrepancies are computed as stated in the table, in which the MBA Moho is subtracted from the seismic Moho, the cosine tapered MBA Moho is subtracted from the seismic Moho, and the cosine tapered MBA Moho is subtracted from the MBA Moho, respectively. The positive/negative signatures are taken into account in the mean and standard deviation computation. From the profiles and numbers in the table, we can see that the MBA-derived Moho correlates better with the seismic Moho than the cosine-tapered MBA Moho. Hence, the subsequent discussions will be focused on the discrepancy between the seismic and MBA Moho.

In Figure 4.14a, we can see that the MBA Moho over the BGR77-17 line correlates closely to the seismic Moho, with the mean discrepancy of 0.80 ± 0.60 km. The MBA Moho also correlates closely with the seismic Moho over the GP19_D line (Figure 4.14d), specifically at the transitional and oceanic domains, with the mean discrepancy of 0.70 ± 0.41 km and 1.17 ± 0.37 km, respectively. However, the correlation is no longer observed at the hyperextended, necking, and weakly thinned domains, where the mean discrepancy is much greater (3.21 ± 1.32 km, 6.54 ± 3.13 km, and 11.49 ± 0.16, respectively). In contrast, we can see that the MBA and seismic Moho over the

GEUS2003-4 line are not always correlated, specifically over the area inferred to have < 2 km thickness (Figure 4.14b). This great discrepancy is also present between the seismic and MBA-derived Moho, which is 2.24 ± 0.95 km. Looking at the very specific Moho signature inferred from the refraction seismic survey, this great discrepancy might occur either from the p-wave velocity computation of the seismic survey, or from the Moho computation from the MBA. For the moment, neither of the interpretations are considered valid depictions of the actual depth of the Moho. Another great discrepancy is found over the GP19_B line (Figure 4.14c), specifically at parts of the OD and largely over the ND, with the mean discrepancy of 1.86 ± 0.96 km and 9.01 ± 2.70 km, respectively.

The observation, specifically at lines covering the continental margin, implies that the MBA Moho might represent a good estimate of crustal thickness over the oceanic and transitional domains, but not as good the closer it is to the continental crust. In addition, the computation depends on the largely generalised crustal layer, that is defined only by a single density value. Despite these issues, we can see that the crustal thickness variation enables us to identify the 'thinner than normal crust' (0 - 6 km) in parts of the area. Afterwards, I compare the computed depth to basement – termed FLW depth – to the seismic depth, as well as the initial depth to basement computed from the GlobSed model. The results are visualised in Figure 4.14 and the discrepancies can be seen in Table 4.3. The discrepancies are computed similarly as how the discrepancy between each model of the Moho is computed in Table 4.2. In the subsequent discussions, we will be focusing on the discrepancies between the seismic and FLW depths.

In GP19_B and GP19_D, we can see a similar trend observed in the Moho computation, where the FLW depth correlates quite well with the seismic depth at the transitional and oceanic domains (TD and OD), with the mean discrepancies 1.30 ± 0.70 km and 0.94 ± 0.55 km, respectively in GP19_B and 1.40 ± 0.85 km and 0.46 ± 0.36 km, respectively in GP19. The correlation ceases at the hyperextended domain, as the FLW depth is limited by the MBA Moho. We can thus say that the depth to basement is reliable over areas with good estimate of depth to Moho.

The basement structures in the study area are defined by applying the ACLAS technique to the gravity (ACLAS-BA) and magnetic data (ACLAS-MA). Specifically, we can see that the ACLAS-MA lineaments reveal not only the general structure of the basement, but also the quality of the data (Figure 4.8). Based on the orientation, we can see that the magnetic lineaments mostly correspond to the magnetic reversals that occurred during the full seafloor spreading. To identify the type of crust in the study area, we can compare and correlate the spatial pattern of the FLW basement depth, the MBA, and the PsGr-MA maps (Figure 4.15), specifically across the extinct spreading axis (BGR77-17) and from the hyperextended to the oceanic domain (GP19_B). The

BGR77-17 line is situated over the oblique spreading axis defined as Segment 5, while the GP19_B line is situated across the Canadian margin seaward to the spreading axis defined as Segment 3. The correlation will be discussed in 4.5.2 and 4.5.3.

Table 4.2: Mean discrepancies between the Moho computed from various techniques. All mean and standard deviation (SD) values are in km. MBA$_{filt}$ is mantle Bouguer anomaly cosine tapered at 25 km (low pass) and 135 km (high pass) at 11 km depth.

		Moho					
		Seismic−MBA		Seismic−MBA$_{filt}$		MBA−MBA$_{filt}$	
		Mean	SD	Mean	SD	Mean	SD
BGR77-17		0.80	0.60	1.12	1.01	0.74	0.55
GEUS2003-4		2.24	0.95	3.12	0.81	0.89	0.54
GP19_B	ND	9.01	2.70	11.72	1.30	2.75	1.57
	HD	1.09	0.99	2.75	2.03	1.79	1.03
	TD	1.68	0.55	2.45	0.48	0.84	0.63
	OD	1.86	0.96	1.91	1.04	0.43	0.18
GP19_D	WTD	11.49	0.16	10.87	0.53	0.63	0.49
	ND	6.54	3.13	3.78	3.03	3.08	0.44
	HD	3.21	1.32	3.31	1.71	1.10	0.57
	TD	0.70	0.41	0.83	0.54	0.61	0.27
	OD	1.17	0.37	1.65	0.78	0.68	0.43

Table 4.3: Mean discrepancies between the top of the crust computed from various techniques. All mean and standard deviation (SD) values are in km. FLW: Finite local wavenumber depth.

		Top of Crust					
		Seismic−FLW		Seismic−GlobSed		GlobSed−FLW	
		Mean	SD	Mean	SD	Mean	SD
BGR77-17		0.42	0.28	0.32	0.25	0.33	0.23
GEUS2003-4		0.24	0.17	0.24	0.18	0.21	0.14
GP19_B	ND	1.07	0.73	1.12	0.95	2.00	1.25
	HD	1.73	0.78	3.25	1.29	3.25	1.29
	TD	1.30	0.70	0.50	0.36	1.29	0.62
	OD	0.94	0.55	0.88	0.53	0.61	0.41
GP19_D	WTD	3.39	0.41	0.19	0.16	3.56	0.27
	ND	1.80	0.86	0.59	0.68	2.17	0.61
	HD	1.36	0.90	1.34	0.82	1.40	0.71
	TD	1.40	0.85	0.96	0.54	0.51	0.43
	OD	0.46	0.36	0.33	0.31	0.24	0.1

4.5.2 Across the extinct spreading axis: BGR77-17 OBS-refraction line

In Figure 4.16, I compare the FLW basement depth, MBA, PsGr-MA, and computed crustal thickness with the interpreted crustal model of Delescluse *et al.* (2015). The crustal model is derived from both forward modelling using the RAYINVR technique and travel-time tomography inversion (Tomo2D) explained in the cited literature. Based on the ages picked from Müller *et al.* (2008), we can see that this segment experienced an asymmetric spreading, with the northern flank (OBS Station-1) spreading faster than the southern flank (OBS Station-18), as the distance between the extinct axes with the 50 Ma mark at the northern flank is greater than the disctance between the extinct axes with the 50 Ma mark at the southern flank. The asymmetry is also observed in the MBA (Figure 4.16b), where the MBA high at the northern flank is wider than the southern flank. As the crustal thickness is derived from the MBA, we can see a larger area of thin crust (< 6 km) over the northern flank (Figure 4.16d).

Structures derived from both Bouger gravity anomaly and reduced-to-pole magnetic anomaly using the ACLAS technique are depicted over the FLW basement depth (Figure 4.16a), with dip directions depicted as small triangles. From these lineaments, we can see that the structures are dipping in alternating directions instead of homogeneously towards the axes. This might imply that the crust was experiencing a typical ultra-slow-spreading accretion, identified by a continuous tectonic extension through detachment faulting with alternating dip directions. The detachment faults might result in the exposure of lower crust and upper mantle rocks. For instance, we can see a prominent local high that correlates with a local MBA high on the FLW basement depth map, over the OBS Station-14 (Figure 4.16a and Figure 4.16b). From the gravity and magnetic lineaments, we can also see that this area represents a local high of both gravity and magnetic signatures, marked by the outward dipping structures. Furthermore, we can observe this significant area of shallow FLW basement and MBA high correlates well with high values of PsGr-MA. The whole observation might indicate the presence of OCC, where upper-mantle rocks like peridotites are exhumed to the ocean floor and followed closely by serpentinisation through seawater infiltration, which altered the rocks to be highly magnetised (e.g., Oufi *et al.*, 2002).

In contrast, a local gravity high observed over the OBS Station-7 is indicated as an oblique magnetic 'footwall' structure. Compared to the seismic crustal model, this area might indicate a breakaway zone of an OCC interpreted by Delescluse *et al.* (2015). This OCC might be exhumed by a longer offset detachment faulting facilitated by the higher tectonic extension over the northern ridge flank.

4.5.3 From transitional to oceanic domain at the Canadian flank: GP19_B

In Figure 4.17, I compare the FLW basement depth, MBA, PsGr-MA, and computed crustal thickness with the interpreted crustal model of Gouiza & Paton (2019). The crustal model is obtained using the GM-SYS 2D Profile Modelling in Geosoft. From the profile, I selected the area starting from the edge of the hyperextended domain (HD) at the southern-most part, up to the transitional and the oceanic domain (TD and OD, respectively). Based on the ages picked at this line, we can see that the ridge was spreading relatively faster at the older ages compared to the younger ones. This might affect the resulting lithology of the crust, in which Gouiza & Paton (2019) separate the upper mantle (3 g/cm^3) from the crust (2.8 g/cm^3) at the TD, while at the OD it is defined as a single layer on top of the mantle (2.9 g/cm^3).

Over the northern part of the segment, we can observe a relatively high MBA that correlates well with high PsGr-MA ('OCC' label in Figure 4.13b and c). This area might indicate the presence of OCC, as it is parallel with a structure indicated at the seismic model at $\sim$50 Ma. Structures with alternating dip directions are also found in the vicinity of the extinct axes. Landward, we observe a rapid increase of MBA values at $\sim$60 Ma, which correlates well with the presence of a shallow FLW basement and the interpreted TD-OD boundary. As discussed in 4.4.1, the low PsGr-MA values (dark blue) observed over this area does not directly reflect the underlying lithology. Instead, it marks the change of the magnetisation field, which means that the area might be highly magnetised but in a reversed field direction.

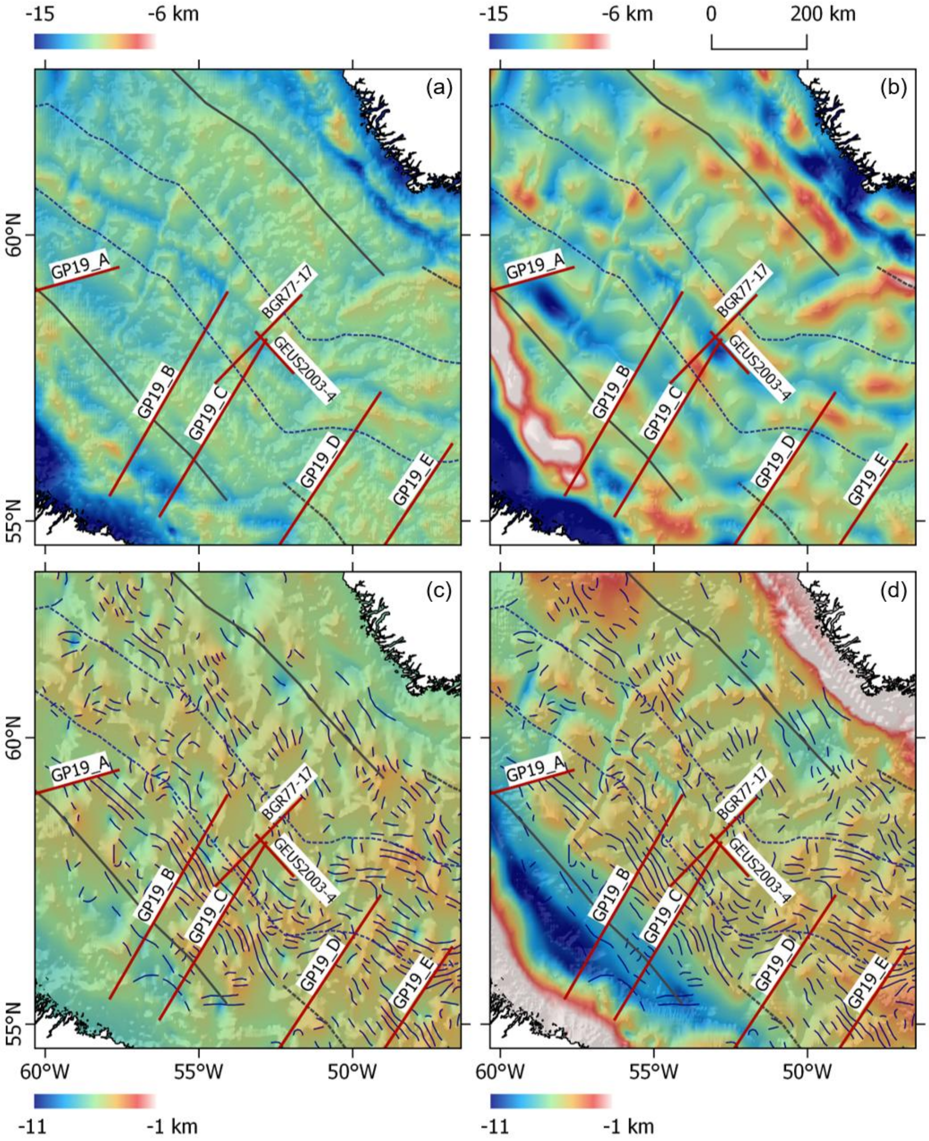

Figure 4.13: Depth to Moho and depth to basement. (a) Depth to Moho inverted from the MBA; (b) Depth to Moho inverted from the MBA cosine tapered at 25 km (low pass) and 135 km (high pass) at 11 km depth; (c) Depth to basement computed using the finite local wavenumber technique. The depth to Moho in (a) is introduced as a limit to the computation. Dark blue lines: magnetic lineaments; (d) Initial depth to basement as a comparison to the computed depth in (c). Cross profiles are described in Figure 4.14.

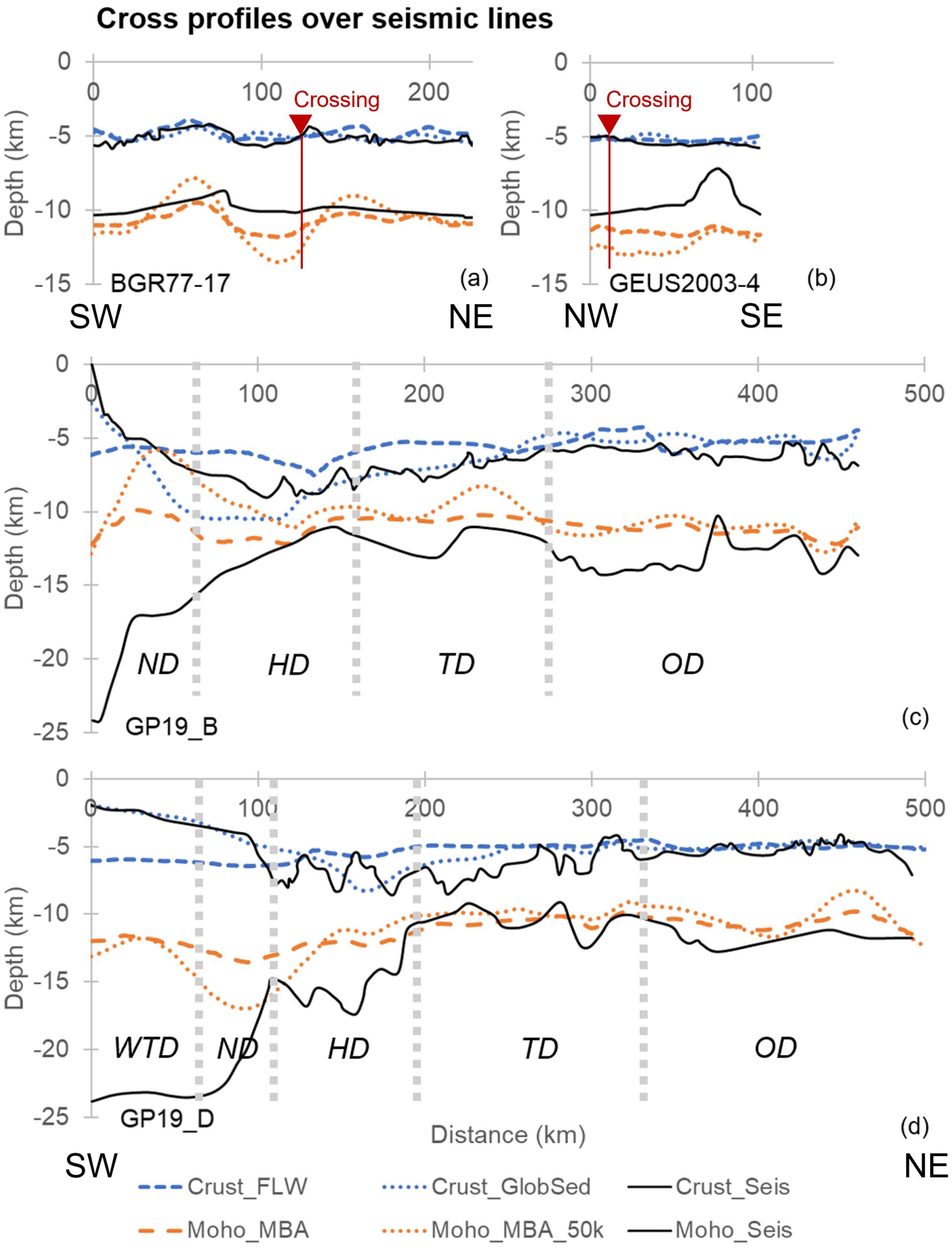

Figure 4.14: Depth profile comparison over seismic lines: (a) BGR77-17; (b) GEUS2003-4; (c) GP19_B, and (d) GP19_D. Dashed light grey lines: domain classification after Gouiza & Paton (2019). WTD: weakly thinned domain. ND: necking domain. HD: hyperextended domain. TD: transitional domain. OD: oceanic domain. Each profile is described in the legend. FLW: finite local wavenumber. MBA: mantle Bouguer anomaly. Depth computation techniques are explained in the text.

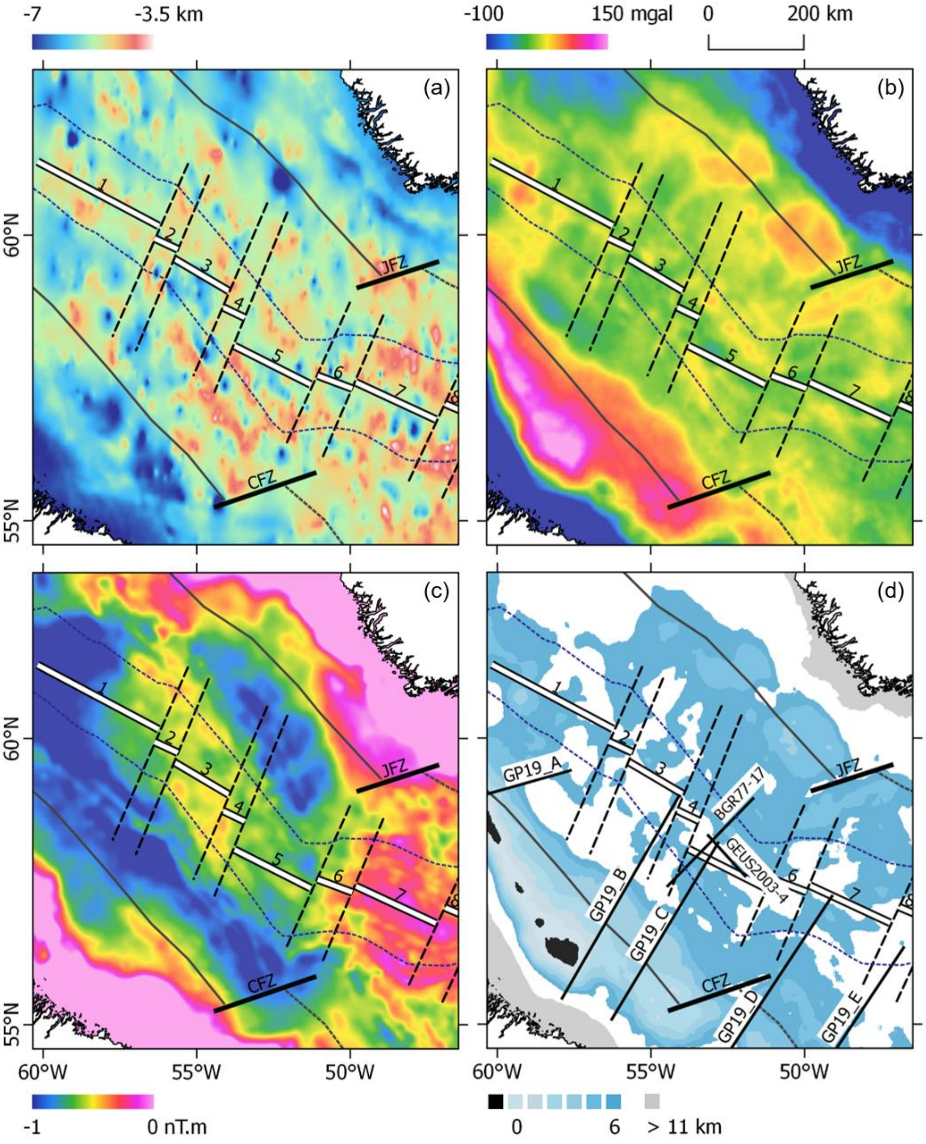

Figure 4.15: The general classification of the area. The spreading axis is divided into eight segments with explanations of each in the text. (a) Depth to magnetic basement; (b) MBA; (c) PsGr-MA; (d) Crustal thickness. Black: underestimated area. Shades of blue: thin crust (< 6 km). White: 6-11 km thick crust. Grey: > 11 km thick crust. Dashed dark blue lines: 50 Ma contour from Müller *et al.* (2008).

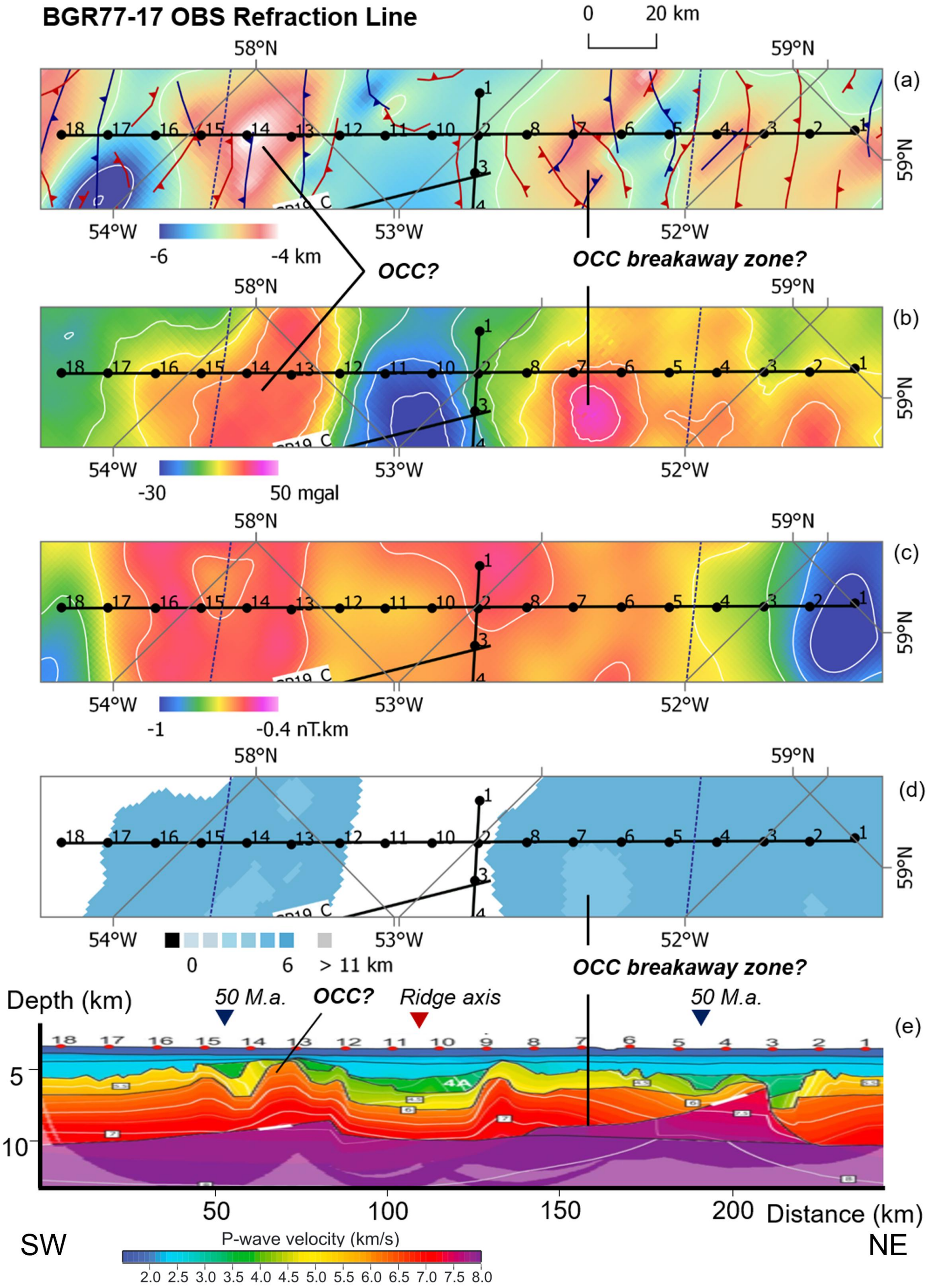

Figure 4.16: Crustal structure over the BGR77-17 line. (a) FLW basement depth overlaid by 1-km contours (white lines). Dark red lines: ACLAS-BA lineaments. Dark blue lines: ACLAS-MA lineaments. Horizontal bold black line: refraction seismic line, with OBS stations as numbered points. Vertical bold black line: reflection seismic survey line, with stations marked as numbered points. Dashed dark blue lines: 50 Ma contour, after Müller *et al.* (2008); (b) IMBA overlaid by 20-mGal contours (white lines); (c) PsGr-MA overlaid by 0.1-nT.km contours (white lines); (d) Crustal thickness; (e) Velocity model, after Delescluse *et al.* (2015).

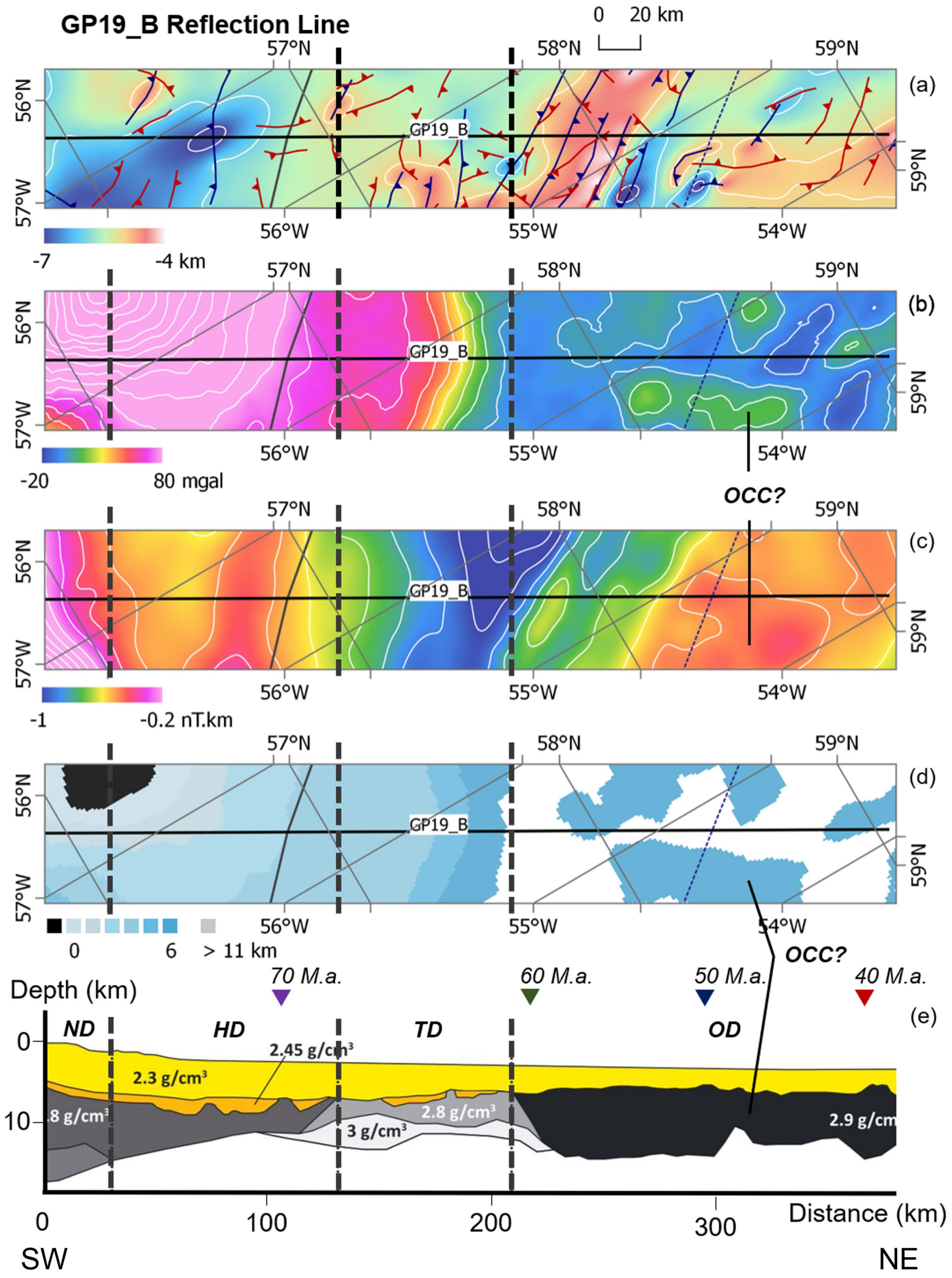

Figure 4.17: Crustal structure over the GP19_B line. (a) Depth to magnetic basement overlaid by 1-km contours (white lines). Dark red lines: ACLAS-BA lineaments. Dark blue lines: ACLAS-MA lineaments. Bold black lines: seismic lines. Numbered points: OBS stations. Dashed dark blue lines: 50 Ma contour, after Müller *et al.* (2008); (b) IMBA overlaid by 20-mGal contours (white lines); (c) PsGr-MA overlaid by 0.1-nT.km contours (white lines); (d) Crustal thickness; (e) Seismic layers, after Gouiza & Paton (2019). ND: necking domain. HD: hyperextended domain. TD: tectonic domain. OD: oceanic domain. Bold dashed lines: domain boundaries, after Gouiza & Paton (2019). Interpreted OCC is discussed in the text.

4.6 Conclusions

A number of gravity and magnetic processes have been employed and tested to propose the basement structure and classification in the Labrador Basin. The major tectonic structures such as these are revealed by employing the first vertical derivative of the free-air gravity anomaly. Afterwards, the smaller-scale structures can be observed by employing the ACLAS technique to the Bouguer gravity anomaly and the reduced-to-pole magnetic anomaly grids. The data are preconditioned by applying a 50-km low-pass filter to limit the size of the structures we would like to see.

The pseudogravity technique is also proven useful for classifying the character of the crust, as it generalises the wavelengths of the reduced-to-pole magnetic anomaly into those mimicking more closely the gravity signature. Coupled with the mantle Bouguer anomaly, the pseudogravity of the reduced-to-pole magnetic anomaly (PsGr-MA) enables us to identify the potential lithology of the crust at different areas based on its amplitude and spatial trend. Potential OCCs are identified based on the presence of high mantle Bouguer anomaly, high PsGr-MA, and the surrounding gravity and magnetic lineaments identified through the ACLAS technique. In BGR77-17, two potential OCCs are found using those identification techniques, supported by the intepreted crustal layers from an OBS-refraction seismic line. Meanwhile, in GP19_B, one potential OCC is found close to the extinct axis using the same identification techniques, supported by an area of elevated Moho interpreted in the reflection seismic line. The sizes of these interpreted OCCs are around 20 km. I also identified a significant area of thin crust, which is likely to be formed by a continuous tectonic extension through detachment faulting with alternating dip directions – a character found over ultra-slow-spreading ridges.

However, the study suggests that the MBA techniques might be more suitable to be employed at oceanic to transitional crust, as it shows great discrepancy with the Moho derived from refraction seismic methods, starting from the hyperextended domain landwards to the continental crust. The issue concerning the MBA and crustal thickness computation might come from the lack of sediment thickness data at areas closer to the continental crust and the highly complex nature of the lithology and rheology of the crust in this relatively large area. The assignment of a single density value for each layer might not work as well as when it is applied at a smaller area.

The study also employs the finite local wavenumber method to compute the depth to the magnetic basement. The depth to basement resulting from this technique generally makes more spatial sense than the one computed solely by subtracting the sediment thickness grid from the bathymetry, as the sediment thickness grid depends strongly on the accuracy of the data incorporated within it. However, it is important to note that the method only works in areas with good coverage of magnetic surveys.

These conclusions are drawn based on the observation over the extinct ridge and the various oceanic and continental domains at the Canadian margin. Similar study at the Greenland margin as the conjugate should be conducted to have an overview of this area as whole. Comparative profiles between these two conjugate margins will further our understanding, specifically on the varying spreading mode from the start of the seafloor spreading to the extinction. However, there is currently no seismic data set publicly available on the Greenland margin. Therefore, a comparison was not able to be carried out during this study, to complement the Canadian margin investigation.

References

Abdelmalak, M. M., Planke, S., Polteau, S., Hartz, E., Faleide, J., Tegner, C., Jerram, D., Millett, J., & Myklebust, R. (2019). Breakup volcanism and plate tectonics in the NW Atlantic. *Tectonophysics*, *760*, 267–296. 154

Baranov, V. (1957). A new method for interpretation of aeromagnetic maps: Pseudo-gravimetric anomalies. *Geophysics*, *22*(2), 359–382. 156

Blakely, R. J., Connard, G. G., & Curto, J. B. (2016). Tilt Derivative Made Easy. *Geosoft Technical Publications*, *4*, 30. 158

Bott, M., Smith, R., & Stacey, R. (1966). Estimation of the direction of magnetization of a body causing a magnetic anomaly using a pseudo-gravity transformation. *Geophysics*, *31*(4), 803–811. 156

Bown, J. W., & White, R. S. (1994). Variation with spreading rate of oceanic crustal thickness and geochemistry. *Earth and Planetary Science Letters*, *121*(3-4), 435–449. 154

Cannat, M. (1996). How thick is the magmatic crust at slow spreading oceanic ridges? *Journal of Geophysical Research: Solid Earth*, *101*(B2), 2847–2857. 154

Cascone, L., Green, C., Campbell, S., Salem, A., & Fairhead, D. (2017). ACLAS – A method to define geologically significant lineaments from potential-field data. *Geophysics*, *82*(4), G87–G100. 157

Chalmers, J. A., & Pulvertaft, T. (2001). Development of the continental margins of the Labrador Sea: A review. *Geological Society, London, Special Publications*, *187*(1), 77–105. 154

Chian, D., Keen, C., Reid, I., & Louden, K. E. (1995). Evolution of nonvolcanic rifted margins: New results from the conjugate margins of the Labrador Sea. *Geology*, *23*(7), 589–592. 154

Cowie, P. A., & Karner, G. D. (1990). Gravity effect of sediment compaction: Examples from the North Sea and the Rhine Graben. *Earth and Planetary Science Letters*, *99*(1-2), 141–153. 160

Delescluse, M., Funck, T., Dehler, S. A., Louden, K. E., & Watremez, L. (2015). The oceanic crustal structure at the extinct, slow to ultraslow Labrador Sea spreading center. *Journal of Geophysical Research: Solid Earth*, *120*(7), 5249–5272. 154, 155, 161, 162, 168, 182, 187

Dick, H. J., Lin, J., & Schouten, H. (2003). An ultraslow-spreading class of ocean ridge. *Nature*, *426*(6965), 405–412. 154

Gaina, C., Gernigon, L., & Ball, P. (2009). Palaeocene–Recent plate boundaries in the NE Atlantic and the formation of the Jan Mayen microcontinent. *Journal of the Geological Society*, *166*(4), 601–616. 154

Gouiza, M., & Paton, D. A. (2019). The role of inherited lithospheric heterogeneities in defining the crustal architecture of rifted margins and the magmatic budget during continental breakup. *Geochemistry, Geophysics, Geosystems*, *20*(4), 1836–1853. 155, 161, 162, 179, 183, 185, 188

Hosseinpour, M., Müller, R., Williams, S., & Whittaker, J. (2013). Full-fit reconstruction of the Labrador Sea and Baffin Bay. *Solid Earth*, *4*(2), 461–479. 154, 162, 164, 174

Kuo, B.-Y., & Forsyth, D. W. (1988). Gravity anomalies of the ridge-transform system in the South Atlantic between 31 and 34.5 S: Upwelling centers and variations in crustal thickness. *Marine Geophysical Researches*, *10*(3-4), 205–232. 174

Larsen, L. M., Heaman, L. M., Creaser, R. A., Duncan, R. A., Frei, R., & Hutchison, M. (2009). Tectonomagmatic events during stretching and basin formation in the Labrador Sea and the Davis Strait: Evidence from age and composition of Mesozoic to Palaeogene dyke swarms in West Greenland. *Journal of the Geological Society*, *166*(6), 999–1012. 154

Lin, J., Purdy, G., Schouten, H., Sempere, J., & Zervas, C. (1990). Evidence from gravity data for focused magmatic accretion along the Mid-Atlantic Ridge. *Nature*, *344*(6267), 627–632. 174

Maus, S., Barckhausen, U., Berkenbosch, H., Bournas, N., Brozena, J., Childers, V., Dostaler, F., Fairhead, J. D., Finn, C., von Frese, R. R. B., Gaina, C., Golynsky, S., Kucks, R., Lühr, H., Milligan, P., Mogren, S., Müller, R. D., Olesen, O., Pilkington, M., Saltus, R., Schreckenberger, B., Thébault, E., & Caratori Tontini, F. (2009). EMAG2: A 2–arc min resolution Earth Magnetic Anomaly Grid compiled from satellite, airborne, and marine magnetic measurements. *Geochemistry, Geophysics, Geosystems*, *10*(8). 163, 166

Meyer, B., Saltus, R., & Chulliat, A. (2017). EMAG2 Version 3-Update of a two arc-minute global magnetic anomaly grid. In *EGU General Assembly Conference Abstracts*, (p. 10614). 163, 166

Müller, R. D., Sdrolias, M., Gaina, C., & Roest, W. R. (2008). Age, spreading rates, and spreading asymmetry of the world's ocean crust. *Geochemistry, Geophysics, Geosystems*, *9*(4). 166, 173, 182, 186, 187, 188

Nabighian, M. N. (1972). The analytic signal of two-dimensional magnetic bodies with polygonal cross-section: Its properties and use for automated anomaly interpretation. *Geophysics*, *37*(3), 507–517. 158

Osler, J. C., & Louden, K. E. (1995). Extinct spreading center in the Labrador Sea: Crustal structure from a two-dimensional seismic refraction velocity model. *Journal of Geophysical Research: Solid Earth*, *100*(B2), 2261–2278. 154

Oufi, O., Cannat, M., & Horen, H. (2002). Magnetic properties of variably serpentinized abyssal peridotites. *Journal of Geophysical Research: Solid Earth*, *107*(B5), EPM–3. 182

Parker, R. (1973). The rapid calculation of potential anomalies. *Geophysical Journal International*, *31*(4), 447–455. 160, 174

Reid, I., & Jackson, H. (1981). Oceanic spreading rate and crustal thickness. *Marine Geophysical Researches*, *5*(2), 165–172. 154

Roest, W., & Srivastava, S. (1989). Sea-floor spreading in the Labrador Sea: A new reconstruction. *Geology*, *17*(11), 1000–1003. 154, 174

Salem, A., Blakely, R., Green, C., Fairhead, D., & Ravat, D. (2014). Estimation of depth to top of magnetic sources using the local-wavenumber approach in an area of shallow Moho and Curie depth – The Red Sea. *Interpretation*, *2*(4), SJ1–SJ8. 159, 177

Salem, A., Williams, S., Fairhead, J. D., Ravat, D., & Smith, R. (2007). Tilt-depth method: A simple depth estimation method using first-order magnetic derivatives. *The leading edge*, *26*(12), 1502–1505. 157, 158

Sandwell, D. T., Müller, R. D., Smith, W. H., Garcia, E., & Francis, R. (2014). New global marine gravity model from Cryosat-2 and Jason-1 reveals buried tectonic structure. *Science*, *346*(6205), 65–67. 161, 162, 164, 165

Srivastava, S., & Keen, C. (1995). A deep seismic reflection profile across the extinct Mid-Labrador Sea spreading center. *Tectonics*, *14*(2), 372–389. 154

Srivastava, S., & Roest, W. (1999). Extent of oceanic crust in the Labrador Sea. *Marine and Petroleum Geology*, *16*(1), 65–84. 154

Straume, E. O., Gaina, C., Medvedev, S., Hochmuth, K., Gohl, K., Whittaker, J. M., Abdul Fattah, R., Doornenbal, J. C., & Hopper, J. R. (2019). Globsed: Updated total sediment thickness in the world's oceans. *Geochemistry, Geophysics, Geosystems*, *20*(4), 1756–1772. 163, 167, 177

Thurston, J. B., & Smith, R. S. (1997). Automatic conversion of magnetic data to depth, dip, and susceptibility contrast using the SPI (TM) method. *Geophysics*, *62*(3), 807–813. 157

Wang, T., Lin, J., Tucholke, B., & Chen, Y. J. (2011). Crustal thickness anomalies in the North Atlantic Ocean basin from gravity analysis. *Geochemistry, Geophysics, Geosystems*, *12*(3). 160

Chapter 5

Discussions and conclusions

5.1 General summary

The aim of this study is to characterise the different crustal morphologies resulting from the different types of spreading at a passive continental margin. The characterisation is first carried out by observing the available bathymetry, gravity, and magnetic data over an active slow-spreading ridge, where two types of spreading occur, namely magmatic and tectonic spreading. The two types of spreading result in two distinct morphologies, where fault-bounded abyssal hills are found over magmatic terrain and long-lived detachment faults exposing mantle rocks are found over tectonic terrain. Parts of the Mid-Atlantic Ridge (MAR) are chosen to carry out this part of characterisation based on data availability and the general assumption that this slow-spreading ridge hosts both types of spreading. However, the distinct morphology is not observable at passive continental margins, as most of these features have been buried by the sediments deposited from the continental crust. Thus, gravity and magnetic data are selected as another identification tool as they correspond to specific physical properties of the basement, i.e. the oceanic crust. By characterising the gravity and magnetic signatures of the different types of spreading over an active slow-spreading ridge, the crustal types classification can be carried out and reapplied over a sedimented passive margin.

Characterisation is firstly carried out by quantifying the directional components of a multibeam bathymetry data. This technique is not suitable to be employed on the gravity and magnetic data as they do not directly reflect the morphology of the crust, but rather they are a sum of the observed physical properties of the layers beneath the observation points. Hence, I employed and assessed a series of gravity and magnetic data enhancement to see how the techniques can aid the classification. Over the ridge, the classification can be carried out by computing the crustal thickness variation inferred from gravity, where areas defined as thin crust (< 6 km, in this study) are interpreted to host detachment faulting. The evolution of the ridge can also be observed by picking the magnetic stripes and observe how the spreading rate changes through time. Comparing the crustal thickness variation, spreading rate, and directional components of multibeam (where available) will offer us an opportunity to understand the evolution of the magmatic and tectonic processes over the ridge. The comparison leads us to understand the relationship between the two processes with the resulting crustal morphology.

Finally, I carried out the observation over a passive margin, specifically over the Labrador Basin. The area is chosen based on the availability of field-surveyed magnetic data. To classify the underlying crust at this area, I computed the crustal thickness and the depth to magnetic basement. In addition, I also carried out tectonic and general structure interpretation using techniques based on potential field derivatives. As the underlying ridge at the Labrador Basin is believed to be the remains of an extinct ultra-slow-spreading ridge, the resulting classification is more typical of an ultra-slow-spreading crust where a significant area of thin crust is observed. The study shows that gravity and magnetic data can play an important role in classifying the types of crust, both over a spreading ridge and over a sedimented area.

5.2 Characterisation of the different types of spreading over the ridge

5.2.1 Quantitative description of tectonic and magmatic spreading based on the directional components of shipboard multibeam bathymetry

In the vicinity of a slow-spreading ridge, magmatic features are identified as fault-bounded abyssal hills parallel to the spreading axis, while tectonic features are identified as chaotic seafloor with the presence of long-lived detachment faults and domed features now known as oceanic core complexes (OCCs). These typical geometries led to an effort to characterise these features based on their directionality. The faults at magmatic ridges are commonly dipping towards the spreading ridge. The rotated blocks leave another steep slope at the opposite side of the fault, creating abyssal hills morphology with bi-directional dipping slopes. Meanwhile, the tectonic terrain is composed of detachment faults, compensating for the creation of the domed OCCs. The domed morphology is indicated in the bathymetry as slopes dipping in an omnidirectional manner. The statistics and behaviour of these directional trends are quantitatively expressed as the eigenvalues of the bathymetric grids, which led to establishing the slope-weighted eccentricity (SWE) technique in Chapter 2.

The principle of SWE is to apply a moving window over gridded multibeam bathymetry data and to first compute the eccentricity of its two horizontal eigenvalues. A high eccentricity number indicates that the governing horizontal eigenvalues at the sampled terrain patch are significantly different, while a low eccentricity number indicates a terrain patch with similar or very close horizontal eigenvalues. Ideally, this means that the area with high eccentricity number indicates the bi-directional abyssal hills, while areas with low eccentricity number indicate the presence of a more omnidirectional tectonic terrain. However, the results may not directly show the expected classification, as we have not introduced the vertical dimension to the computation. Therefore, a vertical dimension is introduced as weights derived from the sine of the slope, regardless of azimuth. The sine is computed to constrain the weights to the range 0 to 1, which is the same range as the eccentricity of the horizontal eigenvalues; hence the term slope-weighted eccentricity. The SWE technique is proven to aid and automate terrain classification, specifically over slow-spreading terrain, where both types of spreading occurred over time. The test is conducted both over the Fifteen-Twenty and the Atlantis fracture zone areas over the Mid-Atlantic Ridge (MAR), where both magmatic and tectonic terrain has been identified from previous studies.

Initially, the SWE technique was expected to be applicable independently of the gravity and magnetic data, as the main idea of this study is to classify the crustal types over areas covered by sediments. However, the SWE technique has not managed to classify the crust based on the directionality of either the gravity or magnetic data, as the signatures observed do not necessarily depict the shape or the morphology of the top of the crust. It is rather a sum of the gravity or the magnetic attraction over the layers beneath the observed grids. In addition, the size of the key features is smaller than the shortest available wavelength of gravity and magnetic data that is observable over the ridge. Some of the reasons are the great distance between the measuring platform and the source and the lateral interval between each survey line. If the distance between the measuring platform and the source is greater than the general diameter of the object of the interest, the object might not be able to be detected. The same thing occurs if the distance/interval between each survey line is greater than the general size of the object of interest. Based on these findings, I decided to explore other techniques to aid the characterisation and classification of the crust into magmatic and tectonic terrain.

5.2.2 Depth to Moho and crustal thickness variation inferred from gravity data: slow-spreading ridge

One of the most common techniques used to identify tectonic and magmatic crust is by computing the residual mantle Bouguer anomaly (RMBA) from the free-air gravity anomaly (FAA). The idea of RMBA is to isolate the gravity signatures within the crustal layer (Kuo & Forsyth, 1988). This is carried out by eliminating signatures resulting from the density contrast between the water and crust layers, as well as from the density contrast between the crust and mantle layers. However, in this technique, each of the layers is assumed to be homogenous. Hence, the variation is assumed to be coming from the varying depths to the interfaces of these layers. The gravity variation observed within the water-crust interface is removed by computing from the FAA the Bouguer anomaly (BA) using the Parker (1973) technique applied through the *gravfft* function in GMT 5.4.5 software. The gravity effects resulting from the variation observed between the crust and mantle layers is commonly defined by computing the gravity thermal effect from a passive upwelling model (Morgan & Forsyth, 1988). The passive upwelling model itself can be computed using the plate model equation to form the depth of the lithosphere, which is explained in Section 3.4.3. Based on the modelling carried out in this study, the computed gravity effects tend to overestimate the gravity signature over the ridge and tend to have little to no impact at distances further than ∼100 km from the spreading axis at the MAR. This is because the lithospheric model is designed to be flattened when the depth of the lithosphere reaches 100 km. In effect, the RMBA tends to work relatively well when applied to a distance up to ∼100 km from the ridge, but is not as useful further away than that.

As the lithospheric model is not correctly depicting a proxy of the crust-mantle interface, I conducted a test by introducing the Moho gravity effect of an elastic plate as the gravity signature from crust-mantle interface, also applied through the *gravfft* function. By introducing this elastic effect as the crust-mantle interface, we will obtain an oceanic crust compensated through flexural isostasy, where bathymetric highs correspond to a deeper Moho, and bathymetric lows correspond to a shallower Moho. The elastic effect is computed from the multibeam bathymetry grid. The resulting elastic anomaly appears to have similar spatial trends to the long wavelength of the computed mantle Bouguer anomaly (MBA). Hence, by subtracting the elastic anomaly from the MBA, we obtain the gravity anomaly whose source is fully isolated within the crustal layer. Following its isostatic character, this anomaly is named the isostatic mantle Bouguer anomaly (IMBA), replacing the 'residual' in RMBA. Similar to the RMBA, high IMBA values indicate thin crust as it depicts the proximity of the mantle to the ocean floor, while low IMBA values indicate thick crust. The thin crust itself corresponds to the tectonically extended terrain, while the thick crust corresponds to the magmatically accreted terrain.

Furthermore, we can estimate the depth to Moho by computing from the IMBA the crustal thickness variation through an infinite slab formula. The computed depths to Moho are statistically well correlated with those observed from various refraction seismic surveys using the ocean-bottom seismometers (OBS-refraction). Based on the statistics, I conclude that the computed crustal thickness can also be used as a proxy to classify the type of the oceanic crust observed in the vicinity of the spreading axis, where crust thinner than the initial crustal thickness (e.g. 6 km) is classified as tectonic crust.

5.2.3 Asymmetric seafloor spreading

In addition to the classification, we can observe how the Mid-Atlantic Ridge at Kane (MARK) area in Chapter 3 shows a typical example of ridge segments with asymmetric spreading over time. The asymmetry is observable by picking the magnetic chrons from the gridded magnetic anomalies and comparing the distance between the chrons from the oldest traceable crust to the youngest crust over the spreading axis. Coupled with the crustal type classification through SWE and the crustal thickness variation through IMBA, we can explore the evolution of the spreading segments over time and how it relates to the construction of specific oceanic crust features.

5.3 Crustal type classification over sedimented area and passive continental margins

5.3.1 Basement structure interpretation

To map out the major tectonic structures, I applied the vertical derivative (VDR) technique over the 50-km low-pass-filtered FAA grid. The major tectonic structures, such as the spreading axis and fracture zones, are traced from the VDR-FAA. To facilitate easier recognition of the relationship between these tectonic structures, I divided the spreading axis into eight segments based on the apparent offsets observed in the VDR-FAA. Afterwards, the smaller-sized structures are defined using the ACLAS technique, applied to both the gravity and magnetic data. In addition to highlighting the structures, the ACLAS technique can also act as a proxy for the quality of the gridded data, where sparse lineaments might correspond to a lack of high-quality field data. This can be observed more clearly by comparing the magnetic lineaments to the reduced-to-pole magnetic anomaly (RTP-MA) and the pseudogravity of the magnetic anomaly (PsGr-MA).

The ACLAS technique was built to aid geologic structure identification from lineaments or edges derived from two or more geophysical processing techniques applied to either gravity or magnetic anomaly datasets. The main advantages of this technique are that it removes artefacts not related to real edges, it detects the direction of lower density or susceptibility over the grid, and it is quick to implement (Cascone *et al.*, 2017). The method can also combine more than two sets of lineaments, according to the interpretation needs. Throughout this study, I combine only the maxima of the total horizontal derivative (THDR) and the zero contour of the tilt derivative (TDR) of both gravity and magnetic data over the same area. However, as the gravity field responds according to $1/\mathrm{r}^2$ (the distance r to centre of mass change) while the magnetic field according to $1/\mathrm{r}^3$ (the distance to top of the body), I applied the vertical derivative (VDR) over the gravity anomaly grid prior to application of the ACLAS technique. The resulting lineaments then act as a guide to interpret the general structure across the basin, especially if complemented with other sets of processed gravity and magnetic data.

5.3.2 Depth to Moho and crustal thickness variation inferred from gravity data: Extinct ultra-slow-spreading ridge

At an extinct ultra-slow-spreading ridge, the depth to Moho is inferred from the MBA as the thermal effect from the lithosphere is assumed to be negligible at an extinct ridge. However, as we are now working at a passive continental margin, we need to take into account the gravity attraction of sediments covering the oceanic crust over the study area. The gravity attraction is computed using the exponential density-depth curve (Cowie & Karner, 1990), where the total sediment thickness is divided into layers with varying density values based on its depth from the seafloor. In Chapter 4, I use the arbitrary layer thicknesses and boundaries defined by Wang *et al.* (2011). Dividing the sediment into more layers could potentially result in better accuracy of the computed gravity attraction, assuming no carbonates, salt, and/or volcanic rocks – or other units of relatively extreme densities – are present. In the Labrador Basin area, the crust-mantle interface is not taken into account as the ”bulls-eye” pattern commonly found over ridges with active upwelling mantle is not observed in the MBA, indicating little to no observable thermal effect from the mantle. From the MBA, I compute the depth to Moho using the infinite slab formula. The computed Moho is then compared with the Moho observed from available refraction and reflection seismic data, both across the extinct ridge and across the ocean-continent transition. In general, the computed Moho is in good accordance with the seismic Moho, specifically over the oceanic and transitional domain. Computing the depth to Moho is key to understanding the crustal thickness variation, which will aid crustal classification into tectonic and magmatic terrain.

Based on the crustal thickness variation inferred from observing the variation of the depth to Moho from the top of the crust layer, I found that the majority of the crust at Labrador Basin is ‘thinner than normal crust’ (< 6 km). This finding correlates well with the hypothesis that over ultra-slow-spreading ridge, the limited magma supply can only accommodate a small fraction of the seafloor spreading. The majority of the spreading thus must be accommodated by tectonic extension. The waning of magma supply, coupled by tectonic extension, results in slower cooling of the newly created oceanic crust. This slow cooling facilitates a more ductile type of deformation at both ridge flanks through the creation of detachment faults. It is important to note that unlike at slow-spreading ridges, detachment faulting can occur at both sides of the ridge, with alternating dip directions. In effect, it is common to find mantle exhumation at both flanks of one ridge segment.

5.3.3 Crustal type classification from gravity and magnetic data

The final goal of this study is to present crustal type classification based on gravity and magnetic data enhancements. In Chapter 4, I presented maps of: (1) gravity and magnetic lineaments interpreted through the ACLAS method, which represents the general crustal structure over the area; (2) depth to basement estimated from the finite local wavenumber (FLW) technique; (3) MBA; (4) PsGr-MA, and; (5) crustal thickness variation. Compared to two interpreted seismic profiles over the area, these maps prove to aid the basement structure classification, where prominent OCCs are indicated as well as a significant area of thin crust. The findings support the general idea that ultra-slow-spreading ridges are mostly composed of thin crust, which hosts a series of alternating detachment faults. Furthermore, the map can be used as a guide for further studies, which may suggest places in which mantle exhumation might occur.

5.4 Recommendations for future work

5.4.1 Testing SWE technique over a different type of morphology and dataset

As explained in the previous section, the SWE tecnique developed in Chapter 2 works well in aiding terrain classification over a mid-ocean ridge environment. In Chapter 2 and 3, the SWE has been applied to classify the oceanic crust into extended tectonic crust or the fully accreted magmatic crust. It will be interesting to see how the SWE will work over an area with different ridge characteristics, such as the fast spreading ridge (e.g., East-Pacific Rise) and the ultraslow spreading ridge (e.g., Southwest Indian Ridge, Gakkel Ridge). By applying this method over areas with different ridge characteristics, we will potentially have a well-rounded metric to describe the overall capability of the technique, as the range of numbers given in Chapter 2 are still an estimate based on the comparison between the SWE grid and the visually interpreted bathymetry.

Testing the SWE method on gravity and magnetic data over a larger area will also be an interesting study to conduct, for instance, in an area as big as shown in Chapter 4. The application of SWE over various sets of gravity and magnetic data in the vicinity of the spreading axis still yields unsatisfactory results as the wavelengths of the data are much longer than those observed in multibeam bathymetry data. The unsatisfactory results are also observed when the pseudogravity and the FLW method were applied to the same sets of gravity and magnetic data, suggesting that it might be worthwhile to test if the SWE method would work if applied to either gravity or magnetic data over a larger area. However, it is important to re-evaluate the parameters given in the algorithm, such as the window size, the determination of the weight matrix, as well as the determination of the cut-off wavelength used in the LoG filters. The evaluation also illustrates that the use of each processing technique depends on the size of the object of interest. For instance, the SWE method might have the potential to aid crustal classification based on the observed gravity and magnetic signature, but might not as far as identifying individual OCCs. The capability the technique relies closely to the general bathymetry and variation of the depth to the top of the crust in the study area, as well the design of the gravity and magnetic survey, manifested in the number of survey lines and the interval of between each of the survey lines.

5.4.2 Automating crustal type classification

In Chapter 4, I have compared the PsGr-MA signatures to the MBA and the resulting crustal thickness variation to interpret the types of the crust within the Labrador basin. Crustal structures derived from the application of the ACLAS technique to the reduced-to-pole magnetic anomaly and to the gravity anomaly are also used to aid the crustal types identification, as the technique is able to identify not only the length of each structure, but also the direction to which the structures are dipping. The interpretation is carried out more specifically along an OBS-refraction seismic line across the extinct axis and along a reflection seismic line within the Canadian ocean-continent transition. The general comparison is used to determine the morphology of the underlying crust. The comparison that has been carried out in Chapter 4 is still limited to visual comparison with no specific quantitative description. It will be interesting to correlate outcomes of multiple gravity and magnetic data processing techniques, for example through GIS-based data processing, to see if the correlation can further characterise the type of the crust observed over the area, which will reduce the subjectivity of the interpretation.

Automating the interpretation means carrying out several tests to assess the statistics of the correlation values. First, we need to have a definition of the range of gravity and magnetic anomaly values over several sets of data at different areas. The definition of the range of each derivatives, specifically the vertical, horizontal, and total derivatives are also assessed at these different areas. Second, having the ranges defined, correlation between at least two sets of data (e.g. PsGr-MA and MBA) can be carried out to set a range of values that might define certain types of lithology. Finally, the resulting correlation grid should be compared with interpreted seismic profiles to test the reliability of the technique.

5.4.3 Interpreting crustal structure from field magnetic surveys

Over the course of this study, I compare the outcome of each method over various sets of data, ranging from the gridded shipborne data, satellite-derived data, global synthesised data, and specific sets of data provided by Getech, plc. In Chapter 3, we can see that the discrepancy between the field and satellite-derived gravity data is negligible over the MARK area, while it is not the case with magnetic anomalies. We can see that the magnetic anomaly maps provided by either the EMAG2v2 or EMAG2v3 are not comparable to those gridded from various magnetic surveys. In the chapter, I chose to work with satellite-derived gravity rather than gridded shipborne gravity anomaly because the tie-line mismatches between the different course of gravity surveys are seen as artefacts after the application of the various gravity data enhancement techniques.

However, these mismatches are less significant over the gridded magnetic data because the range of magnetic anomaly data values is at least four times the range of the gravity anomaly values. For example, a tie-line mismatch of about 10 nT is not as significant in an area with a range of magnetic anomaly values of -200 and 200 nT, compared to a tie-line mismatch of about 10 mgal in an area with a range of gravity anomaly values of 0 to 50 mgal. Therefore, in Chapter 3, I chose to work with satellite-derived gravity anomaly and gridded shipborne magnetic anomaly.

Furthermore, we can see in Chapter 4 how various techniques (e.g. pseudogravity, FLW) depend greatly on the coverage of field magnetic data. For instance, we can see how the initial conventional tilt-depth estimation only works well over the areas with good field survey data coverage while returning extremely underestimated values over areas with less to no field survey data coverage. Other than magnetic anomalies, the lack of multibeam bathymetry data over the study area might also affect the IMBA computation, which might result in an unreliable estimate of depth to Moho. Therefore, in future studies, undertaking and utilising magnetic and multibeam bathymetry surveys is strongly encouraged to deliver better interpretation over a large area. Coupled with established techniques, the field data will aid interpretation over a larger area. The interpretation will guide decision-making on more expensive and time-consuming scientific or commercial expeditions, such as deciding where to conduct seismic surveys, where to dredge, and where to put drill holes to understand the area even better.

5.4.4 2-Dimensional crustal structure modelling

Last, 2D modelling of gravity and magnetic signatures will help assess the quality of the resulting grids. The cross-profile comparison over the extinct ridge and the oceanic to the transitional domain in Chapter 4 is solely based on the interpretations of Delescluse *et al.* (2015) and Gouiza & Paton (2019), respectively. The 2D cross-profiles are sampled from a 3D model resulting from an infinite slab calculation. There might be effects from the surrounding gravity to the sampled cross-profiles, which might constrain the variation in the 2D domain and affect the general depiction of the structure compared to having them as an actual 2D profile. Following the 2D modelling, it will surely be interesting to have 3D gravity and magnetic model over the sedimented area with good coverage of field-surveyed data and compare the models with the results obtained in this thesis.

5.5 Concluding remarks

Based on the aim and objectives of this study, I have been able to classify the types of basement at a passive continental margin based on characteristics observed close to the spreading axis. Observations on the bathymetry, gravity, and magnetic data over parts of the Mid-Atlantic Ridge have been carried out, followed by observation over the extinct ridge and the continental margin of the Labrador Basin. To achieve it, specific objectives have been accomplished, which are:

1. To develop an automatic terrain classification over known structures. In Chapter 2, I established the SWE, an automated interpretation technique to classify magmatic and tectonic crust over a slow-spreading ridge. The algorithm is built based on the parameterisation of the shape, directionality, and curvature of the seafloor around the Central Mid-Atlantic Ridge observed in shipboard multibeam bathymetry data. The seafloor is classified based on its mode of spreading.

2. To undertake blind trial of the developed algorithm and compare the results with gravity and magnetic data over slow-spreading ridges enhanced by more widely known techniques. In Chapter 3, I have applied the SWE technique to a different set of shipboard multibeam bathymetry data, which yields consistent results with those tested in Chapter 2. Various gravity and magnetic data enhancements have been applied over an active spreading axis to test the capability of each technique to aid the crustal structure interpretation. Tectonic maps resulting from the application of these techniques have broadened the understanding of the nature and evolution of the oceanic crust over a slow-spreading ridge.

3. To apply the assessed techniques to characterise and classify the crustal types over a less studied continental margin based on modes of spreading. Various gravity and magnetic data enhancements have been applied over an extinct spreading axis and a conjugate ocean-continent transition. Each method has been evaluated and discussed to describe its use and limitations. The types of crust over sedimented area have been classified with a combination of a modified technique (crustal thickness from IMBA/MBA) and established techniques (ACLAS, FLW, and pseudogravity).

This thesis has contributed to the establishment of a new grid-based interpretation technique, as well as to the assessment of existing gravity and magnetic interpretation techniques that can be applied over a sedimented ocean-continent transition. In addition, it also contributed to the further understanding of the magmatic and tectonic processes over a slow- to ultra-slow-spreading ridge. In addition to the aim and objectives of this study, I documented the asymmetry of an active slow-spreading ridge based on the technique that I have developed combined with the already established techniques. The combination of these approaches successfully classified the types of terrain, and furthermore revealed a comprehensive picture of the evolution of the spreading segments over time.

References

Cascone, L., Green, C., Campbell, S., Salem, A., & Fairhead, D. (2017). ACLAS – A method to define geologically significant lineaments from potential-field data. *Geophysics*, *82*(4), G87–G100. 200

Cowie, P. A., & Karner, G. D. (1990). Gravity effect of sediment compaction: Examples from the North Sea and the Rhine Graben. *Earth and Planetary Science Letters*, *99*(1-2), 141–153. 200

Delescluse, M., Funck, T., Dehler, S. A., Louden, K. E., & Watremez, L. (2015). The oceanic crustal structure at the extinct, slow to ultraslow Labrador Sea spreading center. *Journal of Geophysical Research: Solid Earth*, *120*(7), 5249–5272. 205

Gouiza, M., & Paton, D. A. (2019). The role of inherited lithospheric heterogeneities in defining the crustal architecture of rifted margins and the magmatic budget during continental breakup. *Geochemistry, Geophysics, Geosystems*, *20*(4), 1836–1853. 205

Kuo, B.-Y., & Forsyth, D. W. (1988). Gravity anomalies of the ridge-transform system in the South Atlantic between 31 and 34.5 S: Upwelling centers and variations in crustal thickness. *Marine Geophysical Researches*, *10*(3-4), 205–232. 198

Morgan, J. P., & Forsyth, D. W. (1988). Three-dimensional flow and temperature perturbations due to a transform offset: Effects on oceanic crustal and upper mantle structure. *Journal of Geophysical Research: Solid Earth*, *93*(B4), 2955–2966. 198

Parker, R. (1973). The rapid calculation of potential anomalies. *Geophysical Journal International*, *31*(4), 447–455. 198

Wang, T., Lin, J., Tucholke, B., & Chen, Y. J. (2011). Crustal thickness anomalies in the North Atlantic Ocean basin from gravity analysis. *Geochemistry, Geophysics, Geosystems*, *12*(3). 200

Appendix A

Slope-weighted eccentricity script

`SlopeWeightedEccentricity.m` is a Matlab-based geomorphometric algorithm to obtain the numerical description of both magmatic and tectonic crust in a slow-spreading ridge through a series of calculation based on the distribution of the azimuth and plunge observed in the seafloor morphology. The detailed explanation of this algorithm is discussed in Chapter 2. The script is built and last run in MATLAB 2020b and is made available through:

1. Github: `https://github.com/alodiaga/SlopeWeightedEccentricity`, and
2. MathWorks: `https://uk.mathworks.com/matlabcentral/fileexchange/96509-slopeweightedeccentricity-m`

The script requires two inputs:

1. A gridded shipborne multibeam bathymetry (depths in metres) in *.xyz format: `Input_Bathymetry_15s.xyz`;
2. A Laplacian-of-Gaussian (LoG) mask created from the bathymetry using a third party software/tool in *.xyz format: `Input_LoG_mask.xyz`

The LoG filter was applied to the gridded high-resolution bathymetry through the GETGrid v1.255 software provided by Getech, plc. If the LoG mask is not going to be used, I suggest creating a grid with the size and region of the gridded shipborne multibeam bathymetry and assigning the number '1' to all the cells (a 'no mask' example named '`Input_no_mask.xyz`' is provided) OR by exempting all the lines with the associated 'mask' from this script.

The outputs of this script are:

1. Eccentricity grid: `Output_eccentricity.xyz`;
2. Weight (1-sin θ) grid: `Output_weight.xyz`;
3. SWE grid: `Output_SWE.xyz`, and;
4. LoG-filtered SWE grid: `Output_SWE_masked.xyz`

Each output is exported in *.xyz format. The resulting *.xyz data can be converted into *.grd using the xyz2grd function in GMT (`http://gmt.soest.hawaii.edu/doc/5.3.2/xyz2grd.html`).

The shipborne multibeam bathymetry data sample is downloaded from the GMRT MapTool (`https://www.gmrt.org/GMRTMapTool/`) with the extent `xmin/xmax/ymin/ymax` of `-46/-44/12.5/13.15`

```
%% Slope-weighted eccentricity (SWE)
%  Alodia et al. (2021)
%  A geomorphometric algorithm to obtain the numerical description of
%  both magmatic and tectonic crust in a slow-spreading ridge through
%  a seriesof calculation based on the distribution of the azimuth
%  and plungeobserved in the seafloor morphology.

%% Input needed
%  1. A gridded shipborne multibeam bathymetry (depths in metres)
%     in *.xyz format (here: 'Input_Bathymetry_15s.xyz')
%  2. A Laplacian-of-Gaussian (LoG) mask created from the bathymetry
%     using a third party software/tool in *.xyz format
%     (here: 'Input_LoG_mask.xyz')

%  If the LoG mask is not going to be used, we suggest creating a
%  grid withthe size and region of the gridded shipborne multibeam
%  bathymetry andassigning the number '1' to all the cells (a 'no
%  mask' example named'Input_no_mask.xyz' is provided) OR by
%  exempting all the lines with the associated 'mask' from this
%  script.

%% Output
%  1. Terrain eccentricity (here: 'Output_eccentricity.xyz')
%  2. Weight matrix: 1-sin(slope) (here: 'Output_weight.xyz')
%  3. SWE: Slope-weighted eccentricity (here: 'Output_SWE.xyz')
%  4. Masked SWE (here: 'Output_SWE_masked.xyz')
%  Each output is exported in *.xyz format. An explanation on
%  converting *.xyz files into *.grd is presented at the end of the
%  script.
```

```
%% Closing and clearing the workspace

close all
clear all
clc

%% INPUT: Load data

% Input cell size & window size (in minutes)
cellsize=0.25;      % INPUT: Have to be the same with actual cell size
                    % Here it is 0.25 minutes (15 seconds)
cs=1/cellsize;
winsize=8*cs;       % INPUT: 8 minutes = ~14.8 km
% Window size can be modified but
% the number have to be even (6, 8, 10, etc.)

ss=cellsize*60;     % Cellsize in seconds
dd=cellsize/60;     % Cellsize in degrees

% INPUT: Gridded multibeam bathymetry with depth in METRES
% The resolution must comply with the determined 'cellsize'

data_input=load('Input_Bathymetry_15s.xyz');

lon=data_input(:,1);
lat=data_input(:,2);
depth=data_input(:,3);

% INPUT: Laplacian-of-Gaussian (LoG) mask from a third-party
% software/tool. The resolution must comply with the determined
% 'cellsize'

mask_input=load('Input_LoG_mask.xyz');

mask=mask_input(:,3);
```

```
%% Depth reshaped

l=length(find(lat==lat(1)));
lon_rs1=reshape(lon,l,[]);
lat_rs1=reshape(lat,l,[]);
depth_rs1=reshape(depth,l,[]);
mask_rs1=reshape(mask,l,[]);

%% Data borders for windowing

% Add top and bottom
lon_Ni=[lon_rs1(1,1)-dd*winsize:dd:lon_rs1(1,1)-dd]';
lon_Si=[lon_rs1(end,1)+dd:dd:lon_rs1(end,1)+dd*winsize]';

lat_NSi=lat_rs1(1,:);

for i=1:winsize
    for j=1:length(lon_rs1(1,:))
        depth_NS(i,j)=NaN;
        mask_NS(i,j)=NaN;
        lon_N(i,j)=lon_Ni(i);
        lon_S(i,j)=lon_Si(i);
        lat_NS(i,j)=lat_NSi(j);
    end
end

depth_input2=[depth_NS; depth_rs1; depth_NS];
lon_input2=[lon_N; lon_rs1; lon_S];
lat_input2=[lat_NS; lat_rs1; lat_NS];

mask_input2=[mask_NS; mask_rs1; mask_NS];

% Add left and right
lat_Wi=fliplr([lat_input2(1,1)+dd:dd:lat_input2(1,1)+dd*winsize]);
lat_Ei=fliplr([lat_input2(1,end)-dd*winsize:dd:lat_input2(1,end)-dd]);

lon_EWi=lon_input2(:,1);
```

```
for i=1:winsize
    for j=1:length(depth_input2(:,1))
        depth_EW(i,j)=NaN;
        mask_EW(i,j)=NaN;
        lat_E(i,j)=lat_Ei(i);
        lat_W(i,j)=lat_Wi(i);
        lon_EW(i,j)=lon_EWi(j);
    end
end

depth_rs=[depth_EW' depth_input2 depth_EW'];
lon_rs=[lon_EW' lon_input2 lon_EW'];
lat_rs=[lat_W' lat_input2 lat_E'];

mask_rs=[mask_EW' mask_input2 mask_EW'];

%% Aspect and slope (azimuth and plunge) computation

gridrv=[60*60/ss 0 0];
[aspects,slope,gradN,gradE]=gradientm(depth_rs,gridrv);

for i=1:length(aspects(:,1))
    for j=1:length(aspects(1,:))
        if aspects(i,j) >= 0 && aspects(i,j) <= 270
            aspect(i,j)=aspects(i,j)+90;
        else
            aspect(i,j)=aspects(i,j)-270;
        end
    end
end

%% Depth, aspect, and slope visualisation

figure()

x0=0; y0=0;
width=1000; height=800;
set(gcf,'position',[x0,y0,width,height])
```

```
pcolor(lon_rs,lat_rs,depth_rs/1000); shading flat
colorbar; colormap(gca,'jet')
set(gca,'FontSize',16)
title ('Depth (km)')
ytickangle(90); axis equal
xlim([min(min(lon_rs)) max(max(lon_rs))])
ylim([min(min(lat_rs)) max(max(lat_rs))])

figure()

x0=0; y0=0;
width=1000; height=800;
set(gcf,'position',[x0,y0,width,height])

pcolor(lon_rs,lat_rs,aspect); shading flat
colorbar; colormap(gca,'hsv')
caxis([0 360]); set(gca,'FontSize',16)
title ('Aspect (\circ)')
ytickangle(90); axis equal

figure()

x0=0; y0=0;
width=1000; height=800;
set(gcf,'position',[x0,y0,width,height])

pcolor(lon_rs,lat_rs,slope); shading flat
colorbar; colormap(gca,'bone')
caxis([0 30]); set(gca,'FontSize',16)
title ('Slope (\circ)')
ytickangle(90); axis equal

%% Mask visualisation

figure()

x0=0; y0=0;
width=1000; height=800;
set(gcf,'position',[x0,y0,width,height])
```

```
pcolor(lon_rs,lat_rs,mask_rs); shading flat
colorbar;
oldcmap=colormap(gca,'bone');
colormap(flipud(oldcmap));
caxis([0 1]);
set(gca,'FontSize',16)
title ('LoG Mask')
ytickangle(90); axis equal

%% Making huge matrix: All dip direction (azimuth)

for k=1:winsize:(length(aspect(:,1))-winsize)*winsize
    for l=1:winsize:(length(aspect(1,:))-winsize)*winsize
        mat_aspect(k:k+winsize-1,l:l+winsize-1)=...
        aspect((((k-1)/winsize)+1):(((k-1)/winsize)+1)+winsize-1,...
        (((l-1)/winsize)+1):(((l-1)/winsize)+1)+winsize-1);
    end
end

%% Making huge matrix: All plunge (slope)

for k=1:winsize:(length(slope(:,1))-winsize)*winsize
    for l=1:winsize:(length(slope(1,:))-winsize)*winsize
        mat_slope(k:k+winsize-1,l:l+winsize-1)=...
        slope((((k-1)/winsize)+1):(((k-1)/winsize)+1)+winsize-1,...
        (((l-1)/winsize)+1):(((l-1)/winsize)+1)+winsize-1);
    end
end

%% Divide new matrix into windowed cells

nlin=floor(length(mat_aspect(:,1))/winsize);
ncol=floor(length(mat_aspect(1,:))/winsize);

vcell=ones(nlin,1)'*winsize;
hcell=ones(ncol,1)'*winsize;
```

```
cells=mat2cell(mat_aspect, vcell, hcell);

cells_slope=mat2cell(mat_slope, vcell, hcell);

%% Calculate eccentricity in each cell

for k=1:length(cells(:,1))
    for l=1:length(cells(1,:))
        [m,n]=size(cells{k,l});
        aspr=cells{k,l};
        slpr=cells_slope{k,l};

        % xyz components
        xc=sind(aspr).*cosd(-slpr);
        yc=cosd(aspr).*cosd(-slpr);
        zc=sind(-slpr);

        xr(k,l)=nansum(nansum(sind(aspr).*cosd(-slpr)));
        yr(k,l)=nansum(nansum(cosd(aspr).*cosd(-slpr)));
        zr(k,l)=nansum(nansum(sind(-slpr)));

        % R: resultant
        R(k,l)=sqrt(xr(k,l).^2+yr(k,l).^2+zr(k,l).^2);
        R_m(k,l)=R(k,l)/length(aspr(~isnan(aspr)));;

        % Lon, lat
        lon_win(k,l)=lon_rs(k,l)+(((winsize/cs)/2)/60);
        lat_win(k,l)=lat_rs(k,l)-(((winsize/cs)/2)/60);

        % Theta: plunge
        if xr(k,l) >= 0 && yr(k,l) >= 0
            theta_r(k,l)=atan(xr(k,l)/yr(k,l));
        elseif xr(k,l) < 0 && yr(k,l) >=0
            theta_r(k,l)=atan(xr(k,l)/yr(k,l))+degtorad(360);
        else
            theta_r(k,l)=atan(xr(k,l)/yr(k,l))+degtorad(180);
        end

        theta_d(k,l)=radtodeg(theta_r(k,l));
```

```
        % X-Count and Y-Count
        Xc(k,l)=R_m(k,l).*(sind(theta_d(k,l)));
        Yc(k,l)=R_m(k,l).*(cosd(theta_d(k,l)));
        % Eigen components
        num_x=length((cells{k,l}(~isnan(cells{k,l}))));

        if num_x > 0
            num_x = num_x;
        else
            num_x = 1;
        end

        % The B matrix
        Bs=[nansum(nansum(xc.^2)) nansum(nansum(xc.*yc)) ...
            nansum(nansum(xc.*zc));
            nansum(nansum(yc.*xc)) nansum(nansum(yc.^2)) ...
            nansum(nansum(yc.*zc));
            nansum(nansum(zc.*xc)) nansum(nansum(zc.*yc)) ...
            nansum(nansum(zc.^2))];

        B=Bs/num_x;

        D=eig(B);

        % Eccentricity

        a(k,l)=D(2); % Semi-major axis
        b(k,l)=D(3); % Semi-minor axis

        e(k,l)=sqrt(1-a(k,l).^2/b(k,l).^2);
    end
end
```

```
%% Make weight matrix and mask in the same size as eccentricity

for k=1:(length(depth_rs(:,1))-winsize)
    for l=1:(length(depth_rs(1,:))-winsize)
        sin_slope1(k,l)=sind((-slope(k+winsize/2,l+winsize/2)))/...
        -(sind(max(max(slope))));
        weight(k,l)=1-sin_slope1(k,l);
        mask_filt(k,l)=mask_rs(k+winsize/2,l+winsize/2);
    end
end

%% SWE: Slope weighted eccentricity

SWE=e.*weight;

%% Mask for SWE

for i=1:length(SWE(:,1))
    for j=1:length(SWE(1,:))
    if mask_filt(i,j) >= 0
        SWE_filt(i,j)=SWE(i,j);
    else
        SWE_filt(i,j)=NaN;
    end
    end
end

%% Plot e

figure()

x0=0; y0=0;
width=1000; height=800;
set(gcf,'position',[x0,y0,width,height])

pcolor(lon_win,lat_win,e); shading flat
colorbar
colormap(gca,'jet')
caxis([0.5 1])
```

```
xlim([min(min(lon_rs)) max(max(lon_rs))])
ylim([min(min(lat_rs)) max(max(lat_rs))])
set(gca,'FontSize',16); ytickangle(90)
title ('Eccentricity'); axis equal

%% Plot weight: 1-sin(slope)

figure()

x0=0; y0=0;
width=1000; height=800;
set(gcf,'position',[x0,y0,width,height])

pcolor(lon_win,lat_win,weight); shading flat
colorbar
colormap(gca,'jet')
caxis([0.5 1])
xlim([min(min(lon_rs)) max(max(lon_rs))])
ylim([min(min(lat_rs)) max(max(lat_rs))])
set(gca,'FontSize',16); ytickangle(90)
title ('Weight = 1-sin(slope)'); axis equal

%% Plot e * slope (SWE)

figure()

x0=0; y0=0;
width=1000; height=800;
set(gcf,'position',[x0,y0,width,height])

pcolor(lon_win,lat_win,SWE); shading flat
colorbar
colormap(gca,'jet')
caxis([0.5 1])
xlim([min(min(lon_rs)) max(max(lon_rs))])
ylim([min(min(lat_rs)) max(max(lat_rs))])
set(gca,'FontSize',16); ytickangle(90)
title ('Slope-weighted eccentricity (SWE)'); axis equal
```

```
%% Plot e * weight in masked area ( LoG > 0 )

figure()

x0=0; y0=0;
width=1000; height=800;
set(gcf,'position',[x0,y0,width,height])


cells_count=ncol*nlin;

pcolor(lon_win,lat_win,SWE_filt); shading flat
colorbar
colormap(gca,jet)
caxis([0.5 1])
xlim([min(min(lon_rs)) max(max(lon_rs))])
ylim([min(min(lat_rs)) max(max(lat_rs))])
set(gca,'FontSize',16); ytickangle(90)
title ('Masked SWE'); axis equal

%% WRITING DOWN

len=nlin*ncol;
e_rs=reshape(e,[1,len]);
weight_rs=reshape(weight,[1,len]);
SWE=e.*weight;
SWE_rs=reshape(SWE,[1,len]);
SWE_filt_rs=reshape(SWE_filt,[1,len]);

for i=1:nlin
    for j=1:ncol
        lon_win_sum(i,j)=lon_win(i,j);
        lat_win_sum(i,j)=lat_win(i,j);
    end
end

lon_win_sum_rs=reshape(lon_win_sum,[1,len]);
lat_win_sum_rs=reshape(lat_win_sum,[1,len]);
```

```
%% Eccentricity

fid1=fopen('Output_eccentricity.xyz', 'w');
for i=1:length(e_rs)
    fprintf(fid1, '%f %f %f\n',lon_win_sum_rs(i), ...
    lat_win_sum_rs(i), e_rs(i));
end

%% Weight: 1-sin(slope)

fid1=fopen('Output_weight.xyz', 'w');
for i=1:length(weight_rs)
    fprintf(fid1, '%f %f %f\n',lon_win_sum_rs(i), ...
    lat_win_sum_rs(i), weight_rs(i));
end

%% SWE: Slope-weighted eccentricity

fid1=fopen('Output_SWE.xyz', 'w');
for i=1:length(SWE_rs)
    fprintf(fid1, '%f %f %f\n',lon_win_sum_rs(i), ...
    lat_win_sum_rs(i), SWE_rs(i));
end

%% Masked SWE

fid1=fopen('Output_SWE_masked.xyz', 'w');
for i=1:length(SWE_filt_rs)
    fprintf(fid1, '%f %f %f\n',lon_win_sum_rs(i), ...
    lat_win_sum_rs(i), SWE_filt_rs(i));
end

%% XYZ to GRD

% The resulting *.xyz data can be converted into *.grd using the
% xyz2grd function in GMT
% (http://gmt.soest.hawaii.edu/doc/5.3.2/xyz2grd.html)
```